# STRUCTURAL EFFECTS ON NONADIABATIC PHOTOCYCLIZATION IN ORTHO-ARENES

by
Joshua A. Snyder

A dissertation submitted to Johns Hopkins University in conformity with the requirements for the degree of Doctor of Philosophy.

Baltimore, Maryland

May, 2017

# Abstract

Nonadiabatic photocyclization is the chemical dynamic relevant to the function of many photoswitchable materials as well as photochemical synthesis of polyaromatic hydrocarbons by cyclodehydrogenation. *ortho*-arenes are an under-studied class of molecular photoswitch owing to their low cyclized product stabilities that otherwise provide a unique opportunity for the experimentalist to study photocyclization mechanisms in detail. Through the use of time-resolved absorption spectroscopy on femtosecond to microsecond timescales the entire photocyclization process can be monitored from "birth" to "death," i.e. ring-fusion to ring-fission. Following ultraviolet photoexcitation OTP undergoes cyclization to form DHT. Although global spectral analysis with simple kinetic models adequately fits spectral dynamics, signatures of DHT formation are obscured by spectral overlap with the excited-state that has a lifetime of ~3 picoseconds. Thermal ring-reopening of DHT to regenerate OTP occurs with a 38 nanosecond lifetime and an activation energy of 0.27 eV. Following the study of OTP a variety of other *ortho*-arenes were examined by systematic substitution, including phenyl substituted analogs, 1,2,3-triphenylbenzene, *ortho*-quaterphenyl and hexaphenylbenzene, as well as boron-nitrogen substituted analogs, including hexaphenylborazine and 1,2:3,4:5,6 tris(*o,o'*-biphenylylene) borazine. Generally these substitutions increased the excited-state lifetime relative to OTP due to an increase in either electronic delocalization or structural hindrance within excited-state geometries while the stability of the corresponding photoproducts decreased relative to DHT due to entropic effects. A notable exception is hexaphenylbenzene, which exhibits a 2 microsecond lifetime for ring-reopening of the photoproduct tetraphenyl-DHT that is a consequence of entropic stabilization due to increased phenyl-phenyl steric interactions that constrain thermally activated relaxation to the transition state. Furthermore, excited hexaphenylborazine decays within 3 picoseconds due to the localized electronic character of the borazine ring. No direct spectroscopic observation of cyclization was observed for any boron-nitrogen substituted system due to the increase in charge localization that reduces the stability of the conjugated DHT photoproduct. More recent experiments utilizing pump-repump-probe spectroscopy have determined that the observed excited-state decay is kinetically decoupled from photocyclization, which occurs in less than 200 femtoseconds. The results presented in this thesis provide insight for the improvement of photoswitch and photosynthetic efficiency through the generalization of these structure-dynamics relationships.

Advisor: Dr. Arthur E. Bragg
Thesis Committee: Dr. Paul Dagdigian
Dr. David Yarkony

# Acknowledgements

To my family, friends and co-workers. Especially to my wife and son who make each day worth living. I love you both.

# Table of Contents

Abstract ........................................................ ii

Acknowledgements ........................................................ iv

List of Figures ........................................................ xii

List of Schemes ........................................................ xviii

List of Tables ........................................................ xix

Chapter 1: Introduction ........................................................ 1

1.1 Overview of Photoswitchable Molecular Materials ........................................................ 1

1.2 Photoswitching Explained with the Woodward-Hoffman Rules ........................................................ 7

1.3 Excited-state Photochemistry: Potential Energy Surfaces, Conical Intersections and Nonadiabatic Couplings. ........................................................ 14

1.3.1 Potential Energy Surfaces ........................................................ 14

1.3.2 Wavepackets and Quantum Superposition ........................................................ 16

1.3.3 Nonadiabatic Transitions at Conical Intersections ........................................................ 17

1.4 Overview of Dissertation Contents ........................................................ 20

1.5 References ........................................................ 24

Chapter 2: Experimental Methods ........................................................ 33

2.1 Introduction to Transient Optical Spectroscopies ........................................................ 33

2.2 Steady-State Spectroscopies ........................................................ 34

2.3 Principles of Transient Absorption Spectroscopy (TAS) ........................................................ 36

2.4 Femtosecond Transient Absorption Spectroscopy (fs-TAS) ........................................................ 38

2.4.1 Description of Femtosecond Laser Source ........................................................ 39

2.4.2 Wavelength Tunability: Nonlinear Optical Mixing and

Phase Matching ........................................................................42
2.4.2 Polarization Anisotropy ..............................................................43
2.4.2 fs-TAS Experimental Setup ..........................................................44
2.5 Nanosecond & Microsecond Transient Absorption................................47
2.6 Pump-Repump-Probe Spectroscopy ......................................................50
2.7 Global Fitting Algorithm .......................................................................53
2.8 Computational Chemistry Methods .......................................................56
2.9 References..............................................................................................57
Chapter 3: Ultrafast Excited State Dynamics of *ortho*-Terphenyl and 1,2-Diphenylcyclohexene: The Role of "Ethylenic Twisting" in the Nonadiabatic Photocyclization of Stilbene Analogs ..........................................................62
3.0 Abstract ..................................................................................................62
3.1 Introduction............................................................................................63
3.2 Results....................................................................................................66
3.3 Discussion..............................................................................................69
3.4 Conclusion .............................................................................................74
3.5 Experimental Methods...........................................................................76
3.6 Computational Methods.........................................................................77
3.7 References..............................................................................................79
Chapter 4: Structural Control of Nonadiabatic Bond Formation: The Photochemical Formation and Stability of Substituted 4a,4b-Dihydrotriphenylenes........................................................................................85
4.0 Abstract ..................................................................................................85

4.1 Introduction ....................................................................................86

4.2 Experimental Methods ........................................................................91

  4.2.1 Sample Preparation .......................................................................91

  4.2.2 Ultrafast Transient Absorption Spectroscopy (fs- TAS) .................92

  4.2.3 Nanosecond Transient Absorption Spectroscopy (ns-TAS). ............93

4.3 Computational Methods ......................................................................94

  4.3.1 SA-CASSCF Calculations ..............................................................95

  4.3.2 DFT and TDDFT Computations ....................................................95

4.4 Results and Analysis ..........................................................................96

  4.4.1 Spectroscopic Characterization of the Ultrafast Photoinduced Cyclization of TPB and OQTP ..........................................................................96

  4.4.2 Characterization of Dihydro Intermediate Lifetimes and Relative Stabilities via ns-TAS. ..............................................................................104

  4.4.3 Computational Characterization of Ground- and Excited-State Structures and Spectroscopy of OTP, TPB, OQTP, and Corresponding Dihydro Intermediates. ............................................................................106

    4.4.3.1 Characterization of Ground-State Geometries. ...............106

    4.4.3.2 Excitation Energies ........................................................111

    4.4.3.3 Characterization of Landmarks on Ground- and Excited-State PESs with SA-CASSCF and TDA-TDDFT.. .............................115

    4.4.3.4 Characterization of Intermediate Stabilities....................120

4.5 Discussion .........................................................................................121

  4.5.1 UV Photochemistry of TPB ..........................................................122

4.5.2 Photochemistry of UV-Excited OQTP ........................................124

4.5.3 Relative Stability of DHT Intermediates ......................................128

4.6 Conclusions ..........................................................................................131

4.7 References ...........................................................................................134

Chapter 5: Excited-state Deactivation Pathways and the Photocyclization of BN-doped Polyaromatics ........................................................................................140

5.0 Abstract ................................................................................................140

5.1 Introduction ..........................................................................................141

5.2 Methods ................................................................................................144

5.2.1 Sample Preparation ........................................................................144

5.2.2 Steady-state Spectroscopy, Fluorescence Quantum Yields and Lifetime Determinations ..........................................................................................145

5.2.3 Transient Spectroscopies ................................................................146

5.2.4 Determination of Triplet Yield and Extinction Coefficient ...........148

5.2.5 Matrix Isolation Experiments ........................................................149

5.2.6 Computational Methods .................................................................150

5.3 Results ..................................................................................................150

5.3.1 UV-Vis and Fluorescence Spectroscopy ........................................150

5.3.2 Transient Absorption Spectroscopy ...............................................153

5.3.3 Triplet Yield Determination ...........................................................159

5.3.4 Matrix Isolation Experiments ........................................................160

5.3.5 Computational Investigations ........................................................161

5.4 Discussion ............................................................................................163

5.5 Conclusion ........................................................................................168

5.6 Acknowledgements...................................................................................169

5.7 References.........................................................................................170

Chapter 6: Impacts of Isoelectronic BN-doping on the Photochemistry of Polyaromatic Hydrocarbons: Photocyclization Dynamics of Hexaphenyl Benzene and Hexaphenyl Borazine ..........................................................................................175

6.0 Abstract...........................................................................................175

6.1 Introduction........................................................................................176

6.2 Experimental........................................................................................181

6.2.1 Sample Preparation ..............................................................181

6.2.2 Femtosecond Transient Absorption Spectroscopy..........................182

6.2.3 Nanosecond Transient Absorption Spectroscopy ..........................183

6.2.4 µs-Resolved Broadband Transient Absorption Spectroscopy ........183

6.2.5 Photochemical Cyclodehydrogenation Reactions of **1** and **4** .........184

6.2.6 Quantum-chemical Computations ..............................................185

6.3 Results.............................................................................................186

6.3.1 Photophysical Characterization of **1** and **4** with Time-Resolved Spectroscopies.........................................................................186

6.3.2 Temperature-dependent Kinetics: Thermodynamic Parameters for the Ring Opening of **5**...........................................................190

6.3.3 Photoinduced Cyclodehydogenation of **4** and **1** ............................191

6.3.4 Quantum Chemistry and Computational Spectroscopy of Photoproducts **2** and **5**...........................................................192

6.4 Discussion ........................................................................................197

6.4.1 Photophysics of **1** and **4** and the Photochemistry of C-C bond Formation ........................................................................................197

6.4.2 Structure and Stability of Cyclized Intermediate **5** ........................199

6.4.3 Electronic Structure and Properties of Cyclized Intermediate **2** .....204

6.5 Conclusions ........................................................................................205

6.6 Acknowledgements ...............................................................................207

6.7 References ........................................................................................208

Chapter 7: Sub-Picosecond Nonadiabatic Bond Formation in ortho-arenes Revealed with Pump-repump-probe Spectroscopy ..............................................................214

7.1 Introduction ........................................................................................214

7.2 Experimental ........................................................................................218

7.2.1 Sample Preparation ........................................................................218

7.2.2 fs Pump-Repump-Probe Spectroscopy ..........................................218

7.2.3 Definition of States, Lifetimes and PRP Schemes .........................221

7.3 Results and Discussion ........................................................................225

7.3.1 PRP "Action" and "Bleach" Spectroscopy of DHT and OTP ........225

7.3.2 Anisotropy of the OTP to DHT Photoreaction .............................230

7.3.3 PRP Action Spectroscopy of Hexaphenylbenzene .........................233

7.4 Conclusions ........................................................................................235

7.5 References ........................................................................................236

Appendix 1: Supporting Information for Chapter 3 ..........................................242

Appendix 2: Supporting Information for Chapter 4 ..........................................260

Appendix 3: Supporting Information for Chapter 5 ..........................................279

Appendix 4: Supporting Information for Chapter 6 ..........................................290

Appendix 5: Autocorrelator Operation Guide & Pulse Characterization ...........305

Appendix 6: Details Regarding Prism-Based Femtosecond Transient Absorption Experiment: PDA Operation, Optical Setup and Instructions for Daily Use .....320

Appendix 7: Nanosecond to Microsecond Transient Absorption........................329

Appendix 8: Global Analysis Algorithm ............................................................333

Appendix 9: Curriculum Vitae..............................................................................343

# List of Figures

**Figure 1.1:** Potential applications of photoswitchable materials. ..........................4

**Figure 1.2:** Mallory reaction (photo-oxidation) of ortho-terphenyl (OTP) to triphenylene and orbital symmetries of OTP and dihydrotriphenylene (DHT).….13

**Figure 1.3:** Photoinduced chemical dynamics of a generalized nonadiabatic photochemical reaction.. ........................................................................15

**Figure 1.4:** Influence of conical intersection topology on photodynamics and resultant photoproduct formation.......................................................................19

**Figure 2.1:** Connection between light-induced molecular processes and experimental spectroscopic techniques…...........................................................34

**Figure 2.2:** Generalized femtosecond transient absorption setup and equipment utilized in the Bragg lab… .......................................................................40

**Figure 2.3:** Basic principles of nonlinear optical mixing....................................42

**Figure 2.4:** Comparison of experimental set-ups for femtosecond and nanosecond to microsecond transient absorption... .................................................48

**Figure 2.5:** Generalized pump-repump-probe experiment... ...............................50

**Figure 2.6:** Pump-Repump-Probe Experiment for deconvolution of spectral components and kinetics…........................................................................52

**Figure 2.7:** Flowchart for global fitting procedure and details of algorithm.…....55

**Figure 3.0:** Table of contents figure. ..................................................................62

**Figure 3.1:** Spectral dynamics of UV-exited 1,2-diphenylcyclohexene (DPCH) and *ortho*-terphenyl (OTP). ........................................................................67

**Figure 3.2:** Calculated dihedral and bond angles presented in Table 3.1 and described in the text are defined with respect to the bonds depicted with dotted lines.........................................................................................................70

**Figure 3.3:** Schematic depiction of potential energy surfaces along the nonadiabatic photocyclization coordinate of OTP and DPCH. .................................................73

**Figure 4.0:** Table of contents figure. ..................................................................85

**Figure 4.1:** fs-TAS of OTP (a), TPB (b), and OQTP (c) in THF with 266 nm excitation.. ........................................................................................97

**Figure 4.2:** Single-wavelength fs-TAS traces obtained with 266 nm excitation of TPB (a) and OQTP (b) at 450 , 615 ,and 800 nm.. ............................................98

**Figure 4.3:** Arrhenius analysis via temperature dependent nanosecond TAS of OTP, TPB and OQTP. ........................................................................103

**Figure 4.4:** DFT-optimized (B3LYP/6-31+G*) geometries for reactants and predicted photoproducts. ....................................................................108

**Figure 4.5:** Normalized steady-state UV absorption spectra of OTP (a), TPB (b), and OQTP (c) and UV/vis transient absorption spectra of corresponding dihydro-intermediates.........................................................................................110

**Figure 4.6:** Excited-state minimum and minimum-energy CI geometries for TPB and OQTP from SA-CAS computations.. .........................................................113

**Figure 4.7:** Characterization of potential-energy landscapes for (a) OQTP A and (b) OQTP B obtained from SA-CAS(6,6)-sto3g calculations.. ...............................116

**Figure 4.8:** $S_1$ relaxation pathways for OQTP assessed from ab initio quantum-chemical calculations... .........................................................................118

**Figure 4.9:** Calculated effect of substitution on the relative energies of OTP and DHT ground-state minima .......................................................................120

**Figure 5.0:** Table of contents figure.................................................................140

**Figure 5.1:** Steady-state ground-state absorption and fluorescence spectra of compounds **1** and **3** in cyclohexane..... ..............................................................151

**Figure 5.2:** Time-resolved emission (375 nm) from **1** and **3** photoexcited at 340 nm..... ............................................................................................152

**Figure 5.3:** fs-TAS of **1** in THF solution following 266 nm photoexcitation with corresponding global fit.. ......................................................................154

**Figure 5.4:** Nanosecond and microsecond resolved transient absorption of **1** and **3**... ...........................................................................................................155

**Figure 5.5:** fs-TAS of **3** in THF following photoexcitation with 266 nm with corresponding global fit.... .....................................................................158

**Figure 5.6:** Structures of the cyclized products **2** and **4** and the transition states for cycloreversion on the $S_0$ potential energy surface computed at the UB3LYP/6-31G* level of theory.... ....................................................................................162

**Figure 6.1:** Femtosecond transient absorption spectra of (a) hexaphenyl benzene (4), and (b) hexaphenyl borazine (**1**) in THF under 266 nm excitation.... ..........186

**Figure 6.2:** Normalized fs-TA traces of **1** and **4** at 600 and 650 nm, respectively, following photo-excitation at 266 nm.... ........................................................187

**Figure 6.3:** Ns- and µs-resolved TA spectra obtained following 266-nm excitation of **4** in aerated THF at 298 K... ....................................................................188

**Figure 6.4:** Arrhenius fit to the temperature-dependent ring-opening rate for **5** determined by µs-TA following 266-nm excitation of **4**. ..................................190

**Figure 6.5:** Comparison of simulated UV-Vis Spectra of $S_0$ **2b**, **5a** and **5b** predicted from computations at the TD-U-CAM-B3LYP/6-311+G* level..... ..................196

**Figure 6.6:** Conformers of **5** and associated potential energy landscape...........200

**Figure 7.1:** $S_0$ OTP (steady state), $S_1$ OTP (1 ps), and $S_0$ DHT (1 ns) absorption features as well as spectra of the pump and repump wavelengths used in the present study.........................................................................................................222

**Figure 7.2:** Definition of (a) the general PRP scheme and relevant time delays, as well as more specific definitions of (b) PRP "Action" and (c) PRP "Bleach" experiments...................................................................................................224

**Figure 7.3:** PRP action Spectroscopy of DHT following 266 nm photoexcitation of OTP and re-excited with 580 nm (black solid line)... ......................................226

**Figure 7.4:** PRP action of DHT with a 340 nm repump pulse...........................227

**Figure 7.5:** PRP action (blue line) and bleach (red line) traces for OTP in THF with a 400 nm repump (all parallel polarizations). ..................................................229

**Figure 7.6:** Traditional 2-pulse polarization anisotropy of OTP following 266 nm excitation and band integration from 595-605 nm............................................231

**Figure 7.7:** 3-pulse polarization anisotropy action PRP of photoexcited OTP with a 266 nm pump, 580 nm repump, $\Delta t_{13}$ =1 ns, and the RPD signal of DHT integrated from 310-360 nm. ......................................................................................233

**Figure 7.8:** Isotropic PRP action of HPB in THF pumped with 266 nm, repumped with 360 nm and probed in the visible with the RPD integrated from 510-660 nm. ........................................................................................................234

**Figure A2.1:** $^{13}$C NMR Spectrum of OQTP. ..................................................261

**Figure A2.2:** $^{1}$H NMR Spectrum of OQTP......................................................261

**Figure A2.3:** Fluorescence and excitation spectra of OQTP and TPB in cyclohexane.. ..........................................................................................262

**Figure A2.4:** Temporal Profile of 639 nm laser diode under experimentally optimized pulsing conditions. ............................................................263

**Figure A2.5:** Global analysis of OTP using a 2 state sequential model. ............267

**Figure A2.6:** SVD Analysis focused on vibrational relaxation of OTP.. ...........268

**Figure A2.7:** Global Analysis of TPB using a sequential 3-state model.. ..........269

**Figure A2.8:** SVD Analysis focused on vibrational relaxation of TPB.............270

**Figure A2.9:** Global Analysis of OQTP fs-TA spectra.. ..................................271

**Figure A2.10:** SAS of OQTP from various kinetic models.. ............................272

**Figure A2.11:** The difference in energy between open and closed isomers (ΔH) of various substituted OTPs produced from B3LYP/6-31+G* computations... ......273

**Figure A2.12:** Energy differences between L and S conformers of various substituted DHTs.. ........................................................................................274

**Figure A2.13:** Potential energy surface of TPB constructed from SA-CAS(2,2)-sto3g computations... ......................................................................275

**Figure A3.1:** Schlenk cuvette for air and water-free sample preparation. .........279

**Figure A3.2:** Emission vs. absorption intensities for **1**, **3**, and reference standards. .........................................................................................281

**Figure A3.3:** 320 nm fs-TA data for **1** in THF and global analysis results ........282

**Figure A3.4:** 330 nm μs-TA data for **1** and 3 in THF.......................................283

**Figure A3.5:** ns-TA results for **1** and **3** in THF upon 320 and 330 nm photoexcitation, respectively. .............................................................284

**Figure A3.6:** 330 nm fs-TA data for **3** in THF and global analysis results.. ......285

**Figure A3.7:** 330 nm fs-TA data for **1** and 3 in THF/$H_2O$.. ..............................286

**Figure A3.8:** 360 nm μs-TA data for **1** and benzophenone/**1** in benzene with global analysis results for sensitization kinetics.. .........................................................288

**Figure A3.9:** Minimum energy structure of DHP and the DHP-CS transitions state for cycloreversion calculated at the UB3LYP/6-31G* level.. ............................289

**Figure A4.1:** Custom-built 250 μm pathlength flowcell....................................290

**Figure A4.2:** Comparison of ns-TA traces following 266 nm excitation of **4** under aerated and deaerated conditions. ......................................................................292

**Figure A4.3:** μs-TA spectra at 193 and 273 K following 266 nm excitation of **4**. ..........................................................................................................................293

**Figure A4.4:** Eyring analysis for a barrierless ring opening of **5** .......................294

**Figure A4.5:** $^1$H NMR of **4** ......................................................................295

**Figure A4.6:** $^1$H NMR of a solution of **4** before and after photochemical reaction...........................................................................................................296

**Figure A4.7:** Deconvolution of $^1$H NMR of the **4**/**6** mixture.............................297

**Figure A4.8:** Mass spectrum of **4** following photochemical reaction................299

**Figure A4.9:** UV-Vis of a solution of **4** before and after photochemical reaction.........................................................................................................300

**Figure A4.10:** HOMO and LUMO of **1** and **4** from R-KS ................................301

**Figure A4.11:** HOMO and LUMO of **5b** from BS-U-KS .................................302

**Figure A4.12:** HOMO and LUMO of **2b** from BS-U-KS .................................303

**Figure A4.13:** Constrained PES scan between **4**/**5a**/**5b** and **1**/**2a**/**2b**.................304

**Figure A5.1:** Experimental setup and parts of a autocorrelator. ........................306

**Figure A5.2:** Modifications to autocorrelator for 266 nm measurement based on 2PA in BBO. A pump-probe geometry is used for the decrease in probe transmission on a photodiode...................................................................309

**Figure A5.3:** Experimental Setup of 2 photon absorption (TPA) autocorrelator for the determination of 266 nm pulse widths. .......................................................311

**Figure A5.4:** Comparison of commercial autocorrelator (top) and homebuilt autocorrelator (bottom) collected using SHG in BBO. The voltage waveform used to drive the speaker for scanning time delay (middle). .....................................312

**Figure A5.5:** Autocorrelation of various OPA wavelengths using SHG in BBO..313

**Figure A5.6:** Observation of pulse broadening due to BK7 glass following autocorrelation of 650 nm using SHG in BBO. ................................................314

**Figure A5.7:** Autocorrelation of 450 & 500 nm using 2 photon signal from a GaN (405 nm) laser diode. ..........................................................................315

**Figure A5.8:** Comparison of Autocorrelation methods for 650 nm by SHG in BBO or by two photon signal in GaN.. ......................................................316

**Figure A5.9:** 2PA Autocorrelation of 266 nm in 200 μm BBO in addition to the pulse broadening induced by the addition of fused silica to the beam path. .......317

**Figure A6.1:** Flowchart for operation of photodiode arrays (PDA). (1) The laser timing box (SDG Elite) initiates data acquisition by triggering a DAQ that (2) outputs a clock to the PDA driver for reading pixels........................................320

**Figure A6.2:** Timing diagram for S3901 NMOS array using C7884 driver. The master clock (CLK) and master start (Start) are the necessary inputs for driving pixel readout.........................................................................................321

**Figure A6.3:** Picture of Synchronization waveforms with the master start in yellow and master clock in blue.. ...................................................................322

**Figure A6.4:** Layout of Broadband fs-TAS Experiment with annotated Pump (blue line/text) and Probe (red line/text) lines..........................................................324

**Figure A6.5:** Dual Spectrographs for wavelength dispersion of UV (blue line/text) and Visible (red line/text) wavelengths allowing for simultaneous ultra-broadband (300-1000 nm) collection of fs-TAS spectra. ..................................................325

**Figure A7.1:** Schematic for experimental ns/μs TA setup................................329

**Figure A7.2:** Timing diagram for PWM circuit................................................330

**Figure A7.3:** Homebuilt LED pulsing circuit with IC description and part numbers provided in Table A7.1. ......................................................................332

# List of Schemes

**Scheme 1.1:** Overview of molecular photoswitch prototypes................................2

**Scheme 1.2:** Mallory Reaction of 4a,4b-dihydrophenathrene with $I_2$ to produce phenanthrene by oxidative cyclodehydrogenation.................................................6

**Scheme 1.3:** π orbital symmetry for three structural isomers of $C_4H_6$ for formulation of the Woodward-Hoffmann rules. .....................................................9

**Scheme 3.1:** Photoinduced nonadiabatic isomerization and cyclization of diarylethylenes and *o*-phenylenes. .......................................................................65

**Scheme 4.1:** Photochemical Synthesis of Triphenylene via the Cyclodehydrogentation of OTP via DHT and DBN from the Cyclodehydrogenation of OQTP and TPB.. ...............................................................................................89

**Scheme 5.1:** Photoinduced cyclodehydrogenation of BN-doped polycycles. Compound **1** yields **3** via the proposed intermediate **2**. In contrast, **5** cannot be produced from **3** under the same reaction conditions... .....................................144

**Scheme 6.1:** Photochemical reaction of hexaphenyl borazine (**1**) and hexaphenyl benzene (**4**)..........................................................................................................178

**Scheme 6.2:** Dihydrotriphenylene (**7**) and its BN-doped analogue (**8**)..............194

# List of Tables

**Table 1.1:** Summary of Woodward-Hoffmann Rules for electrocyclic reactions ........................................................................................................11

**Table 2.1:** Supercontinuum spectral ranges of various materials and driving wavelengths........................................................................................................44

**Table 2.2:** Various LED and laser diode wavelengths and associated time resolution........................................................................................................49

**Table 3.1:** Key structural parameters from SA-2-CAS (2/2)-6-31G optimizations and CI searches of OTP and (*DPCH*) ....................................................................69

**Table 4.1:** Relaxation Time Scales Obtained from Fits of Single-Wavelength Traces through Time-Resolved Spectra of TPB and OQTP in THF Excited at 266 nm. ........................................................................................................101

**Table 4.2:** Global Analysis Fit Parameters for OQTP Spectral Dynamics. ........102

**Table 4.3:** Thermodynamic Parameters of Thermal Ring-Reopening. ...............106

**Table 4.4:** Structural Parameters for TPB and OQTP obtained by SA-CAS computations... ........................................................................................114

**Table 5.1:** Fluorescence yields and lifetimes of **1** and **3** in cyclohexane. ...........152

**Table 5.2:** ns-TAS decay timescales for **1** and **3** and oxygen quenching rates...157

**Table 5.3:** Triplet extinction coefficient and quantum yield for **1** obtained by energy-transfer method with benzophenone in benzene as the triplet sensitizer..160

**Table 5.4:** Summary of photophysical processes observed for **1** at 298 K... ......164

**Table 5.5:** Summary of photophysical processes of **3** at 298 K.........................165

**Table 6.1:** Kinetic and thermodynamic parameters for the ring opening of **5** obtained from Arrhenius and Eyring analysis of temperature-dependent μs-TA data. ........................................................................................................191

**Table 6.2:** Characterization of singlet diradical character (SDRC) of cyclized structures at the CAM-B3LYP/6-311+G* level... ...........................................195

**Table 6.3:** Energetic barriers along the potential energy landscape between ring-open structures **1** and **4** and cyclized structures **2** and **5**.. ..................................203

**Table A1.1:** Parameters for fits to transients plotted in the main text. ..............247

**Table A1.2:** Comparison of dihedral angles and energy gaps from State-Averaged-2-CAS (x/y) ..........................................................................................251

**Table A1.3:** Computed properties of ring-closed intermediates ........................252

**Table A4.1:** Computed NMR shifts for **6** ...........................................................298

**Table A7.1:** Description and part numbers for IC components shown in Figure A7.3.....................................................................................................................331

# Chapter 1

# Introduction

## 1.1 Overview of Photoswitchable Molecular Materials

Light-induced molecular transformations by isomerization, bond-formation and bond-breakage are useful processes that have been harnessed by nature for millions of years. As examples, the biological process of vision is dependent on the photoisomerization of retinal and the essential vitamin D is produced by photo-induced bond-breakage of 7-dehydrocholestrol by sunlight.[1-4] Much progress has been made in understanding the photochemical mechanisms that underlie the responses of photoswitchable molecules, resulting in the synthesis of optimized structures to favor particular functions. Scheme 1.1 shows various molecular switch "prototypes" that have been extensively studied and discussed in the literature.

Cis/trans (C/T) isomerization, which underlies photoswitching of azobenzenes and stilbenes (Scheme 1.1), utilizes the rotation of subgroups about a central double bond that results in the same bonding configuration but with an alteration to molecular symmetry.[5, 6] In contrast, cyclization (e.g. *ortho*-terphenyl) involves a change in the bonding configuration of the molecule, i.e. carbon-carbon bond formation across two rings. Each process has its own unique application where C/T isomerization has been used for molecular motors that can move molecules linearly by rotation of their subgroups that resembles a paddle of a waterwheel.[7, 8] Cyclization can induce physical movement as well but is more useful in its ability to change molecular conjugation that has many applications for light-induced optical and electrical switching. A short overview of photoswitch applications is given below with generalized functions given in Figure 1.1. Comprehensive reviews of photoswitch applications can be found in the literature.[9,10]

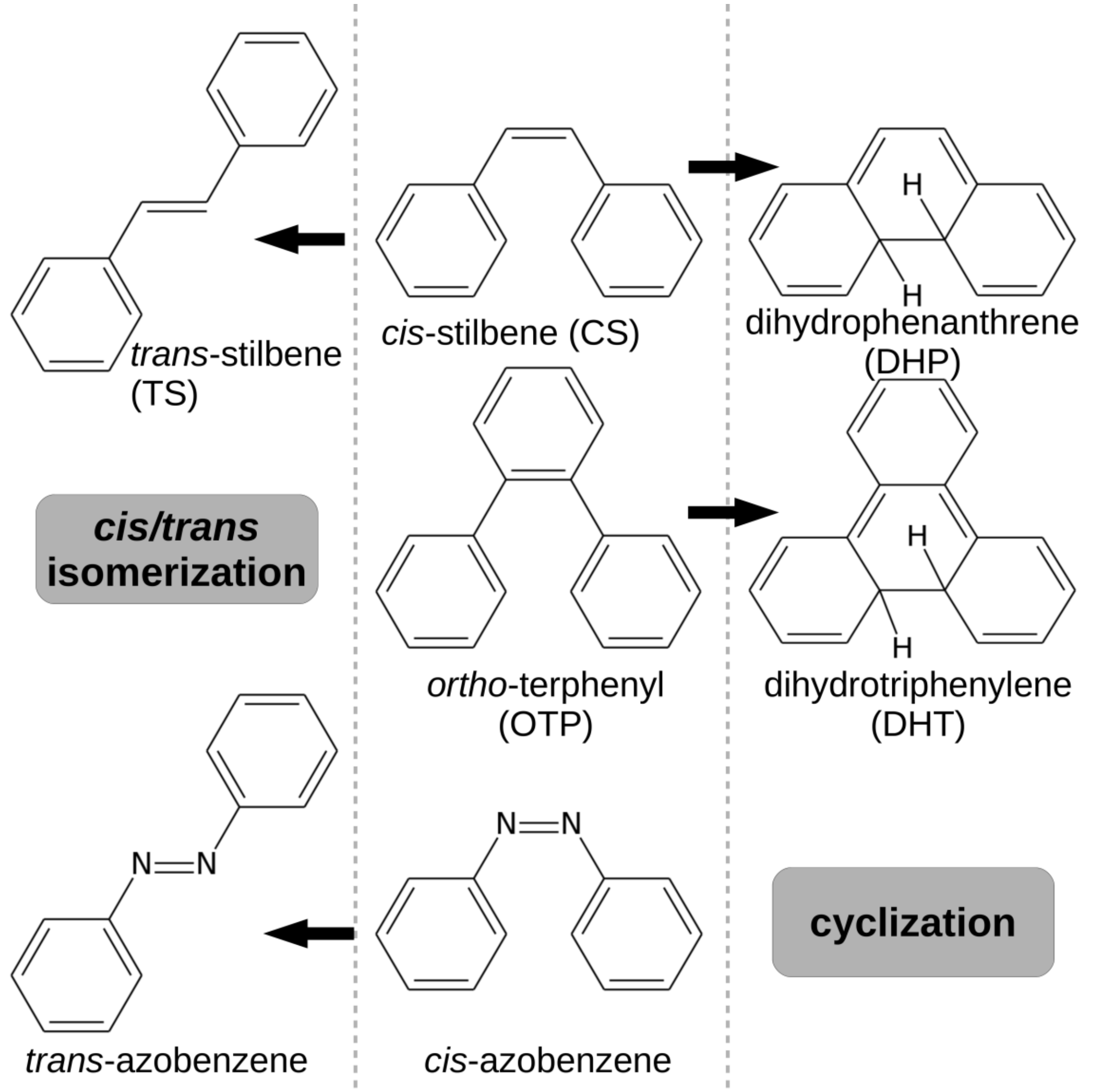
trans-stilbene (TS)
cis-stilbene (CS)
H
H
dihydrophenanthrene (DHP)
cis/trans isomerization
ortho-terphenyl (OTP)
H
H
dihydrotriphenylene (DHT)
N=N
trans-azobenzene
N=N
cis-azobenzene
cyclization

**Scheme 1.1.** Overview of molecular photoswitch prototypes. Stilbene (top) exhibits dual photoswitch behavior, including both cis/trans isomerization and cyclization, while *ortho*-terphenyl (middle) exhibits only cyclization and azobenzene (bottom) exhibits only cis/trans isomerization.

Molecular motors (Figure 1.1a) are typically based on C/T isomerization and harness molecular twisting to drive translational motion.[11] Often molecular motors are designed to have similar or identical cis and trans structures so that each C/T isomerization cycle can be performed without having to reset the molecule. In Figure 1.1a this corresponds to an infinite cycle of alternating red and blue states. Various molecular scaffolds and surface tethering techniques have been utilized for providing the "chassis" or "track" to transfer the energy of the motor.[12-14] The 2016 Nobel Prize was awarded to Ben Feringa, Jean-Pierre Sauvage and Sir J. Fraser Stoddart for their contribution to the field of molecular motors.[15]

Optical memory (Figure 1.1b) based on binary code (0,1 or on,off) can be realized by molecules with photochromic properties.[10] Typically cyclization based systems are chosen for this function, with the open-ring state corresponding to 0 or off and the photoinduced closed-ring state corresponds to 1 or on. Multilevel logic of up to 256 levels (8-bit) of storage have been demonstrated.[16] To utilize this system for optical memory it must be possible to "read," "write," and "delete" the switch state. Usually UV light performs writing via photocyclization and visible light performs deletion via photoinduced cycloreversion. A major problem with optical memory is that reading also utilizes visible light that limits the total number of times data can be read before it is eventually erased. The readout problem can be mediated by fluorescent detection of an unreactive optical transition that requires three lasers for writing or cyclization (<400 nm), fluorescent read-out of an unreactive optical transition of the open structure (400-500 nm) and erasing performed by bleaching the cyclized structure (600-800 nm).[17] A similar nondestructive read-out procedure can be performed by mid-infrared detection of the cyclized structure.[18, 19]

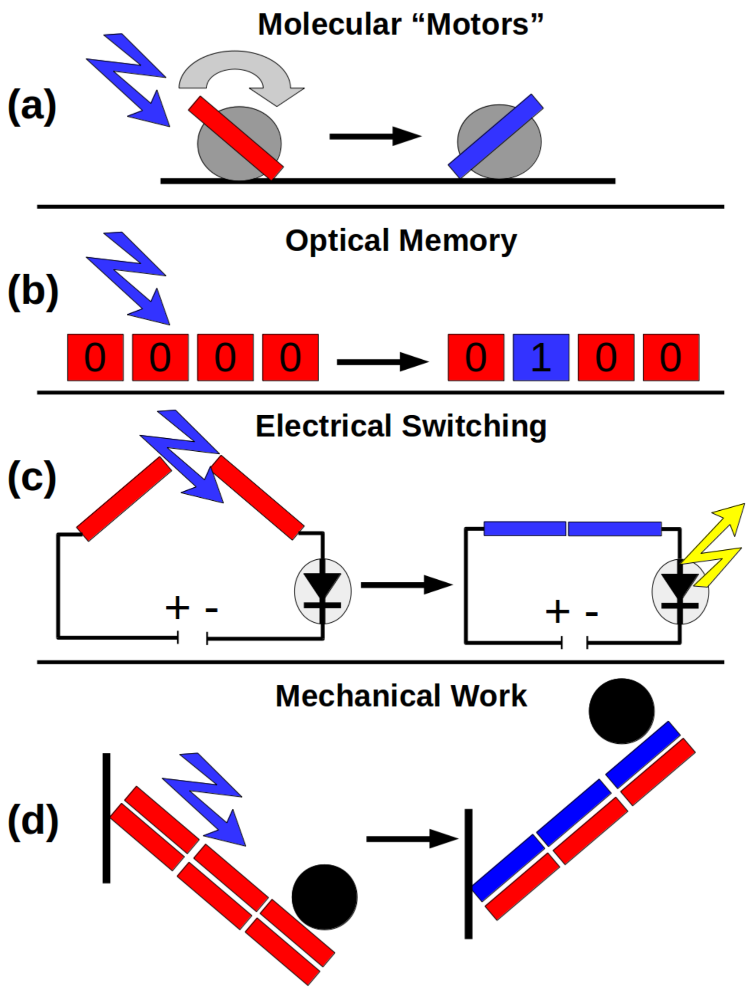
Molecular "Motors"
(a)
Optical Memory
(b)
0 0 0 0
0 1 0 0
Electrical Switching
(c)
+ -
+ -
Mechanical Work
(d)

**Figure 1.1.** Potential applications of photoswitchable materials: (a) A molecular motor that moves across a surface, (b) photoswitch states used as optical memory, (c) an electrical switch that is (de)activated by switching molecular states, and (d) to perform mechanical work, such as lifting, that is a result of the structural change between photoswitchable states.

Electrical switching (Figure 1.1c) utilizes a change in conjugation following irradiation that allows for the flow of current.[20] A major advantage of a molecular switch versus traditional transistors and MOSFETs is that the switching speed of the former should theoretically be on the order of picoseconds, limited by the lifetime for bond formation,[21, 22] compared to the typical >1 ns response for the latter. However the observation of slower switching speeds is most likely due to the bulk switching properties of the crystal requiring longer irradiation times for complete cyclization.[23] Generally cyclization is viewed as the ideal candidate for electrical switching but C/T isomerization also has shown promise with azobenzene-based systems.[24, 25] Recently single molecule photoelectrochemical switches based on a diarylethene photoswitch and graphene substrate have been demonstrated to be highly stable, reproducible and accurate with a on/off current ratio of ~100.[26]

Mechanical work can be utilized from the conformational change induced by cyclization or C/T isomerization and can result in ordered or stochastic macroscopic movement.[27] This movement can be like the lever shown in Figure 1.1d where irradiation and subsequent cyclization on the surface layer of a crystal causes the lever to bend in the direction of the incoming light due to strain induced by differences in molecular packing of open vs. cyclized structures.[28] Other types of mechanical changes are possible such as twisting to generate chiral structures[29] and shape changes[30] (square to rectangle). Even crystal explosion or cracking, termed the photosalient effect,[31, 32] has been observed. The amount of force exerted by these processes is 100 times greater than muscle tissue and comparable to that of piezoelectrics, and photoswitches can often lift objects weighing 200-600 times their own weight.[28]

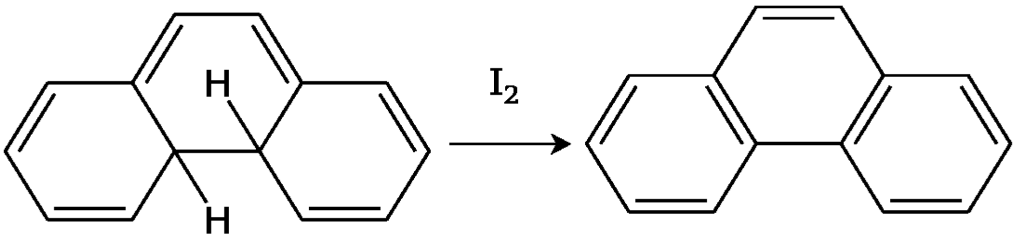

**Scheme 1.2.** Mallory Reaction of 4a,4b-dihydrophenathrene with $I_2$ to produce phenanthrene by oxidative cyclodehydrogenation.

Another application of cyclization is that some cyclized structures can be transformed irreversibly by oxidative cyclodehydrogenation to yield fused polyaromatic hydrocarbons, as illustrated in Scheme 1.2. This photo-oxidation reaction is referred to as the Mallory reaction[33] in honor of Frank Mallory who extensively studied this reaction with *cis*-stilbene analogs. Historically this reaction provided indirect evidence of the cyclization intermediate, 4a,4b-dihydrophenanthrene (DHP), prior to its direct spectroscopic observation by Muszkat and Fisher in the 1960's.[34] Those authors determined that the ring fission activation energy is 17.5 kcal/mol (0.75 eV) and corresponds to a half-life of 96 minutes at 300 K under deaerated conditions (for certain intermediates $O_2$ is a suitable oxidant). The Mallory reaction is still used today[35, 36] as a synthetic chemical tool to generate various fused aromatics or polycyclic aromatic hydrocarbons (PAHs) as it can be more selective and provide unique products when compared to non-photochemical methods, such as the Scholl reaction.[37]

Of particular importance to further improving the efficiency and stability of the photoswitchable molecules is to understand the mechanism of these photo-induced processes. The impact of molecular structure and substitution on the photo-dynamics/chemistry is critical for guiding synthetic design and mechanical, optical or electronic applications. The concept of structure-dynamics relationships is a constant theme throughout this dissertation.

## 1.2 Photoswitching Explained with the Woodward-Hoffman Rules

The molecular driving-force of photoswitching can be realized by simple molecular orbital theory and symmetry considerations that are summarized by the Woodward-Hoffmann (WH) rules.[38, 39] Using $C_4H_6$ as a paradigm we focus on three structural isomers, *cis*-1,3,-butadiene (CBD), *trans*-1,3,-butadiene (TBD) and cyclobutene (CB), that will convey the formulation of the photochemical possibilities using chemical intuition (Scheme 1.3). First we build the molecular orbitals (MOs) based on the number of valence electrons (# of valence $e^-$'s=# of MOs) using p orbitals and organize them according to increasing number of nodes. Next we analyze the symmetry of these MOs in order to build a correlation diagram (i.e. Walsh Diagram), using lines to correlate orbitals that have conserved orbital symmetry.

Analysis of this diagram provides many valuable predictions of the ground and excited-state properties of a particular molecule. When p atomic orbitals of similar sign reside adjacent to each other they form a π MO that is shown as a double bond in Kekule notation and indicates conjugation or an increase in bond order/strength. This implies that the central bond for TBD and CBD is allowed to freely rotate in the ground state or HOMO, due to the absence of π bond character, but the outer carbons (1-2 and 3-4) are fixed rotationally. Interestingly, following promotion of an electron into the LUMO the bond order increases across this central bond but is decreased across the outer carbons, effectively reversing the rotations allowed between the HOMO and LUMO. The implication towards C/T isomerization between TBD and CBD is that this process can occur via thermal activation in the ground-state (e.g. HOMO) but not in the first excited state (LUMO) due to differences in orbital symmetry. This concept has been named the non-equilibrium of excited rotamers (NEER) principle and has been used extensively for successfully predicting the possible outcomes of various photochemical reactions.[40] This illustrates that a particular photochemical mechanism can be state-dependent, a concept that will be revisited later.

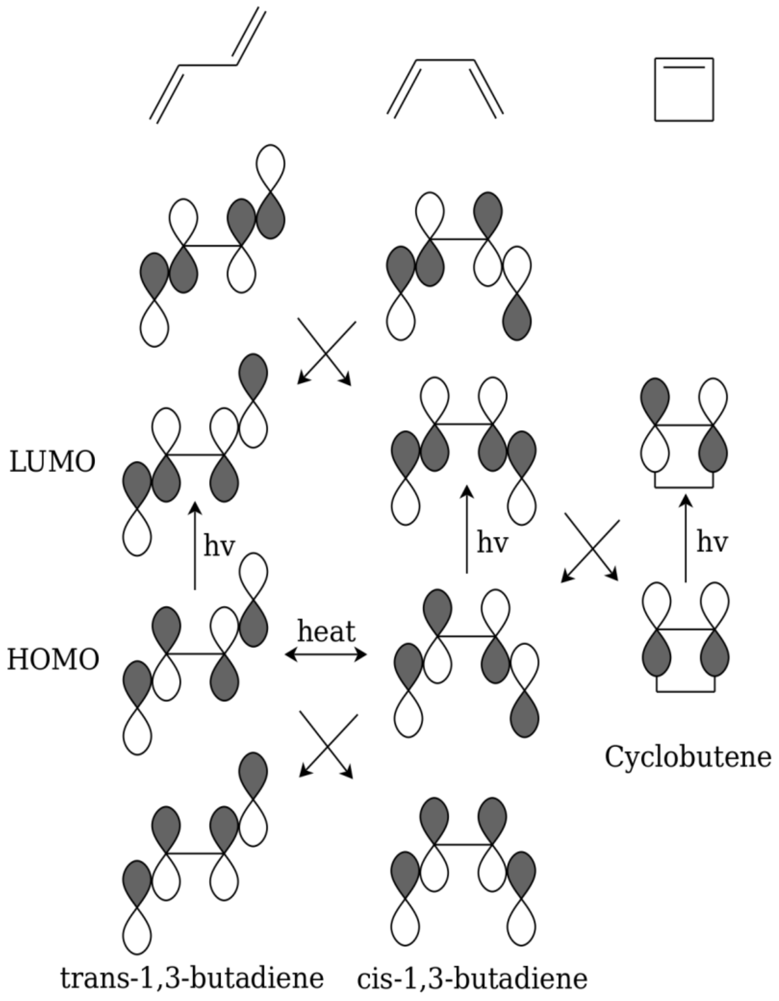
LUMO
HOMO
hv
hv
hv
heat
Cyclobutene
trans-1,3-butadiene
cis-1,3-butadiene

**Scheme 1.3.** π orbital symmetry for three structural isomers of $C_4H_6$. The Woodward-Hoffmann Rules utilize orbital symmetry to determine the correlation between states, which is illustrated with arrows. The Kekule structures (top) show that free rotation about the central bond is expected in the ground state of *trans* and *cis*-1,3-butadiene (TBD & CBD) since the HOMO has conjugation between carbons 1-2 and 3-4. However, upon absorption of a photon into the LUMO the central bond obtains more double bond character and therefore rotation is only allowed between carbons 1-2 and 3-4 that permits cyclization to cyclobutene (CB).

Focusing on photocyclization, the similar symmetry of the LUMO of CBD and the HOMO of CB can be recognized but of particular importance is how to attain this transformation. By rotating the terminal p orbitals towards one another, orbital overlap occurs and a σ bond is formed. This cyclization mechanism is known as disrotary, where subgroups rotate towards each other with opposing rotations, whereas a conrotary mechanism has the subgroups rotating away from each other with identical rotations. It is interesting to note that while the forward cyclization reaction follows a disrotary mechanism the reverse reaction, i.e. bond fission, from the LUMO of CB to the HOMO of CBD follows a conrotary mechanism. A final note is that CB in the ground-state (HOMO) is orbital symmetry "forbidden" to convert thermally into CBD, which increases the lifetime of cyclization product. The activation energy of the ring-reopening process is a very useful parameter when considering the long-term stability of a pericyclic photoswitch for practical applications.

The extension from 4 π electron systems to higher order even electron systems is determined quite simply by the alteration of orbital symmetry of the HOMO and LUMO following the addition of pairs of carbon atoms. The consequence of these symmetry alterations are the basis of the Woodward-Hoffmann "Rules" for electrocyclic reactions, where the conrotary/disrotary mechanism alternates by changing the electronic configuration or number of electrons. These rules are summarized in Table 1.1.

**Table 1.1.** Summary of Woodward-Hoffmann Rules for electrocyclic reactions.

| **Number of $\pi$ Electrons** | **HOMO / Thermally Allowed** | **LUMO / Photochemically Allowed** |
|---|---|---|
| y = 4 | Conrotary | Disrotary |
| y = 6 | Disrotary | Conrotary |
| y = 8 | Conrotary | Disrotary |
| y | For y/2,<br>Even: Conrotary, Odd: Disrotary | For y/2,<br>Even: Disrotary, Odd: Conrotary |

With an understanding of these basic rules we can move beyond the prototypical polyalkene systems to consider the photocyclization mechanism of more complex *ortho*-arenes. The photocyclization of *ortho*-terphenyl (OTP) is illustrated in Figure 1.2. OTP can be described as a $6\pi$ cyclization system since it is essentially a substituted hexatriene derivative and therefore undergoes conrotary photochemical reaction.[41-44] The molecular orbital configuration is more complex than that of the simple polyene cyclization prototypes and therefore modern computational chemistry methods were utilized to determine the orbital symmetry. These results from density functional theory (DFT)[45] were performed using the B3LYP/6-31+G* level of theory and upon visualization of the orbitals the orbital symmetry can be analyzed by a similar procedure to that used previously for butadiene. Following photo-excitation into the LUMO of OTP, orbital overlap of the terminal phenyl rings induces conrotary rotation that causes ring-closure to form dihydrotriphenylene (DHT). Looking closely at the LUMO of OTP and the positioning of the π orbitals it is possible to identify an ortho-quinoidal bonding configuration based on the increased inter-ring bond order and the single π lobe residing on the carbon atoms of the terminal phenyl rings located in the para position to the interring bonds. This builds further intuition into the photocyclization mechanism of OTP since the newly formed inter-ring π bonds benefit energetically by the planarization or flattening of all the phenyl rings relative to one another. In the ground state the lack of an inter-ring π bond means that the phenyl rings undergo free rotation that is only hindered by steric interactions. However if an inter-ring π bond is introduced then the rings will be energetically stabilized when the p orbitals are parallel and will be destabilized when they are orthogonal to each other. This change in molecular orbitals following photo-excitation into the LUMO towards an ortho-quinoidal configuration qualitatively explains the driving-force towards planarization that brings the terminal phenyl groups into close proximity, induces orbital overlap and results in cyclization to form DHT. Following photocyclization DHT can either thermally revert back to OTP or in the presence of a suitable oxidant, commonly $I_2$, undergo dehydrogenation to form triphenylene.[46, 47]

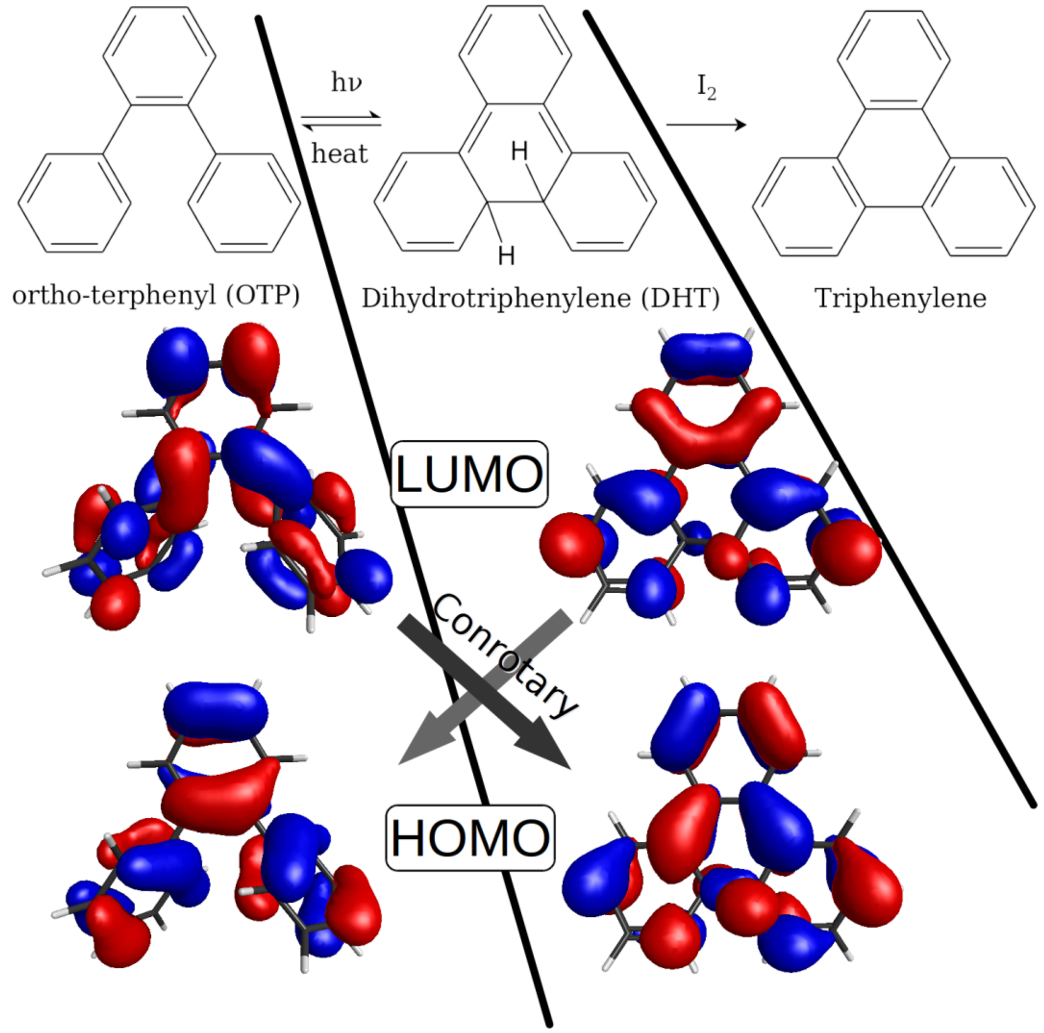
hν
heat
I$_2$
H
H
ortho-terphenyl (OTP)
Dihydrotriphenylene (DHT)
Triphenylene
LUMO
Conrotary
HOMO

**Figure 1.2.** (Top) Mallory reaction (photo-oxidation) of *ortho*-terphenyl (OTP) to triphenylene. The mechanism is based on the 6π photocyclization of 1,3,5-hexatriene and they in fact share similar orbital symmetry. (Bottom) Upon photoexcitation (HOMO to LUMO) OTP has increased inter-ring bond order and an ortho-quinoidal orbital symmetry that drives the system towards planarity. This forces the terminal rings into close proximity by a conrotary (i.e. identical phenyl rotations) mechanism that induces orbital overlap and therefore bond formation. Note the conservation of orbital symmtery between the LUMO of OTP and HOMO of DHT and vice-versa.

## 1.3 Excited-state Photochemistry: Potential Energy Surfaces, Conical Intersections and Nonadiabatic Couplings.

### *1.3.1 Potential energy surfaces*

While analysis of molecular orbitals and correlation diagrams helps to build intuition with light-induced chemical processes they only provide qualitative predictions under very ideal conditions of molecular symmetry. To quantitatively explain these physical phenomena we must explore the shapes and features of potential energy surfaces associated with various molecular geometries in multiple electronic states. Before providing the details and mathematics of these quantitative determinations let us start by surveying and cataloging the nomenclature that we use to define the landmarks on these potential energy surfaces (PESs).

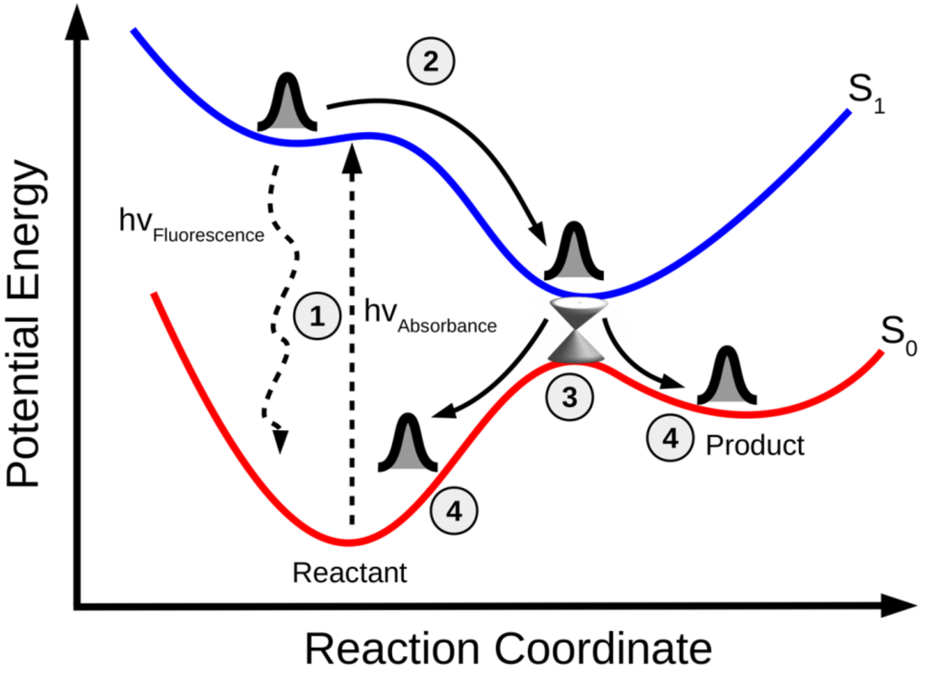

**Figure 1.3.** Photoinduced chemical dynamics of a generalized nonadiabatic photochemical reaction. The process is broken down into four steps from the absorption of photon generating the excited state to the regeneration of the ground state reactant and formation of ground state product. The details are explained in the text.

Figure 1.3 shows a typical PES of a nonadiabatic photo-reaction where a reactant molecule is initially in its ground electronic state ($S_0$) and the molecule is promoted into its excited state by a absorbed photon in step 1. Immediately afterwards the molecule can either dissipate this absorbed energy by re-emitting a photon by fluorescence that regenerates the reactant ground state or move across the $S_1$ surface shown by step 2. We can explain the molecular motion by the force associated with the shape of the potential energy surface defined as Equation 1.1. This force will drive

$$\text{Force} = -\frac{d\ \text{Potential Energy}}{d\ \text{Distance}} \qquad (1.1)$$

the molecule towards a lower energy configuration, such as stable minimum on the potential surface or to a conical intersection. The latter are associated with strong couplings between electronic states and the excited-state population may cross to the ground state via a nonadiabatic transition. Step 3 illustrates an interesting consequence of conical intersections that highlights a departure from classical mechanics into the quantum mechanical nature of the chemical dynamics. The details will be explained further in the following sections but the quantum nature allows for simultaneous splitting of the population to the left and right that generates both reactant and product in step 4. This behavior is curious since classical mechanics would predict an object to continue evolving to the product in 100 % yield. Now that the qualitative mechanism of nonadiabatic photochemistry has been explained in terms of potential energy surfaces and associated forces we will revisit select aspects with more mathematical detail.

### *1.3.2 Wavepackets and Quantum Superposition*

The time-dependent evolution of a molecule impulsively pumped to an excited state is described quantum mechanically by a collection of electronic and vibrational wavefunctions that exist simultaneously, a so-called quantum superposition or "wavepacket." Equation 1.2 shows the mathematical description of a wavepacket with $c_n$ providing the amplitude of a particular state ($\Psi$) that evolves in time (t) with a particular frequency ($\omega$) and phase ($\varphi$).

$$\Psi(r,t) = \sum c_n \exp[-i(\omega_n t - \varphi_n)]\psi_n(r) \qquad (1.2)$$

The time-energy uncertainty principle (Equation 1.3) dictates that as the time becomes more certain the energy becomes less certain.

$$\Delta E \, \Delta t \geq \hbar \qquad (1.3)$$

For femtosecond or attosecond duration laser pulses the duration is so short that their bandwidth becomes large enough to induce vibrational coherence or a superposition of multiple vibrational states.[48] The vibrational coherence contains useful details relevant to the initial nuclear motion that the molecule experiences on the excited state PES that can persist for picoseconds before the wavepacket loses phase due to decoherence processes such as photochemical reaction or intramolecular vibrational energy redistribution (IVR).[49, 50] The time-dependence of wavepacket evolution can be Fourier transformed to reveal the vibrational frequencies associated with regions of the PES it samples. Additionally vibrational wavepackets are important for the multi-state evolution and product state distributions relevant to photochemical reactions where certain vibrational modes can be coupled to a reaction coordinate.[51] Importantly, PES topography can be a source of wavepacket bifurcation,[52, 53] as observed with cis-stilbene,[54] whereby the excited-state relaxation mechanism branches to encompass divergent structural dynamics.

### *1.3.3 Nonadiabatic Transitions at Conical Intersections*

The efficient and fast transfer of the excited state back to the ground state or nonadiabatic transitions are facilitated by potential energy funnels between degenerate electronic states known as conical intersections.[55, 56] Conical intersections (CIs) do not exist as a discrete point but rather as a seam of points in a 3N-8 subspace of the total 3N-6 degrees of freedom for a polyatomic molecule. These two dimensions that describe the seam of degenerate electronic states are the gradient difference (g, equation 1.4) and derivative coupling (h, equation 1.5) vectors.[57] The gradient difference vector is useful for describing and locating CIs since by definition the difference in energy of the ground and excited states should be minimized. The derivative-coupling vector is important since the description of a CI should include the magnitude of coupling between states that effectively quantifies the breakdown of the Born-Oppenheimer approximation.

$$\overrightarrow{g_{01}} = \frac{\partial(E_0 - E_1)}{\partial R} \qquad (1.4)$$

$$\overrightarrow{h_{01}} = \Delta E_{0,1}\langle\psi_0|\frac{\partial}{\partial R}|\psi_1\rangle \qquad (1.5)$$

The gradient difference and derivative coupling vectors are essential for the characterization of CI topography that influence the resultant photo-dynamics and product branching ratio, i.e. the relative percent of two unique final states populated through nonadiabatic relaxation. The influence of topography is illustrated in Figure 1.4, which compares behaviors for “vertical” and “tilted” CIs. Here the branching ratio is represented by the green arrows that pass from the top to bottom of the CI. Pictorially it can be explained that a tilted CI directs the wavepacket in predominately one direction while a vertical CI allows for more equal distribution of photoproduct yields. In some cases even up-funneling ($S_0$ to $S_1$) has been predicted for a situation involving a specific incoming trajectory and the CI tilt that would allow for multiple nonadiabatic transitions and more complex product distributions.[58] For examples of calculated CI topographies and dynamics in specific molecules the reader is directed to references that provide a more exact and formal representation.[59-61]

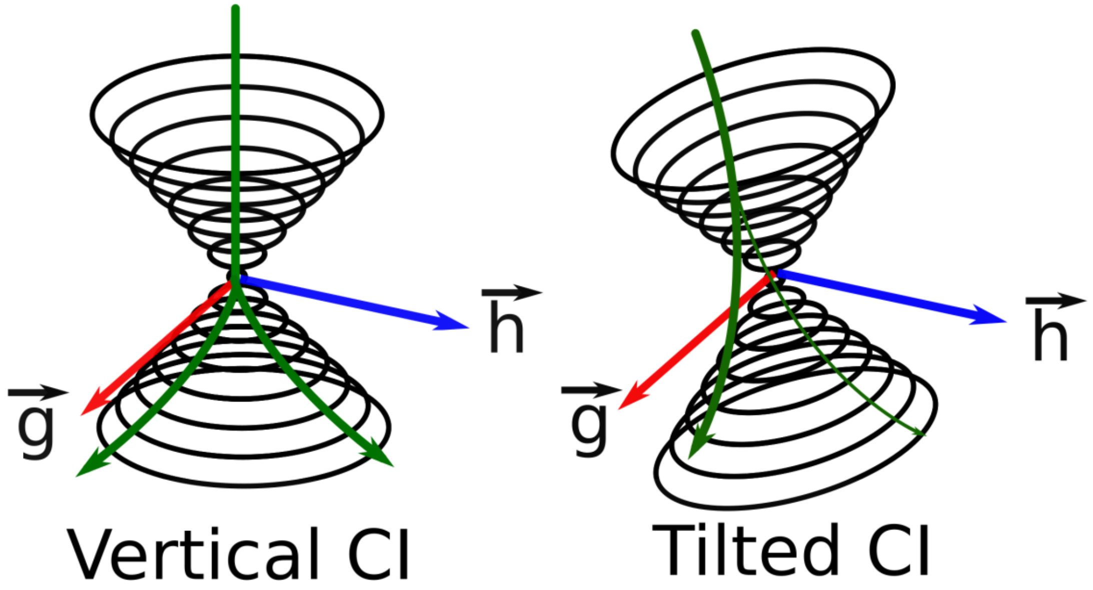

**Figure 1.4.** Influence of conical intersection topology on photodynamics and resultant photoproduct formation. For a vertical CI the molecular population is directed equally between two resultant configurations, whereas a tilted CI favors one over the other. The experimental observable of CI topography is known as the branching ratio where a ~50:50 formation of photoproducts is expected for a vertical CI.

Conical intersections are often vital to understanding photophysical behaviors and interpreting experiment for multiple reasons. CIs are without a doubt ubiquitous and highly relevant to many photochemical processes beyond C/T isomerization and cyclization including charge transfer, photodissociation, and proton transfer.[62, 63] Thirteen minimum energy $S_0/S_1$ CI's (MECIs) have been located computationally in benzene; these are accompanied by seams that make nonadiabatic decay appear to be nearly unavoidable in the excited state.[64] Whenever low fluorescence quantum yields or short excited-state lifetimes are observed experimentally the tendency is to assign this behavior to nonadiabatic transitions through conical intersections. These empirical assignments are often justified theoretically.[65] Conical intersections often result in internal conversion within femtoseconds to picoseconds, whether they correspond with deactivation of roughly the same molecular structure (i.e. $S_2$-to-$S_1$ nonradiative decay)[66] or due to photochemical reaction,[44, 67] and therefore require the application of femtosecond spectroscopic methods to interrogate.[68] Due to these very fast transitions experimentalists are often interested in studying how the breakdown of the Born-Oppenheimer approximation is influenced by specific conditions. In particular studying the influence of molecular friction, both solvent and viscosity/pressure dependent, on the rate of nonadiabatic decay has been useful for understanding microscopic and impulsive solute-solvent interactions.[69-72]

## 1.4 Overview of Dissertation Contents

The remaining contents of this dissertation are organized as follows:

Chapter 2 describes the experimental techniques used to study photoinduced dynamics of *ortho*-arenes. This includes an introduction to steady-state and time-resolved optical spectroscopy on timescales spanning femtoseconds to microseconds. The 3-pulse “pump-repump-probe” method, which is useful for deconvoluting complicated transient spectral dynamics by interrogating spectral and kinetic correlation in time-resolved spectra, is also described. The generation of femtosecond laser pulses, details of experimental set-ups, and polarization anisotropic effects due to the loss of dipole “memory” are described.

Complex data analysis using SVD-based global fitting is presented, including details of the matrix math and algorithm used for fitting multiple spectral components with various kinetic models.

Chapter 3 is based on the first ultrafast time-resolved spectroscopic study of *ortho*-terphenyl (OTP) and the *cis*-stilbene analog 1,2-diphenylcyclohexene (DPCH).[44] The dynamics of OTP and DPCH were compared due to their structural dissimilarities in the central 6-membered ring, which is a rigid benzene ring for OTP and a more flexible cyclohexene ring for DPCH. This comparative study explored the influence of the structural rigidity on excited-state lifetimes that increase in length as the rigidity increases (DPCH < OTP). Quantum-chemical computations were used to examine the effective energetic barriers from the excited-state minima to cyclization CI of OTP and DPCH and were found to be consistent with the experimental lifetimes.

The focus of Chapter 4 is on the implications of increasing the molecular complexity of *ortho*-arenes from OTP to 1,2,3-triphenylbenzene (TPB) and *ortho*-quaterphenyl (OQTP) on excited-state dynamics.[42] TPB exhibits similar photoinduced behavior as OTP but with a dilated excited-state lifetime. In contrast OQTP exhibits two distinct decay channels with disparate lifetimes. The interpretation was that OQTP has major alterations to the OTP chromophore that leads to the possibility of extended "ortho-quinoidalizational," or formation of a delocalized excited state across all four rings, which competes with deactivation by electrocyclization. In addition the activation energies of ring-reopening were quantified for OTP, TPB, and OQTP by temperature-dependent nanosecond spectroscopy.

Chapter 5 explores the effects of boron-nitrogen (BN) doping and extended aromatic substitution on the photocyclization of *ortho*-arenes. Photoinduced dynamics of $B_3N_3$-hexabenzotriphenylene (**1**) and its singly ring-fused Mallory-reaction product (**3**) were studied by a suite of steady-state and time-resolved spectroscopic techniques that revealed no direct spectroscopic signatures of a cyclized intermediate but instead highly efficient intersystem crossing into the triplet manifold. The assignment of the triplet state was confirmed by oxygen quenching experiments and further relaxation from the triplet state was confirmed by broadband microsecond transient absorption. The sum of the fluorescence and triplet quantum yield for compound **1** are approximately unity. However a small quantum yield for cyclization of <5-10 % is possible based on the lower error bounds and is consistent with the reactivity of compound **1** under Mallory reaction conditions.

Chapter 6 describes and compares the photochemistry of hexaphenylbenzene and hexaphenylborazine to address directly how BN doping impacts the photophysics and stability of DHT-like photoproducts of these isoelectronic species. Hexaphenylbenzene exhibits a long excited-state lifetime (~400 ps) that decays to reveal tetraphenyl-DHT (TphDHT), whereas hexaphenylborazine has a very fast excited-state decay (~3 ps) that shows no evidence of cyclization. Further study of TphDHT onto nanosecond timescales revealed a 2 μs lifetime that is 2 orders of magnitude larger than any other DHT analog observed previously. Ring-reopening of this barrier is subject to a very weak energetic barrier (0.02eV), but further thermodynamic analysis revealed a large decrease in the entropy compared to DHT and its analogs. Therefore the persistence of TphDHT is attributed to entropic stabilization as a result of steric crowding around the central benzene ring.

Chapter 7 digs deeper into the kinetics of photocyclization using pump-repump-probe (PRP) spectroscopy. In our previous work (e.g. Chapter 4) global analysis generated adequate fits to transient spectral evolution using sequential kinetic models for all *ortho*-arenes. However, these fits produced species associated spectra that overlap considerably, such that it is unclear if these models are truly appropriate. Pump-repump-probe experiments were used to test this mechanism empirically by photobleaching either the DHT $S_0$ or the OTP $S_1$ absorption with a repump pulse and then monitoring the instantaneous or long time effects on the transient spectral evolution. All PRP results that monitor the long time DHT absorption ($\Delta t$=1ns) following repumping at 340, 400 and 580 nm exhibit a subpicosecond rise and plateau in signal that does not reflect a sequential mechanism with a ~3 ps lifetime, and rather suggests that the photocyclized product is formed instantaneously. Similar results were obtained for hexaphenylbenzene, which was chosen due to its ~400 ps $S_1$ lifetime. The conclusion from PRP experiments is that cyclization is a result of wavepacket bifurcation in the excited state immediately after excitation and that the $S_1$ decay observed on picosecond timescales must be due to a $S_0/S_1$ CI(s) not associated with cyclization.

## 1.5 References

1. Kukura, P., Structural Observation of the Primary Isomerization in Vision with Femtosecond-Stimulated Raman. *Science* **2005,** *310* (5750), 1006-1009.

2. Herbst, J., Femtosecond Infrared Spectroscopy of Bacteriorhodopsin Chromophore Isomerization. *Science* **2002,** *297* (5582), 822-825.

3. Arruda, B. C.; Smith, B.; Spears, K. G.; Sension, R. J., Ultrafast ring-opening reactions: a comparison of α-terpinene, α-phellandrene, and 7-dehydrocholesterol with 1,3-cyclohexadiene. *Faraday Discussions* **2013,** *163*, 159.

4. Smith, B. D.; Spears, K. G.; Sension, R. J., Probing the Biexponential Dynamics of Ring-Opening in 7-Dehydrocholesterol. *The Journal of Physical Chemistry A* **2016,** *120* (33), 6575-6581.

5. Waldeck, D. H., Photoisomerization dynamics of stilbenes. *Chemical Reviews* **1991,** *91* (3), 415-436.

6. Sension, R. J.; Repinec, S. T.; Szarka, A. Z.; Hochstrasser, R. M., Femtosecond laser studies of the cis-stilbene photoisomerization reactions. *The Journal of Chemical Physics* **1993,** *98* (8), 6291-6315.

7. Feringa, B. L., The Art of Building Small: From Molecular Switches to Molecular Motors. *The Journal of Organic Chemistry* **2007,** *72* (18), 6635-6652.

8. Leigh, D. A., Genesis of the Nanomachines: The 2016 Nobel Prize in Chemistry. *Angewandte Chemie International Edition* **2016,** *55* (47), 14506-14508.

9. Irie, M.; Fukaminato, T.; Matsuda, K.; Kobatake, S., Photochromism of Diarylethene Molecules and Crystals: Memories, Switches, and Actuators. *Chemical Reviews* **2014,** *114* (24), 12174-12277.

10. Irie, M., Diarylethenes for Memories and Switches. *Chemical Reviews* **2000,** *100* (5), 1685-1716.

11. Browne, W. R.; Feringa, B. L., Light Switching of Molecules on Surfaces. *Annual Review of Physical Chemistry* **2009,** *60* (1), 407-428.

12. Clayden, J., Chemistry: No turning back for motorized molecules. *Nature* **2016,** *534* (7606), 187-188.

13. Kassem, S.; van Leeuwen, T.; Lubbe, A. S.; Wilson, M. R.; Feringa, B. L.; Leigh, D. A., Artificial molecular motors. *Chem. Soc. Rev.* **2017**.

14. Browne, W. R.; Feringa, B. L., Making molecular machines work. *Nature Nanotechnology* **2006,** *1* (1), 25-35.

15. Le Bailly, B., Nobel Prize in Chemistry: Welcome to the machine. *Nature Nanotechnology* **2016,** *11* (11), 923-923.

16. Leydecker, T.; Herder, M.; Pavlica, E.; Bratina, G.; Hecht, S.; Orgiu, E.; Samorì, P., Flexible non-volatile optical memory thin-film transistor device with over 256 distinct levels based on an organic bicomponent blend. *Nature Nanotechnology* **2016,** *11* (9), 769-775.

17. Tsivgoulis, G. M.; Lehn, J.-M., Photoswitched and Functionalized Oligothiophenes: Synthesis and Photochemical and Electrochemical Properties. *Chemistry - A European Journal* **1996,** *2* (11), 1399-1406.

18. Stellacci, F.; Bertarelli, C.; Toscano, F.; Gallazzi, M. C.; Zerbi, G., Diarylethene-based photochromic rewritable optical memories: on the possibility of reading in the mid-infrared. *Chem Phys Lett* **1999,** *302* (5-6), 563-570.

19. Seibold, M.; Port, H., Mid-infrared recognition of the reversible photoswitching of fulgides. *Chem Phys Lett* **1996,** *252* (1-2), 135-140.

20. Barachevsky, V. A., Electrical properties of photochromic organic systems (review). *High Energy Chemistry* **2016,** *50* (5), 371-388.

21. Tamai, N.; Saika, T.; Shimidzu, T.; Irie, M., Femtosecond Dynamics of a Thiophene Oligomer with a Photoswitch by Transient Absorption Spectroscopy. *The Journal of Physical Chemistry* **1996,** *100* (12), 4689-4692.

22. Ishibashi, Y.; Umesato, T.; Fujiwara, M.; Une, K.; Yoneda, Y.; Sotome, H.; Katayama, T.; Kobatake, S.; Asahi, T.; Irie, M.; Miyasaka, H., Solvent Polarity Dependence of Photochromic Reactions of a Diarylethene Derivative As Revealed by Steady-State and Transient Spectroscopies. *The Journal of Physical Chemistry C* **2016,** *120* (2), 1170-1177.

23. Ebisawa, F.; Hoshino, M.; Sukegawa, K., Self-holding photochromic polymer Mach–Zehnder optical switch. *Applied Physics Letters* **1994,** *65* (23), 2919-2921.

24. del Valle, M.; Gutiérrez, R.; Tejedor, C.; Cuniberti, G., Tuning the conductance of a molecular switch. *Nature Nanotechnology* **2007,** *2* (3), 176-179.

25. Zhang, C.; Du, M. H.; Cheng, H. P.; Zhang, X. G.; Roitberg, A. E.; Krause, J. L., Coherent Electron Transport through an Azobenzene Molecule: A Light-Driven Molecular Switch. *Phys Rev Lett* **2004,** *92* (15).

26. Jia, C.; Migliore, A.; Xin, N.; Huang, S.; Wang, J.; Yang, Q.; Wang, S.; Chen, H.; Wang, D.; Feng, B.; Liu, Z.; Zhang, G.; Qu, D. H.; Tian, H.; Ratner, M. A.; Xu, H. Q.; Nitzan, A.; Guo, X., Covalently bonded single-molecule junctions with stable and reversible photoswitched conductivity. *Science* **2016,** *352* (6292), 1443-1445.

27. Commins, P.; Desta, I. T.; Karothu, D. P.; Panda, M. K.; Naumov, P., Crystals on the move: mechanical effects in dynamic solids. *Chem. Commun.* **2016,** *52* (97), 13941-13954.

28. Morimoto, M.; Irie, M., A Diarylethene Cocrystal that Converts Light into Mechanical Work. *J Am Chem Soc* **2010,** *132* (40), 14172-14178.

29. de Jong, J. J. D., Reversible Optical Transcription of Supramolecular Chirality into Molecular Chirality. *Science* **2004,** *304* (5668), 278-281.

30. Karothu, D. P.; Weston, J.; Desta, I. T.; Naumov, P., Shape-Memory and Self-Healing Effects in Mechanosalient Molecular Crystals. *J Am Chem Soc* **2016,** *138* (40), 13298-13306.

31. Kitagawa, D.; Okuyama, T.; Tanaka, R.; Kobatake, S., Photoinduced Rapid and Explosive Fragmentation of Diarylethene Crystals Having Urethane Bonding. *Chemistry of Materials* **2016,** *28* (14), 4889-4892.

32. Medishetty, R.; Sahoo, S. C.; Mulijanto, C. E.; Naumov, P.; Vittal, J. J., Photosalient Behavior of Photoreactive Crystals. *Chemistry of Materials* **2015,** *27* (5), 1821-1829.

33. Mallory, F. B.; Mallory, C. W., Photocyclization of Stilbenes and Related Molecules. In *Organic Reactions*, John Wiley & Sons, Inc.: 2004.

34. Muszkat, K. A.; Fischer, E., Structure Spectra Photochemistry and Thermal Reactions of 4a,4b-Dihydrophenanthrenes. *J Chem Soc B* **1967,** (7), 662-&.

35. Matsushima, T.; Kobayashi, S.; Watanabe, S., Air-Driven Potassium Iodide-Mediated Oxidative Photocyclization of Stilbene Derivatives. *The Journal of Organic Chemistry* **2016,** *81* (17), 7799-7806.

36. Fukumoto, H.; Ando, M.; Shiota, T.; Izumiya, H.; Kubota, T., Efficient Synthesis of Fluorinated Phenanthrene Monomers Using Mallory Reaction and Their Copolymerization. *Macromolecules* **2017,** *50* (3), 865-871.

37. Scholl, R.; Mansfeld, J., meso-Benzdianthron (Helianthron),meso-Naphthodianthron, und ein neuer Weg zum Flavanthren. *Berichte der deutschen chemischen Gesellschaft* **1910,** *43* (2), 1734-1746.

38. Woodward, R. B.; Hoffmann, R., The Conservation of Orbital Symmetry. *Angewandte Chemie International Edition in English* **1969,** *8* (11), 781-853.

39. Hoffmann, R.; Woodward, R. B., Conservation of Orbital Symmetry. *Accounts Chem Res* **1968,** *1* (1), 17-&.

40. Whitesell, J. K.; Minton, M. A.; Tran, V. D., The non-equilibration of excited rotamers (NEER) principle. Ground-state conformational bias in triene photocyclizations. *J Am Chem Soc* **1989,** *111* (4), 1473-1476.

41. Molloy, M. S.; Snyder, J. A.; Bragg, A. E., Structural and Solvent Control of Nonadiabatic Photochemical Bond Formation: Photocyclization of o-Terphenyl in Solution. *The Journal of Physical Chemistry A* **2014,** *118* (22), 3913-3925.

42. Snyder, J. A.; Bragg, A. E., Structural Control of Nonadiabatic Bond Formation: The Photochemical Formation and Stability of Substituted 4a,4b-Dihydrotriphenylenes. *The Journal of Physical Chemistry A* **2015,** *119* (17), 3972-3985.

43. Molloy, M. S.; Snyder, J. A.; DeFrancisco, J. R.; Bragg, A. E., Structural Control of Nonadiabatic Photochemical Bond Formation: Photocyclization in Structurally Modified ortho-Terphenyls. *The Journal of Physical Chemistry A* **2016,** *120* (23), 3998-4007.

44. Smith, M. C.; Snyder, J. A.; Streifel, B. C.; Bragg, A. E., Ultrafast Excited-State Dynamics of ortho-Terphenyl and 1,2-Diphenylcyclohexene: The Role of “Ethylenic Twisting” in the Nonadiabatic Photocyclization of Stilbene Analogs. *The Journal of Physical Chemistry Letters* **2013,** *4* (11), 1895-1900.

45. Cohen, A. J.; Mori-Sánchez, P.; Yang, W., Challenges for Density Functional Theory. *Chemical Reviews* **2012,** *112* (1), 289-320.

46. Sato, T.; Shimada, S.; Hata, K., A New Route to Polycondensed Aromatics: Photolytic Formation of Triphenylene and Dibenzo[fg,op]naphthacene Ring Systems. *Bulletin of the Chemical Society of Japan* **1971,** *44* (9), 2484-2490.

47. Copeland, P. G.; Dean, R. E.; McNeil, D., The cyclodehydrogenation of o-terphenyl and 1,2′-biphenylyl-3,4-dihydronaphthalene. *J. Chem. Soc.* **1960,** *0* (0), 1687-1689.

48. Ranitovic, P.; Hogle, C. W.; Riviere, P.; Palacios, A.; Tong, X. M.; Toshima, N.; Gonzalez-Castrillo, A.; Martin, L.; Martin, F.; Murnane, M. M.; Kapteyn, H., Attosecond vacuum UV coherent control of molecular dynamics. *Proceedings of the National Academy of Sciences* **2014,** *111* (3), 912-917.

49. Takeuchi, S.; Ruhman, S.; Tsuneda, T.; Chiba, M.; Taketsugu, T.; Tahara, T., Spectroscopic Tracking of Structural Evolution in Ultrafast Stilbene Photoisomerization. *Science* **2008,** *322* (5904), 1073-1077.

50. Ishii, K.; Takeuchi, S.; Tahara, T., A 40-fs time-resolved absorption study on cis-stilbene in solution: observation of wavepacket motion on the reactive excited state. *Chem Phys Lett* **2004,** *398* (4–6), 400-406.

51. Piermarini, V.; Balint-Kurti, G. G.; Gray, S. K.; Gögtas, F.; Laganà, A.; Hernández, M. L., Wave Packet Calculation of Cross Sections, Product State Distributions, and Branching Ratios for the O(1D) + HCl Reaction. *The Journal of Physical Chemistry A* **2001,** *105* (24), 5743-5750.

52. Ando, T.; Shimamoto, A.; Miura, S.; Nakai, K.; Xu, H.; Iwasaki, A.; Yamanouchi, K., Wave packet bifurcation in ultrafast hydrogen migration in CH3OH+ by pump-probe coincidence momentum imaging with few-cycle laser pulses. *Chem Phys Lett* **2015,** *624*, 78-82.

53. Lasorne, B.; Dive, G.; Lauvergnat, D.; Desouter-Lecomte, M., Wave packet dynamics along bifurcating reaction paths. *The Journal of Chemical Physics* **2003,** *118* (13), 5831-5840.

54. Harabuchi, Y.; Keipert, K.; Zahariev, F.; Taketsugu, T.; Gordon, M. S., Dynamics Simulations with Spin-Flip Time-Dependent Density Functional Theory: Photoisomerization and Photocyclization Mechanisms of cis-Stilbene in ππ* States. *The Journal of Physical Chemistry A* **2014**.

55. Domcke, W.; Yarkony, D.; Köppel, H., *Conical Intersections: Electronic Structure, Dynamics & Spectroscopy*. World Scientific: 2004; p 852.

56. Yarkony, D. R., Diabolical conical intersections. *Reviews of Modern Physics* **1996,** *68* (4), 985-1013.

57. Matsika, S.; Krause, P., Nonadiabatic Events and Conical Intersections. *Annual Review of Physical Chemistry* **2011,** *62* (1), 621-643.

58. Snyder, J. W.; Curchod, B. F. E.; Martínez, T. J., GPU-Accelerated State-Averaged Complete Active Space Self-Consistent Field Interfaced with Ab Initio

Multiple Spawning Unravels the Photodynamics of Provitamin D3. *The Journal of Physical Chemistry Letters* **2016,** *7* (13), 2444-2449.

59. Ben-Nun, M.; Molnar, F.; Schulten, K.; Martinez, T. J., The role of intersection topography in bond selectivity of cis-trans photoisomerization. *Proceedings of the National Academy of Sciences* **2002,** *99* (4), 1769-1773.

60. Tuna, D.; Sobolewski, A. L.; Domcke, W., Conical-Intersection Topographies Suggest That Ribose Exhibits Enhanced UV Photostability. *The Journal of Physical Chemistry B* **2016,** *120* (41), 10729-10735.

61. Yarkony, D. R., Nuclear dynamics near conical intersections in the adiabatic representation: I. The effects of local topography on interstate transitions. *The Journal of Chemical Physics* **2001,** *114* (6), 2601-2613.

62. Yarkony, D. R., Conical Intersections: The New Conventional Wisdom. *The Journal of Physical Chemistry A* **2001,** *105* (26), 6277-6293.

63. Coe, J. D.; Martínez, T. J., Competitive Decay at Two- and Three-State Conical Intersections in Excited-State Intramolecular Proton Transfer. *J Am Chem Soc* **2005,** *127* (13), 4560-4561.

64. Li, Q.; Mendive-Tapia, D.; Paterson, M. J.; Migani, A.; Bearpark, M. J.; Robb, M. A.; Blancafort, L., A global picture of the S1/S0 conical intersection seam of benzene. *Chemical Physics* **2010,** *377* (1-3), 60-65.

65. Harabuchi, Y.; Taketsugu, T.; Maeda, S., Exploration of minimum energy conical intersection structures of small polycyclic aromatic hydrocarbons: toward an understanding of the size dependence of fluorescence quantum yields. *Phys. Chem. Chem. Phys.* **2015,** *17* (35), 22561-22565.

66. Horio, T.; Fuji, T.; Suzuki, Y.-I.; Suzuki, T., Probing Ultrafast Internal Conversion through Conical Intersection via Time-Energy Map of Photoelectron Angular Anisotropy. *J Am Chem Soc* **2009,** *131* (30), 10392-10393.

67. Larson, E. J.; Pyszczynski, S. J.; Johnson, C. K., Solvent Dependence of Electronic Relaxation in All-trans Retinal Studied by One- and Two-Photon Induced Transient Absorption. *The Journal of Physical Chemistry A* **2001,** *105* (35), 8136-8144.

68. Zewail, A. H., Femtochemistry: Atomic-Scale Dynamics of the Chemical Bond. *The Journal of Physical Chemistry A* **2000,** *104* (24), 5660-5694.

69. Nikowa, L.; Schwarzer, D.; Troe, J.; Schroeder, J., Viscosity and solvent dependence of low-barrier processes: Photoisomerization of cis-stilbene in compressed liquid solvents. *The Journal of Chemical Physics* **1992,** *97* (7), 4827-4835.

70. Todd, D. C.; Fleming, G. R., Cis-stilbene isomerization: Temperature dependence and the role of mechanical friction. *The Journal of Chemical Physics* **1993,** *98* (1), 269-279.

71. Anna, J. M.; Kubarych, K. J., Watching solvent friction impede ultrafast barrier crossings: A direct test of Kramers theory. *The Journal of Chemical Physics* **2010,** *133* (17), 174506.

72. Jin, H.; Liang, M.; Arzhantsev, S.; Li, X.; Maroncelli, M., Photophysical Characterization of Benzylidene Malononitriles as Probes of Solvent Friction. *The Journal of Physical Chemistry B* **2010,** *114* (22), 7565-7578.

# Chapter 2

# Experimental Methods

## 2.1 Introduction to Transient Optical Spectroscopies

To study the nonadiabatic photocyclization and subsequent ring-reopening of *ortho*-arenes the physical chemist requires tools that detect meta-stable species as they form and decay on timescales much too fast to be perceived by the human eye. Since the reactants absorb ultraviolet radiation and the products absorb visible radiation a logical choice is transient optical spectroscopy, which due to advances in laser technology allow for events on the order of femtoseconds in duration to be observed.[3] Typically chemical bonds are formed and broken in less than a picosecond but other processes, such as the thermal reversion of photoproducts or intersystem crossing to states of different spin multiplicity, are slower occurring on timescales greater than a nanosecond. Therefore, more conventional optical spectroscopic methods are necessary for extension into longer time regimes that can extend from nanoseconds up to the steady-state (seconds, hours, etc.).

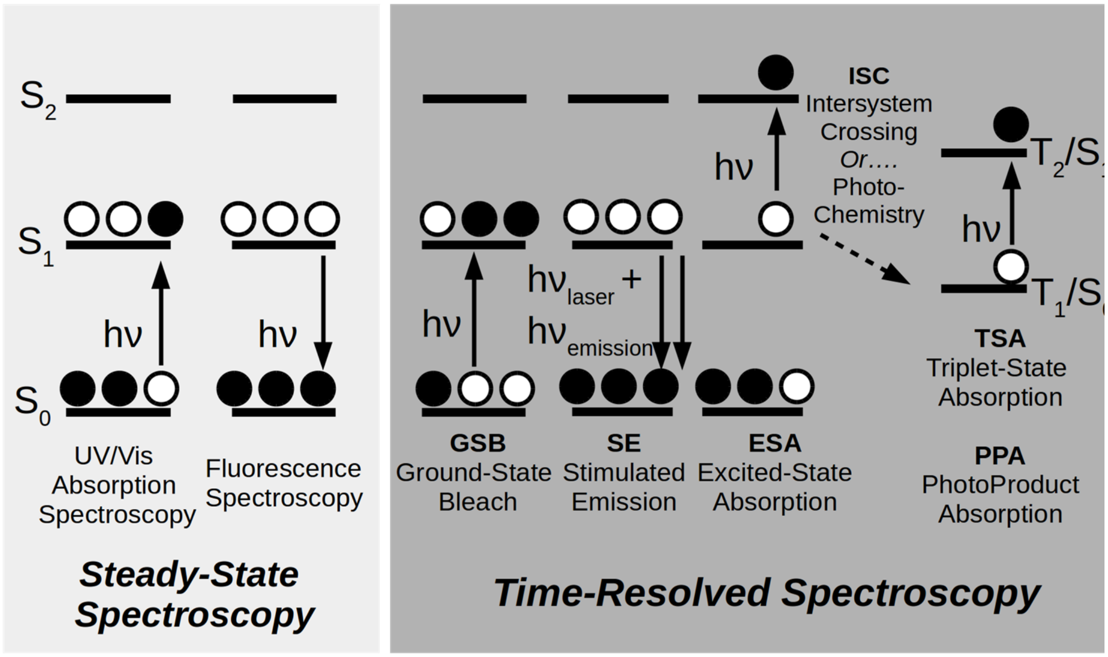

$S_2$
$S_1$
$S_0$
hν
hν
UV/Vis Absorption Spectroscopy
Fluorescence Spectroscopy
Steady-State Spectroscopy
hν
$h\nu_{laser}$ +
$h\nu_{emission}$
hν
ISC
Intersystem Crossing
Or....
Photo-Chemistry
hν
$T_2/S$
$T_1/S$
GSB
Ground-State Bleach
SE
Stimulated Emission
ESA
Excited-State Absorption
TSA
Triplet-State Absorption
PPA
PhotoProduct Absorption
Time-Resolved Spectroscopy

**Figure 2.1**. Connection between light-induced molecular processes and experimental spectroscopic techniques. The left panel highlights transitions that can be observed by steady-state spectroscopic methods. The right panel illustrates molecular transitions observable by transient absorption or "pump-probe" spectroscopy.

## 2.2 Steady-State Spectroscopies

The simplest optical spectroscopic methods are UV/VIS absorption and fluorescence spectroscopy (Figure 2.1), which quantify the absorption or emission of light by molecules, respectively. Each method has four general components: a light source, a molecular solution or sample, a spectrometer for dispersion of light by wavelength or photon energy, and a light detector. The distinction between these two methods is that absorption spectroscopy detects an attenuation of light intensity, $I$, through a sample and fluorescence spectroscopy measures the photons emitted from the sample. Therefore fluorescence spectroscopy is a background or reference free measurement while absorption spectroscopy requires a reference intensity, $I_0$, and is a differential measurement. Equations 2.1-2 give the relationships that quantify absorption, which can be given in units of percent transmittance (%T) or absorbance (ABS) (i.e. optical density (OD)).

$$\%\mathrm{T} = 100\frac{I}{I_0} \qquad (2.1)$$

$$Absorbance/OD = -\log\frac{I}{I_0} \qquad (2.2)$$

$$I_0 = \text{Incident light}$$

$$I = \text{Incident light after sample}$$

The relationship between absorbance and concentration is important for quantitative determinations of quantum yields for photophysical processes and is provided by the Beer-Lambert Law, $A = \varepsilon lc$. $\varepsilon$ is the molar extinction coefficient that reflects how strongly a molecule absorbs light at any given wavelength and relates $A$ to the solution concentration ($c$) or pathlength ($l$); $\varepsilon$ determines what sample concentrations to be prepared for fluorescence or other spectroscopic techniques.

A common interrogation of photophysical processes that utilizes both steady-state absorbance and fluorescence spectroscopies is the determination of the fluorescence efficiency known as the fluorescence quantum yield ($\Phi_{\mathrm{Fl}}$, equation 2.3).[5] The fluorescence quantum yield provides information regarding the photophysical deactivation mechanism since the summation of quantum yields for all deactivation pathways is equal to unity. The fluorescence quantum yield is often determined by relative comparison of the integrated fluorescence intensity under identical absorption conditions of a sample ($I_{Fl}^{X}$) to a reference ($I_{Fl}^{Ref}$) with a known quantum yield ($\Phi_{Fl}^{Ref}$). For example, if the fluorescence quantum yield is large (~1) then the yield of any other competing mechanism is negligible and it can be assumed that deactivation occurs predominately due to fluorescence. Both the absorption and fluorescence spectra are prerequisites for more complex spectroscopic methods that monitor the sample changes induced by perturbations with light, heat, pressure, etc.

$$\Phi_{fl}^{X} = \Phi_{fl}^{Ref} \frac{I_{fl}^{X}(A^{X})}{I_{fl}^{Ref}(A^{Ref})} \qquad (2.3)$$

$$\Phi_{fl}^{X,Ref} = \text{Fluorescence quantum yield of X or reference}$$

$$I_{fl}^{X,Ref}(A^{X,Ref}) = \text{Fluorescence intensity of X or ref. as a function of absorbance}$$

## 2.3 Principles of Transient Absorption Spectroscopy (TAS)

TAS or “pump-probe” spectroscopy is a derivative of UV/VIS spectroscopy where instead of acquiring a time-averaged or steady-state absorption spectrum, a time-resolved absorption spectrum is acquired following perturbation of the sample with a light pulse.[6] However a light source, i.e. the “pump”, is required to initiate the photo-physical or photochemical process by photo-excitation in addition to the light source that monitors the change in sample absorption, i.e. the “probe.” The pump-probe measurement is a differential measurement like UV/VIS spectroscopy except that the sample is always present and instead the transmission of probe light following sample excitation with the pump, $I_{pump-probe}$, is referenced against the probe transmission with the pump absent, $I_{probe}$. Modulation of the pump is generally achieved by using an optical chopper that physically blocks the light. Two phases, i.e. pump on/probe on and pump off/probe on, are required for determining the differential absorbance (ΔOD) at a given pulse time delay as given by equation 2.4.

$$\Delta OD = -\log \frac{I_{pump-probe}}{I_{probe}} \quad (2.4)$$

The spectra acquired from TAS contain a wealth of information regarding the dynamics/kinetics that follow the initial photo-excitation through time-dependence of various photo-induced spectroscopic signatures (Figure 2.1) such as ground-state bleach (GSB), excited-state absorption (ESA), stimulated emission (SE), triplet state absorption (TSA), or photo-product absorption (PPA).[7] GSB is the signal due to increased light transmission following reduction of the ground-state absorption by the population transfer to an excited state induced by a pump pulse. ESA is the reduction in probe intensity due to the absorption of the excited state. SE is the increase in probe intensity due to the stimulated emission of the excited state, which has a spectrum quite similar to the steady-state fluorescence spectrum but which can have a time-dependent evolution. TSA is the decrease in probe transmission due to absorption of a triplet-state that is formed by intersystem crossing from the singlet manifold. PPA results in a decrease in probe transmission due to the absorption of photochemically generated stable or metastable ground-state species due to processes such as cis/trans isomerization or electrocyclization.

In order to track the photo-physical evolution of a molecule following photo-excitation snapshots must be acquired along a well-defined time coordinate or time delay (Δt), which can vary from femtoseconds to microseconds. Depending on the molecular process of interest this time delay can be achieved by different methods that generally separates TAS into two variants, femtosecond/ultrafast and nanosecond-to-microsecond (and beyond). Each variant operates through the same principles described above but with different time-resolution and time-delay ranges that often require different equipment and experimental implementation. The time resolution and relevant photophysical processes for each variant are described as follows: femtosecond TAS with a time resolution of <200 fs is optimal for studying dynamics of excited states (100s of fs to ~1 ns) and nanosecond/microsecond TAS with a time-resolution of >1 ns is optimal for studying the decay of meta-stable photochemical products such as triplet-states, radicals, and cyclization adducts. More specifically femtosecond and nanosecond/microsecond TAS are necessary for the study of *ortho*-arene photochemistry so that all processes can be monitored from "birth" to "death" providing details pertaining to the kinetics of formation and decay of excited states and photoproducts as well as their stability or activation energy against reversion to reactant structures.

## 2.4 Femtosecond Transient Absorption Spectroscopy (fs-TAS)

Figure 2.2 presents a schematic of the fs-TAS setups used in the Bragg lab.[8-10] Generally, transient absorption requires 2 light sources but femtosecond transient absorption utilizes one source, consisting of the oscillator and amplifier, that is split into an intense pump and weak probe. Using nonlinear optical mixing (described in detail below) the narrow bandwidth pump and broadband probe are generated prior to optical delay being applied using a translation stage. After overlapping each beam at the sample the probe is spectrally conditioned using various optical filters and analyzed according to wavelength using a spectrograph and detector. Further details of each component are given below.

### *2.4.1 Description of Femtosecond Laser Source*

The laser source consists of two parts, an oscillator that generates a weak femtosecond laser pulse train (Ti:Sapphire, 800 nm, 80 MHz, ~6 nJ/pulse, 35 fs) that seeds a regenerative amplifier to generate a high power femtosecond laser source (~4.5 mJ/pulse, 1 kHz, 35 fs, 800 nm) through Chirped-Pulse Amplification (CPA). A detailed discussion of mode-locking and regenerative amplification can be found in various textbooks.[1, 2] Briefly, a Titanium-Sapphire crystal in the oscillator is pumped with a CW solid-state diode laser (532nm, ~5 W). Through constructive interference of various CW laser modes by passive Kerr-lens mode-locking a weak femtosecond laser pulse or "seed" is generated.

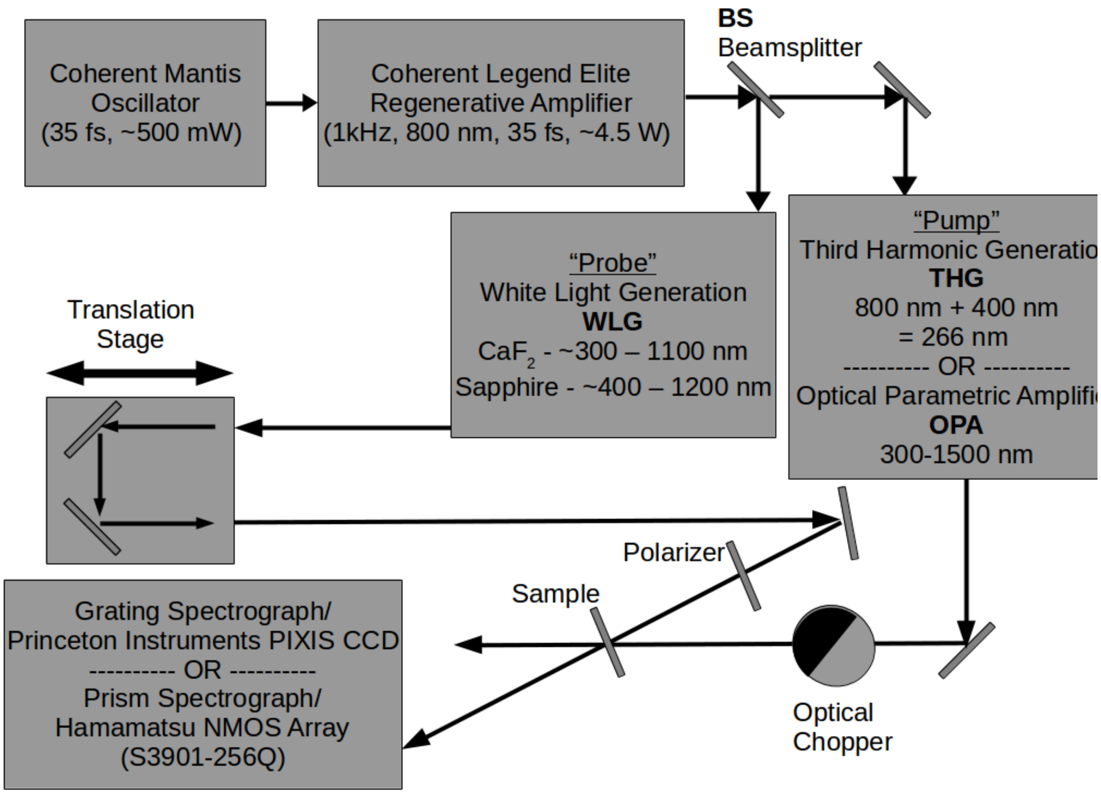
Coherent Mantis
Oscillator
(35 fs, ~500 mW)
Coherent Legend Elite
Regenerative Amplifier
(1kHz, 800 nm, 35 fs, ~4.5 W)
BS
Beamsplitter
"Probe"
White Light Generation
WLG
CaF2 - ~300 – 1100 nm
Sapphire - ~400 – 1200 nm
"Pump"
Third Harmonic Generatio
THG
800 nm + 400 nm
= 266 nm
---------- OR ----------
Optical Parametric Amplifi
OPA
300-1500 nm
Translation
Stage
Polarizer
Sample
Grating Spectrograph/
Princeton Instruments PIXIS CCD
---------- OR ----------
Prism Spectrograph/
Hamamatsu NMOS Array
(S3901-256Q)
Optical
Chopper

**Figure 2.2.** Generalized femtosecond transient absorption setup and equipment utilized in the Bragg lab. While two separate fs-TA experiments are available the same components are used for each: a laser source, pump and probe lines, a motorized translation stage, chopper, wavelength dispersion and light detection.

Following the generation of the femtosecond seed pulse the oscillator output is amplified by a regenerative amplifier from pulse energies of ~6 nJ to 4.5 mJ. Due to the very high peak power of femtosecond laser pulses the amplification is preceded by pulse "stretching" (i.e. pulse "chirping") whereby a diffraction grating pair spatially disperses the pulse by wavelength and then recombines the pulse spatially to regenerate the initial circular beam profile. The dispersion of wavelengths creates a pathlength difference between colors within the spectral bandwidth that temporally stretches the pulse, which allows for increased amplification due to a decrease in peak power. Next the amplification takes place by optically pumping a Ti:Sapphire rod with ~ 30 mJ of 532 nm at 1 kHz from a solid state laser (Coherent Evolution), which creates a gain medium for the seed pulse. The amplified seed pulse makes multiple passes in the laser cavity. The entrance and exit timing of the seed and amplified pulse, respectively, are synchronized to firing of the pump laser (Evolution) and manipulated by a set of Pockels cells triggered at the rate of the pump laser; hence, while amplification increases the pulse power, it also reduces the pulse repetition rate from 80 MHz down to 1 kHz. Finally the amplified output is recompressed to the initial temporal pulse width by reversing the stretching process in a "compressor" stage. The pulse compressor uses a diffraction grating pair in a different configuration which applies the reverse pathlength difference across the dispersed wavelengths that was applied in the stretcher stage.[11]

### 2.4.2 Wavelength Tunability: Nonlinear Optical Mixing and Phase Matching

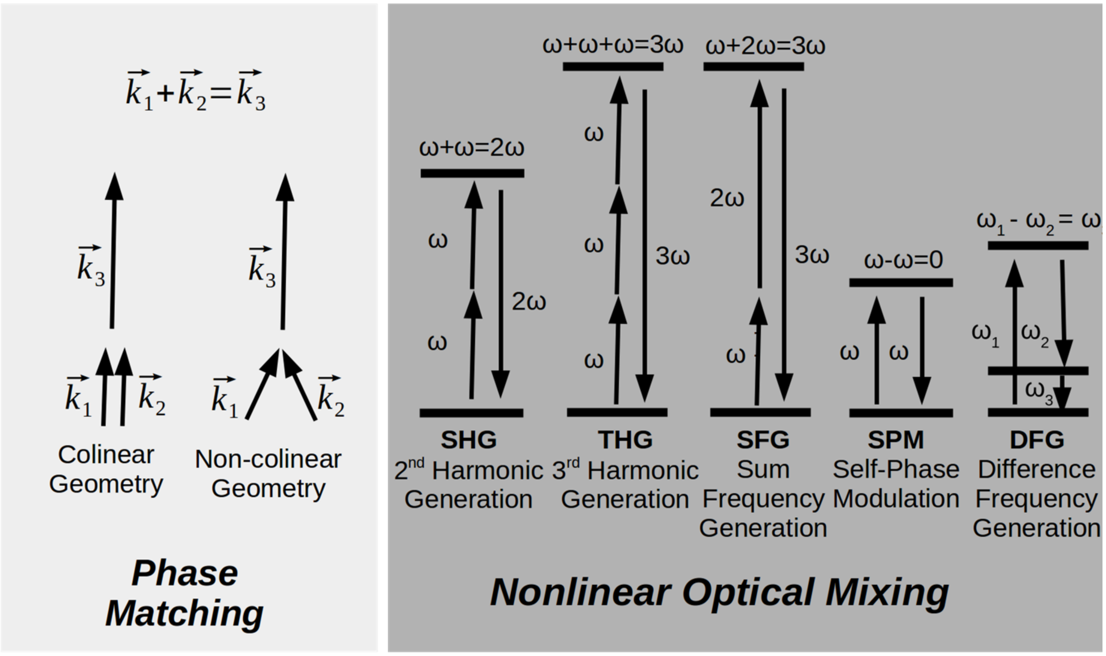
$\vec{k}_1+\vec{k}_2=\vec{k}_3$
$\vec{k}_3$
$\vec{k}_1$
$\vec{k}_2$
Colinear Geometry
Non-colinear Geometry
Phase Matching
ω+ω=2ω
ω+ω+ω=3ω
ω+2ω=3ω
ω-ω=0
$\omega_1$ - $\omega_2$ = ω
ω
2ω
3ω
$\omega_1$
$\omega_2$
$\omega_3$
SHG
2nd Harmonic Generation
THG
3rd Harmonic Generation
SFG
Sum Frequency Generation
SPM
Self-Phase Modulation
DFG
Difference Frequency Generation
Nonlinear Optical Mixing

**Figure 2.3.** Basic principles of nonlinear optical mixing.[1, 2] (left) Phase matching is analogous to momentum conservation and results in the output wave direction being the sum of the input wave vectors. (right) Nonlinear optical mixing can be viewed as energy conservation where the input energy is the sum or difference of the input waves. Self-phase modulation (SPM) is vital to the process of supercontinuum generation, i.e. the broadband probe pulse.[4]

The fundamental wavelength (800 nm) of the Ti:Sapphire laser is not directly useful for photo-excitation or monitoring of most molecules and materials of interest to chemists. However the high peak power of femtosecond laser pulses allow for nonlinear optical mixing that can be explained simply by comparison to energy or momentum conservation. These laws can be applied to photons provided their intensity is sufficiently high and a suitable material is used so that photons of the same or different energy may be added or subtracted. Additionally these photons have “momentum” so that the new, mixed photons direction is determined by the vector addition of the incident photons, which is commonly referred to as phase matching. Figure 2.3 reviews the most prevalent nonlinear processes that are utilized for generation of wavelengths from 266-2000 nm in our laboratory. Finally it should be noted that the nonlinear crystal, typically BBO (beta barium borate) or KDP (potassium dihydrogenphosphate) are non-centrosymmetric, i.e. not having inversion symmetry.

### *2.4.3 Polarization Anisotropy*

When molecular samples are excited with polarized light pulses, the polarization memory of the molecular transition dipoles can be lost due to the rotation/diffusion of a solute molecule through solvent that occurs simultaneously with excited-state population dynamics. For transient spectroscopies the pump laser excites molecules with transition dipole moments aligned with the laser polarization that creates a polarized excited-state population. Once this population is generated it subsequently diffuses and rotates through solution eventually losing memory of its initial dipole/polarization alignment, occurring simultaneously but on a different timescale as excited-state population dynamics. Additionally, changes in electronic states or nonadiabatic photochemical transformations can be accompanied by changes in dipole moment (and therefore polarization anisotropy) that further complicate transient absorption intensities. Typical timescales for rotational diffusion are picoseconds, while electronic or nonadiabatic photochemical changes occur much faster (~<1ps).[12, 13]

The polarization effects can either be quantified or removed by selection of relative pump and probe polarization. To quantify the polarization dynamics we isolate the polarization anisotropy (r(t)) by performing separate TA experiments with identical pump and probe polarization (parallel, $I_{\parallel}$) *and* perpendicular polarization (perpendicular, $I_{\perp}$).[14]

$$r(t) = \frac{I_{\parallel} - I_{\perp}}{I_{\parallel} + 2I_{\perp}} = r_o \mathrm{e}^{-Dt} = r_o \mathrm{e}^{\frac{-6kT}{\zeta}t} \quad (2.5)$$

$I_{\parallel}$ = Parallel Pump/Probe Polarization
$I_{\perp}$ = Perpendicular Pump/Probe Polarization
$r_o$ = Initial Anisotropy
$D$ = Rotational Diffusion Constant
$k$ = boltzmann constant
$T$ = Temperature
$\zeta$ = Solvent Friction

To remove these effects we can select a relative polarization angle known as magic angle (54.7°) which samples an effectively isotropic population.[15] Optics for polarization control include wire-grid polarizers, half-wave plates and depolarizers which vary by usable wavelength ranges, transmission and damage thresholds that must be carefully chosen for the given application.

### *2.4.4 fs-TAS Experimental Setup*

The amplified laser output is used to generate the broadband probe and pump or excitation pulses by non-linear mixing processes. The probe is generated by focusing approximately a microjoule or less of the fundamental (800 nm), second harmonic (400 nm), or third harmonic (266 nm) into a thin crystal, typically sapphire or $CaF_2$, to drive supercontinuum generation. Each combination of driving wavelength and crystal produces a different spectral range (Table 2.1), which is selected based on the molecule or material to be studied. Generally the process of supercontinuum generation is regarded as a self-phase modulation process (see Figure 2.3) but further details are provided elsewhere.[1, 4]

Table 2.1. Supercontinuum spectral ranges ($\lambda_{out}$) of various materials and driving wavelengths ($\lambda_{in}$).[4, 16, 17]

| Material | $\lambda_{in}$ / nm | $\lambda_{out}$ / nm |
|---|---|---|
| $CaF_2$ | 800 | 300 - 1200 |
| $CaF_2$ | 400 | 250 - 600 |
| $CaF_2$ | 266 | 225 - 270 |
| Sapphire | 800 | 400 - 1400 |

The pump or excitation pulse can be a variety of wavelengths generated by nonlinear optical mixing. For UV excitation the third harmonic of the laser fundamental is typically employed (266 nm). In our experimental setup this wavelength is generated in a two-step process: 400 nm pulses are generated by second harmonic generation (SHG) of the fundamental; these are then mixed with the fundamental by sum frequency generation to make 266 nm. For longer wavelengths an optical parametric amplifier (OPA, TOPAS Light Conversion) is utilized. The OPA can generate excitation pulses from 300 to 2500 nm using various nonlinear processes (see Figure 2.3) in a single or cascaded stages.

The relative time delay between pump and probe is set via a difference in optical pathlength (related to the time through the speed of light (~ 1ft/ns)). This can be controlled precisely when the path of one beam is routed along a motorized translation stage (Newport ILS250CC). Additionally the pump and/or probe must be modulated before arriving at the sample by an optical chopper (Thorlabs). For standard transient absorption two phases are necessary, probe only and pump/probe on, that requires modulating only the pump beam. However, a 4 phase transient absorption experiment is often necessary for removing fluorescence or pump scattering that requires chopping both the pump and probe. Finally both beams are focused into the sample. The polarization of the probe and pump is selected immediately before the sample using a broadband wire-grid polarizer (Thorlabs) and a monochromatic half-wave plate (Thorlabs, 266 nm), respectively.

After the sample the probe light must be spectrally filtered with long-pass or band-pass filters to remove the scattered pump and residual fundamental or harmonic that drives white-light generation for the probe, since both are very intense compared to the white-light continuum. Finally the probe is dispersed using a grating or prism and imaged onto a CCD or photodiode array. Two experimental fs-TAS setups are available in the lab that are based on a grating/CCD or prism/photodiode array detection, each have their advantages.[6] The grating based spectrograph has linear diffraction across wavelength and careful selection of the grating blaze allows for either broad or very fine spectral coverage. However, the disadvantage of a grating spectrograph are that the higher orders of diffraction overlap (i.e. order sorting) with the 1st order making only one octave (i.e. 2 times the lowest wavelength) of spectral coverage possible. Additionally gratings have high intensity losses due to the multiple orders of diffraction and their blaze being designed for a specific spectral range. The advantage of a prism is the high light throughput (theoretically lossless at Brewster's angle) and the absence of order sorting allowing for ultrabroadband dispersion and simultaneous detection. Therefore prisms are optimal for UV/Visible transient absorption while gratings are better suited for smaller spectral coverage with higher resolution as necessary for techniques like femtosecond stimulated raman. As for the difference between CCD's and photodiode arrays, the CCD is often considered more sensitive but it has been shown that the shot-to-shot laser noise is the limiting factor, not the choice of detector.[6] For further details comparing gratings, prisms, photodiode arrays and CCDs see reference 6. For further details pertaining to the prism-based fs-TAS setup employed for much of the results in this thesis the reader is directed to appendices 2 and 6.

## 2.5 Nanosecond & Microsecond Transient Absorption

Extended time ranges beyond fs TAS measurements into the nanosecond and microsecond timescales requires a different approach since the pathlength difference between pump and probe would be prohibitively large with hundreds to thousands of feet of pathlength (~1 ft/ns) necessary.[18, 19] In our measurements the time delay between pump and probe is controlled electronically using the laser timing electronics (Coherent SDG Elite) or an external timing generator (Berkeley Nucleonics BNC1000) that synchronize either an external laser diode pulser (Highland Technologies) or a home-built circuit for pulsing LEDs. Therefore this technique uses two separate light sources. Various combinations are possible such as two synchronized fs or ns lasers, or one high power fs/ns laser for the pump and a low power LED or laser diode for the probe.

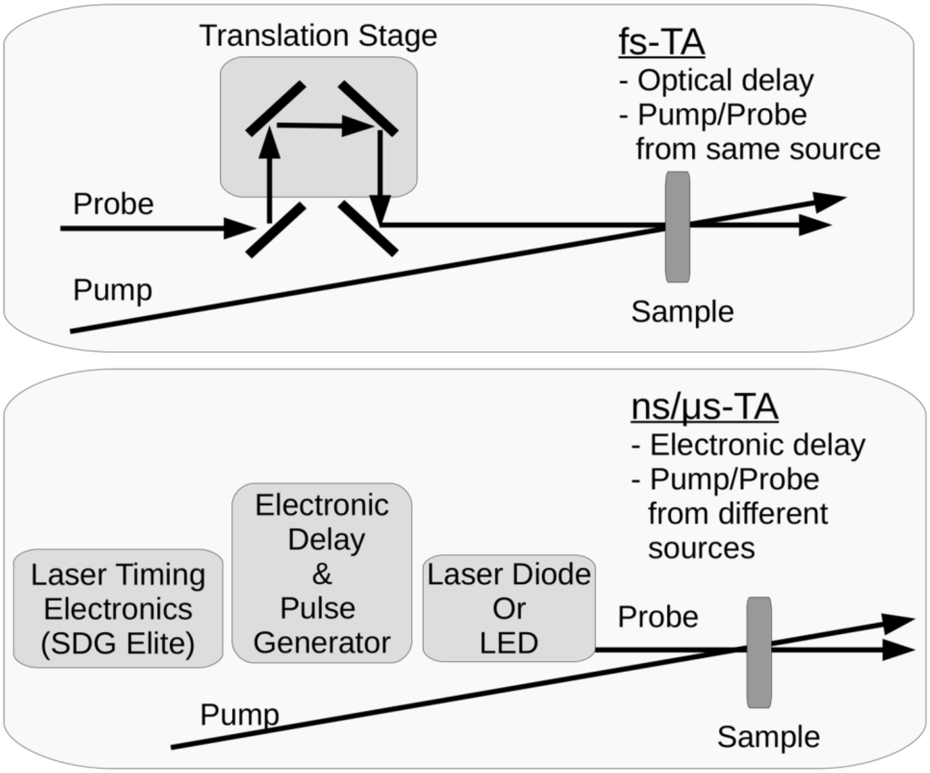
Translation Stage
fs-TA
- Optical delay
- Pump/Probe
from same source
Probe
Pump
Sample
ns/μs-TA
- Electronic delay
- Pump/Probe
from different
sources
Laser Timing
Electronics
(SDG Elite)
Electronic
Delay
&
Pulse
Generator
Laser Diode
Or
LED
Probe
Pump
Sample

**Figure 2.4.** Comparison of experimental set-ups for femtosecond (top) and nanosecond to microsecond transient absorption (bottom).

We employ our fs laser system as the pump source and various LED/laser diodes as our probe source. The latter are highly compact and economical choices that can be easily integrated into the preexisting fs-TAS setup. The LED/laser diode light source replaces the fs probe and utilizes the same focusing and collimation optics as well as light dispersing and detection elements for fast and easy implementation and integration. The light sources readily available in our lab are given in Table 2.2 with their respective wavelength ranges and time resolution. Additional information regarding their general operation, circuitry, and electronic components (including part numbers) are given in appendix 7.

Table 2.2. Various LED and laser diode wavelengths and associated time resolution (FWHM)[8, 20]

| Light Source | λ / nm | FWHM / ns |
|---|---|---|
| White LED | 410-750 | 300 |
| Laser Diode | 405, 450, 520, 639 | 1 |

## 2.6 Pump-Repump-Probe Spectroscopy

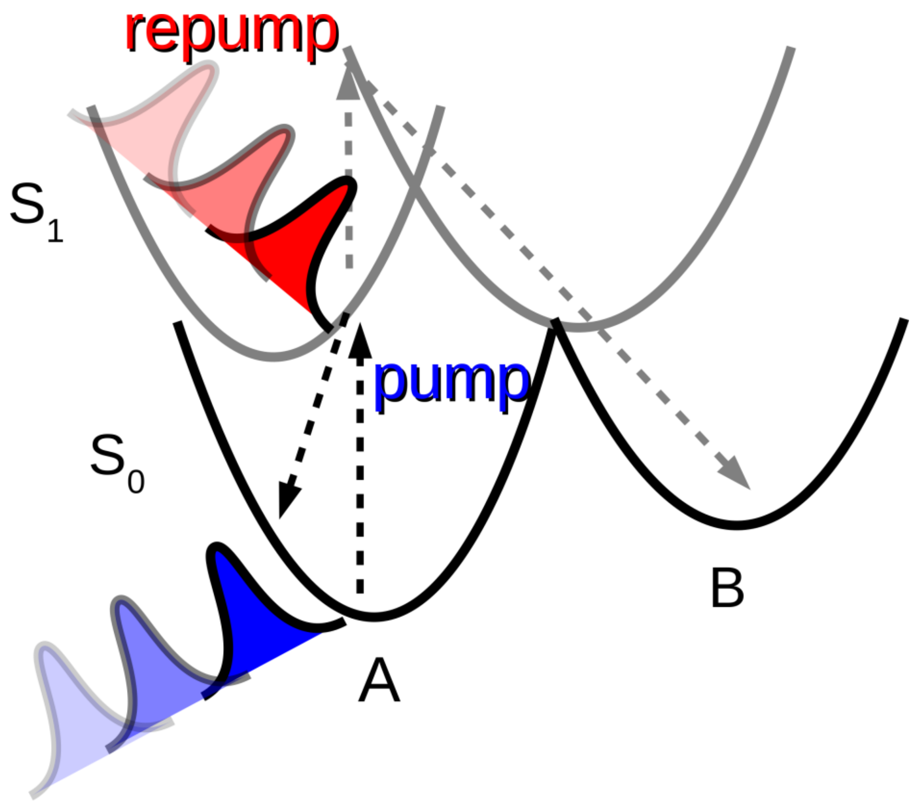

**Figure 2.5.** Generalized pump-repump-probe experiment with molecules A (reactant) and B (product). Under normal excitation conditions (pump only) there is not enough energy to cross the excited-state ($S_1$) barrier and molecule A is regenerated. When a repump pulse is added at the correct time delay to intercept the excited-state population the molecules can overcome the barrier and funnel downwards to form molecule B. Only with the addition of the repump pulse will molecule B be generated.

In order to further interrogate excited-state photophysics a "double difference" transient absorption (ΔΔOD) or pump-repump-probe experimental scheme can be employed.[21] This can be used to interrupt or alter the 1-photon induced dynamics, determine correlation between states and disentangle overlapping spectral/kinetic components. A prototypical example is given in Figure 2.5 where the reactant (A) only produces product (B) by population transfer to a higher electronic state using an appropriately timed repump pulse. The experimental setup can be viewed as a "double" transient absorption experiment with two excitation pulses, optical choppers and delay stages that allow for two variable time delays. This experiment requires various pump (Pu), repump (Re), probe (Pr) and background (BG) combinations or phases to be collected and organized that can be summarized by equations 2.6-8 with the final corrected pump-repump-probe signal given by Equation 2.9.

$$\Delta OD_{Fl.Corr.} = -\log\left(\frac{PuPr - Pu}{Pr - BG}\right) \qquad (2.6)$$

$$\Delta OD_{Fl.Corr.PRP} = -\log\left(\frac{PuRePr - RePu}{Pr - BG}\right) \qquad (2.7)$$

$$\Delta OD_{Fl.Corr.RP} = -\log\left(\frac{PuRePr - RePu}{Pr - BG}\right) \qquad (2.8)$$

$$\Delta\Delta OD_{Fl.Corr.} = \Delta OD_{Fl.Corr.PRP} - \Delta OD_{Fl.Corr.} - \Delta OD_{Fl.Corr.RP} \qquad (2.9)$$

Application of PRP spectroscopy to the photocyclization of *ortho*-arenes is particularly useful for deconvoluting the kinetics of overlapped spectral components due to the ESA and PPA. The generalized PRP experiment is given in Figure 2.6, where the proposed sequential kinetic model (A to B or $S_1$ OTP to $S_0$ DHT) is interrogated. The influence of bleaching the observed ESA with a repump pulse on the TA signal of DHT at long time delays (>1 ns) is monitored. Alternatively, a direct depletion of DHT is also possible which would show weaker depletion of DHT at early time delays and stronger depletion at later time delays that would correlate with the lifetime of the ESA of OTP.

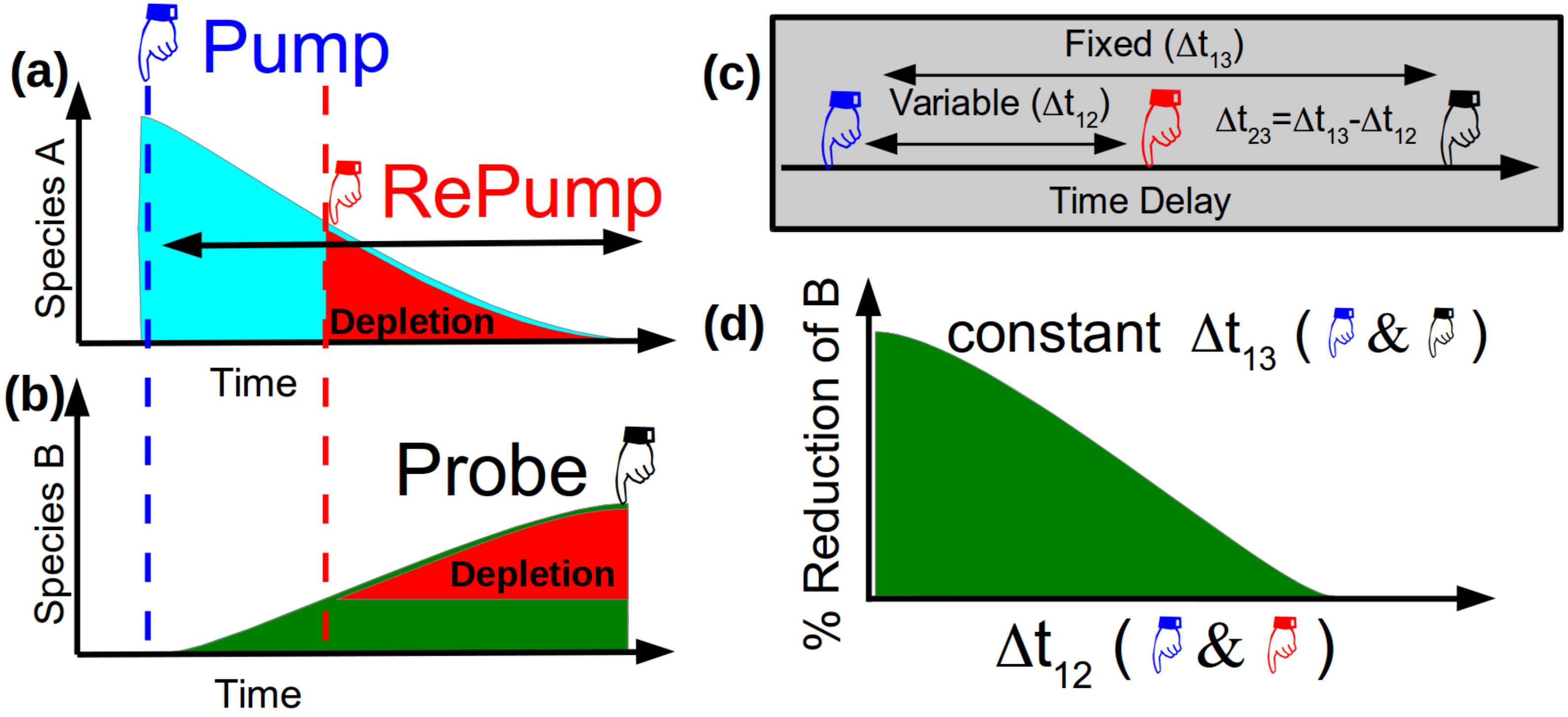
(a)
Pump
RePump
Species A
Depletion
Time
(b)
Species B
Probe
Depletion
Time
(c)
Fixed (Δt13)
Variable (Δt12)
Δt23=Δt13-Δt12
Time Delay
(d)
% Reduction of B
constant Δt13 ( & )
Δt12 ( & )

**Figure 2.6.** Pump-Repump-Probe Experiment for deconvolution of spectral components and kinetics. (a) For a sequential two component kinetic scheme a population "A" is created by the pump and then depleted with a repump pulse . (b) The effect on "B" is that the final population will be reduced (t=∞). By scanning the time delays given in the top right (c) we can extract the kinetics (d) regarding the formation of B by examining the relative reduction in the final population monitored by the probe at t=∞ ($\Delta t_{13}$>1 ns).

## 2.7 Global Fitting Algorithm

Global fitting has become a common analysis amongst spectroscopists due to its ability to simultaneous fit spectral components and kinetics.[22, 23] Often global analysis is preferred over conventional exponential decay fitting since global analysis can be viewed as a spectrally constrained fitting process. Global analysis has a few variants that are unique in their choice of spectral decomposition but are quite similar in their fitting procedure. Singular value decomposition (SVD)[24, 25] will be the chosen method herein but other methods, such as principal component analysis (PCA)[26, 27] or matrix least squares (MLS, this method requires the spectra as user input),[28] provide nearly identical results.

The SVD-based global fitting algorithm begins with the SVD procedure (Data=$USV^T$) that decomposes the transient absorption spectra into its spectral (U) and time (V) components as well as their relative weighting (diagonal elements of the matrix S). The S matrix is essential to the fitting process as its weights along the diagonal provide information about the predicted number of kinetic species and their relative significance. Next the time resolution of the experiment or instrument response function (IRF) must be determined by fitting the rise in signal or can be provided as user input from an external source such as a pump-probe cross-correlation experiment. Undoubtedly the most important user input is the selection of a kinetic model that can be determined using the number of relevant components in the S matrix in combination with chemical intuition for guidance towards the most sensible and relevant model. Our algorithm currently has a library of >20 kinetic models and the addition of models only requires one to derive the analytic solution. With some effort the algorithm could be adapted for numerical kinetics that would allow for quite complex kinetic models at the expense of computational time.

Using the selected kinetic model, IRF and SVD information an initial guess is constructed and subjected to nonlinear least-squares fitting for parameter optimization. Note that the initial guess also includes a Gaussian function with a duration of the IRF as an extra kinetic component which is used to extract coherent artifacts, such as cross phase modulation, stimulated Raman amplification, etc.[29] Also the kinetics are convoluted with the IRF at each iteration since the provided models are not convoluted making input of new models more simplistic and user friendly. Finally the resultant fit is evaluated by checking the residuals as a function of time and qualitative matches of the fit spectral components or species associated spectra (SAS), the D matrix in Figure 2.7, to the observed spectral components. If an adequate fit is not determined a new kinetic model is selected and the fitting process is repeated. The algorithm was prepared in MATLAB and the corresponding code is presented in Appendix 8.

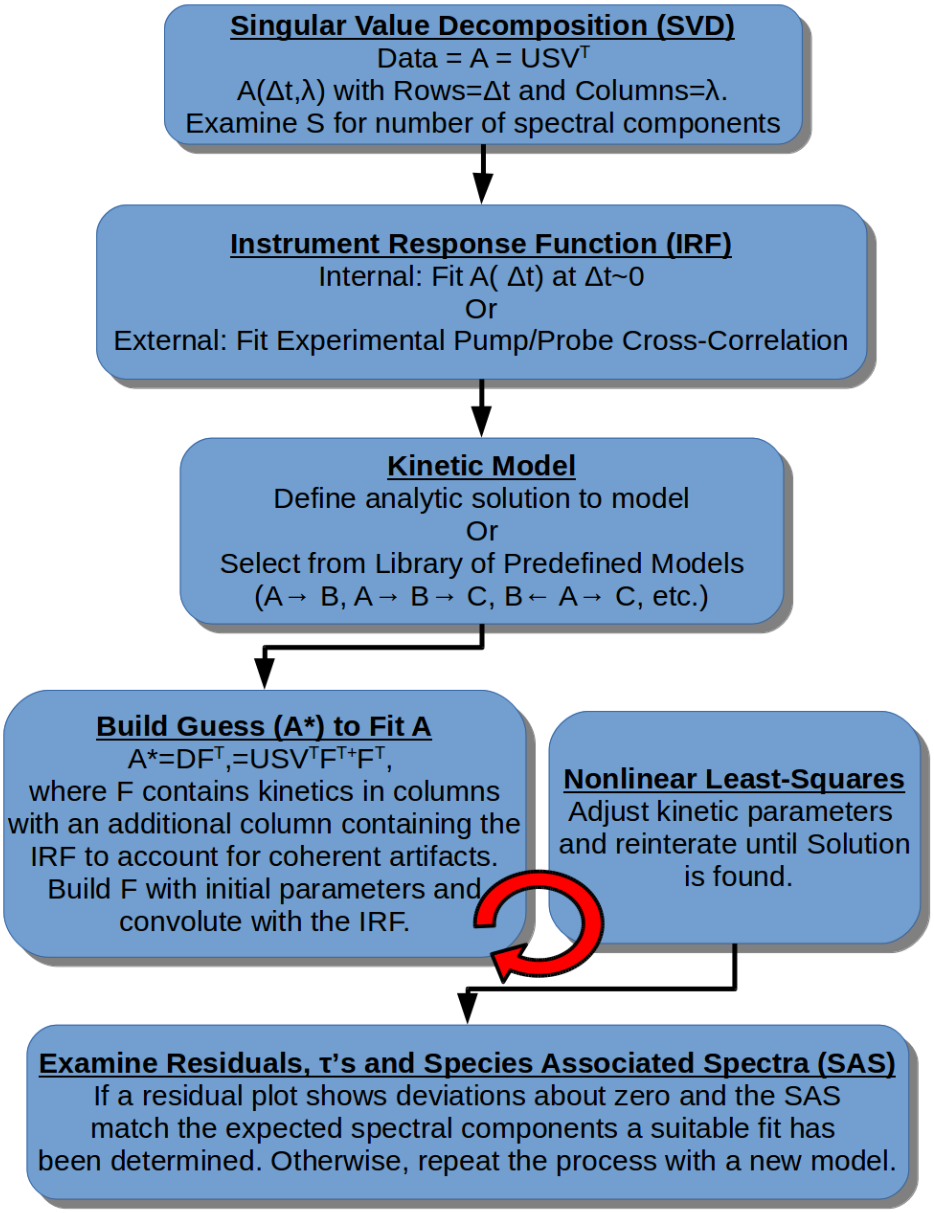
Singular Value Decomposition (SVD)
Data = A = USV$^T$
A(Δt,λ) with Rows=Δt and Columns=λ.
Examine S for number of spectral components
Instrument Response Function (IRF)
Internal: Fit A( Δt) at Δt~0
Or
External: Fit Experimental Pump/Probe Cross-Correlation
Kinetic Model
Define analytic solution to model
Or
Select from Library of Predefined Models
(A→ B, A→ B→ C, B← A→ C, etc.)
Build Guess (A*) to Fit A
$A^*=DF^T,=USV^TF^{T+}F^T$,
where F contains kinetics in columns
with an additional column containing the
IRF to account for coherent artifacts.
Build F with initial parameters and
convolute with the IRF.
Nonlinear Least-Squares
Adjust kinetic parameters
and reinterate until Solution
is found.
Examine Residuals, τ's and Species Associated Spectra (SAS)
If a residual plot shows deviations about zero and the SAS
match the expected spectral components a suitable fit has
been determined. Otherwise, repeat the process with a new model.

**Figure 2.7**. Flowchart for global fitting procedure and details of algorithm.

## 2.8 Computational Chemistry Methods

Much of the experimental work herein is accompanied by supportive quantum chemistry computations.[30] Specifically the computation of the transition states for ring-reopening, simulation of UV/Vis spectra and prediction of $S_0/S_1$ CI's have been quite useful for complementing experimental results. For most ground state properties density-functional theory (DFT)[31] was the method of choice due to its speed and general applicability. Both spin restricted and unrestricted DFT formalisms have been used where the unrestricted formalism has been particularly useful for the location of transition states for ring-reopening.[32] The extension of DFT methods for calculation of excited-state properties and particularly the prediction of excitation energies for simulation of UV/Vis spectra with quantitative accuracy in most cases has been performed using time-dependent DFT (TDDFT).[33-35] For calculation of conical intersections and other excited-state geometries the SA-CASSCF[30, 36] method has been utilized. However, recent advances in TDDFT methods by application of the spin-flip TDDFT (SF-TDDFT)[37-39] method that includes dynamic electron correlation[40] promises improvement in both speed and accuracy. Predominantly SA-CASSCF was used herein but SF-TDDFT has also been used to explore the PES of OTP. Specific details of quantum-chemical computations are discussed in each chapter accordingly.

## 2.9 References

1. Weiner, A. M., *Ultrafast optics*. Wiley: Hoboken, N.J., 2009; p xvii, 580 p.

2. New, G., *Introduction to Nonlinear Optics*. Cambridge University Press: Cambridge ; New York, 2011; p xv, 257 pages.

3. Zewail, A. H., Femtochemistry: Atomic-Scale Dynamics of the Chemical Bond. *The Journal of Physical Chemistry A* **2000,** *104* (24), 5660-5694.

4. Nagura, C.; Suda, A.; Kawano, H.; Obara, M.; Midorikawa, K., Generation and characterization of ultrafast white-light continuum in condensed media. *Applied Optics* **2002,** *41* (18), 3735.

5. Brouwer, A. M., Standards for photoluminescence quantum yield measurements in solution (IUPAC Technical Report). *Pure and Applied Chemistry* **2011,** *83* (12).

6. Megerle, U.; Pugliesi, I.; Schriever, C.; Sailer, C. F.; Riedle, E., Sub-50 fs broadband absorption spectroscopy with tunable excitation: putting the analysis of ultrafast molecular dynamics on solid ground. *Applied Physics B* **2009,** *96* (2-3), 215-231.

7. Berera, R.; van Grondelle, R.; Kennis, J. T. M., Ultrafast transient absorption spectroscopy: principles and application to photosynthetic systems. *Photosynthesis Research* **2009,** *101* (2-3), 105-118.

8. Snyder, J. A.; Bragg, A. E., Structural Control of Nonadiabatic Bond Formation: The Photochemical Formation and Stability of Substituted 4a,4b-Dihydrotriphenylenes. *The Journal of Physical Chemistry A* **2015,** *119* (17), 3972-3985.

9. Molloy, M. S.; Snyder, J. A.; Bragg, A. E., Structural and Solvent Control of Nonadiabatic Photochemical Bond Formation: Photocyclization of o-Terphenyl in Solution. *The Journal of Physical Chemistry A* **2014,** *118* (22), 3913-3925.

10. Smith, M. C.; Snyder, J. A.; Streifel, B. C.; Bragg, A. E., Ultrafast Excited-State Dynamics of ortho-Terphenyl and 1,2-Diphenylcyclohexene: The Role of “Ethylenic Twisting” in the Nonadiabatic Photocyclization of Stilbene Analogs. *The Journal of Physical Chemistry Letters* **2013,** *4* (11), 1895-1900.

11. Treacy, E., Optical pulse compression with diffraction gratings. *IEEE Journal of Quantum Electronics* **1969,** *5* (9), 454-458.

12. Farrow, D. A.; Qian, W.; Smith, E. R.; Ferro, A. A.; Jonas, D. M., Polarized pump-probe measurements of electronic motion via a conical intersection. *The Journal of Chemical Physics* **2008,** *128* (14), 144510.

13. Levitus, M.; Garcia-Garibay, M. A., Polarized Electronic Spectroscopy and Photophysical Properties of 9,10-Bis(phenylethynyl)anthracene. *The Journal of Physical Chemistry A* **2000,** *104* (38), 8632-8637.

14. Gaab, K. M.; Bardeen, C. J., Nonstationary Rotational Diffusion in Room Temperature Liquids Measured by Femtosecond Three-Pulse Transient Anisotropy. *Phys Rev Lett* **2004,** *93* (5), 056001.

15. Lessing, H. E.; Von Jena, A., Separation of rotational diffusion and level kinetics in transient absorption spectroscopy. *Chem Phys Lett* **1976,** *42* (2), 213-217.

16. Riedle, E.; Bradler, M.; Wenninger, M.; Sailer, C. F.; Pugliesi, I., Electronic transient spectroscopy from the deep UV to the NIR: unambiguous disentanglement of complex processes. *Faraday Discussions* **2013,** *163*, 139.

17. Johnson, P. J. M.; Prokhorenko, V. I.; Miller, R. J. D., Stable UV to IR supercontinuum generation in calcium fluoride with conserved circular polarization states. *Optics Express* **2009,** *17* (24), 21488.

18. Schmidhammer, U.; Roth, S.; Riedle, E.; Tishkov, A. A.; Mayr, H., Compact laser flash photolysis techniques compatible with ultrafast pump-probe setups. *Rev Sci Instrum* **2005,** *76* (9), 093111.

19. Gottlieb, S. M.; Corley, S. C.; Madsen, D.; Larsen, D. S., Note: A flexible light emitting diode-based broadband transient-absorption spectrometer. *Rev Sci Instrum* **2012,** *83* (5), 056107.

20. Pitts, C. R.; Ling, B.; Snyder, J. A.; Bragg, A. E.; Lectka, T., Aminofluorination of Cyclopropanes: A Multifold Approach through a Common, Catalytically Generated Intermediate. *J Am Chem Soc* **2016,** *138* (20), 6598-6609.

21. Ward, C. L.; Elles, C. G., Cycloreversion Dynamics of a Photochromic Molecular Switch via One-Photon and Sequential Two-Photon Excitation. The Journal of Physical Chemistry A **2014,** 118*, 10011-10019.*

22. van Stokkum, I. H. M.; Larsen, D. S.; van Grondelle, R., Global and target analysis of time-resolved spectra. *Biochimica et Biophysica Acta (BBA) - Bioenergetics* **2004,** *1657* (2-3), 82-104.

23. Ruckebusch, C.; Sliwa, M.; Pernot, P.; de Juan, A.; Tauler, R., Comprehensive data analysis of femtosecond transient absorption spectra: A review. *Journal of Photochemistry and Photobiology C: Photochemistry Reviews* **2012,** *13* (1), 1-27.

24. Hendler, R. W.; Shrager, R. I., Deconvolutions based on singular value decomposition and the pseudoinverse: a guide for beginners. *Journal of Biochemical and Biophysical Methods* **1994,** *28* (1), 1-33.

25. Ernsting, N. P.; Kovalenko, S. A.; Senyushkina, T.; Saam, J.; Farztdinov, V., Wave-Packet-Assisted Decomposition of Femtosecond Transient Ultraviolet−Visible Absorption Spectra: Application to Excited-State Intramolecular Proton Transfer in Solution. *The Journal of Physical Chemistry A* **2001,** *105* (14), 3443-3453.

26. Abdi, H.; Williams, L. J., Principal component analysis. *Wiley Interdisciplinary Reviews: Computational Statistics* **2010,** *2* (4), 433-459.

27. Segtnan, V. H.; Šašić, Š.; Isaksson, T.; Ozaki, Y., Studies on the Structure of Water Using Two-Dimensional Near-Infrared Correlation Spectroscopy and Principal Component Analysis. *Analytical Chemistry* **2001,** *73* (13), 3153-3161.

28. Frans, S. D.; Harris, J. M., Reiterative least-squares spectral resolution of organic acid/base mixtures. *Analytical Chemistry* **1984,** *56* (3), 466-470.

29. Lorenc, M.; Ziolek, M.; Naskrecki, R.; Karolczak, J.; Kubicki, J.; Maciejewski, A., Artifacts in femtosecond transient absorption spectroscopy. *Applied Physics B: Lasers and Optics* **2002,** *74* (1), 19-27.

30. Cramer, C. J., *Essentials of computational chemistry : theories and models*. 2nd ed.; Wiley: Chichester, West Sussex, England ; Hoboken, NJ, 2004; p xx, 596 p.

31. Cohen, A. J.; Mori-Sánchez, P.; Yang, W., Challenges for Density Functional Theory. *Chemical Reviews* **2012,** *112* (1), 289-320.

32. Williams, R. V.; Edwards, W. D.; Mitchell, R. H.; Robinson, S. G., A DFT Study of the Thermal, Orbital Symmetry Forbidden, Cyclophanediene to Dihydropyrene

Electrocyclic Reaction. Predictions to Improve the Dimethyldihydropyrene Photoswitches. *J Am Chem Soc* **2005,** *127* (46), 16207-16214.

33. Casida, M. E.; Huix-Rotllant, M., Progress in Time-Dependent Density-Functional Theory. *Annual Review of Physical Chemistry* **2012,** *63* (1), 287-323.

34. Hirata, S.; Head-Gordon, M.; Szczepanski, J.; Vala, M., Time-Dependent Density Functional Study of the Electronic Excited States of Polycyclic Aromatic Hydrocarbon Radical Ions. *The Journal of Physical Chemistry A* **2003,** *107* (24), 4940-4951.

35. Laurent, A. D.; Jacquemin, D., TD-DFT benchmarks: A review. *International Journal of Quantum Chemistry* **2013,** *113* (17), 2019-2039.

36. Docken, K. K.; Hinze, J., LiH Potential Curves and Wavefunctions for X $^1\Sigma^+$, A $^1\Sigma^+$, B $^1\Pi$, $^3\Sigma^+$, and $^3\Pi$. *The Journal of Chemical Physics* **1972,** *57* (11), 4928-4936.

37. Harabuchi, Y.; Yamamoto, R.; Maeda, S.; Takeuchi, S.; Tahara, T.; Taketsugu, T., Ab Initio Molecular Dynamics Study of the Photoreaction of 1,1′-Dimethylstilbene upon $S_0 \rightarrow S_1$ Excitation. *The Journal of Physical Chemistry A* **2016,** *120* (44), 8804-8812.

38. Harabuchi, Y.; Keipert, K.; Zahariev, F.; Taketsugu, T.; Gordon, M. S., Dynamics Simulations with Spin-Flip Time-Dependent Density Functional Theory: Photoisomerization and Photocyclization Mechanisms of cis-Stilbene in ππ* States. *The Journal of Physical Chemistry A* **2014**.

39. Rinkevicius, Z.; Vahtras, O.; Ågren, H., Spin-flip time dependent density functional theory applied to excited states with single, double, or mixed electron excitation character. *The Journal of Chemical Physics* **2010,** *133* (11), 114104.

40. Borden, W. T.; Davidson, E. R., The Importance of Including Dynamic Electron Correlation in ab Initio Calculations. *Accounts Chem Res* **1996,** *29* (2), 67-75.

# Chapter 3

## Ultrafast Excited-State Dynamics of *ortho*-Terphenyl and 1,2-Diphenylcyclohexene: The Role of "Ethylenic Twisting" in the Nonadiabatic Photocyclization of Stilbene Analogs

Reproduced with permission from Snyder, J. A.; Smith, M. C.; Streifel, B. C.; Bragg, A. E. *The Journal of Physical Chemistry Letters* **2013**, *4*, 1895–1900. Copyright 2013, American Chemical Society.

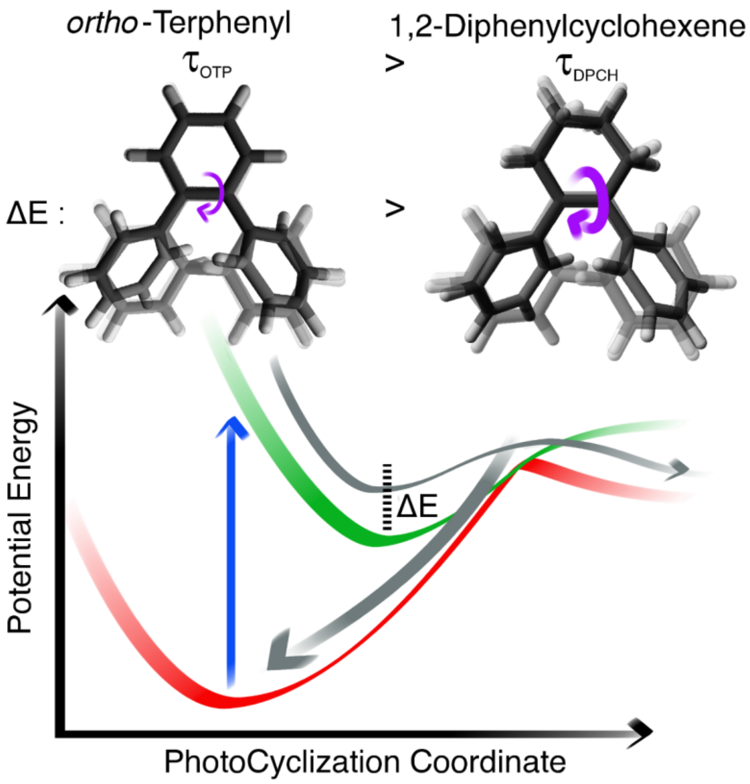
*ortho*-Terphenyl
$\tau_{OTP}$
>
1,2-Diphenylcyclohexene
$\tau_{DPCH}$
ΔE :
>
Potential Energy
ΔE
PhotoCyclization Coordinate

**Figure 3.0.** Table of contents figure.

## 3.0 Abstract

Nonadiabatic photocyclization is the fundamental step underlying photo-switching and light-assisted bond formation within diarylethylenes, yet the details of the nuclear

dynamics leading to cyclization remain unclear. We have examined the ultrafast excited-state dynamics of o-terphenyl (OTP) and 1,2-diphenylcyclohexene (DPCH) in solution to determine how variation in structural constraints impacts the course of nonadiabatic photocyclization specifically in stilbenoids. Measured spectral dynamics reflect cyclization through a $S_1$ -to-$S_0$ transition for both systems on picosecond time scales, with excited-state decay appreciably faster for DPCH versus OTP. Supportive ab initio calculations reveal a higher energetic penalty in OTP versus DPCH for reaching the lowest-energy conical intersection from the $S_1$ minimum; this penalty is associated primarily with twisting about the carbon−carbon bond that bridges terminal phenyl groups, a structural change that has a critical role in nonadiabatic cis−trans isomerization of diarylethylenes. Findings provide a new experimental perspective on the elusive nuclear dynamics underlying cis-stilbene photocyclization.

## 3.1 Introduction

Nonadiabatic transitions and crossings through conical intersections (CIs) have become paradigmatic concepts for describing the dynamics of electronically excited states and underlie processes ranging from photodissociation of small molecules to the isomerization of large pigments critical to biological processes such as vision. [1−4] Capturing glimpses of crossings between electronic states as they occur in time and assessing how they are influenced by molecular structure has become a common goal for experimental research in molecular energy transfer in recent years. [5−9] Much of this work has concentrated on nonadiabatic photocyclization, which is central to molecular photoswitching and photochromic material applications [7,8,10,11] as well as light-assisted synthetic strategies. [12,13] Understanding both how energy flows between electronic states and how structural constraints influence nonadiabatic cyclization pathways is critical for determining how to control bond formation effectively in these applications.

Diarylethylenes make up a core group of photoswitching molecules that operate via nonadiabatic photoinduced electro-cyclization.[10] *cis*-Stilbene (CS, Scheme 3.1) is perhaps the simplest member of this group in terms of molecular structure, exhibits rich photoinduced nonadiabatic behavior, and remains a favorite exemplary molecular system for exploring the nuclear dynamics that facilitate fast nonadiabatic transitions: [2,14–27] By way of various CIs, $S_1$ CS is known to isomerize to generate ground-state *trans*-stilbene (TS), return to its own ground state, and, to a lesser degree, photocyclize to form 4a,4b-dihydrophenanthrene (DHP). Given the dominance of the CS-to-TS pathway, cyclization dynamics have been difficult to study directly through experiments, and even basic questions about CS photocyclization remain unresolved: Does cyclization to form DHP occur through a direct transition to the ground or an excited state, and what structural dynamics are critical to reaching the gateway CI (or intersection seam) for cyclization?

In this work we have investigated how structural variation gives rise to different nonadiabatic photocyclization behavior for two stilbene analogs, 1,2-diphenylcyclohexene (DPCH) and *o*-terphenyl (OTP), with the outlook that work with these analogs structurally inhibited against cis−trans isomerization can help to clarify critical features of the CS ring-closure pathway. [18,19,28,29] DPCH can be viewed as CS structurally constrained against cis−trans isomerization through the addition of a bridging aliphatic chain. [18,28,29] Previous work with DPCH has shown that, much like CS, DPCH has a short-lived $S_1$ state (<20 ps) and cyclizes to form 9,10-cyclohexano-4a,4b-dihydrophenanthrene (CDHP). [28,29] Likewise, OTP is thought to photocyclize into 4a,4b-dihydrotripheneylene (DHT) as the first step in the photochemical synthesis of triphenylene. [12,13] We present ultrafast time-

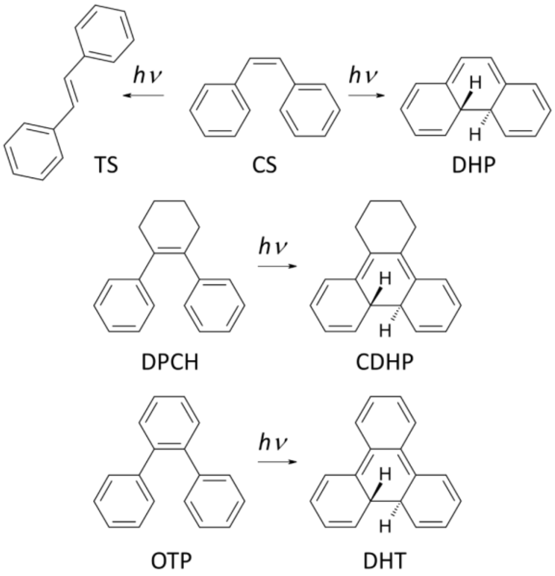

**Scheme 3.1.** Photoinduced nonadiabatic isomerization and cyclization of diarylethylenes and *o*-terphenyl

resolved interrogations of UV-induced OTP and DPCH nonadiabatic cyclization in THF solution, demonstrating that $S_1$ nonadiabatic decay occurs in both cases on picosecond time scales and with the formation of ground-state cyclized products. Importantly, DPCH and OTP differ according to the relative flexibility of the central ring that bridges the terminal phenyl groups, a difference reflected in their relative nonadiabatic decay rates. By exploiting this key structural difference we show through our measurements and supportive ab initio calculations that twisting about the central C−C bond is a key motion in the nonadiabatic relaxation coordinate of stilbene analogs. Although CS photophysics have been studied extensively over the last half-century to elucidate the dynamics of a prototypical nonadiabatic cis−trans isomerization, details concerning the competing photocyclization pathway remain unclear. Our findings with CS analogs offer new perspective on the nuclear dynamics underlying the cyclization pathway. [18,19,28,29]

## 3.2 Results

Our experimental measurements have utilized ultrafast broadband pump−probe transient absorption spectroscopy (TAS); we offer extensive technical details regarding sample preparation and optical setup in the Experimental Section and in appendix 1. Experimental measurements are summarized as follows: Solutions of OTP and DPCH in THF were excited with sub-100-fs excitation pulses with a center wavelength of 266 nm, which is resonant with the $S_0$ −$S_1$ transition of both molecules. Photoinduced transient excited- state absorption dynamics were probed at various picosecond and subpicosecond time delays after excitation with ultrafast broadband continua (470−720 nm).

Figure 3.1a presents the TAS of UV-excited DPCH in THF as probed in the visible. The photoinduced absorption spectrum of DPCH is characterized by short-lived features that peak near 660 nm and below 500 nm. DPCH excited-state spectra exhibit remarkable similarity to the $S_1$ absorption spectrum of CS, [26,30] such that we can readily assign it to $S_1 \rightarrow S_N$ transitions of DPCH. Although a fast spectral shift is observed at early delays (e.g.,

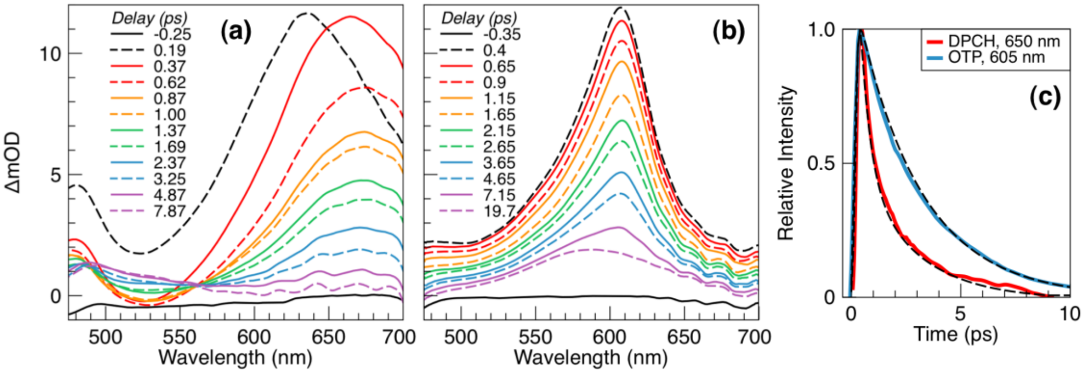

**Figure 3.1.** Spectral dynamics of UV-excited 1,2-diphenylcyclohexene (DPCH) (a) and *o*-terphenyl (OTP) (b). (c) $S_1$ decay of OTP and DPCH. OTP has an $S_1$ lifetime of 2.91 ps; DPCH in THF exhibits an average $S_1$ lifetime of 2.05 ps, although appreciable $S_1$ decay occurs on a subpicosecond time scale. The long-time constant offset from the DHT absorption has been subtracted from the 605 nm OTP trace to focus attention on the relative time scales for nonadiabatic decay.

190 vs 370 fs), TA spectral dynamics of $S_1$ DPCH are dominated by a rapid decrease in the absorption intensity near 660 nm over the picoseconds that follow excitation; this is accompanied by the appearance of a broad, weak absorption band that peaks below 500 nm and that remains at the latest delays probed. The latter feature is reminiscent of the absorption spectrum of ground-state DHP that appears near 450 nm after UV photoexcitation of CS and its analogs, [20,26,31] and we thus attribute this to the lowest-energy transition of CDHP. Isosbestic points appear near 560 and 490 nm after the fast spectral red shift, indicating a kinetic interconversion between relaxed $S_1$ DPCH and $S_0$ CDHP as part of the excited- state nonadiabatic decay. The time-dependent decay of the $S_1$ state is readily quantified from the intensity decay near 650 nm; a trace of this decay is plotted in Figure 3.1c and has been fitted with a biexponential decay convoluted with the instrument

response. The DPCH $S_1$ state exhibits an average lifetime of 2.05 ps, although more than 50% of the excited-state decay occurs on subpicosecond time scales. These time scales are comparable to CS nonadiabatic cyclization rates deduced by Rodier and Myers [20] but considerably faster than the bracketed DPCH cyclization rate previously determined from product yields. [28,29]

Figure 3.1b presents the visible TAS of UV-excited OTP. The photoinduced absorption peaks at 605 nm initially, decaying substantially over the first several picoseconds and giving rise to a weak transient absorption band that peaks near 580 nm. The band at 605 nm is similar to the lowest-energy excited-state absorption bands of both DPCH and CS, and this feature can be assigned readily to $S_1 \rightarrow S_N$ absorption of OTP. We assign the long-lived absorption band peaked at 580 nm to ground-state absorption of DHT based on its similarity to the weak, broad absorption observed after photoexcitation of both DPCH and CS; the relative red shift in the peak absorption is consistent with the increased conjugation in DHT relative to DHP. To validate this assignment, we have carried out TDDFT calculations of the lowest vertical excitation energies from the DFT-optimized DHT and DHP ground-state geometries (B3LYP, 6-31+G*). These calculations predict peak absorption wavelengths for DHP and DHT at 520 and 670 nm, respectively. (See appendix 1 for full calculation details.) Although the corresponding calculated transition energies differ from experimental values (e.g., the calculated DHP absorption maximum is 70 nm to the red of the experimental value), the sign and magnitude of the difference between calculated transition energies is consistent with a DHT absorption peak at 580 nm; calculated values are also roughly consistent with the onset of measured absorption spectra. It is interesting to note that the difference in lowest excitation energies for DHT and CDHP

(~0.6 eV) is considerably larger than the difference in lowest excitation energies for OTP and DPCH (~0.3 eV from both steady-state absorption and ab initio calculations, see appendix 1); this most likely reflects that the extra conjugation in the central six-carbon ring of OTP/DHT has a larger impact on the energetics when a more planar product configuration is obtained. Kinetics of the OTP $S_1$ population decay is visualized by plotting the time- dependence (decay) in TA intensity at 605 nm, as shown in Figure 3.1c. OTP $S_1$ decay occurs with a fitted exponential lifetime of 2.91 ps.

**Table 3.1.** Key Structural Parameters from SA-2-CAS(2/2)-6-31G Optimizations and CI Searches of OTP (in bold) and DPCH (in italics)

| geometry | twist (θ)/ ° | torsion (φ)/° | bend (α)/° |
|---|---|---|---|
| $S_0$ min. | **2.64** (*8.36*) | **55.43, 61.98** (*56.30, 58.54*) | **123.62, 123.39** (*123.48, 123.5*) |
| $S_1$ min. | **12.22** (*21.84*) | **13.20, 14.13** (*11.48, 6.21*) | **120.0, 120.6** (*119.94, 120.92*) |
| $S_0$ /$S_1$ CI | **24.97** (*24.16*) | **1.3, 9.77** (*2.82, 11.44*) | **119.94, 119.73** (*119.18, 116.62*) |

## 3.3 Discussion

Although excited-state decay occurs considerably slower in OTP compared with DPCH, the measured excited-state lifetimes alone do not directly illuminate what intra- or intermolecular effects control nonadiabatic dynamics in either case. Direct crossings through CIs are generally very fast (a few to tens of femtoseconds), such that the relatively long-lived excited-state population in both cases must reflect nuclear dynamics on the excited-state surface that produces a slow effective approach to the CI or crossing seam. [1–3] Such dynamics can be due to either the nature of intrinsic intramolecular interactions or the influence of solvent-induced barriers. As illustrated below with ab initio calculations, the ground-state geometries of OTP and DPCH involve significant ring-to-ring nonplanarity such that nuclear rearrangement in the excited state between the Franck−Condon region and a cyclized structure must involve appreciable torsional twisting of terminal phenyl groups. Indeed, phenyl-ring rotations have been argued to be the most critical nuclear motions along the cyclization coordinate for CS and its analogs. [18,19] We anticipate that the fastest nonadiabatic cyclization rate will be limited by the time scale for phenyl-ring rotation in solution but expect that ring-rotation time scales should be fairly similar for these molecules. Thus, we conclude that the different nonadiabatic rates observed for OTP and DPCH reflect intrinsic intra- molecular effects on other nuclear coordinates.

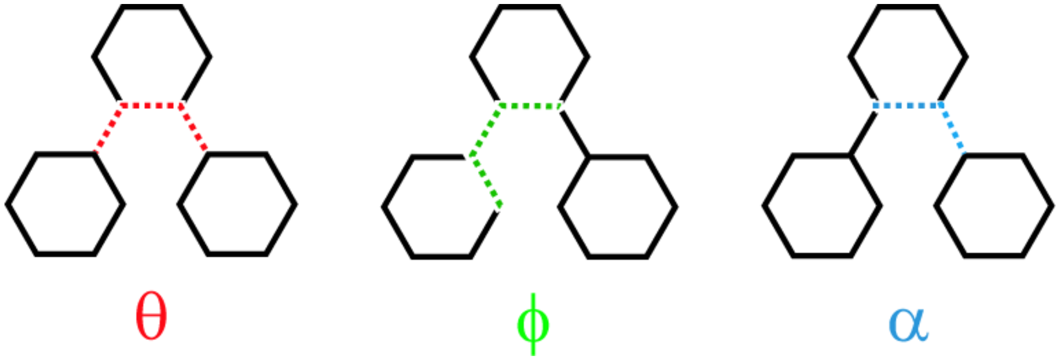

**Figure 3.2.** Calculated dihedral and bond angles presented in Table 3.1 and described in the text are defined with respect to the bonds depicted with dotted lines. Given the symmetries of both OTP and DPCH, each molecule is characterized by two φ's and two α's.

To better understand how molecular structure influences the excited-state potential-energy landscape (and, therefore, the cyclization kinetics) for OTP and DPCH, we have carried out a limited set of electronic structure calculations. These include geometry optimizations of the $S_0$ and $S_1$ minima for each of these molecules as well as searches for the lowest-energy CIs accessible from the $S_1$ minima. These calculations are not intended to provide a complete theoretical description of the nonadiabatic photocyclization dynamics but rather an overview of critical landmarks on the $S_1$ potential-energy surfaces that are likely to have bearings on cyclization dynamics. Calculations were carried out at the state-averaged complete active-space SCF (SA-CASSCF) level 32 using GAMESS. [33] The precedent for using this method to calculate CIs and minima in the vicinity of CIs has been previously demonstrated with CS, [22] and its superiority over other methods (e.g., TDDFT) has also been documented. [34] Calculations were performed with two- state averaging (with equal weighting) and a (2/2) active space to minimize the computational expense; similar qualitative trends were recovered using a larger active space. (See Experimental Section and appendix 1 for more details.)

Geometry optimizations were carried out as follows: The $S_0$ minimum geometry was determined first. The $S_0$ minimum geometry and orbitals were then used as the initial input for calculating the $S_1$ minimum. The $S_0$ / $S_1$ CI search was initiated using parameters optimized for the $S_1$ minimum. The minimal energy CI searches utilized the method of Bearpark et al.[35] This local searching procedure was important for determining the CI geometries that are closest to the $S_1$ minima along the CI seam. [35] Additional details of structural optimizations and searches are provided in the Experimental Section and in appendix 1.

Table 3.1 lists values of critical dihedral and bond angles relevant to cyclization for each state and molecule.[22;28] These angles are described pictorially through Figure 3.2 and include: The dihedrals spanning all three phenyl rings, θ, which correspond primarily to twisting of the central C−C bond that bridges the terminal rings; the dihedrals between adjacent phenyl rings, φ, which corresponds primarily to torsional twisting of the terminal phenyl rings; and the angles between the terminal phenyl groups and the central C−C bond, α. The optimized ground-state geometries of these molecules are very similar with respect to these dihedral angles, with terminal phenyl rings twisted by φ ~55−60° and very low values for θ (<10°). In both systems additional inter-ring bond-order in the $S_1$ state prompts a decrease in φ at the $S_1$ minimum and the lowest-energy CI. In contrast, θ increases steadily for both molecules from the $S_0$ to $S_1$ to CI geometries. However, the change in θ between the $S_1$ minimum and the CI is much larger for OTP relative to DPCH.

Our calculations further illustrate that opening θ between the $S_1$ minimum and the lowest-energy CI consistently comes at a higher energetic penalty (ΔE, Figure 3.3) in OTP relative to DPCH: 0.147 versus 0.02 eV, respectively, with the (2/2) active space and 0.995 versus 0.235 eV with a (6/6) active space. These results are consistent with the anticipated energetic penalty for straining the nominal $sp^2$ hybridization of the bridging carbon atoms in the central ring of OTP. In contrast, the cyclohexene ring in DPCH should more readily accommodate structural strain introduced by twisting the central ethylenic bond, such that the minimum and CI may be much closer in energy, as depicted through Figure 3.3. Although it is possible that intramolecular barriers may also exist along the excited-state surface between the Franck−Condon region and the CI seam, a smaller energetic penalty for reaching the CI from the $S_1$ minimum in DPCH is consistent with a faster nonadiabatic cyclization relative to OTP.

We also note that there is very little change in the calculated values of α between states (particularly between the $S_1$ minimum and CI) and even between OTP and DPCH for any given state/configuration. We also find that C−C bond lengths within the newly forming ring exhibit little variation between the $S_1$ minimum and CI geometries. Similarities in these structural parameters imply that the energetic penalty for reaching the CI cannot be associated with straining bond angles or bond lengths to bring the terminal rings closer together but rather with moving them to the correct relative configuration by twisting θ. Thus, our comparison between OTP and DPCH is not complicated by differences in structure and dynamics that might be expected between diphenylcycloalkenes with varying sizes of cycloalkene. [18,19] For example, although the smaller central ring of diphenylcyclobutene (DPCB) should constrain twisting about θ much like the central phenyl ring in OTP, the structure of DPCB also strongly constrains

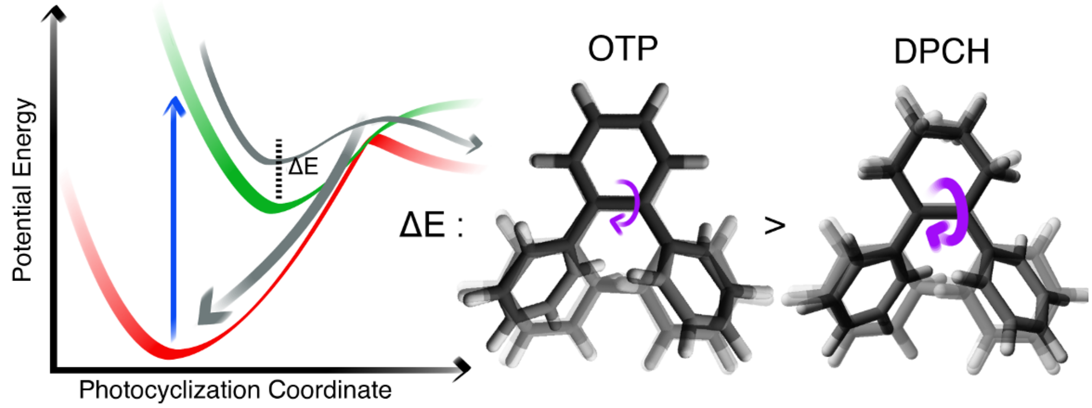

**Figure 3.3.** Schematic depiction of potential energy surfaces along the nonadiabatic photocyclization coordinate of OTP and DPCH. ΔE represents the energy difference between the $S_1$ minimum and lowest-energy CI. Compared with DPCH, "ethylenic" twisting (θ) in OTP is constrained by a higher energetic penalty for flexing the central ring.

α; it has been suggested that the latter constraint has a large bearing on the slow cyclization documented for DPCB. [29]

It is important to note that nonadiabatic decay of $S_1$ OTP and DPCH is not expected to generate cyclized photoproducts in 100% quantum yields: Branching at the surface-crossing is also anticipated to lead to ground-state recovery, although we were not able to observe a spectroscopic signature of recovery directly from our measurements. Of course, nonadiabatic cyclization and ground-state recovery (or generation of other products) that occur through a common state-crossing will be rate-limited by common nuclear dynamics leading up to the crossing on the excited potential energy surface. In contrast, variation in nonadiabatic decay rates measured here would not necessarily correspond with cyclization if a competing relaxation pathway was available in one or both molecules. Structural constraints in these systems should prevent a cis−trans isomerization about the "ethylenic" bond; furthermore, we have found no evidence of other photoproducts (and, therefore, other nonadiabatic relaxation pathways) from our transient spectroscopic measurements in the near UV, visible, and near-IR. We also estimate that the quantum yield for cyclization is roughly the same for OTP and DPCH ($\Phi_{\mathrm{DHT}}$ / $\Phi_{\mathrm{CDHP}} \approx 0.95$) based on an analysis of frequency-integrated band intensities. (See appendix 1 for more details.) Taken together, these observations imply that the nonadiabatic decay of $S_1$ OTP and DPCH occurs only via the CI that involves cyclization and that the variation in excited- state decay rates we have measured reflects differences in the nuclear dynamics leading to this crossing, not variations in the rate of a competing nonadiabatic process.

## 3.4 Conclusion

The excited-state dynamics and structural characteristics of OTP and DPCH offer new perspective on the minor cyclization pathway of UV-excited CS and its analogs. Spectral dynamics shown in Figure 3.1 illustrate a direct interconversion between the $S_1$ ring-opened and $S_0$ cyclized states of CS analogs. Furthermore, our results illustrate that structural constraints on the central carbon−carbon bond that bridges the terminal phenyl rings induce a reduction in the cyclization rate of stilbene analogs, providing evidence that twisting motions around this bond play a critical role in reaching state crossings relevant for cyclization. Although details of the nuclear dynamics along both the CS-to-TS or CS-to-DHP pathways remain unresolved, it is now commonly accepted that cis−trans isomerization of CS involves twisting about the central ethylenic bond as part of a multicoordinate reaction pathway. [15,18,22] Myers and Mathies argued that an ethylenic torsional twist of ~25° occurs in the first 20 fs following excitation based on the analysis of their resonance Raman measurements with $S_0$ CS in solution, [15] and more recent calculations by Quenneville and Martinez illustrated that ethylenic twisting is part of a more complex coordinate that also involves pyramidalization of the ethylenic carbon atoms. [22] Calculated geometries associated with the CS-to-DHP cyclization pathway likewise suggest an increase in the ethylenic twist angle on the way to the CI or state-crossing seam; [21,23,36] therefore, it is quite likely that the initial nuclear wave-packet propagation along the excited-state potential-energy surface involves an increase along this coordinate prior to branching between reaction pathways. Phenyl ring rotations undoubtedly play a critical role in cyclization, [18,19] but our findings suggest that the effectiveness of these motions in reaching a state crossing is likely to be governed by the orientation at which the reacting carbon atoms are able to approach one another: a steric relationship controlled strongly by θ. We anticipate that closer examination of the ultrafast excited-state dynamics that precedes nonadiabatic $S_1$ decay of DPCH − and that underlies the early spectral dynamics seen in Figure 3.1a − will provide further clues about the structural evolution leading up to the region of the CI associated with the cyclization of stilbene analogs.

## 3.5 Experimental Methods

OTP was purchased and used as-is; DPCH was synthesized as described in appendix 1. Solutions of both molecules were prepared with air-free THF at low millimolar concentrations (5−10 mM for DPCH, 5−20 mM for OTP). Sample solutions were circulated through a 0.5-mm path-length flow cell via an Ar-purged flow loop for optical measurements. All experiments utilized a regeneratively amplified Ti:Sapphire laser (Coherent Legend Elite, 4.5 mJ/pulse, 1 kHz, 35 fs pulse duration). Roughly 1 mJ of the laser output was used to generate ~20 μJ UV photoexcitation pulses by frequency conversion. Weak broadband probing pulses were obtained through white-light generation in synthetic sapphire. The visible continuum was generated using 800 nm pulses polarized at 45°; a thin broadband wire-grid polarizer (Thorlabs) was then used to select the polarization of the visible probe light immediately before the sample. UV photoexcitation pulses were collimated to a 4 mm beam diameter before the flow cell. The broadband probe pulse was focused at the sample to a spot size of <100 μm and overlapped at a small angle with respect to the photoexcitation pulse in the sample. The excitation pulse was blocked after the sample with a beam dump, and residual pump scatter along the probe propagation direction was blocked with a 280 nm long-pass filter. The probe was also passed through additional bandpass filters to shape spectra for detection and to remove residual 800 nm light that was used to drive continuum generation.

The probe continuum was dispersed using a 0.3 m spectrograph (Acton-2360, Princeton Instruments) outfitted with a low-resolution grating (800 nm blaze, 150 lines/mm). Probe spectra were detected using a CCD camera (Pixis- 100BR, Princeton Instruments), which collects the continuum probe on each laser shot at 1 kHz. The photoexcitation beam was synchronously chopped at 500 Hz, such that transient absorption spectra can be calculated using consecutive pairs of probe spectra. The pump pulse was retroreflected off of a pair of 266 nm high reflectors mounted to a motorized translation stage (Newport), which was adjusted to change the relative optical path length of the pump and probe pulses. Transient spectra shown here were collected by averaging at each time delay, with 30 000−50 000 on/off ratios for visible TAS. Positioning of the translation stage, collection of probe spectra, synchronization with the chopper phase, and calculation and averaging of transient spectra were all coordinated through a home-built LabVIEW data acquisition program. Pump−probe measurements of neat solvents were made such that transient spectra could be chirp-corrected according to the time dependence of the nonlinear, two-pulse solvent response.

## 3.6 Computational Methods

All calculations were performed using GAMESS. [33] Optimized geometries were determined at the SA- CASSCF level, [32] abbreviated as SA-x-CAS(y/z) (x averaged states, y active electrons, and z active orbitals) with a STO-3G or 6-31G basis set, equal weighting of states, and no symmetry restrictions. All visualization of results was performed using MacMolPlt. [37] The minimal energy CI searches utilized the method of Bearpark et. al. [35]

Optimizations were carried out as described in the text. Calculations with different active spaces were performed to investigate how the size of the active space affects the relative size of the $S_1$ -minimum-to-CI energy for OTP and DPCH. For the SA-2-CAS calculations the active space was selected to be minimalistic due to the computational expense of working with these methods in combination with relatively large molecules. (The most appropriate active spaces would correspond to: 18 $\pi, \pi^*$ orbitals for OTP, 14 $\pi, \pi^*$ orbitals for DPCH, 16 $\pi, \pi^*$ and 2 $\sigma, \sigma^*$ orbitals for DHT, and 12 $\pi, \pi^*$ and 2 $\sigma, \sigma^*$ orbitals for CDHP.) The active spaces used in our calculations utilized an equal split of $\pi$ and $\pi^*$ orbitals (up to 4 $\pi$ and 4 $\pi^*$ orbitals with the (8/8) active space). Although the energetics and geometries change slightly between each active space, similar qualitative differences between OTP and DPCH were observed with each active space, suggesting that the smaller active spaces are satisfactory in describing the relative characteristics of the $S_1$ surfaces of these two molecules. More details of these calculations and a list of numeric results obtained with various active spaces and basis sets are reported in appendix 1.

To confirm the identity of the long-lived band in the TA spectrum of OTP as a ground-state absorption of the DHT intermediate, we used TDDFT [38] with the B3LYP functional [39,40] and a 6-31+G* [41,42] basis set to calculate the lowest-energy vertical transitions for DHT and DHP. First, both DHP and DHT were optimized in the ground state using DFT, and it was confirmed by vibrational analysis that these optimized structures correspond with stationary points (zero imaginary frequencies). Using these optimized geometries, a single-point energy calculation was performed to obtain the $S_0 \rightarrow S_1$ excitation energy for each molecule.

## 3.7 References

(1) Yarkony, D. Conical Intersections: The New Conventional Wisdom. *J. Phys. Chem. A* **2001**, *105*, 6277−6293.

(2) Levine, B. G.; Martínez, T. J. Isomerization through Conical Intersections. *Annu. Rev. Phys. Chem.* **2007**, *58,* 613−634.

(3) Worth, G. A.; Cederbaum, L. S. Beyond Born-Oppenheimer: Molecular Dynamics through Conical Intersection. *Annu. Rev. Phys. Chem.* **2004**, *55*, 127−158.

(4) Matsika, S.; Krause, P. Nonadiabatic Events and Conical Intersections. *Annu. Rev. Phys. Chem.* **2011**, *62*, 621−643.

(5) Kohler, B. Nonradiative Decay Mechanisms in DNA Model Systems. *J. Phys. Chem. Lett.* **2010**, *1*, 2047−2053.

(6) Lim, J. S.; Kim, S. K. Experimental Probing of Conical Intersection Dynamics in the Photodissociation of Thianisole. *Nat. Chem*. **2010**, *2*, 627−632.

(7) Dunkelberger, A. D.; Kieda, R. D.; Shin, J. Y.; Paccani, R. R.; Fusi, S.; Olivucci, M.; Crim, F. F. Photoisomerization and Relaxation Dynamics of a Structurally Modified Biomimetic Photoswitch. *J. Phys. Chem. A* **2012**, 116, 3527−3533.

(8) Ward, C. L.; Elles, C. G. Controlling the Excited-State Reaction Dynamics of a Photochromic Molecular Switch with Sequential Two-Photon Excitation. *J. Phys. Chem. Lett.* **2013**, *3*, 2995−3000.

(9) Polli, D.; Altoe, P.; Weingart, O.; Spillane, K. M.; Manzoni, C.; Brida, D.; Tomasello, G.; Orlandi, G.; Kukura, P.; Mathies, R. A.; et al. Conical Intersection Dynamics of the Primary Photoisomerization Event in Vision. *Nature* **2010**, *467*, 440−443.

(10) Irie, M. Diarylethenes for Memories and Switches. *Chem. Rev*. **2000**, *100*, 1685−1716.

(11) Tamai, N.; Miyasaka, H. Ultrafast Dynamics of Photochromic Switches. *Chem. Rev.* **2000**, *100*, 1875−1890.

(12) Mallory, F. B.; Mallory, C. W. Photocyclization of Stilbenes and Related Molecules. In Organic Reactions; Boswell, G. A., Jr., Danishfesky, S., Gschwend, H. W., Heck, R. F., Hirschman, R. F., Paquette, L. A., Posner, G., Reich, H. J., Eds.; John Wiley & Sons, Inc.: New York, 1984; Vol. 30, pp 1−456.

(13) Sato, T.; Shimada, S.; Hata, K. A New Route to Polycondensed Aromatics: Photolytic Formation of Tripheneylene and Dibenzo-[fg,op]naphthacene Ring Systems. *Bull. Chem. Soc. Jpn.* **1971**, *44*, 2484−2490.

(14) Waldeck, D. H. Photoisomerization Dynamics of Stilbenes. *Chem. Rev.* **1991**, *91,* 415−436.

(15) Myers, A. B.; Mathies, R. A. Excited-State Torsional Dynamics of cis-Stilbene from Resonance Raman Intensities. *J. Chem. Phys.* **1984**, *81*, 1552−1558.

(16) Sension, R. J.; Szarka, A. Z.; Hochstrasser, R. M. Vibrational Energy Redistribution and Relaxation in the Photoisomerization of cis-Stilbene. *J. Chem. Phys.* **1992**, *97*, 5239−5242.

(17) Todd, D. C.; Jean, J. M.; Rosenthal, S. J.; Ruggiero, A. J.; Yang, D.; Fleming, G. R. Fluorescence Upconversion Study of cis-Stilbene Isomerization. J. Chem. Phys. **1990**, 93, 8658−8668.

(18) Petek, H.; Yoshihara, K.; Fujiwara, Y.; Lin, Z.; Penn, J. H.; Frederick, J. H. Is the Nonradiative Decay of $S_1$ cis-Stilbene Due to the Dihydrophenanthrene Isomerization Channel? Suggestive Evidence from Photophysical Measurements on 1,2-Diphenylcycloalkenes. J. Phys. Chem. **1990**, *94*, 7539−7543.

(19) Frederick, J. H.; Fujiwara, Y.; Penn, J. H.; Keitaro, Y.; Petek, H. Models of Stilbene Photoisomerization: Experimental and Theoretical Studies of the Excited-State Dynamics of 1,2-Diphenylcycloalkenes. *J. Phys. Chem*. **1991**, *95*, 2845−2858.

(20) Rodier, J.-M.; Myers, A. B. cis-Stilbene Photochemistry: Solvent Dependence of the Initial Dynamics and Quantum Yields. *J. Am. Chem. Soc.* **1993**, *115*, 10791−10795.

(21) Bearpark, M. J.; Bernardi, F.; Clifford, S.; Olivucci, M.; Robb, M. A.; Vreven, T. Cooperating Rings in cis-Stilbene Lead to an $S_0$ /$S_1$ Conical Intersection. *J. Phys. Chem. A* **1997***, 101*, 3841−3847.

(22) Quenneville, J.; Martínez, T. J. Ab Initio Study of cis-trans Photoisomerization in Stilbene and Ethylene. *J. Phys. Chem. A* **2003**, *107*, 829−837.

(23) Dou, Y.; Allen, R. E. Detailed Dynamics of a Complex Photochemical Reaction: cis-trans Photoisomerization of Stilbene. *J. Chem. Phys***. 2003**, *119*, 10658−10666.

(24) Takeuchi, S.; Ruhman, S.; Tsuneda, T.; Chiba, M.; Taketsugu, T.; Tahara, T. Spectroscopic Tracking of Structural Evolution in Ultrafast Stilbene Photoisomerization. *Science* **2008**, *322*, 1073−1077.

(25) Weigel, A.; Ernsting, N. P. Excited Stilbene: Intramolecular Vibrational Redistribution and Solvation Studied by Femtosecond Stimulated Raman Spectroscopy. *J. Phys. Chem. B* **2010**, *114*, 7879−7893.

(26) Kovalenko, S. A.; Dobryakov, A. L.; Ioffe, I.; Ernsting, N. P. Evidence for the Phantom State in Photoinduced cis-trans Isomerization of Stilbene. *Chem. Phys. Lett.* **2010**, *493*, 255−258.

(27) Nakamura, T.; Takeuchi, S.; Taketsugu, T.; Tahara, T. Femtosecond Fluorescence Study of the Reaction Pathways and Nature of the Reactive $S_1$ State of cis-Stilbene. *Phys. Chem. Chem. Phys.* **2012**, *14*, 6225−6232.

(28) Penn, J. H.; Gan, L.-X.; Chan, E. Y.; Loesel, P. D.; Hohlneicher, G. Steric Inhibition of Photochemical Reactions: The [2 + 2] Cycloaddition Reaction. *J. Org. Chem*. **1989**, *54*, 601−606.

(29) Penn, J. H.; Gan, L.-X.; Eaton, T. A.; Chan, E. Y.; Lin, Z. J. Photochemical Reactions of Model cis-Stilbenes: The [2 + 2]-Cycloaddition Reaction. *J. Org. Chem*. **1988**, *53*, 1519−1523.

(30) Ishii, K.; Takeuchi, S.; Tahara, T. A 40-fs Time-Resolved Absorption Study of cis-Stilbene in Solution: Observation of Wavepacket Motion on the Reactive Excited State. *Chem. Phys. Lett*. **2004**, *398*, 400−406.

(31) Muszkat, K. A.; Fischer, E. Structure, Spectra, Photochemistry, and Thermal Reactions of the 4a,4b-Dihydrophenanthrenes. *J. Chem. Soc. B* **1967**, 662−678.

(32) Docken, K. K.; Hinze, J. LiH Potential Curves and Wavefunctions for X $^1\Sigma^+$ , A $^1\Sigma^+$ , B $^1\Pi$, $^3\Sigma^+$ , and $^3\Pi$. *J. Chem. Phys.* **1972**, *57*, 4928−4936.

(33) Schmidt, M. W.; Baldridge, K. K.; Boatz, J. A.; Elbert, S. T.; Gordon, M. S.; Jensen, J. H.; Koeski, S.; Matsunaga, N.; Nguyen, K. A.; Su, S. J.; et al. General Atomic and Molecular Electronic Structure System. *J. Comput. Chem.* **1993**, *14*, 1347−1363.

(34) Levine, B. G.; Ko, C.; Quenneville, J.; Martínez, T. J. Conical Intersections and Double Excitations in Time-dependent Density Functional Theory. *Mol. Phys.* **2006**, *104*, 1039−1051.

(35) Bearpark, M. J.; Robb, M. A.; Schlegel, H. B. A Direct Method for the Location of the Lowest Energy Point on a Potential Surface Crossing. *Chem. Phys. Lett.* **1994**, *223*, 269−274.

(36) Quenneville, J. Ph.D. Thesis, University of Illinois at Urbana-Champaign, 2003.

(37) Bode, B.; Gordon, M. S. MacMolPlt: A Graphical User Interface for GAMESS. *J. Mol. Graphics Modell.* **1998***, 16*, 133−138.

(38) Runge, E.; Gross, E. K. U. Density-Functional Theory for Time-Dependent Systems. *Phys. Rev. Lett*. **1984**, *52*, 997−1000.

(39) Becke, A. D. Density-Functional Thermochemistry. III. The Role of Exact Exchange. *J. Chem. Phys*. **1993**, *98*, 5648−5652.

(40) Stephens, P. J.; Devlin, J. F.; Chabolowski, C. F.; Frisch, M. J. Ab Initio Calculation of Vibrational Absorption and Circular Dichroism Spectra Using Density Functional Force Fields. *J. Phys. Chem.* **1994**, *98*, 11623−11627.

(41) Frisch, M. J.; Pople, J. A.; Binkley, J. S. Self-Consistent Molecular Orbital Methods 25. Supplementary Functions for Gaussian Basis Set. *J. Chem. Phys.* **1984***, 80*, 3265−3269.

(42) Hehre, W. J.; Ditchfeld, R.; Pople, J. A. Self-Consistent Molecular Orbital Methods. XII. Further Extensions of Gaussian-Type Basis Sets for Use in Molecular Orbital Studies of Organic Molecules. *J. Chem. Phys.* **1972**, *56*, 2257−2261.

# Chapter 4

# Structural Control of Nonadiabatic Bond Formation: The Photochemical Formation and Stability of Substituted 4a,4b-Dihydrotriphenylenes

Reproduced with permission from Snyder, J. A.; Bragg, A. E. *The Journal of Physical Chemistry A* **2015**, *119*, 3972–3985. Copyright 2015, American Chemical Society

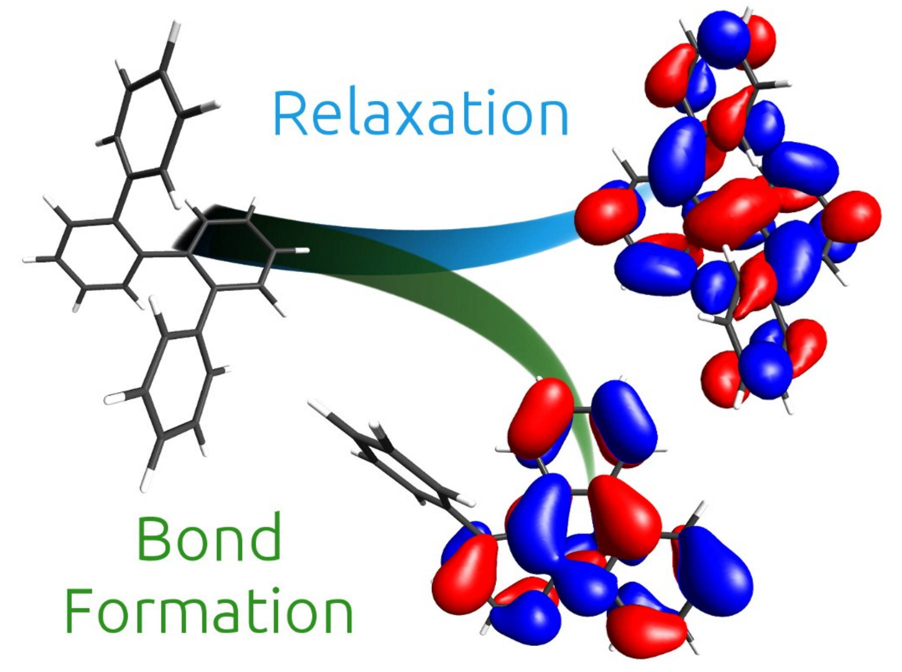

**Figure 4.0.** Table of contents figure

## 4.0 Abstract

Nonadiabatic photocyclization makes bonds and is the first step in the photoinduced cyclodehydrogenation of *ortho*-arenes to yield polycyclic aromatic hydrocarbons. How molecular structure alters potential-energy landscapes, excited-state dynamics, and stabilities of reactants and intermediates underlies the feasibility of desirable photochemistry. In order to gain insight into these structure−dynamics relationships, we have used femtosecond transient absorption spectroscopy (TAS) to examine photoinduced dynamics of 1,2,3-triphenylbenzene (TPB) and *ortho*-quaterphenyl (OQTP), phenyl-substituted analogues of *ortho*-terphenyl (OTP). Dynamics of TPB and OTP are quite similar: TPB exhibits fast (7.4 ps) excited-state decay with concomitant formation and vibrational relaxation of 9-phenyl-dihydrotriphenylene (9-phenyl DHT). In contrast, photoexcited OQTP exhibits multistate kinetics leading to formation of 1-phenyl DHT. Excited-state calculations reveal the existence of two distinct minima on the OQTP $S_1$ surface and, together with photophysical data, support a mechanism involving both direct cyclization by way of an asymmetric structure and indirect cyclization by way of a symmetric quinoid-like minimum. Temperature-dependent nanosecond TAS was utilized to assess the relative stabilities of intermediates, substantiating the observed trend in photochemical reactivity OTP > OQTP > TPB. In total, this work demonstrates how specific structural variations alter the course of the excited-state dynamics and photoproduct stability that underlies desired photochemistry.

## 4.1 Introduction

Time-dependent crossings between molecular electronic states, or nonadiabatic dynamics, are fundamental excited-state relaxation pathways and underlie a variety of photochemical processes, including fast deactivation of molecular excited states, [1,2] bond-selective photodissociation, [3,4] photoisomerization, [5−9] and photoinduced bond formation. [6,10] Nonadiabaticity has become a paradigmatic concept for describing chemical dynamics of excited molecules in recent years. [11−13] As light-driven dynamics hold great promise for fast and photoselective energy conversion and photochemical reaction schemes, there is much interest in harnessing nonadiabaticity within chemical applications. For example, many novel photochromic molecular switches take advantage of nonadiabatic photochemical bond making and breaking to quickly switch between persistent “on” and “off” states. [14–16] Nonadiabatic photocyclization has also been utilized synthetically as it enables formation of carbon−carbon bonds via reactant activation with light and can be used for the small-scale synthesis of novel polyaromatic structures. [17–20] A critical step toward utilizing and controlling photochemical bond formation for such applications is to establish how access to specific nonadiabatic pathways and the stability of photochemical intermediates formed are determined by molecular structure. In this work we specifically examine the structure−dynamics relationships that underlie nonadiabatic photochemistry of a related set of *ortho*-arenes: *ortho*-terphenyl(OTP), *ortho*-quaterphenyl (OQTP), and 1,2,3-triphenylbenzene (TPB). These systems form related photoproducts via nonadiabatic cyclization, such that the impact of molecular structure on bond-formation dynamics can be examined explicitly.

Photochemical carbon−carbon bond formation via cyclization was first noted for stilbenes and related diarylethenes in the 1940s and 1950s, [6,21,22] with analogous reactions of *ortho*-arenes recognized shortly thereafter.[23,24] These reactions are illustrated at the top of Scheme 4.1 for OTP: The Woodman−Hoffmann rules for orbital symmetry conservation predict that UV photoexcitation to the $S_1$ state of OTP leads to conrotatory electrocyclization to form $S_0$ 4a,4b-dihydrotriphenylene (DHT). [25] Once formed, DHT can subsequently react with a strong oxidant (e.g., $I_2$) to form triphenylene via H abstraction, a process that competes with thermally activated ring reopening. [24] Photochemical studies with OTP were key to determining the optimal reaction conditions for the photo-induced cyclodehydrogenation of *ortho*-arenes; in fact, under optimal reaction conditions OTP can be converted to triphenylene in very high yield (>90% yield). [24,26]

In contrast, lower product yields are generally obtained from similar photochemical reactions with more complex *ortho*-arene reactants under the same conditions. [24,26] For example, dibenzonaphthacene (DBN, Scheme 4.1) can be synthesized from either OQTP or TPB through two successive cyclodehydrogenation reactions: The first reaction goes by way of different phenyl-DHT intermediates, 1- and 9-phenyl-DHT, respectively, whereas the second cyclodehydrogentation step occurs from a common phenyl-triphenylene structure. No measurable quantity of phenyl-triphenylene is recovered from reactions with either starting material, indicating that the second reaction cycle is facile and that the first is the yield- determining step. [27] The observation of lower product yields from these more complex reactants suggest that differences in reactant structures (OTP vs OQTP vs TPB)

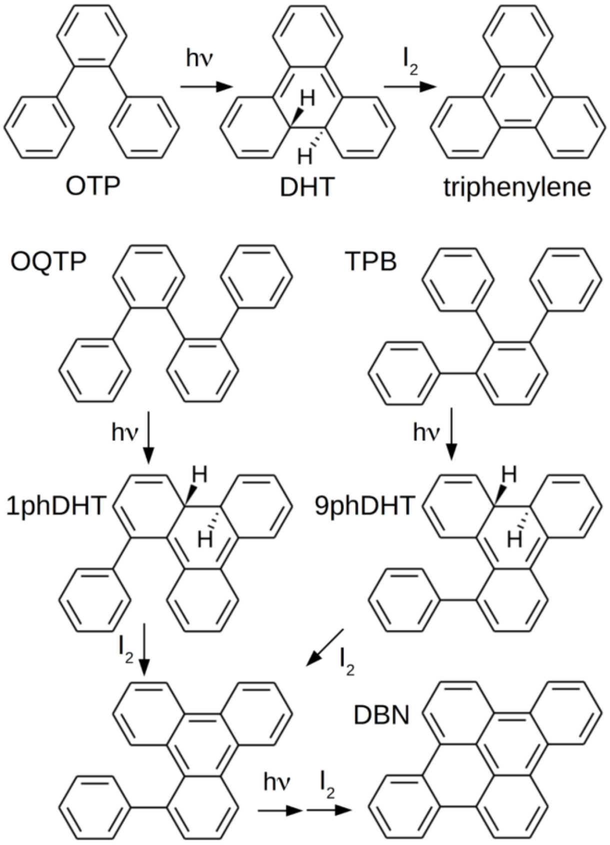

**Scheme 4.1.** (Top) Photochemical Synthesis of Triphenylene via the Cyclodehydrogentation of *o*-Terphenyl (OTP) via 4a,4b-Dihydrotriphenylene (DHT) and (Bottom) Dibenzonaphthacene (DBN) from the Cyclodehydrogenation of *o*-Quarterphenyl (OQTP) and 1,2,3-Triphenylbenzene (TPB).

may alter nonadiabatic cyclization dynamics and/or the relative stability of phenyl-DHT intermediates to impact the net reaction efficiency for forming DBN.

These qualitative comparisons of photochemical reaction yields raise various questions about what bearings structure−dynamics relationships have on photochemistry that involves nonadiabatic events: How exactly does structure affect the topography of excited- and ground-state potential-energy surfaces that dictate nonadiabatic chemical dynamics for a particular reactant? To what degree is net reaction efficiency limited by the stability of the intermediate, or rather reaction branching between alternate pathways along the excited-state potential-energy surface? What reactant structures would be most conducive to effective and efficient photochemical preparation of specific product structures given structure−dynamics relationships? Elucidating the details of each key process underlying these reactions and how they are influenced by reactant structure is essential for establishing conditions under which they can be utilized effectively within photochemical strategies.

The work presented here is a continuation of our investigation of the nonadiabatic photochemical dynamics of *ortho*-arenes and how these dynamics are impacted by molecular structure. In previous work we used a combination of ultrafast and nanosecond spectroscopies to characterize the UV-induced photochemistry of OTP. [10,28] Broadband ultrafast transient absorption measurements revealed spectral dynamics associated with OTP excited-state relaxation occurring on picosecond time scales and giving rise to the metastable intermediate DHT. We also contrasted the cyclization dynamics of OTP to those of a closely related diarylethene. In total, this previous work suggests that these differences in structural characteristics of *ortho*-arenes give rise to significantly different photochemical reactivity compared with diarylethenes.

Here we further examine the role of reactant and intermediate structure on photochemical bond formation, with a specific focus on the photochemistry of TPB and OQTP. To first order both systems can be viewed as OTP with an additional phenyl substituent, the presence of which can be expected to impact excited-state structural evolution and the stabilities of corresponding phenyl-DHT intermediates as a result of intramolecular steric interactions. However, the location of the extra phenyl ring also may be expected to nontrivially alter the electronic structure and, hence, excited- state potential-energy surfaces through extended conjugation of excited states. In this work we have characterized the ultrafast and nanosecond time-resolved photochemistry of these molecules and compare them with that of OTP. Using a combination of experimental results and supportive electronic structure calculations we present a comprehensive evaluation of how differences in reactant structure impact the photochemistry of these simple *ortho*-arenes and their corresponding dihydro-intermediate structures.

## 4.2 Experimental

***4.2.1 Sample Preparation.*** OTP and TPB were purchased from Sigma-Aldrich and used "as-is". OQTP was synthesized through a Cu-catalyzed Ullman reaction of 2-iodobiphenyl based on literature procedures. [29] Additional details regarding the synthesis, purification, and characterization of OQTP samples are provided in appendix 2. Hexane and unstabilized tetrahydrofuran (THF) were obtained from Sigma-Aldrich and used "as-is". Solution samples used for ultrafast measurements were made at concentrations of 10 mM and were circulated with a peristaltic pump (Master- flex) through a 0.5 mm path length flow cell. The windows of the cell are polished UV-grade fused silica, ensuring high transmission of UV light. The sample flow loop was constructed from PTFE tubing and connections to ensure chemical compatibility with all solvents used. Sample solutions for nanosecond measurements were sealed into a 1 cm quartz cuvette and had an optical density (OD) of 1 at 266 nm; the sample cuvette was loaded into a liquid-nitrogen cooled cryostat (Unisoku, Unispeks) for temperature dependent measurements.

***4.2.2 Ultrafast Transient Absorption Spectroscopy (fs- TAS).*** Photoinduced dynamics were interrogated using fs-TAS. General features of the laser setup used in our laboratory for these measurements have been reported in detail elsewhere. [10,28] In all cases excited states were prepared (pumped) through photoexcitation at 266 nm (~1 mJ/cm 2 ); pump pulses were generated via the nonlinear frequency conversion of a portion of the 800 nm output of the Ti-sapphire amplifier (35 fs pulse duration, 990 Hz repetition rate). Spectral dynamics were probed using a broadband continuum spanning 300−1100 nm that was obtained by driving white-light generation in a 2 mm thick crystal of $CaF_2$ with a low-intensity 800 nm pulse. Driving pulses were aligned along a variable optical path to control the arrival time of the probe pulse at the sample relative to pump. The relative pump−probe polarization was maintained at magic angle by passing the probe through a broadband wire-grid polarizer immediately before the sample cell. Transient signals were observed to be independent of pump fluence.

Ultrafast spectral measurements utilized a home-built prism- based spectrometer that is based on the design of Riedle et al. [30] Collimated continuum probe beams were dispersed using equilateral prisms of UV-fused silica (CVI) or NSF-11 (Edmund) for detection of UV−vis or vis−NIR light, respectively; dispersed beams were subsequently reimaged onto photodiode arrays (Hamamatsu S3901-256Q) using concave mirrors. Spectra were obtained by averaging 2000− 3000 consecutive pump on/off cycles at each time delay. The typical temporal response of this setup is 300 fs determined by convoluting a Gaussian instrument response function (IRF) with a step function and fitting to the rise of a long-lived transient signal. With a 266 nm excitation pulse the resolution is limited primarily by the group-velocity mismatch of the pump and probe light pulses within the liquid sample. Transient spectra were time-corrected for the chirp of the probe, as described in previous work. [28] Quantitative wavelength calibration was performed using the absorption spectrum of a BG-36 filter as acquired with the prism-dispersed probe. A detailed description of supercontinuum conditioning, wavelength calibration, optics, and electronics is available in appendix 2.

***4.2.3 Nanosecond Transient Absorption Spectroscopy (ns-TAS).*** ns-TAS measurements were used to characterize the lifetimes and stabilities of dihydro-intermediates (DHT, 1- and 9-phenyl DHT) generated via photocyclization of *ortho*-arenes. Two different experimental setups were used for these measurements. The first was used for temperature-dependent studies of intermediate stabilities and has been described in detail elsewhere. [31,32] Briefly, samples were excited at 266 nm with the fourth harmonic of a pulsed Nd:YAG laser, with pump-induced changes in sample absorptivity probed with light from a microsecond-pulsed flash lamp. Changes in transient absorption at a given wavelength were determined by monitoring the time-dependent intensity of the dispersed probe as measured by a PMT with and without the pump pulse present. The resolution of this setup is limited by the laser pulse duration and oscilloscope rise time (~5 ns effective time resolution).

A second setup was used to record room temperature kinetics of cyclized intermediates at slightly higher time resolution. For these measurements solution samples were excited with the ultrafast pump pulses at 266 nm. A 639 nm laser diode (Opnext) was pulsed with a high-speed (ps-to-ns) diode driver (Highland Technologies, T165) at the laser amplifier's repetition rate; variable probe pulse timing was controlled using a trigger from the amplifier's signal delay generator (Coherent SDG Elite). Pump and probe beams passed through the sample at a ∼10° angle. The mono-chromatic probe beam was imaged onto a photodiode array with a cylindrical lens; as with ultrafast measurements, transient absorption was calculated from consecutive measurements of the probe intensity (pump-on/pump-off). Transients were obtained by stepping the pulse timing of the diode driver relative to the amplifier's Pockels Cell timing. Transient absorption at a given delay was obtained by averaging ∼500 pump on/off cycles. Diode probe pulses were observed to have a pulse duration of ∼2 ns as viewed with a fast photodiode and oscilloscope (see appendix 2).

## 4.3 Computational Methods.

Quantum chemical calculations were performed in order to (1) determine ground-state structures of reactants and their corresponding dihydro-intermediates, (2) calculate vertical excitation energies for comparison with experimental absorption spectra (i.e., steady- state reactant and transient intermediate spectra), (3) identify structural characteristics of excited-state minima and various conical intersections on excited-state potential-energy surfaces of the reactants, and (4) assess the relative stabilities of dihydro-intermediates formed photochemically. All calculations were carried out with GAMESS and have been performed without symmetry constraints and using default convergence tolerances. [33] MacMolPlt was used for the visualization of calculated geometries. [34]

***4.3.1 SA-CASSCF Calculations.*** $S_1$ optimizations and minimum-energy conical intersection (MECI) searches [3] were performed for OQTP and TPB using the State-Averaged Complete Active Space (SA-CASSCF) method. [35] A minimal basis set (STO-3G) [36] was used with equal weights for the $S_0$ and $S_1$ states and 2 to 6 active π and π* orbitals (i.e., (2,2)− (6,6) active spaces). A localized geometry searching procedure was performed by using the $S_0$ minimum as the initial geometry for $S_1$ optimization; this was followed by a $S_0$ /$S_1$ MECI search from the optimized $S_1$ minimum. [37] These computations provide a survey of landmarks on excited-state potentials and insights on possible excited-state relaxation pathways, but by no means present a complete picture of the potential-energy landscape.

***4.3.2 DFT and TDDFT Computations.*** Density functional theory [38,39] was also used for geometry optimization of various substituted OTP analogues (including TPB and OQTP conformers), and relevant conformers of their corresponding cyclized intermediates in order to access factors that control the relative stability of intermediate structures. All calculations were performed with the B3LYP [7] functional with a 6-31+G* [40,41] basis; optimized structures were verified by frequency analyses that produced zero imaginary frequencies. The first 5 spectroscopic transitions for ground-state OTP, TPB, and OQTP and their corresponding cyclized intermediates were calculated using time-dependent DFT [42] with the 6-31+G* basis for comparison with spectra obtained experimentally. LR-TDDFT within the Tamm−Dancoff approximation, [43] denoted simply as TDDFT henceforth for brevity, was also used for select $S_1$ optimizations with a 6-31G basis for supporting SA-CAS results that are limited by small basis sets, active spaces, and the neglect of dynamic correlation. More discussion regarding the merits of using both TDDFT and SA- CAS methods for excited-state calculations is provided in appendix 2.

## 4.4 Results and Analysis

***4.4.1 Spectroscopic Characterization of the Ultrafast Photoinduced Cyclization of TPB and OQTP.*** Figure 4.1 presents the ultrafast transient absorption spectroscopy of OTP, TPB, and OQTP following excitation at 266 nm. Photoinduced spectral dynamics of OTP shown in Figure 4.1a are similar to what we have published previously. [10,28] Relatively narrow and broad transient bands appear at 606 and 380 nm, respectively, following excitation and correspond to $S_1 - S_N$ transitions of OTP. These features decay over several picoseconds, giving rise to weaker absorption features in both regions: A broad, weak absorption centered at 580 nm and a more intense band peaking at 340 nm. We have previously characterized this evolution as reflecting the relaxation of excited OTP by nonadiabatic decay with concomitant formation of the cyclized intermediate DHT. Vibrational relaxation of DHT was also identified in our previous work from the time-dependent spectral shift of the 340 nm band on a solvent-dependent time scale of 10−25 ps. The photoinduced spectral dynamics of OTP reflect the photochemical dynamics of the smallest cyclizing *ortho*-arene in the absence of electronic and steric interactions introduced by substituent groups and thus provide a valuable metric for understanding the structure-dependent photochemical dynamics of TPB and OQTP.

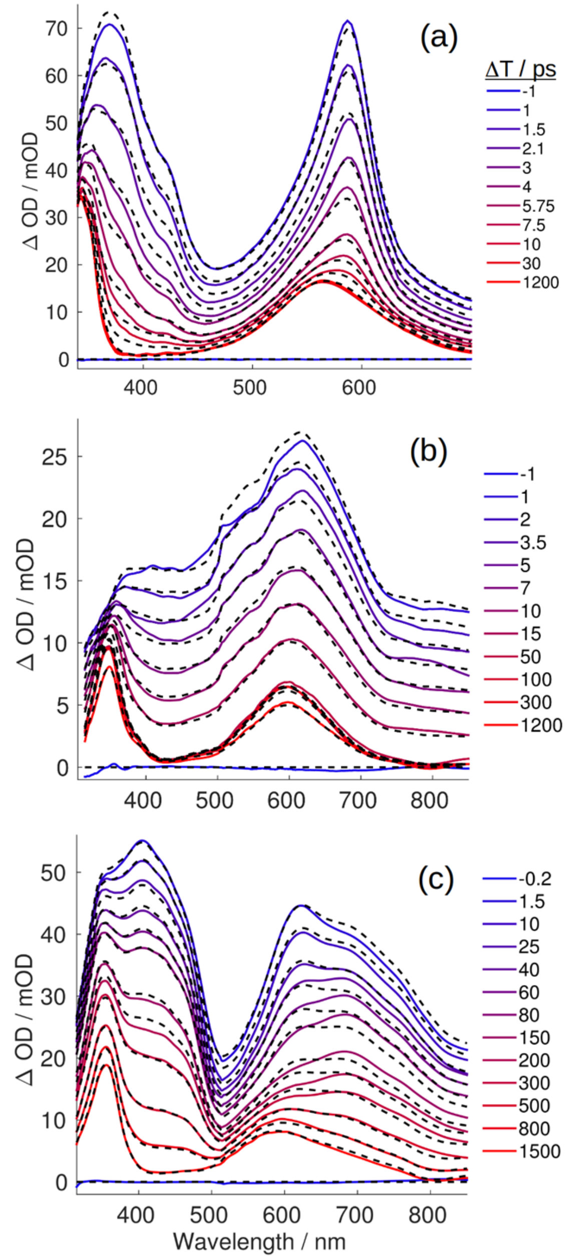

**Figure 4.1**. fs-TAS of OTP (a), TPB (b), and OQTP (c) in THF with 266 nm excitation; dashed lines are global fits to simple kinetic models explained in the text.

The ultrafast transient spectral dynamics of UV-excited TPB and OQTP are presented in Figures 4.1b and 4.1c. For both molecules, the transient spectra obtained at delays long after UV excitation (e.g., 1.5 ns) are remarkably similar to that of the DHT intermediate formed after the photoexcitation of OTP; this reveals that a substituted DHT structure is formed after UV excitation and as predicted for the cyclodehydrogenation reaction mechanisms of these two reactants (cf. Scheme 4.1). However, excited-state

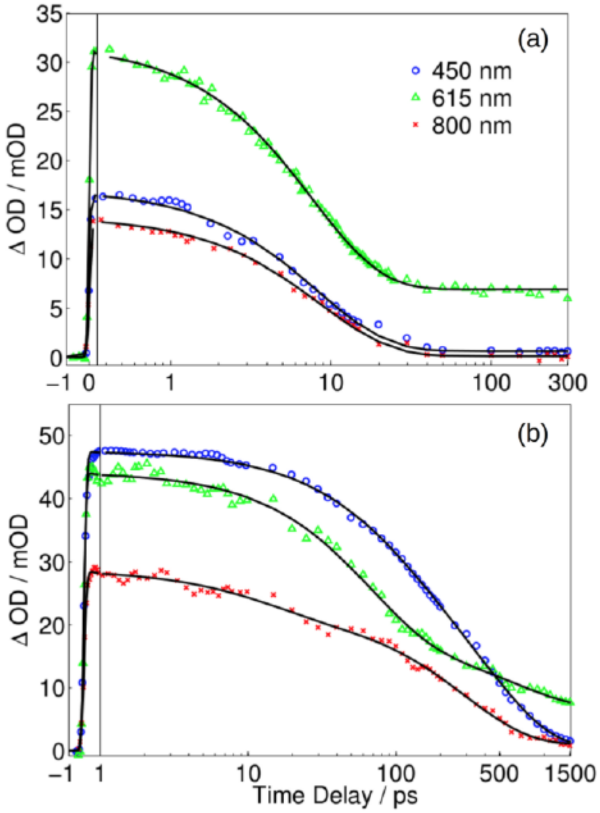

**Figure 4.2.** Single-wavelength fs-TAS traces obtained with 266 nm excitation of TPB (a) and OQTP (b) at 450 (blue ○), 615 (green □),and 800 nm (red ×). TPB and OQTP data have been fitted with single-exponential and biexponential fitting functions convoluted with the instrument response, respectively (black lines). Time axes are linear from −1 to 1 ps, logarithmic for t > 1 ps.

spectral dynamics differ from what is observed for OTP in both cases. For example, the excited-state absorption spectrum of TPB measured immediately after excitation is characterized by at least 2 broad overlapping bands, with a dominant band peaking just above 600 nm and a noticeable shoulder appearing below 400 nm. In contrast, UV- excited OQTP exhibits two groupings of overlapped excited- state bands above and below 525 nm. For TPB, the excited- state absorption decays uniformly on a time scale of ∼10 ps, giving rise to the spectrum of the corresponding DHT intermediate. In contrast, OQTP exhibits more complex spectral dynamics: At very early delays, relatively sharp features appear at 400 and 620 nm that sit on top of broader underlying features in both regions; the sharper features disappear over several 10s of picoseconds, whereas the broad underlying spectral intensity at 400−500 nm and 500−900 nm decays on much slower time scales (100s of ps). The spectrum of a dihydro-intermediate only dominates ∼1 ns after photo-excitation of OQTP.

In order to characterize relevant relaxation time scales and to constrain choices of kinetic models for the global analysis of the measured spectral dynamics, we first examined the time- dependent absorption decay at selected probe wavelengths: 450, 615, and 800 nm. Traces at these wavelengths obtained upon excitation of TPB are plotted with symbols in Figure 4.2a. Because the spectrum of the presumed dihydro-intermediate is weakest at 450 and 800 nm, whereas photoinduced absorption at earlier delays is quite strong, single-wavelength transients at these two wavelengths should closely reflect decay of the photoprepared TPB excited state. Each transient was fitted independently using a single-exponential decay (with an additive constant offset) that was convoluted with the temporal instrument response. Fits to all three traces provide similar excited-state absorption decay time scales (to within error) and reveal that photoexcited TPB decays with a lifetime of ~8 ± 1 ps, resulting in the formation of 9-phenyl DHT. Spectral transients collected with OQTP exhibit greater complexity, which is reflected in the single-wavelength traces plotted in Figure 4.2b. Transients were fitted using biexponential decay functions (with constant additive offsets) convoluted with the instrument response. In total, fits demonstrate that photo-induced dynamics include at least two relaxation time scales that differ by an order of magnitude: ~35−40 ps vs ~330−340 ps (see Table 4.1). Both of these relaxation time scales are considerably longer that what is measured with photoexcited TPB.

Guided by the results of these fits at selected wavelengths, we identified plausible kinetic relaxation models for fitting the full spectral data sets with global target analysis based on singular value decomposition (SVD). [44] Goodness of fit was assessed from the size of residuals between experimental data and time- and wavelength-dependent models. Given that the 450, 615, and 800 nm transients obtained with TPB all were fitted remarkably well with single-exponential decays and with similar relaxation lifetimes, our first global model for the TPB spectral dynamics was a simple ultrafast kinetic interconversion (A → B). (A 4.4 ns decay of state B was incorporated to improve the fit agreement at longer time scales and is based on ns-TAS results described below.) Dashed lines in Figure 4.1b plot the spectral fits obtained with this model at selected probe delays; residuals for these fits are presented in appendix 2. This simple model can account for most of the spectral dynamics at all wavelengths, with exception of the region around 360 nm; here significant residuals exhibit a clear trend, changing from negative to positive with time delay. This discrepancy indicates that the simple 2-state kinetic interconversion is not entirely adequate to fit the ultrafast spectral dynamics of photoexcited TPB. We present results of fitting with a sequential 3-state interconversion model (A → B → C) in appendix 2. Introducing an intermediate state virtually eliminates the time-dependent residuals obtained when the 2-state model is applied. However, we have reason to believe that this model does not provide a physically meaningful explanation of the photochemical dynamics: The shape of the residual spectrum changes with delay, suggesting that it arises from a time-dependent spectral shifting or narrowing rather than a simple kinetic interconversion; the relevance of this observation is discussed further below.

**Table 4.1.** Relaxation Time Scales Obtained from Fits of Single-Wavelength Traces through Time-Resolved Spectra of TPB and OQTP in THF Excited at 266 nm.

| molecule/ solvent | $\lambda$ / nm | Prefactor 1 | $\tau_1$ / ps | Prefactor 2 | $\tau_2$ / ps | offset |
|---|---|---|---|---|---|---|
| TPB/THF | 450 | - | 7.87 (±0.62) | - | - | 0.04 |
| | 615 | - | 7.77 (±0.69) | - | - | 0.21 |
| | 800 | - | 7.87 (±0.97) | - | - | 0.00 |
| OQTP/THF | 450 | 0.20 | 53 (±40) | 0.78 | 372 (±87) | 0.02 |
| | 615 | 0.41 | 31 (±16) | 0.41 | 290 (±134) | 0.18 |
| | 800 | 0.24 | 15 (±15) | 0.72 | 334 (±106) | 0.04 |

Figure 4.1c reveals the presence of multiple spectral components in the 500−800 nm and 310−500 nm ranges following UV excitation of OQTP. Fits to single-wavelength traces at various wavelengths (Figure 4.2b) reveal a strong correlation in the relaxation behavior in each of these spectral regions, suggesting that sets of bands correspond to common photochemical transients. In fact, SVD analysis reveals that 3 distinct components

account for 95% of the time-dependent spectral variation. SVD weights and the biexponential relaxation observed from transient traces in Figure 4.2b indicate that an appropriate global model must involve at least 3 spectroscopically distinctive kinetic states and 2 relaxation time scales. [45]

**Table 4.2** Global Analysis Fit Parameters for OQTP Spectral Dynamics

| | $\tau_1$ / ps | $\tau_2$ / ps | *f* |
|---|---|---|---|
| Model 1 | 46.5 | 369.9 | 1 |
| Model 2 | 46.5 | 369.9 | 1 |
| Model 3 | 46.5 | 369.9 | 0.79 |

[a] *f* refers to the fraction of state C populated from state A (directly or indirectly).

As there are numerous ways these criteria could be achieved, we have applied 3 simple global kinetic models to account for the identified behaviors:

$$A \overset{\tau_1}{\rightarrow} B \overset{\tau_2}{\rightarrow} C + D \tag{4.1}$$

$$A \overset{\tau_1}{\rightarrow} C, B \overset{\tau_2}{\rightarrow} D \tag{4.2}$$

$$A \overset{\tau_1}{\rightarrow} C + D, B \overset{\tau_2}{\rightarrow} C + D \tag{4.3}$$

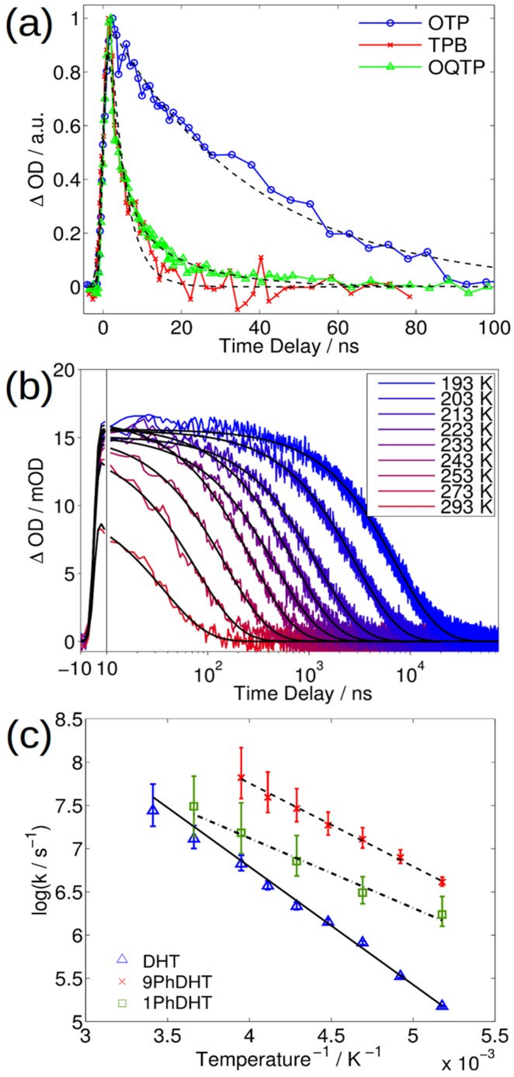

**Figure 4.3.** (a) Nanosecond TAS decay after 266 nm excitation of OTP (τ = 37.8 ns), TPB (τ = 4.1 ns), and OQTP (τ = 2.3, 15.5 ns) in THF (room temperature, 293 K); absorption decay on ns time scales corresponds with thermal decay of corresponding dihydro intermediates. (b) Thermal decay of DHT in hexane at high (red) to low (blue) temperatures; exponential fits convoluted with the instrument response are shown in black. (c) Arrhenius plots of DHT (blue △), 9-phenyl DHT (red ×), and 1-phenyl DHT (green □) decay kinetics following UV excitation of OTP, TPB, and OQTP, respectively, in hexane.

These models can be summarized briefly as follows: (1) sequential interconversion between three spectroscopically distinct species; (2) parallel relaxation of two spectroscopically distinguishable transient states by different pathways; (3) parallel relaxation of two spectroscopically distinct transient states to the same final states. In general, all of these models can exhibit biexponential time-dependent behavior. Models 1 and 2 have the fewest parameters (2 relaxation time scales). In contrast, model 3 formally requires a branching ratio for product formation. Note that “D” must be spectroscopically dark for model 2 to appear as a 3-state model; as described in more detail in the Discussion, this is included here to represent partial recovery of the reactant ground state.

Fitting parameters obtained with these models are summarized in Table 4.2. Because each of these models is capable of reproducing biphasic relaxation behavior, the discrepancies between the data and global fits are comparable. A fit obtained with model 3 is overlaid in Figure 4.1c (dashed lines). We have attempted other 3-state models to explain the photoinduced dynamics of OQTP, but the models enumerated above provide the simplest and most meaningful physical interpretation of the dynamics and also are most consistent with insights obtained from computational results described below. We assess the merits of each model in the discussion in connection with computational results and other photophysical data.

***4.4.2 Characterization* of Dihydro Intermediate Life- times and Relative Stabilities via ns-TAS.** Figure 4.3a plots the nanosecond decay at 639 nm following UV excitation of all three reactants in room temperature THF solution; 639 nm light probes the red edge of the absorption band associated with the dihydro-intermediates formed on the picosecond-to-nanosecond time scales. The OTP and TPB traces have been fitted with a single exponential convoluted with the instrument response. In contrast, the ns-TAS collected after 266 nm excitation of OQTP exhibits biexponential character in room temperature measurements. The faster component of this decay is quite close to the temporal resolution of the probe pulse and most likely reflects that the ns-TAS of OQTP is sensitive to the strong transient absorption in this region that is seen in Figure 4.1c and that decays over the course of 1 ns in ultrafast measurements; in contrast, the longer time scale must be associated with the corresponding dihydro-intermediate. Thus, the average lifetime of the dihydro-intermediate appears to get successively shorter from DHT (37.8 ns) to 1-phenyl DHT (15.5 ns) to 9-phenyl DHT (4.1 ns). Decay time scales are associated with the thermal ring reopening of the dihydro-intermediates, and hence the trend in lifetime reflects differences in the overall stability of intermediates produced from these various reactants.

Temperature-dependent nanosecond measurements were used to further characterize the relative stability of the dihydro-intermediates formed from each reactant. Figure 4.3b plots a set of temperature-dependent nanosecond absorption transients obtained with the 266 nm excitation of OTP in hexane. Each transient has been fitted with a single-exponential decay convoluted with the instrument response in order to determine the ring-opening rate at each temperature. Temperature- dependent rates were then fitted using an Arrhenius-type analysis (eq 4.4) in order to obtain the activation energy for thermal ring reopening, $E_a$ , and the rate prefactor, A:

$$\ln(k) = \ln(A) - E_a \,/\, k_B\, T \tag{4.4}$$

$$\Delta G = \Delta H + RT \tag{4.5}$$

$$k(T) = \frac{k_B T}{h} \exp\left(\frac{\Delta S}{R}\right) \exp\left(\frac{-E_a + RT}{RT}\right) \tag{4.6}$$

Temperature dependent rates and their fits to the Arrhenius expression are plotted in Figure 4.3c for DHT, 9-phenyl DHT, and 1-phenyl DHT in hexane. The activation energies and prefactors obtained from this analysis were further used to determine thermodynamics parameters associated with the stability of dihydro-intermediates against a unimolecular ring reopening reaction, as expressed in eqs 4.5 and 4.6.[46] Table 4.3 lists the parameter values obtained from both analyses for each reactant in hexane. Although room temperature rates were not obtained for TPB and OQTP in hexane, we note that the rates obtained in THF solution closely match extrapolations of the linear trends plotted in Figure 4.3c (log(1/τ) = 8.4 and 7.8, respectively).

**Table 4.3.** Thermodynamic Parameters of Thermal Ring-Reopening (at 253 K)

| | A / ns$^{-1}$ | $E_a$ / eV | $\Delta S^‡$ / kJ/mol | $\Delta H^‡$ / kJ/mol | $\Delta G^‡$ / kJ/mol |
|---|---|---|---|---|---|
| DHT/Hexane | 1788.4±7.3 | 0.2709±1 | -0.362 | 24.028 | 115.625 |
| 9phDHT/Hexane | 400.6±2.4 | 0.1908±1 | -0.375 | 16.320 | 110.807 |
| 1phDHT/Hexane | 22.7±0.8 | 0.1604±6 | -0.398 | 13.369 | 114.421 |

### 4.4.3 Computational Characterization of Ground- and Excited-State Structures and Spectroscopy of OTP, TPB, OQTP, and Corresponding Dihydro Intermediates.

***4.4.3.1 Characterization of Ground-State Geometries.*** $S_0$ minimum geometries were located for OTP, TPB, and OQTP through DFT calculations (B3LYP, 6-31+G*). Calculated structures are presented in Figure 4.4. Although OTP and TPB have only one low-energy conformer, OQTP has two. The OQTP conformers differ according to the torsional twisting of one biphenyl unit by ~60°, resulting in a closed-helical form (A) and an open-helical form (B) (see bottom left of Figure 4.4). These conformers have been reported previously by Hartley and are in rapid exchange at room temperature as determined by NMR. [47,48] According to our calculations the A and B conformers differ in energy by 0.011 eV after zero-point-energy correction. We did not calculate the activation energy for conformer exchange, but based on this previous report we assume that the activation energy is comparable to (or less than) kT at room temperature.

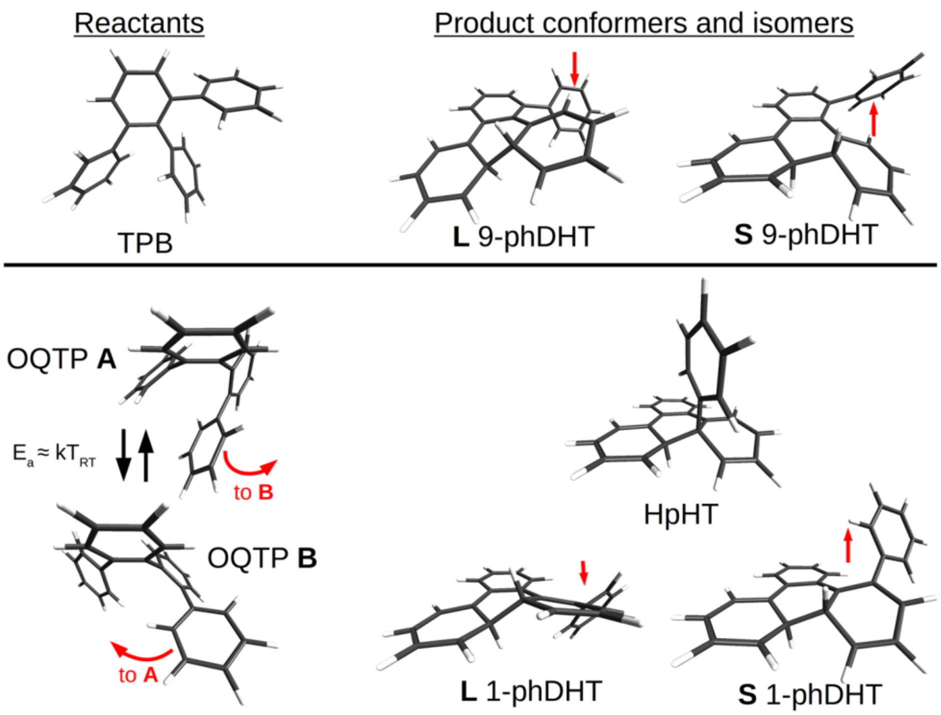

**Figure 4.4.** DFT-optimized (B3LYP/6-31+G*) geometries for reactants and predicted photoproducts. The interconversion between OQTP A and B involves the concerted rotation of two phenyl rings that results in compression (A) or decompression (B) of the outermost phenyl groups. The red arrows for L and S photoproducts highlight the steric effects that place the 1 or 9 substituted phenyl group above or below the plane of the DHT core. HphT has only one isomer.

We similarly determined the optimized ground-state structures for the dihydro-intermediates DHT, 9-phenyl DHT, and 1-phenyl DHT formed through UV excitation of OTP, TPB, and OQTP, respectively. Interestingly, TPB has two unique photoproduct conformations; these are similar to the two conformations of 4,5-substituted dihydrophenanthrenes noted by Muszkat et al.[49] Those authors labeled these structures with the empirical nomenclature "L" and "S" according to their relative peak absorption wavelengths ("L" = "long"; "S" = "short"). They also demonstrated that the S conformer was most stable, but the L conformer was formed initially via cyclization. An alternate labeling scheme associated with these conformers is based on whether the 4a (4b) hydrogen and the hydrogen on the adjacent 4 (5) carbon site are either on the same side (cis, C) or opposite side (trans, T) relative to the average plane of the DHT frame. In the case of TPB the L (C) and S (T) forms arise due to steric interactions of the phenyl group in the 9-position with the adjacent ring in the DHT unit that either raises or lowers the phenyl group relative to that ring and concomitantly alters the structure in the region of the newly formed carbon−carbon bond (see right side of Figure 4.4). Possible conformations for 1-phenyl DHT are more varied: OQTP B can form either of the L or S 1-phenyl DHT conformers, whereas OQTP A can form the unique photoproduct 4a,4b-H,phenyl-triphenylene (HphT, see bottom right of Figure 4.4). To our knowledge an intermediate similar to HphT has never been reported.

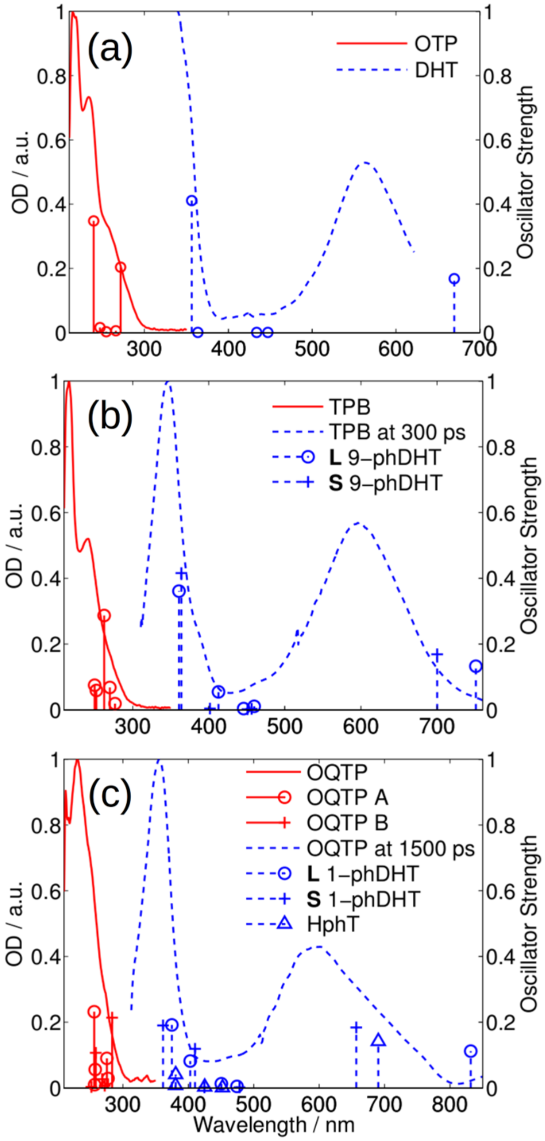

**Figure 4.5.** Normalized steady-state UV absorption spectra of OTP (a), TPB (b), and OQTP (c) (red solid lines) and UV/vis transient absorption spectra of corresponding dihydro-intermediates (blue dashed lines). Computed vertical excitation energies for the first 5 excited states of each reactant and intermediate structure as determined with TD-B3LYP/6-31+G* at the DFT-optimized ground-state geometries are plotted with symbols and vertical lines.

***4.4.3.2 Excitation Energies.*** TDDFT calculations (B3LYP, 6- 31+G*, 5 states) were performed using these optimized ground-state geometries in order to obtain excitation energies for comparison with the steady-state absorption spectra of reactants and the transient spectra of corresponding dihydro-intermediates, and, hence, for the assignment of the states involved in various electronic transitions. Calculated oscillator strengths as a function of excitation energy are plotted as stick spectra in Figure 4.5. For OTP, TDDFT calculations predict that transitions to the first and fifth singlet excited states have appreciable oscillator strength; these calculated transitions line up with the longest wavelength features in the experimental absorption spectrum at 242 and 260 nm. Calculations thus indicate that 266 nm excitation promotes OTP to its lowest singlet excited state, and that nonadiabatic cyclization occurs directly from this level. For TPB, absorption transitions into the first 5 excited states are predicted to fall between 280 and 250 nm, with the largest oscillator strength at 262.73 nm for a transition to the $S_3$ state.

The steady-state spectroscopy of OQTP is complicated by the fact that two unique ground-state minima can exist in equilibrium at room temperature. The two most significant transitions for OQTP B (among its lowest 5 transitions) occur at 283.46 and 258.57 nm to the first and fourth singlet excited states. The two strongest absorptions predicted for OQTP A occur at 275.52 and 256.22 nm and correspond to the $S_0$ to $S_2$ and $S_5$ transitions. Both sets of features approximately match the positions of the two shoulders at 252 and 275 nm in the steady-state absorption spectrum of OQTP. These calculations also predict that the lower energy transition is stronger for B, whereas the higher energy transition is stronger for A.

For the dihydro-intermediate structures (DHT, L 9-Ph- DHT, and L 1-Ph-DHT) a distinct trend in the positions of the first and fifth transitions is observed from our TDDFT calculations, with a red shift apparent from DHT to L 9-Ph- DHT to L 1-Ph-DHT. A similar trend appears from our experimental transient absorption spectra, with both the UV and visible bands at late time delays (>1 ns) showing a 10−20 nm shift across the three intermediates (DHT to L 9-Ph-DHT to L 1-Ph-DHT); this shift is somewhat smaller than predicted by calculations, but supports the assignment of these bands to transitions of the corresponding dihydro-intermediates. Discrepancies between experimentally observed transition energies and calculated transition energies are ∼0.3 eV in the visible; this is typical for TDDFT computations of large π- conjugated systems. [50]

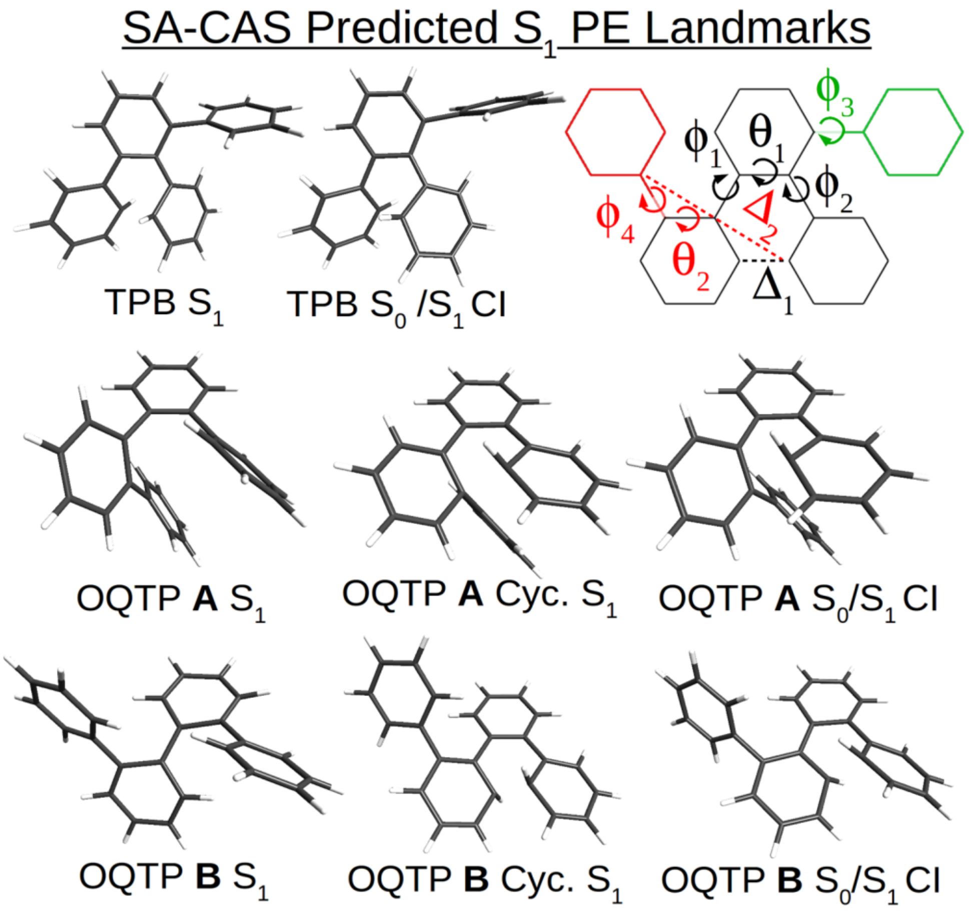
SA-CAS Predicted $S_1$ PE Landmarks
TPB $S_1$
TPB $S_0$ /$S_1$ CI
$\phi_3$
$\phi_1$
$\theta_1$
$\phi_2$
$\phi_4$
$\Delta_2$
$\theta_2$
$\Delta_1$
OQTP **A** $S_1$
OQTP **A** Cyc. $S_1$
OQTP **A** $S_0$/$S_1$ CI
OQTP **B** $S_1$
OQTP **B** Cyc. $S_1$
OQTP **B** $S_0$/$S_1$ CI

**Figure 4.6.** Excited-state minimum and minimum-energy CI geometries for TPB and OQTP from SA-CAS computations. The torsional (φ), twisting (θ), and photochemically formed bond length (Δ) coordinates are illustrated for TPB (green) and OQTP (red) in the upper right.

**Table 4.4** Structural Parameters for TPB and OQTP obtained by SA-CAS computations. TPB calculations were performed with SA-2-CAS(2,2)-sto3g and OQTP with SA-2-CAS(6,6)-sto3g levels of theory.

| Geometry | $\Delta_1$/Å | $\Delta_2$/Å | $\theta_1$/° | $\theta_2$/° | $\varphi_1$/° | $\varphi_2$/° | $\varphi_3$/° | $\varphi_4$/° |
|---|---|---|---|---|---|---|---|---|
| TPB $S_0$ | 3.48 | - | 1.0 | - | 58.0 | 65.2 | 54.8 | - |
| TPB $S_1$ | 1.74 | - | 4.6 | - | 19.6 | 17.7 | 57.7 | - |
| TPB $S_0$ /$S_1$ CI | 1.86 | - | 17.5 | - | 28.3 | 6.3 | 70.4 | - |
| **S** 9-phDHT $S_0$ | 1.55 | - | 21.5 | - | 3.5 | 7.7 | 136.2 | - |
| OQTP **A** $S_0$ | - | 3.55 | 1.6 | 0.9 | 68.1 | 51.9 | - | 53.3 |
| OQTP **A** $S_1$ | - | 3.32 | 4.6 | 23.4 | 52.9 | 50.8 | - | 34.7 |
| OQTP **A** Cyc. $S_1$ | - | 1.86 | 3.1 | 52.8 | 24.6 | 9.5 | - | 22.0 |
| OQTP **A** $S_0$ /$S_1$ CI | - | 1.95 | 13.9 | 21.3 | 14.9 | 3.3 | - | 36.7 |
| HphT $S_0$ | - | 1.57 | 12.5 | 96.8 | 2.1 | 8.0 | - | 41.5 |
| OQTP **B** $S_0$ | 3.43 | 3.43 | 2.0 | 1.8 | 57.9 | 56.8 | - | 54.5 |
| OQTP **B** $S_1$ | 3.43 | 3.43 | 35.0 | 40.0 | 23.9 | 41.4 | - | 39.1 |
| OQTP **B** Cyc. $S_1$ | 1.58 | 1.58 | 4.3 | 13.8 | 20.5 | 9.0 | - | 51.0 |
| OQTP **B** $S_0$ /$S_1$ CI | 1.89 | 1.89 | 16.9 | 0.2 | 6.9 | 31.4 | - | 73.9 |
| **L** 1-phDHT $S_0$ | 1.55 | 1.55 | 15.5 | 14.8 | 14.7 | 3.8 | - | 57.8 |

***4.4.3.3 Characterization of Landmarks on Ground- and Excited-State Potential Energy Surfaces with SA-CASSCF and TDA-TDDFT.*** In order to explore possible decay mechanisms for each excited reactant, the SA-CAS method was used to locate the $S_1$ minimum and $S_0/S_1$ conical intersection geometries (Figure 4.6 and Table 4.4) and energetics (Figure 4.7) for TPB and OQTP; results for OTP have been reported previously.[28] Excited-state calculations were carried out for only the $S_1$ surface. The use of a small basis set (STO-3G) and active space (2,2−6,6) without dynamic electron correlation makes computations with these large molecules economical at the cost of accuracy; consequently, these calculations are only meant to provide a qualitative picture of the $S_1$ potential-energy landscape. TPB calculations were performed with SA-2- CAS(2,2)/STO-3G and OQTP with to SA-2-CAS(6,6)/STO- 3G levels of theory.

Calculations with TPB locate qualitatively similar landmarks as those found for OTP, with a single $S_1$ minimum in close geometric vicinity to a $S_0/S_1$ conical intersection that leads to photocylization; the energetics of these landmarks are summarized in appendix 2 (Figure A2.5). The twisting angle $\theta_1$ increases only 3.6° from the $S_0$ to $S_1$ minimum geometries for TPB, compared with 9.6° for OTP. 28 The largest change still occurs between the $S_1$ minima and $S_0$ /$S_1$ CIs with similar changes of 12.9° for TPB and 12.8° for OTP. The change in "phenyl twist" torsional angle ($\varphi$) between structures is slightly altered for TPB due to the presence of the fourth phenyl ring that effectively spectates the photoreaction. Interestingly the torsional angle of the spectator ring ($\varphi_3$) increases steadily as the photoreaction proceeds, enabling the other two rings to form a carbon−carbon bond.

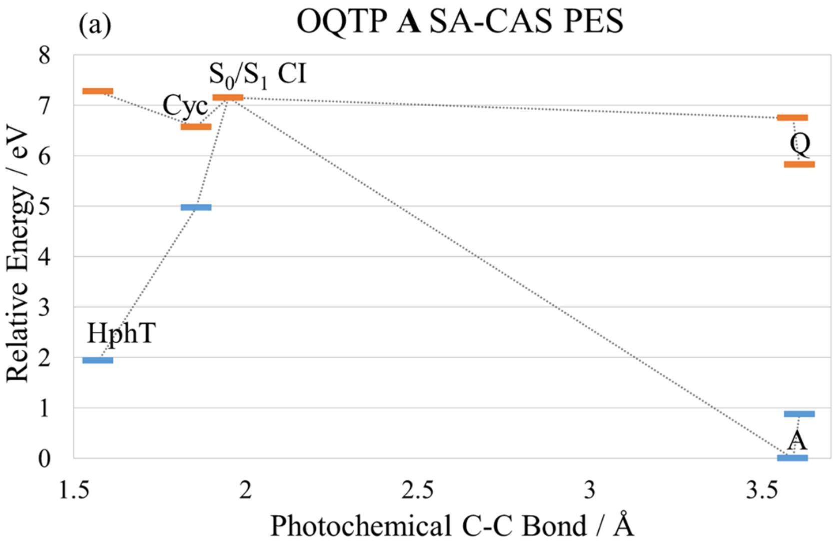

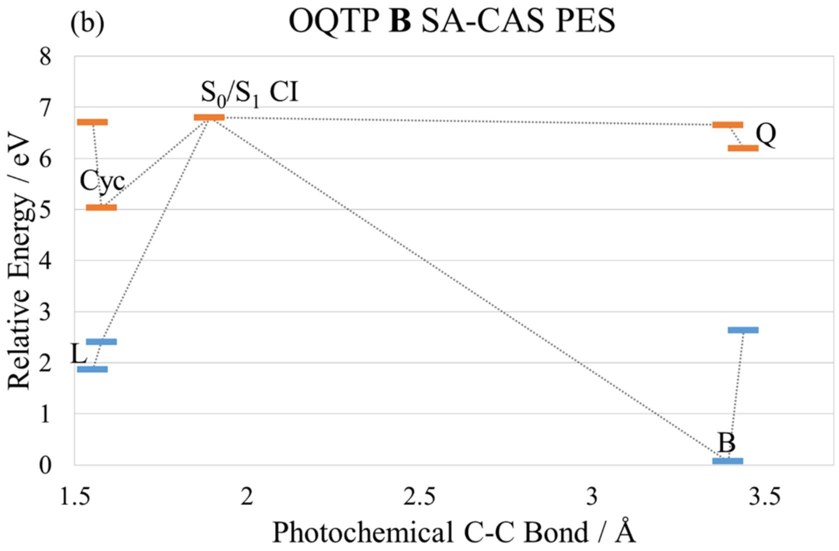

**Figure 4.7.** Characterization of potential-energy landscapes for (a) OQTP A and (b) OQTP B obtained from SA-CAS(6,6)-sto3g calculations. Calculations suggest the existence of quinoidal $S_1$ minima(Q) for both conformers. $S_0/S_1$ CIs similar to that of OTP and TPB are also found that are associated with cyclization to L 1-ph-DHT(OQTP B) or HphT (OQTP A). An excited state minimum (Cyc) is also found for each conformer.

The excited-state topography for OQTP is somewhat more complex than that of OTP and TPB; the energies of relevant configurations explained below are mapped according to the C−C bond distance in Figure 4.7. OQTP A and B both exhibit $S_1$ minima and $S_0/S_1$ CIs at geometries that are compatible with a photocyclization pathway. In addition, the $S_0/S_1$ CI is slightly uphill from the Franck−Condon region for both OQTP conformers. Interestingly, no excited-state minima were located within the 1.5 Å range in $\Delta$ between the CI and A/B $S_0$ minimum geometries. The twist ($\theta_1$) and torsional ($\varphi_1$, $\varphi_2$) angles still increase and decrease, respectively, between the FC region and the CI as they do for OTP and TPB, reflecting the importance of these coordinates in the photocyclization reaction coordinate.

We have also found that both conformers of OQTP have a second characteristic minimum on the $S_1$ surface. For OQTP B this unique $S_1$ minimum resembles an ortho-quinoidal configuration and is characterized by a symmetric relaxation of the terminal phenyl rings toward planarity, in contrast with the asymmetric relaxation that occurs between the FC region and the CI leading to cyclization. While a secondary $S_1$ minimum was also located for the A conformer, this configuration does not approach the same quinoidal geometry, requiring a further decrease in $\varphi_1$ and $\varphi_2$ to approach quasi-planarity. The LUMO at this minimum-energy structure obtained from TDDFT calculations is compared to the LUMO of $S_0$ OQTP B, the HOMO of L 1-phDHT, and the LUMO of $S_0$ biphenyl in Figure 4.8.

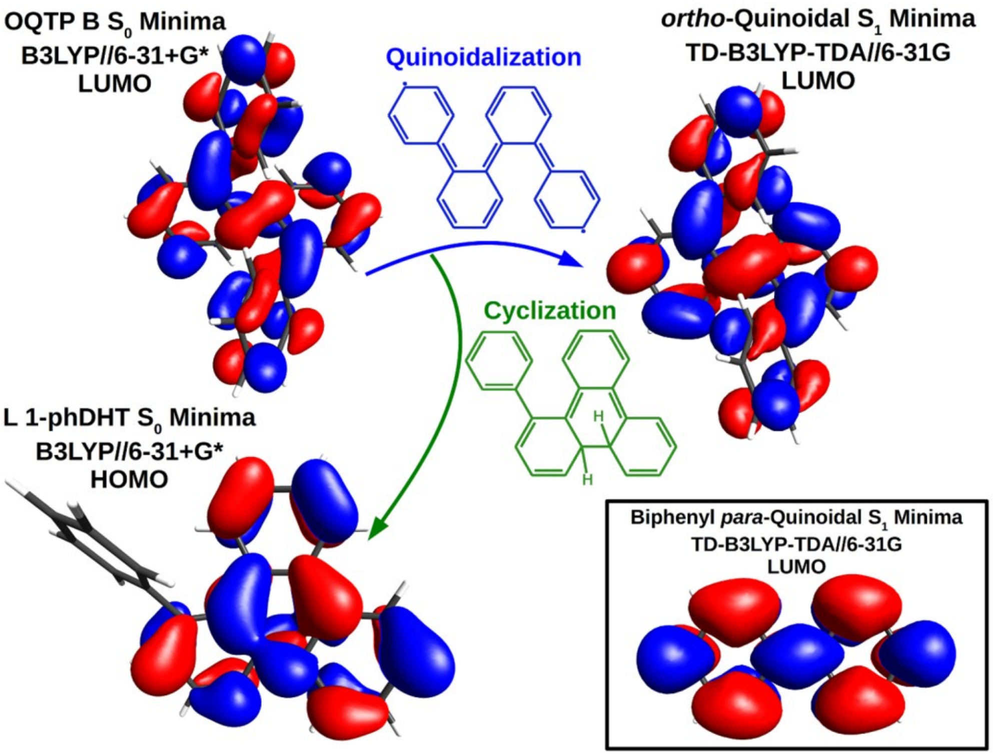
OQTP B $S_0$ Minima
B3LYP//6-31+G*
LUMO
Quinoidalization
*ortho*-Quinoidal $S_1$ Minima
TD-B3LYP-TDA//6-31G
LUMO
Cyclization
H
H
L 1-phDHT $S_0$ Minima
B3LYP//6-31+G*
HOMO
Biphenyl *para*-Quinoidal $S_1$ Minima
TD-B3LYP-TDA//6-31G
LUMO

**Figure 4.8.** $S_1$ relaxation pathways for OQTP assessed from ab initio quantum-chemical calculations. Shown are the LUMO of ground-state optimized OQTP B (top, left); the quinoidal $S_1$ minimum of OQTP B (top, right); and the HOMO of the cyclized photoproduct (bottom left). The central portion $S_1$ LUMO exhibits similarities with that of biphenyl (bottom, right).

From previous TDDFT results, 48 the $S_1$ minimum of OQTP A showed a more delocalized LUMO than that of the SA-CAS results presented here; this delocalization leads to a more uniform torsional angle ($\varphi$) and quasi-planar structure. We performed our own TDDFT $S_1$ optimizations (TDA-B3LYP/ 631G) for comparison; these show ortho-quinoidal character for both OQTP A and B with $\varphi_1$, $\varphi_2$, and $\varphi_4$ equal to 28.6, 35.7, and 29.7° for OQTP B. Comparison to SA-CAS results shows that the difference between the largest and smallest torsional angles is 17.5° versus 7.1° for the TDDFT results, illustrating the qualitative differences in calculation methods explained in more detail in appendix 2. However, both methods support characterization of this minimum as resulting from a relatively symmetric relaxation of the torsional angles, in contrast with the cyclization pathway.

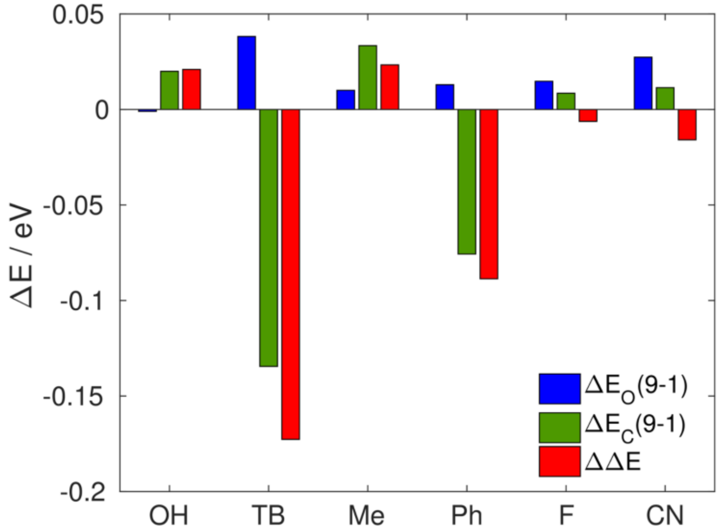

**Figure 4.9.** Calculated effect of substitution on the relative energies of OTP and DHT ground-state minima; DFT calculations were performed at the B3LYP/6-31+G* level. $\Delta\Delta E = \Delta E_9 (o-c) - \Delta E_1 (o-c)$ (red) reveals how relative energies are affected by specific substituents. Energy differences between 9- and 1-substituted reactants, $\Delta E_o$ (9−1) (blue), and products, $\Delta E_c$ (9−1) (green), reveal that substitution has greater impact on the energy of intermediate structures.

***4.4.3.4 Characterization of Intermediate Stabilities.*** The energy differences between the ground-state reactants (OTP, TPB, and OQTP B) and their corresponding dihydrointermediates were calculated at the DFT level in order to assess changes in relative intermediate stability with changes in reactant structure. We have also considered reactants analogous to TPB and OQTP in which the fourth phenyl ring is replaced with different substituents in the 9- and 1-positions of DHT (i.e., OH, CN, methyl, tert-butyl, and F). These substitutions permit evaluation of the relative contribution of steric hindrance and electronic effects to the stabilization or destabilization of dihydro-intermediate structures. All DHT analogues correspond with the L isomer, except 9-F and 9-OH substituted DHT, for which only an S isomer could be located. Figure 4.9 plots energy differences between OTP (blue) and DHT (green) substituted with each of the various substituents located at positions corresponding with the 1 and 9 carbon sites of DHT. In total, substitution at the 9 vs 1 site gives a ground-state energy for the substituted OTP that is consistently higher by 0−40 meV regardless of the nature of the substituent. In contrast, differences in the minimum energy as large as −120 meV are observed for substituted DHT. Red bars signify the change in the energy gap between open and closed structures induced by changing the substitution pattern for each individual substituent. Excluding the sizable impact of tert-butyl and phenyl substitution on these energy differences, a slight correlation is observed between ΔΔE and traditional electron-donating/withdrawing character of the substituents. Energy differences between each of the (open-ring) reactants and its corresponding dihydro-intermediates in their optimized geometries are shown in appendix 2; these are consistently higher than the energy difference between OTP and DHT.

## 4.5 Discussion

Spectral dynamics presented in Figure 4.1 demonstrate that all three reactants (OTP, TPB, and OQTP) form similar transient species following UV excitation, with virtually identical transient spectra from all three reactants measured within 1 ns. This similarity and results of TDDFT calculations presented in Figure 4.5 support assignment of these spectral intermediates to dihydro-intermediate structures (Scheme 4.1 and Figure 4.4). ns-TAS measurements indicate that these intermediates are all metastable (Figure 4.3). Transient decay of all 3 intermediates is single-exponential across a broad temperature range and yields highly linear van't Hoff plots, further indicating either that only a single product conformer or isomer is formed photochemically in each case or, alternatively, that structural variations between conformers/isomers are energetically indistinguishable given the excess vibrational energy imparted via the nonadiabatic transition. Beyond these similarities, the details of photochemical bond formation and the stability of the intermediate structures formed for each reactant are intimately connected with how reactant structure alters critical regions of potential-energy surfaces. Here we consider the photochemical dynamics of each species in view of our computational results as well as similarities or differences with the photophysical properties of OTP and other *ortho*-arenes.

***4.5.1 UV Photochemistry of TPB.*** The spectral analyses presented in Figures 4.1 and 4.2 reveal that the ultrafast spectral dynamics of TPB excited at 266 nm can be explained reasonably with as few as two photochemical transients. Figure 4.1b shows a global fit of these spectral dynamics to a simple 2-state ultrafast kinetic model (A→B) with an interconversion lifetime of 7.4 ps. Based on comparisons with the photo- chemistry of OTP and the calculated vertical excitation energies plotted in Figure 4.5, these kinetic species must correspond with TPB in a metastable excited state (A) and the dihydro-intermediate 9-phenyl DHT (B). Discrepancy between the experimental data and the 2-state global fit in the near-UV can be eliminated with a 3-state ultrafast kinetic model, as demonstrated in appendix 2. However, the region of this discrepancy and time dependence of the residuals observed when the 2-state model is applied are consistent with evolution in the Franck–Condon profile of the higher-energy absorption band as a result of vibrational relaxation of the nascent intermediate. This is precisely what we observed previously in the photochemical formation of DHT following UV excitation of OTP. [10] In fact, time dependence of the residuals from the 2-state model exhibits a ∼30 ps relaxation time scale, which is similar to the solvent-dependent vibrational relaxation time scales we determined for OTP. Given these similarities, we conclude that excited TPB cyclizes on a time scale of 7.4 ps, and that 9-phenyl DHT relaxes vibrationally on a time scale of 32.6 ps. Thus, the photochemical dynamics of TPB are qualitatively quite similar to those of OTP.

The similarity between TPB and OTP relaxation dynamics is perhaps not surprising given the similar "landmark" geometries on their excited-state potential-energy surfaces: Our CAS calculations find qualitatively similar structures for TPB and OTP at the $S_0$ minimum (FC region), $S_1$ minimum, and the $S_1$/ $S_0$ CI nearest the $S_1$ minimum, despite differences in the sizes of the basis sets and active spaces used in these calculations. Thus, a similar picture of the excited-state decay mechanism is suggested: After photoexcitation TPB relaxes toward the CI that links excited TPB to $S_0$ 9-phDHT and $S_0$ TPB and that is within close energetic and geometrical proximity to the minimum on the excited singlet potential-energy surface. The longer lifetime observed for TPB relaxation may signify a larger effective barrier (when compared with OTP) to reaching the CI for cyclization, or may be attributed to a mass effect [51] or steric interactions introduced by the fourth/extra phenyl substituent, which calculations predict to be a spectator in the cyclization mechanism.

Interestingly, TDDFT calculations indicate that the absorption spectrum of TPB is dominated by the $S_0$–$S_3$ transition (Figure 4.5b). This would imply that the relevant nonadiabatic cyclization dynamics occur directly via this higher-lying state or via lowerlying excited singlets (i.e., $S_1$) after a fast relaxation within the excited singlet manifold; such a relaxation could occur on time scales beyond the resolution of our measurements or could be masked by slow nuclear relaxation on the $S_3$ surface itself. Based on symmetry considerations (Woodward−Hoffmann rules), it is conceivable that cyclization could occur from either the $S_1$ or $S_3$ state. Nonetheless, the nuclear dynamics that enable these nonadiabatic cyclization reactions are anticipated to be fairly similar.

**4.5.2** ***Photochemistry of UV-Excited OQTP.*** Based on the analysis of our ultrafast data, the photochemical dynamics of UV-excited OQTP involves at least 3 photochemical states. One of these remains on the longest time scales probed in these experiments (~1.5 ns) and can be attributed to the dihydro-intermediate 1-phenyl DHT (or HphDHT) in its ground electronic state; this assignment is supported by the spectroscopic similarity with the metastable transients observed after the photoexcitation of OTP and TPB, as well as comparisons with calculated excitation energies presented in Figure 4.5c. Spectral relaxation that leads to the formation of intermediates occurs on two characteristic time scales (46.5 and 369.9 ps), and spectral dynamics can be fitted reasonably with various simple global kinetic models. As comparable residuals are obtained with the multiple models presented in Results and Analysis and appendix 2, deduction of the relevant photochemical pathway requires consideration of additional photophysical data and insights from quantum-chemical calculations.

To this end we first consider the various ground- and excited-state configurations predicted from quantum-chemical calculations and their relative energetics (Figure 4.7). Ground-state calculations have located 5 minima on the $S_0$ potential-energy surface: open-ring conformers of OQTP (A and B) and the closed-ring isomers 1-phDHT (L and S) and

HphT that correspond to cyclization reactants and possible photochemical products, respectively. Excited-state calculations have located landmarks that include one $S_0/S_1$ CI per OQTP conformer that links electronically excited OQTP to the ground-state cyclized L product conformer and a structurally similar $S_1$ minimum. Another $S_1$ minimum, the quinoidal minimum, was also located for each OQTP conformer and is characterized by symmetric torsional twisting of the phenyl units toward a common plane, rather than asymmetric relaxation that is anticipated along the photocyclization pathway (cf. Figure 4.8).

Based on these calculated results we propose the following relaxation mechanism, which is restricted to the $S_1$ surface for a single reactant conformer: Photoexcitation of OQTP results in a branching between relaxation toward the $S_0/S_1$ CI and relaxation to the quinoidal $S_1$ minimum (a relaxation process we term as "quinoidalization"). Branching between these pathways implies a weighted summation of their associated spectral relaxation dynamics. Our quantum-chemical calculations did not locate a CI geometry near the quinoidal $S_1$ minimum; as the OQTP fluorescence quantum yield is quite low (0.01), [47] it is reasonable to assume that internal conversion of this quinoidal population likewise occurs by way of a cyclization CI. Model 3 is the simplest kinetic model that can be used to fit the data accordingly, with species A, B, C, and D representing an excited-state minimum nearer to the cyclization CI, the quinoidal $S_1$ geometry, the ground-state dihydrostructure, and the (open-ring) ground-state geometry, respectively. The ground state is dark in our spectroscopic measurements, as it absorbs outside of the probing region (cf. Figure 4.5c). An implicit assumption of this model is that the initial wavepacket branching is considerably faster than the time resolution of the current experiment (<300 fs).

The time scales and spectra obtained from the global analysis are sensible, particularly in comparison to spectral dynamics of OTP and TPB and based on the computed relative energies mapped in Figure 4.7. First, the spectrum of the direct "cyclizing" subpopulation closely matches that of excited OTP and TPB (Figure A2.1 in appendix 2), with two distinct features at 600 and 400 nm; we expect that direct relaxation toward cyclization should create an excited-state configuration quite similar to $S_1$ OTP and thus should exhibit similar spectroscopy, as predicted by TDDFT results. Interestingly, the lifetime for this fraction (A) is considerably longer than the photoprepared excited states of OTP and TPB. A tentative explanation for this difference can be derived from calculations, which suggest that the CI for cyclization is slightly uphill from the Franck−Condon region in OQTP, but downhill for the other two structures; this suggests that there is an effective barrier to cyclization for OQTP that could lower the reaction rate. The longer 369.9 ps time scale obtained for the decay of the second, quinoidal minimum-energy configuration is also sensible if there is an even larger barrier between this minimum and the cyclization CI.

The transient spectral data and our interpretation are consistent with other pieces of experimental data obtained with OQTP and related molecules. The presence of a quinoidal minimum is supported by recent work by Hartley that explored the excited-state properties of *ortho*-phenylene oligomers; [48] he notes a geometrical "compression" of the closed helical (A) conformers that occurs as the excited state takes on a localized quinoidal character within the *ortho*-phenylene chain that shares characteristics with biphenyl. Although the TAS of *ortho*-phenylenes has not been explored to our knowledge, it is noteworthy that fs-TAS of biphenyl in solution exhibits transient absorbance at 680 nm; [52]

this closely matches the broad, longer-lived TA band of OQTP observed here (peak near 695 nm), a correspondence that is suggestive of a similar quinoidal minimum on the $S_1$ surface of OQTP (Figure 4.8).Our interpretation of OQTP photophysics is also consistent with general trends in the fluorescence spectroscopy of *ortho*-phenylenes. [47,48] TCSPC measurements with OQTP obtain fluorescence lifetime of ~400 ps, similar to the longest lifetime measurement here via fs-TAS. The fluorescence quantum yields 0.18 for biphenyl, drops to essentially 0 for OTP, and rises back to 0.18 as the *ortho*-oligophenylene length is increased to the octomer. Much of the recovery in fluorescence quantum yield occurs between 4 and 6 units, indicating that the cyclization channel that dominates the photophysics of OTP becomes less significant at longer oligomer lengths. Nonetheless, the OQTP exhibits signatures of both cyclization and a fluorescent state, with a fluorescence lifetime that is substantially shorter than that of longer *ortho*-phenylene oligomers. Indirect cyclization by way of the quinoidal minimum would compete with radiative and other nonradiative processes, resulting in a considerably faster fluorescence decay of OQTP relative to larger *ortho*-phenylene oligomers and lower fluorescence quantum yields. Based on these various comparisons, the existence of a quinoidal excited-state minimum and a competition between cyclization and quinoidalization in the photochemical relaxation of UV-excited OQTP is highly plausible.

Although the combination of experimental and computational results suggests a relatively simple mechanism following the UV excitation of OQTP, it is conceivable that experimentally measured spectral dynamics could also arise from the incoherent summation of the photophysics of both conformers. However, our results seem to be compatible only with a mechanism that involves either branching between two minima on the excited-state potential of a single conformer or identical photophysical behavior for both conformers: First, TDDFT calculations predict that the B isomer dominates the spectrum at lower transition energies where the sample is excited, which supports a selective excitation of a single isomer. Second, temperature-dependent ns-TAS measurements indicate that only a single photoproduct persists into the nanosecond regime, suggesting either that 266 nm photo-selectively excites a single conformer (B), that two products are formed from the A and B conformers (HphT and 1-phT, respectively) that have nearly identical stability, or that that both conformers are excited with only one reacting to cyclize (B). The second possibility seems plausible based on the energetic similarity in excited-state landmarks found computationally for both conformers (Figure 4.7); the third possibility seems less plausible, as it would imply that one conformer is stable relative to cyclization and would be expected to have a longer fluorescence lifetime comparable to that of longer *ortho*-phenylene oligomers. Third, the fluorescence excitation and absorption spectra of OQTP closely match between 250 and 300 nm (Figure A2.3 in appendix 2), suggesting no significant difference in the fluorescence quantum yield for the two conformers. Thus, all pieces of data indicate that either one conformer (B) dominates the photophysical dynamics at this excitation energy, or else that both conformers have nearly identical kinetics and photoproduct stabilities when excited at 266 nm despite structural differences between the conformers and metastable photoproducts.

**4.5.3** ***Relative Stability of DHT Intermediates.*** Although the feasibility for nonadiabatic photochemistry relies on the success for reaching a conical intersection, the stability of intermediate products is critical for further steps in a photochemical mechanism, as is the case for the cyclodehydrogenation reactions depicted in Scheme 4.1. Of particular interest for this class of reactions is how the nature and location of substituent groups affect the stability of DHT intermediates. The activation energies determined experimentally via temperature-dependent ns-TAS place the relative stability of 9-ph-DHT greater than that of 1-ph-DHT (in hexane), with both much less stable than DHT itself. However, it is not directly clear why one positional isomer may be more stable than another. There are two general factors that can explain the relative differences in ground-state stabilities of 1- and 9- phDHT: positional influences on electronic stabilizing/ destabilizing capabilities of the substituent and on intra-molecular steric interactions. Computational analysis is highly instructive for distinguishing these contributions.

The best metrics of the relative stability of intermediate structures are activation energies themselves. Computationally, calculation of activation energies would require a transition-state search for each derivative; these searches are complicated by the presence of multiple product conformations. Instead, we have resorted to a somewhat cruder method for assessing the relative stability of intermediate structure, whereby we assume a correlation between the relative energy gap between the reactant and photoproduct energy minimum, $\Delta\Delta E = \Delta E_9$ (o− c) − $\Delta E_1$ (o−c), and the activation energy. Under this ansatz a larger energy gap between limiting structures would correspond with lower activation energy, and the difference in these energy gaps for the two substitution patterns $\Delta\Delta E = \Delta E_9$ (o−c) − $\Delta E_1$ (o−c) should roughly reflect the relative stabilizing or destabilizing effect of a specific substituent.

These calculated energy differences in Figure 4.9 are arranged in the typical order and strength of electron donating vs withdrawing. The relative impact of steric vs electronic effects can be assessed by considering the impact of substituent type and size. For example, typical electron-donating groups, such as OH and methyl groups, slightly increase this energy difference, suggesting that these groups effectively stabilize the 1-substituted relative to the 9-substituted intermediate. In contrast, typical electron-withdrawing groups, such as F and CN, stabilize the 9-substituted relative to the 1-substituted intermediate at a comparable magnitude. Interestingly, significant destabilization of the 1-substituted vs 9-substituted intermediate is observed for both tert-butyl and phenyl substituents, and in both cases well beyond the magnitude associated with any of the smaller electron-donating and withdrawing groups. The direction of this shift matches that of a simplistic resonance-structure argument for the relative stabilization of 9- vs 1-phDHT. However, the fact that the comparable-sized tert-butyl electron-donating group has a similar impact on the energy difference indicates that this difference may also be associated with steric interactions that destabilize one structure relative to the other. Thus, computational results suggest that the difference in activation energies measured experimentally is associated with the relative structure-induced destabilization of the energy minimum for 1- relative to 9-phenyl DHT. Interestingly, the overall thermodynamic stability of 1-phenyl DHT is actually greater, as evidenced by consistently longer intermediate lifetimes across a large range of temperatures (Figure 4.3), indicating that the faster ring opening of 9-phenyl DHT is promoted by entropic factors (Table 4.3).

Our calculations also provide insight into the relative stability of substituted DHT conformers. A few trends between the L and S conformers can be noted: The S conformer is consistently lower in energy except in cases of bulky substituents (TB and Ph), where positioning dictates the most stable conformer. The absolute energy difference between L and S conformers is smaller for 9-substituted analogues and is largest for bulky substituents. The implication for TPB and OQTP is that the initial photoproduct of TPB, L 9-PhDHT, is the most stable conformer while L 1-PhDHT is the least stable conformer. As steric repulsion is increased in a specific position (e.g., by replacing F with TB), energy differences between conformers also increase; this suggests the formation of a potential barrier between and therefore the isolation of two distinct conformers.

We note that it is unclear empirically whether one or both of the L and S 1- and 9-phDHT conformers is formed upon cyclization of TPB and OQTP. However, our calculated excited state structures suggest that the L isomer may be formed more readily via cyclization. Muszkat and co-workers also reasoned that the L conformer forms initially upon photocyclization of substituted diarylethenes, whereas subsequent isomerization to the more stable S isomer occurs on very long time scales (μs to s); [49] thermal conversion studies and related calculations suggested a barrier of 10−17 kcal between forms. Our temperature-dependent ns-TAS measurements indicate the presence of only a single kinetically distinct product for both TPB and OQTP (Figure 4.3a,c). This indicates that a single product conformer is formed initially subject to the structural evolution along the photocyclization pathway and is stable to conformational relaxation on the time scale of thermal ring opening; alternatively, the energy barrier between the two isomers may be negligible relative to the excess internal energy imparted to the product following nonadiabatic cyclization.

## 4.6 Conclusions

We have examined the ultrafast photochemical dynamics of the *ortho*-arenes TPB and OQTP, finding similarities in both cases to the photoinduced dynamics of OTP. OTP and

TPB exhibit highly similar relaxation dynamics, including excited-state relaxation to form the dihydro-intermediate structures DHT and 9-phenyl DHT via cyclization on a time scale of picoseconds (2.9 vs 7.4 ps in THF, respectively), followed by a slower vibrational relaxation of photoproducts on somewhat longer time scales (32.6 ps for TPB in THF). In contrast, OQTP exhibits more complex behavior on ultrafast time scales with the presence of two spectroscopically distinguishable species appearing before the formation of 1-phenyl DHT. Based on the results of excited-state structure calculations and kinetic modeling of our experimental data, we ascribe this behavior to branching of the excited-state wavepacket between direct and indirect pathways to cyclization. The direct pathway is associated with the appearance of shorter-lived (46 ps) transient spectral features that are highly similar to the $S_1 - S_N$ absorption transitions of both OTP and TPB. The indirect pathway involves the relaxation along the excited-state surface to a symmetric "ortho-quinoid" structure, which persists on longer time scales (380 ps) due to a presumed barrier to the asymmetric relaxation pathway required to reach the CI for nonadiabatic cyclization. Complementary steady-state and nanosecond spectroscopic data for OQTP and related *ortho*-phenylene oligomers support this mechanism of excited-state relaxation.

Findings from our work can be used to better understand how structure−dynamics relationships control the photochemistry of *ortho*-arenes. Regarding the photoinduced cyclodehydrogenation of OTP, TPB, and OQTP, it is clear that structure does not impact the possibility for carbon−carbon bond formation for any of these reactants. Rather, the cyclodehydrogenation chemistry of these systems is determined predominantly by the relative thermodynamic stability of their dihydro-intermediates: The reported yields for these reactions correlate roughly with the relative lifetimes of dihydro-intermediates over a broad range of temperatures, OTP > OQTP > TPB, such that reaction yields must be limited primarily by the bimolecular reaction with an oxidant ($I_2$).

Nonetheless, our findings illustrate how reactant structure can alter ultrafast excited-state dynamics, and specifically the length-dependent photoinduced dynamics of *ortho*-phenylenes. For these systems, excited-state dynamics can be characterized by a competition between asymmetric relaxation, leading to cyclization, and symmetric relaxation, leading to a long-lived excited state: Biphenyl relaxes on the sub-picosecond time scale to its quinoidal/planar excited-state minimum. In the cases of OTP and TPB, relaxation favors a cyclization pathway, and the picosecond formation of DHT and 9-phDHT. OQTP is the first *o*-arene that exhibits both symmetric relaxation (quinoidalization) and asymmetric relaxation (cyclization), but with surmountable barriers that enable the quinoidal structure to reach a CI for cyclization. Increasing the oligomer length should further favor the symmetric ortho-quinoidal minimum, as an asymmetric relaxation must overcome steric constraints, such as those imposed by the helical structures (similar to OQTP A) favored at longer lengths. [47,48] Thus, the branching between quinoidalization and cyclization is a direct function of chain length with the increase in chain length favoring the modest conjugation possible via symmetric relaxation over a highly localized (asymmetric) relaxation required to promote bond formation. Hence, photochemical schemes for synthesizing extended polyaromatic structures requires reactant structures that eliminate the competition between such reactive and nonreactive excited-state relaxation pathways.

## 4.7 References

(1) Guo, Y.; Bhattacharya, A.; Bernstein, E. R. Ultrafast $S_1$ to $S_0$ Internal Conversion Dynamics for Dimethylnitramine through a Conical Intersection. *J. Phys. Chem. A* **2011**, *115*, 9349−9353.

(2) Kohler, B. Nonradiative Decay Mechanisms in DNA Model Systems. *J. Phys. Chem. Lett.* **2010**, 1, 2047−2053.

(3) Deb, S.; Weber, P. The Ultrafast Pathway of Photon-Induced Electrocyclic Ring Opening Reactions: The Case of 1,3-Cyclohexadiene. *Annu. Rev. Phys. Chem.* **2011**, *62*, 19−39.

(4) Lim, J. S.; Kim, S. K. Experimental Probing of Conical Intersection Dynamics in the Photodissociation of Thianisole. *Nat. Chem.* **2010**, *2*, 627−632.

(5) Levine, B. G.; Martinez, T. J. Isomerization through Conical Intersections. *Annu. Rev. Phys. Chem*. **2007**, *58*, 613−634.

(6) Budyka, M. F. Diarylethylene Photoisomerization and Photocyclization Mechanisms. *Russ. Chem. Rev*. **2012**, *81*, 477−493.

(7) Dunkelberger, A. D.; Kieda, R. D.; Shin, J. Y.; Paccani, R. R.; Fusi, S.; Olivucci, M.; Crim, F. F. Photoisomerization and Relaxation Dynamics of a Structurally Modified Biomimetic Photoswitch. *J. Phys. Chem. A* **2012**, *116*, 3527−3533.

(8) Polli, D.; Altoe, P.; Weingart, O.; Spillane, K. M.; Manzoni, C.; Brida, D.; Tomasello, G.; Orlandi, G.; Kukura, P.; Mathies, R. A.; et al. Conical Intersection Dynamics of the Primary Photoisomerization Event in Vision. *Nature* **2010**, *467*, 440−443.

(9) Waldeck, D. H. Photoisomerization Dynamics of Stilbenes. *Chem. Rev.* **1991**, *91*, 415−436.

(10) Molloy, M. S.; Snyder, J. A.; Bragg, A. E. Structural and Solvent Control of Nonadiabatic Photochemical Bond Formation: Photo- cyclization of O-Terphenyl in Solution. *J. Phys. Chem. A* **2014**, *118*, 3913−3925.

(11) Yarkony, D. Conical Intersections: The New Conventional Wisdom*. J. Phys. Chem. A* **2001**, *105*, 6277−6293.

(12) Matsika, S.; Krause, P. Nonadiabatic Events and Conical Intersections. *Annu. Rev. Phys. Chem.* **2011**, *62*, 621−643.

(13) Worth, G. A.; Cederbaum, L. S. Beyond Born-Oppenheimer: Molecular Dynamics through a Conical Intersection. *Annu. Rev. Phys. Chem*. **2004**, *55*, 127−158.

(14) Irie, M.; Fukaminato, T.; Matsuda, K.; Kobatake, S. Photochromism of Diarylethene Molecules and Crystals: Memories, Switches, and Actuators. *Chem. Rev.* **2014**, *114*, 12174−12277.

(15) Hou, L.; Zhang, X.; Pijper, T. C.; Browne, W. R.; Feringa, B. L. Reversible Photochemical Control of Singlet Oxygen Generation Using Diarylethene Photochromic Switches. *J. Am. Chem. Soc.* **2014**, *136*, 910–913.

(16) Gö stl, R.; Senf, A.; Stefan, H. Remote-Controlling Chemical Reactions by Light: Towards Chemistry with High Spatio-Temporal Resolution. *Chem. Soc. Rev.* **2014**, *43*, 1982−1996.

(17) Bach, T.; Hehn, J. P. Photochemical Reactions as Key Steps in Natural Product Synthesis. *Angew. Chem., Int. Ed.* **2011**, *50*, 1000− 1045.

(18) Müller, M.; Behnle, S.; Maichle-Mö ssmer; Bettinger, H. F. Boron-Nitrogen Substituted Perylene Obtained through Photocyclisation. *Chem. Comm.* **2014**, *50*, 7821−7823.

(19) Węcławski, M. K.; Tasior, M.; Hammann, T.; Cywiń ski, P. J.; Gryko, D. T. From P-Expanded Coumarins to P-Expanded Pentacenes. *Chem. Comm.* **2014**, *50*, 9105−9108.

(20) Mallory, F. B.; Butler, K. E.; Bé rubé , A.; Luzik, E. D., Jr.; Mallory, C. W.; Brondyke, E. J.; Hiremath, R.; Ngo, P. L.; Carrol, P. J. Phenacenes: A Family of Graphite Ribbons. 3. Iterative Strategies for the Synthesis of Large Phenacenes. *Tetrahedron* **2001**, *57*, 3715−3724.

(21) Mallory, F. B.; Mallory, C. W. Photocyclization of Stilbenes and Related Molecules. In Organic Reactions; Boswell, G. A., Jr., Danishfesky, S., Gschwend, H. W., Heck, R. F., Hirschman, R. F., Paquette, L. A., Posner, G., Reich, H. J., Eds.; John Wiley & Sons, Inc.: New York, 1984; Vol. 30, pp 1−456.

(22) Laarhoven, W. H.; Cuppen, T. J. H. M.; Nivard, R. J. F. Photodehydrocyclizations in Stilbene-Like Compounds. *Tetrahedron* **1970**, *26*, 1069−1083.

(23) Kharasch, N.; Alston, T. G.; Lewis, H. B.; Wolf, W. The Photochemical Conversion of *o*-Terphenyl into Triphenylene. *Chem. Comm.* (London) **1965**, 242−243.

(24) Sato, T.; Shimada, S.; Hata, K. A New Route to Polycondensed Aromatics: Photolytic Formation of Triphenylene and Dibenzo- [Fg,Op]Naphthacene Ring Systems. *Bull. Chem. Soc. Jpn*. **1971***, 44,* 2484−2490.

(25) Woodward, R. B.; Hoffmann, R. The Conservation of Orbital Symmetry. Angew. *Chem., Int. Ed. Engl.* **1969**, *8*, 781−853.

(26) Liu, L.; Yang, B.; Katz, T. J.; Poindexter, M. K. Improved Methodology for Photocyclization Reactions. *J. Org. Chem*. **1991**, *56,* 3769−3775.

(27) Sato, T.; Shimada, S.; Hata, K. Phyto-Aryl Coupling and Related Reactions 0.7. New Route to Polycondensed Aromatics Photolytic Formation of Triphenylene and Dibenzo[Fg,Op]Naphthacene Ring Systems. *Bull. Chem. Soc. Jpn*. **1971**, *44,* 2484−2490.

(28) Smith, M. C.; Snyder, J. A.; Steifel, B. C.; Bragg, A. E. Ultrafast Excited-State Dynamics of ortho-Terphenyl and 1,2-Diphenylcyclohexene: The Role of ″Ethylenic Twisting″ in the Non-Adiabatic Photocyclization of Stilbene Analogs. *J. Phys. Chem. Lett.* **2013**, *4*, 1895−1900.

(29) Bachmann, W. E.; Clarke, H. T. The Mechanism of the Wurtz-Fittig Reaction. *J. Am. Chem. Soc.* **1927**, *49*, 2089−2098.

(30) Megerle, U.; Pugliesi, I.; Schriever, C.; Sailer, C. F.; Riedle, E. Sub-50 Fs Broadband Absorption Spectroscopy with Tunable Excitation: Putting the Analysis of Ultrafast Molecular Dynamics on Solid Ground*. Appl. Phys. B: Lasers Opt.* **2009**, *96*, 215−231.

(31) Heimer, T. A.; Bignozzi, C. A.; Meyer, G. J. Molecular Level Photovoltaics: The Electrooptical Properties of Metal Cyanide Complexes Anchored to Titanium Dioxide. *J. Phys. Chem.* **1993**, *97*, 11987−11994.

(32) Castellano, F. N.; Stipkala, J. M.; Friedman, L. A.; Meyer, G. J. Spectroscopic and Excited-State Properties of Titanium Dioxide Gels. *Chem. Mater.* **1994**, *6*, 2123−2129.

(33) Schmidt, M. W.; Baldridge, K. K.; Boatz, J. A.; Elbert, S. T.; Gordon, M. S.; Jensen, J. H.; Koeski, S.; Matsunaga, N.; Nguyen, K. A.; Su, S. J.; et al. General Atomic and Molecular Electronic Structure System. *J. Comput. Chem*. **1993***, 14*, 1347−1363.

(34) Bode, B. M.; Gordon, M. S. Macmolplt: A Graphical User Interface for Gamess. *J. Mol. Graphics Modell.* **1998**, *16*, 133−138.

(35) Docken, K. K.; Hinze, J. LiH Potential Curves and Wavefunctions for X $^1\Sigma^+$ , A $^1\Sigma^+$ , B $^1\Pi$, $^3\Sigma^+$ , and $^3\Pi$. *J. Chem. Phys*. **1972**, *57*, 4928−4936.

(36) Hehre, W. J.; Stewart, R. F.; Pople, J. A. Self-Consistent Molecular-Orbital Methods.I. Use of Gaussian Expansions of Slater- Type Atomic Orbitals. *J. Chem. Phys.* **1969***, 51*, 2657−2664.

(37) Bearpark, M. J.; Robb, M. A.; Schlegel, H. B. A Direct Method for the Location of the Lowest Energy Point on a Potential Surface Crossing. *Chem. Phys. Lett.* **1994***, 223*, 269−274.

(38) Hohenberg, P.; Kohn, W. Inhomogeneous Electron Gas. *Phys. Rev.* **1964**, 136, B864−B871.

(39) Kohn, W.; Sham, L. J. Self-Consistent Equations Including Exchange and Correlation Effects. *Phys. Rev.* **1965**, *140*, A1133− A1138.

(40) Frisch, M. J.; Pople, J. A.; Binkley, J. S. Self-Consistent Molecular-Orbital Methods Supplementary Functions for Gaussian-Basis Sets. *J. Chem. Phys*. **1984**, *80*, 3265−3269.

(41) Hehre, W. J.; Ditchfie, R.; Pople, J. A. Self-Consistent Molecular-Orbital Methods 0.12. Further Extensions of Gaussian- Type Basis Sets for Use in Molecular-Orbital Studies of Organic- Molecules. *J. Chem. Phys*. **1972**, *56,* 2257−2261.

(42) Runge, E.; Gross, E. K. U. Density-Functional Theory for Time- Dependent Systems. *Phys. Rev. Lett*. **1984**, *52*, 997−1000.

(43) Hirata, S.; Head-Gordon, M. Time-Dependent Density Functional Theory within the Tamm-Dancoff Approximation. *Chem. Phys. Lett.* **1999**, *314*, 291−299.

(44) Hendler, R. W.; Shrager, R. I. Deconvolutions Based on Singular-Value Decomposition and the Pseudoinverse a Guide for Beginners. *J. Biochem. Biophys. Methods* **1994**, *28*, 1−33.

(45) Bobrovnik, S. A. Determination the Rate Constants of Some Biexponential Reactions. *J. Biochem. Biophys. Methods* **2000**, *42*, 49− 63.

(46) Laidler, K. J. Chemical Kinetics, 2nd ed.; McGraw-Hill: New York, 1965; p ix, 566 pp.

(47) Mathew, S. M.; Hartley, C. S. Parent *o*-Phenylene Oligomers: Synthesis, Conformational Behavior, and Characterization. *Macromolecules* **2011**, *44*, 8425−8432.

(48) Hartley, C. S. Excited-State Behavior of *ortho*-Phenylenes. *J. Org. Chem*. **2011**, *76*, 9188−9191.

(49) Muszkat, K. A.; Eisenstein, M.; Fischer, E.; Wagner, A.; Ittah, Y.; Luttke, W. The Two Conformations of Hindered Photochromic 4a,4b- Dihydrophenanthrenes. *J. Am. Chem. Soc*. **1997**, *119*, 9351−9360.

(50) Parac, M.; Grimme, S. A TDDFT Study of the Lowest Excitation Energies of Polycyclic Aromatic Hydrocarbons. *Chem. Phys.* **2003**, *292*, 11−21.

(51) Schalk, O.; Boguslavskiy, A. E.; Schuurman, M. S.; Brogaard, R. Y.; Unterreiner, A. N.; Wrona-Piotrowicz, A.; Werstiuk, N. H.; Stolow, A. Substituent Effects on Dynamics at Conical Intersections: Cycloheptatrienes. *J. Phys. Chem. A* **2013**, *117*, 10239−10247.

(52) Mank, D.; Raytchev, M.; Amthor, S.; Lambert, C.; Fiebig, T. Femtosecond Probing of the Excited State Absorption and Structural Relaxation in Biphenyl Derivatives. *Chem. Phys. Lett.* **2003**, *376*, 201− 206.

# Chapter 5

# Excited-state Deactivation Pathways and the Photocyclization of BN-doped Polyaromatics

Reproduced with permission from Snyder, J. A.; Grüninger, P.; Bettinger, H. F.; Bragg, A. E. *Physical Chemistry Chemical Physics* **2017** ***Under Review***. Copyright 2017, Royal Society of Chemistry.

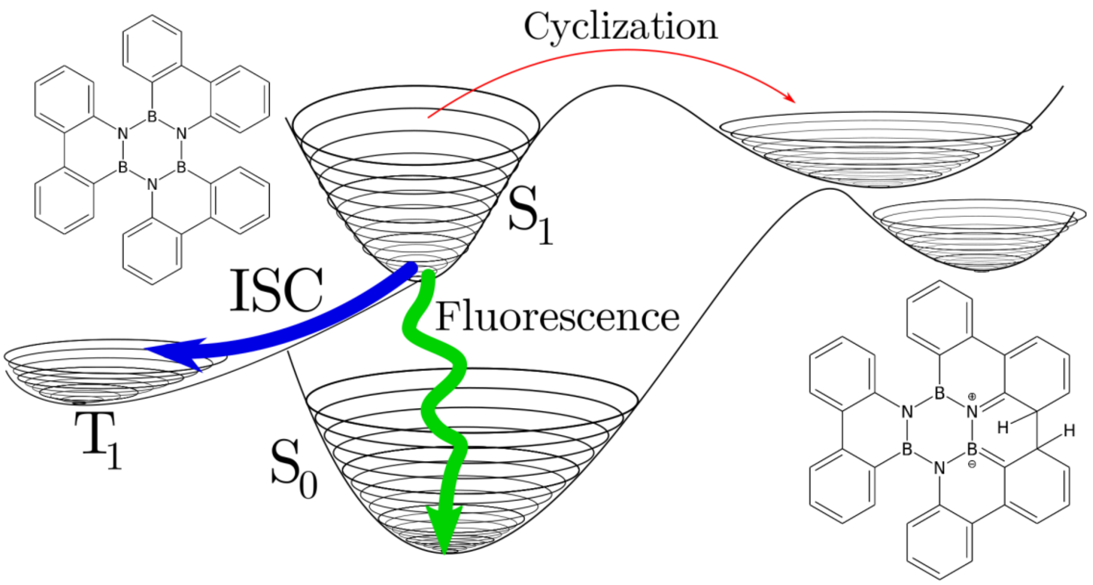

**Figure 5.0.** Table of contents figure.

## 5.0 Abstract

Boron-nitrogen doping of polyaromatic hydrocarbons (PAH), such as borazine-core hexabenzocoronene (HBC), presents possibilities for tuning the properties of organic electronics and nanographene materials while preserving the structural characteristics of pure hydrocarbons. Previous photochemical studies have demonstrated the extension of a borazine-core PAH network (1,2:3,4:5,6 tris(*o,o'*-biphenylylene) borazine, **1**) by photoinduced cyclodehydrogenation, but also revealed that photochemical synthesis alone cannot be used to prepare BN-doped HBC from this precursor. We present steady-state and fs-to-μs time-resolved spectroscopic characterization of the photophysics of **1** and a related borazine-core PAH in order to identify competing excited-state relaxation pathways that impact the efficacy of bond formation by photocyclization of BN-doped structures. Ultrafast measurements reveal sub-ps internal conversion dynamics when both compounds are excited at high but not low energies (266 vs. 320-330 nm), supporting their Kasha-rule emission behavior. Time-resolved spectra evolve on timescales consistent with the fluorescence $S_1$ lifetimes (1-3 ns) to a terminal spectrum that persists onto μs timescales. Ns-resolved oxygen-quenching reveals efficient triplet formation. Fluorescence and triplet quantum yields indicate that photochemical bond formation is a minor channel at best in the relaxation of **1**, whereas highly efficient fluorescence and triplet formation appear to result in negligible bond formation via photoexcitation of more extended borazine-core networks.

## 5.1 Introduction

Large polycyclic aromatic hydrocarbons (PAHs) and their 1- and 2D assemblies (including "nanographenes") have received considerable attention as components for organic electronics[1-3] – including, but not limited to, organic photovoltaics (OPV), organic field-effect transistors (OFET), and organic light-emitting diodes (OLED). Judicious atom-specific doping of pure hydrocarbon structures with boron and nitrogen presents the means to tune (generally increase) the HOMO-LUMO gap in these materials,[4-6] while at the same time preserving structural characteristics – as, for example, when a CC unit is replaced with an isoelectronic BN pair. BN-doping also presents a means for incorporating intramolecular charge polarization that can imbue enhanced nonlinear optical properties or be used to control intermolecular packing.[7-9] Hexabenzocoronene (HBC) has remained a PAH target of particular interest, as selectively alkylated HBC can undergo a temperature-controlled phase change to a liquid crystal that forms conducting columns, i.e. nanowires.[1] Consequently an HBC analog with a borazine core has therefore remained an attractive target for BN doping strategies,[6, 10-12] with recent studies demonstrating efficient preparation of ordered 2D nanographene materials built from borazine-core HBC via surface-assisted catalysis (SAC) on Ag(111) substrates.[13]

Various approaches have been explored for preparing BN-doped polyaromatic structures in solution, beginning with the synthetic inclusion of BN in pure-carbon frameworks[2, 4, 5, 12, 14-17] and extending to thermal[11, 13] and photochemical[10] treatments of BN-doped precursors, such as those presented in Scheme 5.1, to yield larger polycycles. Notably, recent work has demonstrated that Scholl reactions give rise to C-C coupling within and between BN-doped PAHs,[6] pressing the need for alternative pathways for inducing purely intramolecular carbon-carbon bond formation in the preparation of borazine-core HBC. Given the structural similarities of pure PAHs and their BN-doped analogs, Bettinger proposed that photoinduced electrocyclization is a potential route for synthesizing borazine-core PAHs from simpler BN-doped precursors,[10] demonstrating that the near-UV irradiation of 1,2:3,4:5,6 tris(*o,o'*-biphenylylene) borazine (Scheme 5.1,

**1**) in the presence of THF and $I_2$ results in cyclodehydrogenation to yield compound **3.** It was hypothesized that the reaction mechanism proceeds via conrotatory electrocyclization from the $S_1$ state of **1** to a dihydro structure **2** that is the anticipated intermediate of photoinduced cyclodehydrogenation;[18, 19] by contrast, **3** could not be produced by triplet energy transfer to **1**.[10] Curiously, no further cyclization could be induced from **3**. Fusion of a single cycle within a larger structure is not unusual, with photocyclization reactions resulting in selective or incomplete bond formation reactions.[18] Hence, these observations imply limitations for bond formation from the photoprepared excited state of **3** and raises questions about the photophysical relaxation and photochemical reaction mechanisms of these BN-doped structures.

The goal of this work is to assess the nature of photophysical processes that induce or stifle bond formation in these compounds via electrocyclization. Specifically we have utilized a suite of transient spectroscopies resolved on timescales ranging from femtoseconds to microseconds and have also quantified fluorescence and triplet-formation yields in order to build a comprehensive picture of the photophysics of **1** and **3.** These measurements have been conducted with solution conditions that do not lead to dehydrogenation so that it may be possible to capture signatures of intermediate structures such as **2**. The photophysics of BN-doped structures have only been explored modestly, with few examples existing in the literature.[15, 20-22] Thus an examination of the photophysics of BN-doped PAHs provides insights into how they differ from their pure hydrocarbon analogs as well as what fundamental limitations exist for using photocyclization to induce selective bond formation in the preparation of novel polycycles.

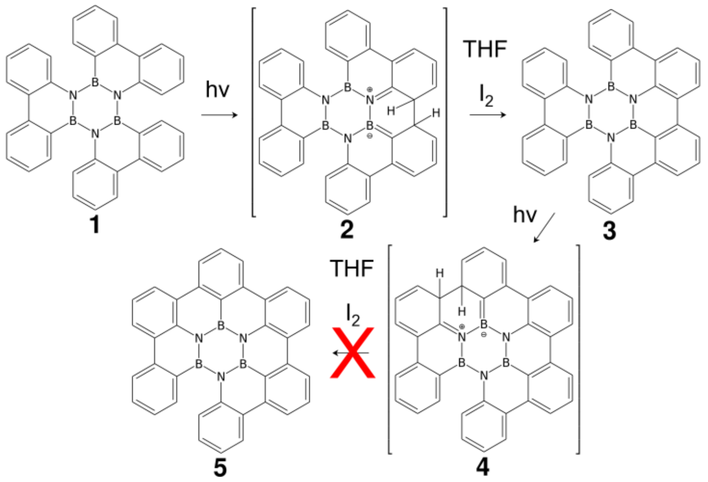

**Scheme 5.1** Photoinduced cyclodehydrogenation of BN-doped polycycles. Compound **1** (1,2:3,4:5,6 tris(*o,o'*-biphenylylene) borazine) yields **3** via the proposed intermediate **2**. In contrast, **5** cannot be produced from **3** under the same reaction conditions.

## 5.2 Methods

### *5.2.1 Sample preparation*

**1** and **3** were synthesized according to literature procedures.[10, 17] Tetrahydrofuran (THF, anhydrous & inhibitor-free, Sigma 401757) and cyclohexane (Acros, 167740010) were dried by storing solvent under nitrogen with pre-dried 3Å molecular sieves (Sigma 334286) at a 1:5 volume ratio of sieves to solvent for at least 24 hours.[23] Benzophenone (Sigma B9300), naphthalene (Sigma 185604), biphenyl (Sigma B34656) and benzene (Sigma 401765) were purchased from a commercial source and used "as-is."

Sample solutions were prepared entirely under nitrogen: solute solids were transferred to a Schlenk flask in a glove bag, with dry solvent added to achieve a 3 mM concentration *via* cannula transfer once the flask was connected to an air-free line. The sample flask was then sealed and sonicated for 15 minutes. Solutions were then degassed by a minimum of 3 Freeze-Pump-Thaw cycles and backfilled with nitrogen. For measurements with aerated solutions, samples were pressurized with dry compressed air and shaken vigorously. The oxygen concentration was assumed to be air saturated and taken from a literature source as 1.81 mM in THF.[24] Control experiments were also conducted to determine the impact of solute hydrolysis on transient spectral measurements and utilized solutions made with 95:5 THF:$H_2O$ by volume that were heated gently (~40 °C), sonicated for 30 minutes, and degassed with nitrogen. All sample solutions were ultimately transferred to the 25 mL reservoir of a custom schlenk flask, a sidearm of which is fused to a 5 mm path-length cuvette (a picture of the flask is shown in Figure A3.1). Solutions were stirred continuously during irradiation using a micro-stirbar (Sigma). The irradiated solution was periodically removed through a PTFE-lined septum and fresh (i.e. unexposed) solution within the flask reservoir was used to recharge the cuvette.

### *5.2.2 Steady-state spectroscopy, fluorescence quantum yields and lifetime determinations*

Steady-state absorption spectra of these samples were collected using a diode array spectrometer with a fiber-coupled lamp (Stellarnet). Steady-state emission was measured with a Perkin Elmer LS-5B fluorometer. Fluorescence quantum yields were determined using literature procedures.[25] Measurements used identical experimental parameters, including excitation wavelength (270 nm), solvent (cyclohexane), slit widths, emission spectral range, $N_2$ sparging times (20 minutes) and sample cells (1 cm path length), for all samples and standards (napthalene and biphenyl). Samples with absorbances less than 0.1 OD at 270 nm were used in order to avoid internal filter effects. Several pairs of absorbance and fluorescence measurements were performed for each sample and standard at various concentrations in order to determine quantum yields relative to a standard by a least squares fitting procedure (see appendix 3 and Figure A3.2 for details).

Fluorescence lifetimes were determined using time-correlated single-photon counting (TCSPC, PTI Quantmaster). Samples were excited with a fast LED (340 nm, ~1 ns FWHM) and emission was monitored at 375 nm. TCSPC lifetimes were determined by fitting data to the convolution of the temporal instrument response, determined from a LUDOX scattering solution (Sigma), with single or multiple exponential decay(s) using MATLAB. All measurements were performed in degassed cyclohexane and a 1 cm fluorescence cuvette.

### *5.2.3 Transient spectroscopies*

Our experimental setups for fs, ns, and μs transient absorption spectroscopies have been described in detail previously.[26, 27] Briefly, a regeneratively amplified Ti:sapphire laser (Coherent Legend Elite, 800 nm, 35 fs) was used to generate excitation pulses at 266 nm by a doubling-mixing scheme or at 320-360 nm via optical parametric amplification (Coherent OPerA Solo). For fs-TAS measurements a few nJ of the laser fundamental was focused into a 2 mm $CaF_2$ plate to generate a supercontinuum spanning the near-UV to near-IR (350-900 nm); this continuum probe was refocused at the sample using a parabolic mirror and polarized at magic angle relative to the pump using a wire-grid polarizer immediately before the sample. The probe source for ns TAS measurements was a 405 nm (Thorlabs L405P20) or 450 nm (Osram PL450B) laser diode driven by a pulsed laser diode driver (Highland Technologies T165) triggered electronically by the amplifier's signal delay generator (Coherent SDG Elite). µs-TAS measurements utilized a white-light LED (Thorlabs LEDWE-15, 410-700 nm) driven by a signal delay generator (Berkeley Nucleonics BNC 555) and amplified with transistors (Central Semiconductor 2N2222A) that allows for variable driving pulse widths and voltages. The LED output was masked with an iris to create an approximate point source, with subsequent collimation with a 75 mm convex lens; the probe beam was then focused to a 1-2 mm spot size at the sample with a parabolic mirror.

Light detection for fs and ns TA experiments utilized NMOS diode arrays (Hamamatsu S3901-256Q). The probing continuum for fs-TAS was dispersed onto the arrays with a Fused-Silica (CVI) or NSF-11 (Edmund Optics) equilateral prism for broadband detection. For single-wavelength detection (ns-TA) monochromatic probe light from a pulsed LED was focused onto the detector array using a cylindrical lens, with diode signals integrated across the linear array. For µs TA measurements a 0.3 m spectrograph (Acton-2360, Princeton Instruments) was used to disperse the probe (whitelight LED emission) onto a CCD camera (Pixis-100BR, Princeton Instruments). Optical time delay between the pump and probe pulses was controlled with a motorized translation stage (Newport ILS250CCL) for fs time-resolved measurements, while ns and µs time delays were achieved electronically. The time resolution for the fs, ns, and µs experiments were approximately 200 fs, 1 ns and 0.3 µs, respectively. All transient measurements were actively corrected for fluorescence emission using a four-phase acquisition sequence realized by chopping both the excitation and probe beams.[28] Data acquisition was performed using a home-built LabVIEW program.

### *5.2.4 Determination of triplet yield and extinction coefficient*

The quantum yield for triplet formation for **1** was determined using literature procedures.[29] Quantification of quantum yields for triplet formation ($\Phi_T^X$) first requires determination of the extinction coefficient ($\varepsilon_X$) of the sample relative to that of a reference standard; both quantities are used to determine the relative triplet yields from the triplet absorption intensities of the unknown and reference standard under identical excitation conditions. This procedure therefore requires a reference standard with both well-known triplet yield ($\Phi_T^{Ref}$) and extinction coefficient ($\varepsilon_{Ref}$). Benzophenone in benzene was used as the reference standard because it exhibits near unity triplet yield upon photoexcitation, possibility for triplet-energy transfer to **1**, and non-overlapping steady-state singlet and distinguishable triplet absorption spectra from those of **1**. The triplet quantum yield or extinction coefficient of **3** could not be determined due to complete overlap of its ground-state absorption spectrum with that of the reference standard, such that the triplet energy-transfer mechanism is obscured by triplet formation via direct excitation of **3**.

Two solutions of 100 mM benzophenone with and without 0.1 mM of compound **1** in benzene were prepared and degassed *via* sparging with $N_2$ for 45 minutes and were subsequently photo-excited at 360 nm in order to resonantly excite only benzophenone. Transient absorption spectra were captured on μs timescales in order to determine the triplet extinction coefficient of **1** according to Equation 5.1 (here $P_{TD}$ and $P_{tr}$ are terms for kinetic correction, see SI for definitions and details).

$$\varepsilon_X = \varepsilon_{Ref} \frac{\Delta OD_X \; P_{TD}}{\Delta OD_{Ref} \; P_{tr}} \tag{5.1}$$

The triplet yield was then determined from comparisons of transient triplet spectra measured with a 1 mM solution of benzophenone and a 1 mM solution of **1** photoexcited at 340 nm under identical experimental (i.e. optical) conditions. The triplet absorption spectra, relative extinction coefficients, and known triplet yield of benzophenone were used to calculate the triplet yield via Equation 5.2.

$$\Phi_T^X = \Phi_T^{Ref} \frac{\Delta OD_X}{\Delta OD_{Ref}} \frac{\varepsilon_{Ref}}{\varepsilon_X} \tag{5.2}$$

### *5.2.5 Matrix isolation experiments*

Matrix experiments were carried out according to standard techniques[30] with a Sumitomo CKW-21 or a CTI-Cryogenics 8200 closed-cycle helium cryostat. Compound **1** was sublimed out of a quartz tube, which was resistively heated by Ta wire coiled around it, onto a CsI (IR) or a sapphire (UV/vis) window with large excess of argon (Westfalen, 99.9999 %). The windows were kept at 30 K during deposition by resistive heating using a temperature controller. Irradiations were carried out at the base temperature of the systems (4 K for IR, and 8 K for UV-Vis detection) with a high-pressure mercury lamp with wavelength selection by dichroic mirrors (350-450 nm and 280-400 nm) and appropriate cut-off filters or with a low-pressure mercury lamp (254 nm). Infrared spectra were recorded on a Bruker Vertex 70 and UV-Vis spectra on a Lambda 1050 spectrometer.

### *5.2.6 Computational methods*

Geometry optimizations were performed without symmetry constraints using the hybrid density functional B3LYP[31, 32] as implemented[33] in Gaussian 09[34] in conjunction with the 6-31G* basis set.[35] Computation of analytic harmonic vibrational frequencies confirmed that minima and transition states have no or only one imaginary vibrational frequency. The harmonic vibrational frequencies were employed in the standard approximation for obtaining Gibbs free energies at 298.15 K.

## 5.3 Results

### *5.3.1. UV-Vis and fluorescence spectroscopy*

Figure 5.1 presents the steady-state absorption and fluorescence spectra (solid and dashed lines, respectively) of compounds **1** (black) and **3** (red). The absorption spectra of both compounds are comprised of multiple overlapping features spanning the near-UV region; the absorption of **3** is slightly red-shifted compared to that of **1**. Fluorescence from both compounds exhibit vibronic structure, which is more distinct for **3**. Fluorescence excitation scans reproduce the shape of the UV-Vis spectra,[10] indicating that all optically accessible states emit from the same electronic state, presumably $S_1$.

Time-resolved emission decays for these compounds (340-nm excitation) are plotted in Figure 5.2 and have been fitted with exponential decay functions convoluted with the temporal instrument response. Table 5.1 presents the fitted fluorescence decay lifetimes and experimentally determined fluorescence quantum yields. Compound **3** exhibits a substantially larger fluorescence quantum yield ($\Phi_{Fl}$) than **1**, which explains in part the longer fluorescence lifetime of the former. We note that the fluorescence decay for compound **1** dissolved in cyclohexane is best fit by including a minor secondary decay component with a longer time constant.

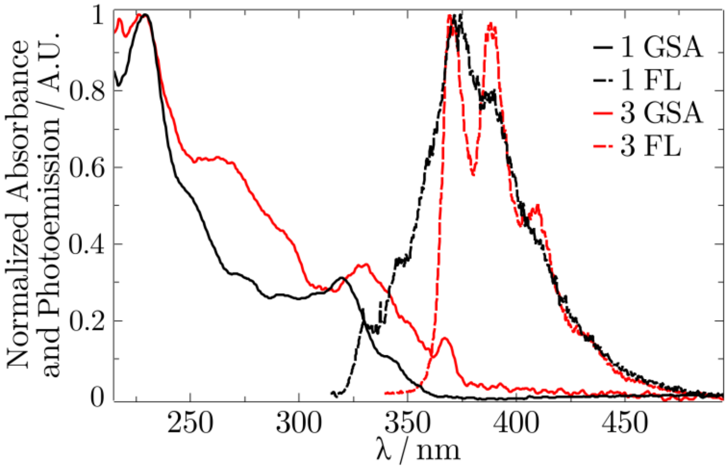

**Figure 5.1.** Steady-state ground-state absorption (GSA, solid lines) and fluorescence spectra (FL, dashed lines) of compounds **1** (black lines) and **3** (red lines) in cyclohexane.

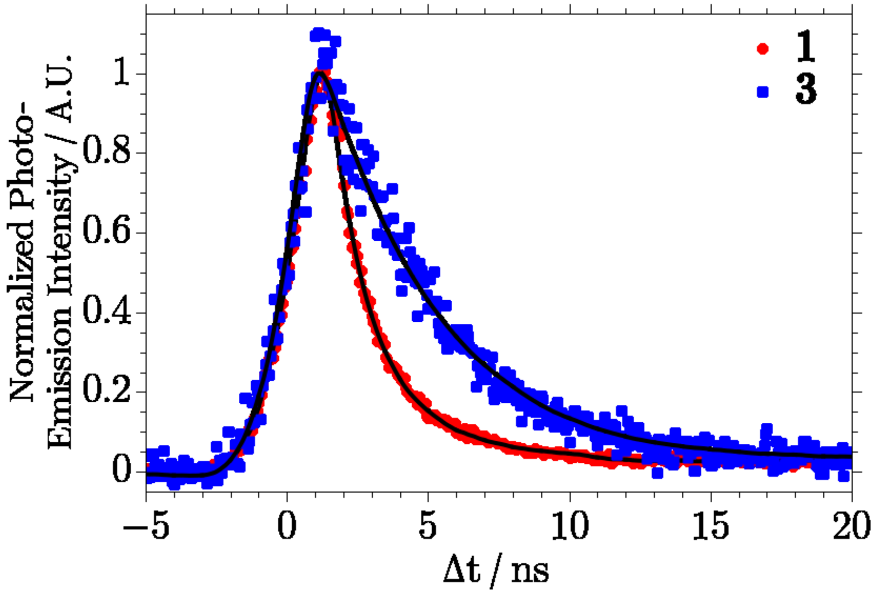

**Figure 5.2.** Time-resolved emission (375 nm) from **1** (red) and **3** (blue) photoexcited at 340 nm. Data – points ; fits – lines. See Table 5.1 for fitted timescales.

**Table 5.1** Fluorescence yields and lifetimes of **1** and **3** in cyclohexane (unless otherwise noted).

| | $\Phi_{fl}$[a] | $\tau_{fl}^{TCSPC}$ (ns)[c] | $k_r$ ($ns^{-1}$)[d] | $k_{nr}$ ($ns^{-1}$)[d] |
|---|---|---|---|---|
| **1** | 0.28 (0.18); 0.09[b] | 1.29 (95%), 10.98 (5%) | 0.217 | 0.5582 |
| **3** | 0.74 (0.43) | 3.87 | 0.191 | 0.0672 |

[a] – Numbers in parentheses denote $\Phi_{Fl}$ for aerated solutions

[b] – Measured in benzene

[c] – Numbers in parentheses denote the relative amplitudes for components of biexponential fit to the fluorescence decay of **1**

[d] – Radiative ($k_r$) and nonradiative ($k_{nr}$) decay rates were determined from quantum yields and fluorescence lifetimes, i.e. $\Phi_{fl} = k_r \tau_{fl}^{TCSPC}$ and $\tau_{fl}^{TCSPC} = 1 / k_r + k_{nr}$.

### *5.3.2. Transient absorption spectroscopy*

Femtosecond TA was performed on **1** with both 266 and 320 nm photoexcitation. Data obtained following excitation at 266 nm is presented in Figure 5.3a. Identical spectral dynamics were observed for both excitation energies for time delays beyond 2 ps; data obtained with 320-nm excitation is presented in Figure A3.3a. At delays < 2 ps a short-lived transient feature centered at ~420 nm appears only with 266-nm excitation; this feature decays rapidly, and we therefore attribute it to excited-state absorption from a high-lying state prepared directly by photoexcitation (e.g. $S_N$ state).[36] Fitting an exponential decay to the transient absorption intensity observed at 700 nm yields a lifetime of 1.82 ns – roughly in agreement with the TCSPC lifetime for this compound (Table 5.1) and signifying that the broad intensity appearing above 500 nm on picosecond to nanosecond timescales arises predominantly from $S_1$ absorption. The spectral evolution presented in Figure 5.3a illustrates that $S_1$ decay results in a persistent absorption feature on nanosecond timescales with peak wavelength near 400 nm that corresponds with a metastable state or species. The complete spectral evolution was fit to a simple kinetic model ($S_N \rightarrow S_1 \rightarrow T_1$/metastable product) by global analysis, which generated a 470 fs lifetime for the initial ultrafast decay of the photoprepared state and a ~700 ps time constant for the appearance of this final spectrum; species associated spectra obtained are presented in Figure 5.3b. Data collected with 320-nm excitation were likewise analyzed with a two-state kinetic interconversion ($S_1 \rightarrow T_1$/metastable product), yielding species associated spectra similar to the $S_1$ and $T_1$/metastable product spectra plotted in Figure 5.3b (Figure A3.3b). Additionally, μs broadband TA spectra presented in Figures 5.4a and A3.4 collected under oxygen-free conditions reveal that the final spectrum observed by fs-TAS persists onto the μs timescale and does not undergo any further spectral evolution within the wavelength range explored in this study (425-700 nm).

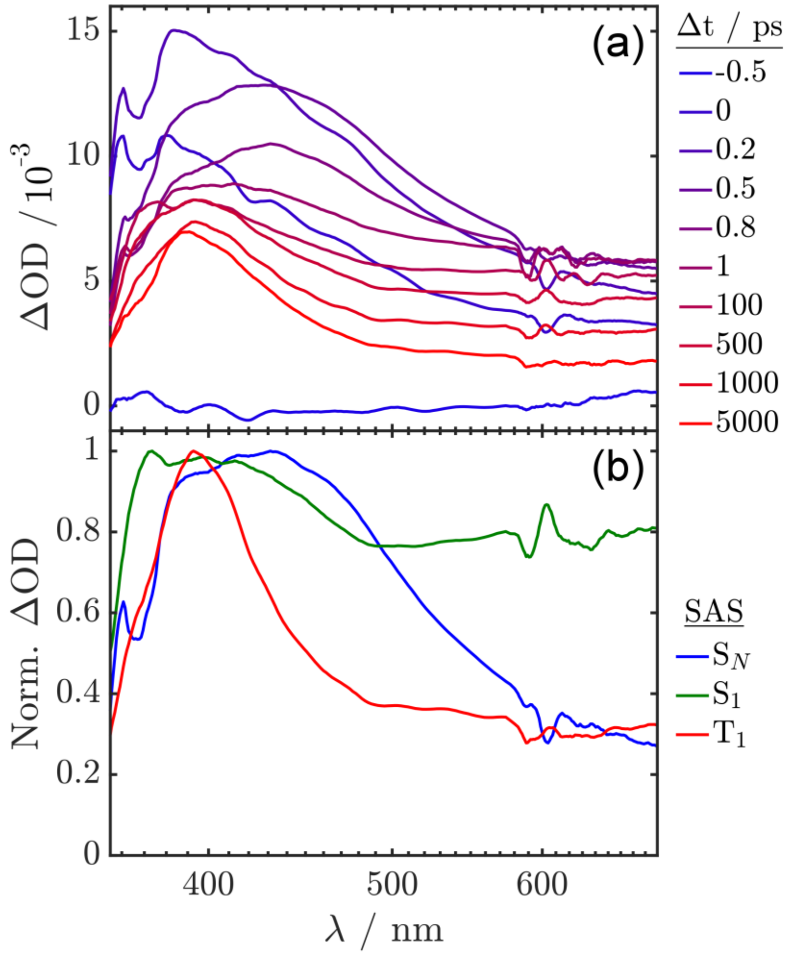

**Figure 5.3.** (a) fs-TAS of **1** in THF solution following 266 nm photoexcitation. (b) Species associated spectra (SAS) obtained via global analysis of transient data using a sequential 3-component model ($S_N$ → $S_1$ → $T_1$/metastable product).

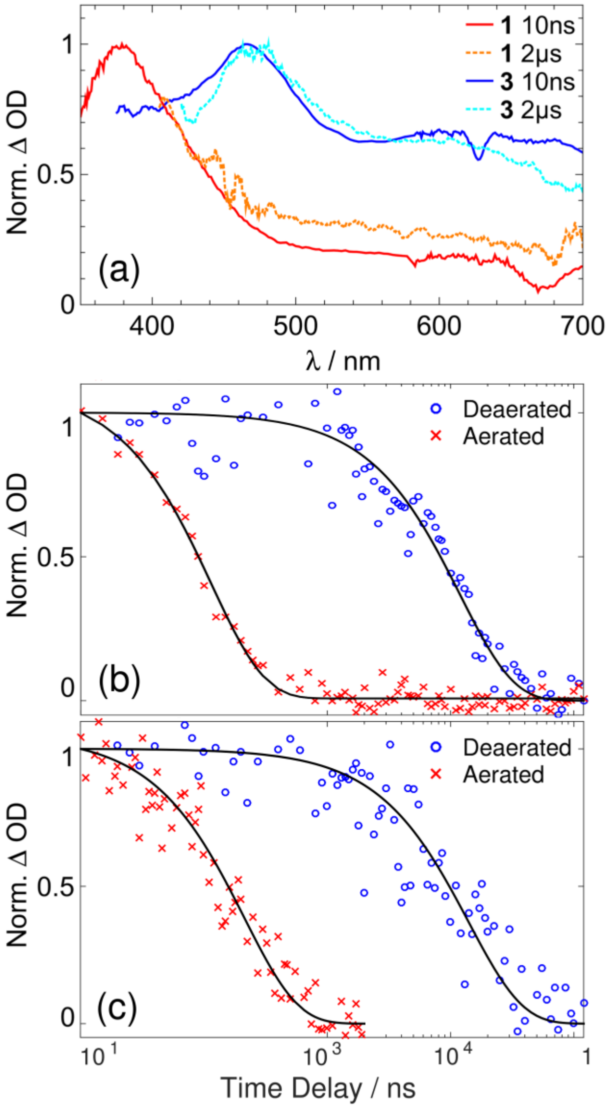

**Figure 5.4.** Nanosecond and microsecond resolved transient absorption of **1** and **3**. (a) Comparison of broadband-TA spectra of **1** and **3** collected at 10 ns and 2 μs; a full set of μs-TAS data at various time delays is presented in Figure A3.4. (b) ns-TA of **1** in THF solution, under aerated (red x's) or deaerated (blue circles) conditions with 266 nm photoexcitation and probed at 405 nm (exponential fits in black). (c) ns-TA of **3** in THF under aerated (red x's) or deaerated (blue circles) conditions following 266 nm photoexcitation and probed at 450nm (exponential fits in black).

Given the reported photochemistry of **1**,[10] a definitive assignment of this long-lived absorption feature to a triplet state or metastable product is critical. We investigated this by performing ns-TAS under both aerated and deaerated conditions to obtain rates for oxygen quenching of the corresponding metastable species. Figure 5.4b presents the ns-TA decay of **1** under aerated and deaerated conditions following 266 nm photoexcitation and probed with a 405 nm laser diode (complementary measurements were performed with 320 and 330 nm excitation for **1** and **3**, respectively, and are presented in Figure A3.5). Table 5.2 lists lifetimes obtained from fits of these traces and reveals a substantial (~100 fold) decrease in transient lifetime in the presence of oxygen. The typical oxygen quenching rates for triplet and singlet biradicals are ~5 and 0.01-1 $M^{-1}$ $ns^{-1}$, respectively, such that the determined quenching rate ($k_Q$) for **1** indicates formation of a triplet state.[37] Notably, dehydrogenation of cyclized intermediates through reaction with oxygen generally occurs on timescales ranging from seconds to minutes.[38]

**Table 5.2** ns-TAS decay timescales for **1** and **3** and oxygen quenching rates.

| Molecule | $\lambda_{Exc}$ / nm | $\tau_{air}$ / ns | $\tau$ / ns | $k_Q$ / ns$^{-1}$ M$^{-1a}$ |
|---|---|---|---|---|
| **3** | 266 | 205 | 16286 | 2.41 |
|  | 330 | 130 | 17466 | 3.81 |
| **1** | 266 | 137 | 13409 | 3.62 |
|  | 320 | 116 | 10210 | 4.27 |

[a] – Dissolved oxygen concentration was 1.81 mM[24]

The same sets of time-resolved experiments and analyses were performed with samples of **3** in order to compare with the photophysical properties of **1**. fs-TA spectra for **3** following photoexcitation with 266 nm (Figure 5.5) reveal an ultrafast decay of a transient feature centered at 420 nm that is absent with 330 nm photoexcitation (Figure A3.6a). This indicates that the initial excitation prepares a high-lying electronic state that rapidly internally converts to a lower level, similar to the photophysics of **1**. On longer timescales, transient absorption at longer wavelengths decays on a timescale of few nanoseconds; given the consistency with $S_1$ decay observed through TCSPC fluorescence measurements (3.4 ns at 330 nm excitation), we attribute this signal to $S_1$ absorption. The spectral kinetics observed by fs-TAS fit by global analysis to a 3 state sequential kinetic model, $S_2 \rightarrow S_1 \rightarrow T_1$/metastable product, that resulted in the 450 fs internal conversion lifetime and a 3.7 ns lifetime for the $S_1$ decay (similar to the TCSPC results). µs-TA was performed to investigate spectral dynamics on longer timescales (Figure 5.4a and A3.4b), revealing the appearance and decay of the same absorption band ($\lambda_{max}$=475 nm) observed in fs-TA experiments, with no further absorption features observed within the spectral window of the probe.

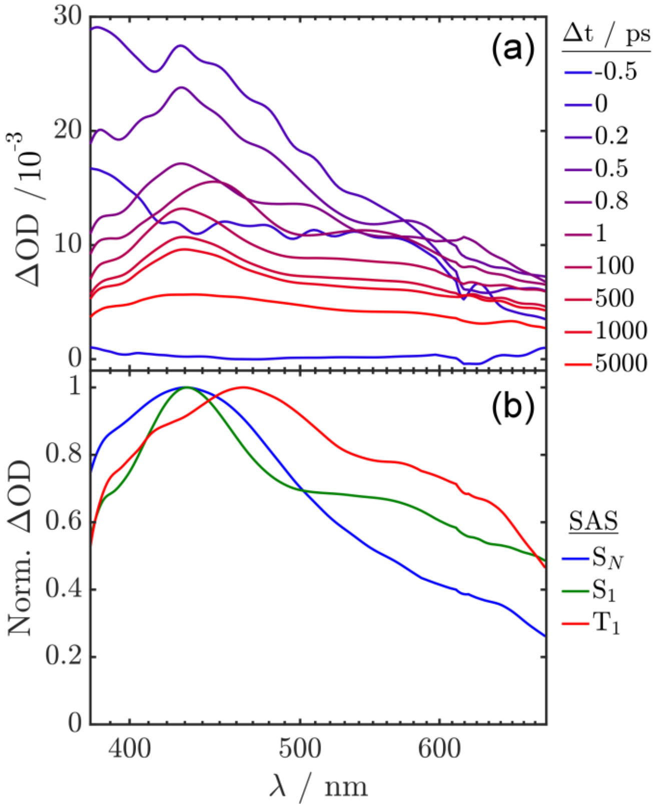

**Figure 5.5** (a) fs-TA of **3** in THF following photoexcitation with 266 nm. (b) Spectral results from global analysis using a sequential 3-component model ($S_N \rightarrow S_1 \rightarrow T_1$/metastable product) with species associated spectra (SAS) shown for each component.

Ns-TA measurements of **3** under aerated and deaerated conditions (Figures 5.4c and A3.5b) likewise revealed a large decrease in transient lifetime in the presence of oxygen. Table 5.2 illustrates that **3** has very similar quenching kinetics to that of **1**, and therefore we likewise assign the long-lived transient absorption at 475 nm to a metastable triplet state.

Finally, various control experiments were performed to identify any possible hydrolysis products that may form due to the highly reactive nature of B-N compounds in $H_2O$, the presence of which would result in contamination of our experiments. Following the addition of water and gentle heating, we performed both fs and μs TA on **1** and **3.** These experiments produced unique spectral signatures and kinetics that did not match those obtained from experiments with "dry" solutions (see Figure A3.7), thereby confirming that photophysical data is representative of the title compounds.

### *5.3.3 Triplet yield determination*

The triplet quantum yield ($\Phi_T$) of **1** was determined in order to infer the relative magnitude of the quantum yield for cyclization (and other nonradiative relaxation processes). A prerequisite for determining $\Phi_T$ is to quantify the extinction coefficient ($\varepsilon$) of the triplet state, which was determined using the energy-transfer method with benzophenone as the triplet donor using Equation 5.1.[29] Following determination of the extinction coefficient, the time dependence for the absorption intensity of a sample of pure **1** and benzophenone were determined separately under identical experimental conditions in order to calculate the triplet yield of **1** using Equation 5.2. Experimentally determined values for $\varepsilon$, $\Phi_T$, and kinetic correction factors are tabulated in Table 5.3. Microsecond TA data (Figure A3.8) and details on the analysis used to calculate kinetic correction factors for this determination of $\varepsilon$ are provided in the SI.

**Table 5.3** Triplet extinction coefficient and quantum yield for **1** obtained by energy-transfer method with benzophenone in benzene as the triplet sensitizer.

| $\varepsilon$ ($M^{-1}$ $cm^{-1}$)[a] | $\Phi_T$[b] | $P_{TD}$[c] | $P_{tr}$[c] |
|---|---|---|---|
| 3383 ± 465 | 0.94 ± 0.18 | 2.067 | 0.256 |

[a] – 360 nm excitation was used to determine molar extinction coefficient. Error was determined by error propagation from literature $\varepsilon$ of benzophenone.[29]

[b] – 340 nm excitation was used to determine quantum yields by direct excitation of benzophenone and **1**. Error was determined by error propagation from $\varepsilon$ of **1**.

[c] – Kinetic correction factors explained in the SI.

### *5.3.4 Matrix isolation experiments*

Photoirradiation of compound **1** isolated in an argon matrix with light of varying wavelengths (254 nm, 350-450 nm) and extended periods of time (up to 3 hours) was monitored by IR and UV-Vis-NIR spectroscopy at 4 K and 8 K, respectively. No new signals could be detected by either spectroscopic technique, indicating that the photoisomerization did not proceed in detectable amounts. We noticed, however, an intense turquoise phosphorescence of the sample after photoexcitation. The emission was detectable with the naked eye in a darkened laboratory and lasted for roughly 5 seconds. The emission wavelength is roughly consistent with the $T_1$-$S_0$ gap calculated from the $T_1$

optimized geometry at the B3LYP/6-31G* (2.37 eV, 523 nm). These observations indicate that at cryogenic temperatures triplet formation and phosphorescence rather than photoisomerization is the dominating decay channel of **1** after photoexcitation.

### *5.3.5 Computational investigations*

Knowledge of the barriers for formation of **2** or **4** from **1** or **3** on the $S_1$ potential energy surface (PES) as well as those for *thermal* cycloreversion of the photoproducts to the precursor molecules on the $S_0$ PES are important for understanding observed photochemical behaviors. As the barriers for photoisomerization of *cis*-stilbene (CS) to 4a,4b-dihydrophenanthrene (DHP) and its thermal cycloreversion have been determined experimentally,[39] we used this system to gauge the reliability of the B3LYP/6-31G* level of theory that was necessary in view of the size of systems **1**-**4**.

On the $S_0$ PES a transition state could be located for the cycloreversion of DHP to CS using a spin-unrestricted treatment (UB3LYP); see Figure A3.9 for minimum-energy DHP and transition-state structures. The free energy of activation, $\Delta G^{\ddagger}_{298.15}$ = 17.2 kcal mol$^{-1}$, computed for this process agrees quite well with the barrier of 17.5 kcal mol$^{-1}$ obtained experimentally from an Arrhenius treatment.[39] This suggests that the UB3LYP/6-31G* treatment can reasonably describe the barrier heights for the electrocyclic ring opening reaction.

The geometries of the dihydro compounds **2** and **4** were optimized using a spin-unrestricted Kohn-Sham treatment and are shown in Figure 5.6. The finding of a spin-unrestricted KS solution for **2** and **4** indicates that the HOMO-LUMO gap is rather small, and indeed, the computed singlet-triplet energy splitting of **2** is only 0.1 kcal mol$^{-1}$ in favor of the singlet state (UB3LYP/6-31G*). Almost identical singlet-triplet energy splitting was also computed for the dihydro species **4**. The barriers for thermal ring opening of **2** to **1** or of **4** to **3** are quite low, $\Delta G^{\ddagger}_{298.15}$ are 1.3 kcal $mol^{-1}$, and 1.5 kcal $mol^{-1}$, respectively, at UB3LYP/6-31G*. These computations show that the photoproducts correspond to rather shallow minima on their respective $S_0$ potential energy surfaces. The fact that no cyclized intermediate can be trapped cryogenically at 4 K suggests that these barriers may actually be much lower than predicted computationally or that the intermediate is not formed at all.

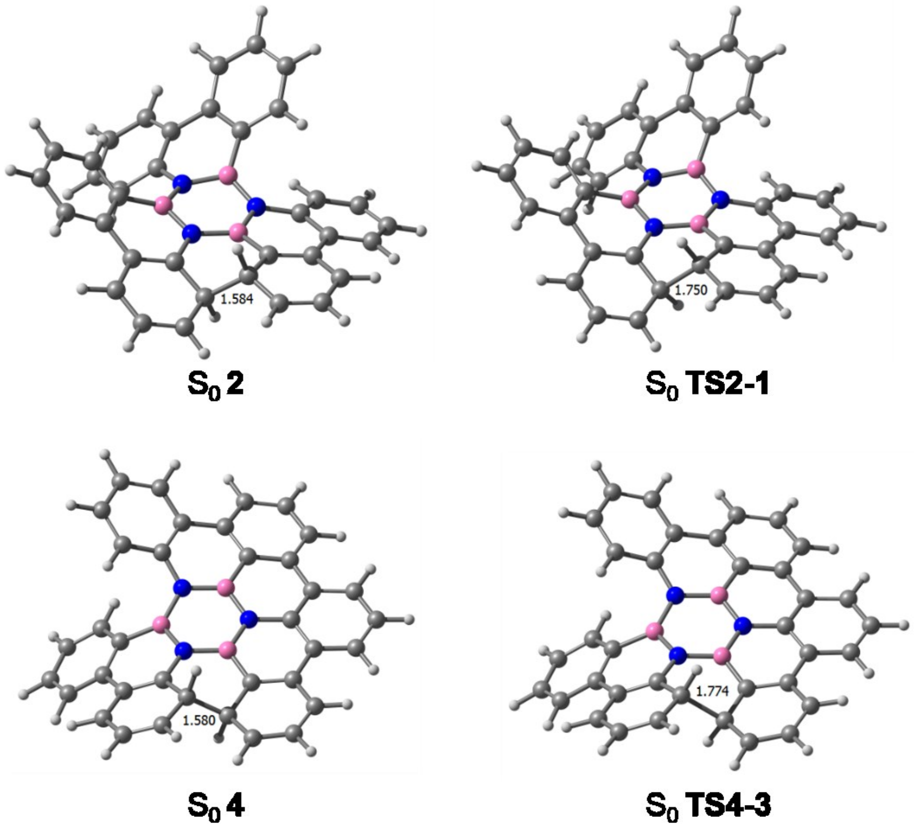

$S_0$ **2**

$S_0$ **TS2-1**

$S_0$ **4**

$S_0$ **TS4-3**

**Figure 5.6.** Structures of the cyclized products **2** and **4** and the transition states for cycloreversion on the $S_0$ potential energy surface computed at the UB3LYP/6-31G* level of theory. The inter-ring C-C bond length is given in Å.

## 5.4 Discussion

Observations from the photophysical characterization of **1** and **3** can be summarized as follows: fs-TA measurements reveal sub-ps internal conversion dynamics from the photoprepared state ($S_N \rightarrow S_1$) when **1** and **3** are excited at high but not low energies (266 vs. 320/330 nm), consistent with the Kasha-rule emission behavior observed. Time-resolved spectral evolution on the timescale of a few nanoseconds is similar at the two excitation wavelengths for each compound and is consistent with the fluorescence lifetimes measured by TCSPC. Transient spectra evolve to a terminal feature that persists into the microsecond time regime and that is efficiently quenched by oxygen, indicating that direct excitation gives rise to efficient triplet formation ($S_1 \rightarrow T_1$); this is consistent with observation of phosphorescence from **1** in cryogenic matrix isolation studies. However, neither time-resolved nor cryogenic studies reveal signatures of cyclized structures. Nonetheless, photochemical oxidation of **1** suggests the possibility for reactive dynamics from $S_1$ via 6π electrocyclization.

A general set of possible excited-state relaxation mechanisms for UV-excited **1** and **3** is summarized with Equations 5.3a-h.

$$S_N \xrightarrow{k_{IC1}} S_1 \tag{5.3a}$$

$$S_1 \xrightarrow{k_{rad1}} S_0 \tag{5.3b}$$

$$S_1 \xrightarrow{k_{ISC1}} T_1 \tag{5.3c}$$

$$S_1 \xrightarrow{k^S_{cyclize}} S_0(\text{Product}) \tag{5.3d}$$

$$S_1 \xrightarrow{k_{IC2}} S_0(\text{Reactant}) \tag{5.3e}$$

$$T_1 \xrightarrow{k_{ISC2}} S_0 \text{ (Reactant)} \tag{5.3f}$$

$$T_1 \xrightarrow{k^T_{cyclize}} S_0 \text{ (Product)} \tag{5.3g}$$

$$T_1 \xrightarrow{k_{rad2}} S_0 \text{ (Reactant)} \tag{5.3h}$$

Our measurements provide direct signatures for pathways 3a-3c for both compounds; rates and quantum yields for these processes extracted from our various measurements are presented for **1** and **3** in Tables 5.4 and 5.5, respectively. Importantly, we find that the photophysical and photochemical deactivation of photoprepared $S_1$ state of both compounds occurs predominantly via radiative decay and intersystem crossing.

**Table 5.4** Summary of photophysical processes observed for **1** at 298 K.

| Solvent | $\tau_{IC1}^{Exp}$ (ps) | $\tau_{S1}^{Exp}$ (ns) | $k_{ISC1}$ ($ns^{-1}$) | $k_{rad1}$ ($ns^{-1}$) | $1/\tau_T^{Exp}$ ($\mu s^{-1}$) | $\Phi_{Fl}$ | $\Phi_T$ |
|---|---|---|---|---|---|---|---|
| THF | 0.47[a] | 0.71[a] | - | - | 0.098 | - | - |
| Cyclohexane | - | 1.29[b] | 0.558[c] | 0.217[c] | - | 0.28 | - |
| Benzene | - | - | - | - | - | 0.09<br>±0.01 | 0.94<br>±0.18 |

[a] Global fitting results from fs-TA with 266 nm excitation.

[b] Results from TCSPC with 340 nm excitation.

[c] Assuming $k_{IC2}$ and $\Phi_{IC2}$~0 then $k_{nr} = k_{ISC1}$ (see Table 5.1) .

**Table 5.5** Summary of photophysical processes of **3** at 298 K.

| Solvent | $\tau_{IC1}^{Exp}$ (ps) | $\tau_{S1}^{Exp}$ (ns) | $k_{ISC1}$ ($ns^{-1}$) | $k_{rad1}$ ($ns^{-1}$) | $1/\tau_T^{Exp}$ ($\mu s^{-1}$) | $\Phi_{Fl}$ | $\Phi_T$ |
|---|---|---|---|---|---|---|---|
| THF | 0.45[a] | 3.66[a] | - | - | 0.057 | - | - |
| Cyclohexane | - | 3.87[b] | 0.067[c] | 0.191[c] | - | 0.74 | - |

[a] Global fitting results from fs-TA with 266 nm excitation.

[b] Results from TCSPC with 340 nm excitation.

[c] Assuming $k_{IC2}$ and $\Phi_{IC2}$~0 then $k_{nr} = k_{ISC1}$ (see Table 5.1) .

The dominance of these pathways is consistent with the impact of structural planarity and rigidity on excited-state kinetics and relaxation quantum yields that has considerable precedent in the photochemistry literature.[40] This impact for PAH photophysics, specifically, can be summarized by Ermolaev's rule: for sufficiently rigid molecules with $S_0 \rightarrow S_1$ transitions at wavelengths lower than 670 nm, i.e. most aromatic hydrocarbons, the sum of the fluorescence and triplet quantum yields approach unity ($\Phi_{Fl}+ \Phi_T=1$).[41] The dominance of these pathways given the structures of **1** and **3** and our experimentally determined kinetic rates and quantum yields corroborate this well-known behavior: indeed the sum of the fluorescence and triplet quantum yields for **1** in benzene are within error of unity, such that any other photophysical or photochemical process (e.g. 3d or 3e) is predicted to be a minor pathway at best in competition with deactivation by emission and ISC.

Notably, the fluorescence quantum yield for **3** is three-fold larger than what is measured for **1**. This is also consistent with expectations that fluorescence dominates over intersystem crossing in the excited state deactivation of increasingly rigid and planar molecular structure, as efficient intersystem crossing generally requires the structural flexibility for nuclear dynamics that tend to improve couplings between electronic surfaces.[42] This behavior was most clearly demonstrated previously with the photophysical deactivation of various tethered alkylated biphenyls or para-terphenyls but is also true for other PAHs.[43]

A stated goal of this investigation was to clarify the nature of the photo-induced cyclodehydrogenation of **1** that was hypothesized to proceed through a dihydro structure **2** (Scheme 5.1 and Equation 5.3d), and further to identify photophysical limitations for similar photochemistry for **3**. However, unlike related studies of the photochemical dynamics of aryl ethenes and ortho-arenes,[26, 28, 44-46] our measurements with **1** and **3** do not reveal any direct spectroscopic signatures of a photocyclization intermediate (e.g. **2**) by either time-resolved or cryogenic spectroscopic studies. We also note that the possibility for photochemical reactivity from the triplet state (Equation 5.3g) can be ruled out, as previous studies observed no reaction products in response to triplet-photosensitization with benzophenone;[10] therefore the triplet decay would only be a consequence of intersystem crossing (Equation 5.3f) and phosphorescence (Equation 5.3h), although we only see evidence of the latter at cryogenic temperatures.

Given the magnitudes and errors in fluorescence and triplet quantum yields determined here, nonradiative relaxation pathways between singlet states (Equation 5.3d or 3e) could account for at most ~16% of the initially excited population following excitation in benzene. This assessment is consistent with observations of very small quantum yields for internal conversion ($\Phi_{IC}$~0) for rigid, planar PAHs.[40] We also note that cyclization via nonadiabatic relaxation (Equation 5.3d) should involve branching between the cyclized and reactant state geometries, commonly occurring in ratios ranging 1:2 to 2:1 for related systems and depending on the topography of the conical intersection seam.[47, 48] Thus, we estimate that the quantum yield for electrocyclic bond formation from excited **1** is at most 5-10%, provided that no alternative singlet relaxation pathways exist (e.g. Equation 5.3e), but also that it could be as low as ~1% or less.

Given this low quantum yield, cyclization in **1** must therefore occur via one of two pathways: In one scenario, cyclization occurs via weak wave-packet branching on the $S_1$ surface following excitation, such that the minor cyclization pathway and the dominant nonradiative relaxation pathways are associated with distinct excited-state populations (possibly also involving variations in initial ground-state conformations in solution). Through comparison with similar work with diaryl ethenes and *ortho*-arenes, the former would be expected to give rise to a distinct, observable spectroscopic signature of a cyclized structure that appears on a relatively prompt timescale. [26, 28, 44-46] We do not see such features, but note that these could be difficult to identify in our measurements for a small (few percent or less) quantum yield. Such an observation would be complicated further by the very low calculated activation energies that suggest that cycloreversion likely occurs on timescales comparable with IC and ISC (this is also consistent with observation of no cyclized product from **1** in cryogenic matrix studies).

Alternatively, cyclization may occur in direct kinetic competition against ISC and emission, but subject to a significant barrier on the $S_1$ excited-state surface, such that the bond formation rate is considerably slower than the total $S_1$ relaxation rate. To explore the feasibility of this pathway, we have preliminarily investigated the $S_1$ PES of **1** and **3** at the TD-B3LYP/6-31G* level; when the same level of theory is applied to CS, cyclization is found to be nearly barrierless, $\Delta G^{\ddagger}_{298.15} = 0.6$ kcal mol$^{-1}$, as has been demonstrated experimentally and by other computational studies.[39, 49] Transition states for bond formation on the $S_1$ PES of **1** and **3** exhibit C-C distances of 1.997 Å and 2.008 Å and similar activation barriers ($\Delta G^{\ddagger}_{298.15}$ are 17.2 kcal mol$^{-1}$ for **1** and 18.0 kcal mol$^{-1}$ for **3)**. Although further computational studies will be required to accurately treat the excited states of these large systems and also to locate relevant conical intersections for cyclization, such barriers on the $S_1$ PES are substantial and may explain the inefficiency of **1** and reluctance of **3** to undergo photocyclization. If electrocyclization occurs in (parallel) kinetic competition with the dominant ISC and emission pathways, it can be expected that spectroscopic signatures of a short-lived intermediate **2** would likewise be virtually unobservable. The possible presence of significant barriers on the $S_1$ PES would suggest that an increased photochemical reaction yield might be obtained at elevated temperatures, a possibility we are currently exploring.

## 5.5 Conclusion

Comprehensive photophysical characterization of **1** and **3** provides insight into the impact of reactant structure on the excited-state dynamics associated with the photochemical bond formation within BN-doped PAHs. We find that photoinduced electrocyclization occurs in these systems must occur with only very small quantum yields at best (5-10%) or not at all. The photophysical behaviors of **1** and **3** are consistent with behaviors of similarly rigid PAH structures that are dominated by excited-state deactivation via emission or intersystem crossing, thus giving rise to a relatively weak reactive nature for **1** and no or negligible reactivity for **3**. Nonetheless **1** undergoes cyclodehydrogenation to **3** with reasonable yield in the presence of $I_2$ and near-UV light. Despite the low quantum yield we infer for photoinduced electrocyclization, the multiple excitation-relaxation cycles that occur in a photochemical reactor over the course of a >24 hour period can give rise to a sizable product yield of the dehydrogenated photoproduct. Other photocyclization pathways for **1** also could be relevant given typical reaction conditions. For example, one possibility is that direct photoexcitation of **1** is not the cause of reaction, but rather that photoexcitation of $I_2$ results in homolytic radical formation that initiates the cyclodehydrogenation reaction. We are continuing to explore these possibilities. However, the photophysical behaviors of **1** and **3** are consistent with their observed photochemical reactivity, suggesting that these differences may be the primary contributor.

## 5.6 Acknowledgements

Spectroscopic investigations described in this work were supported by the National Science Foundation (NSF), CHE-1455009 (A. E. B.). J. A. S. gratefully acknowledges support from the Langmuir-Cresap fellowship (JHU). We thank the Tovar Lab (JHU) for use of their TCSPC instrumentation and Dr. Jamie Young for his review of the manuscript. We thank Dr. Matthias Krieg for synthesis of samples of compounds **3**. Computations were performed on the BwForCluster Justus. H. F. B. acknowledges support by the state of Baden-Württemberg through bwHPC and the German Research

Foundation (DFG) through grant no INST 40/467-1 FUGG.

## 5.7 References

1. A. C. Grimsdale and K. Müllen, *Angew. Chem. Int. Ed.*, 2005, 44, 5592-5629.
2. Z. Liu and T. B. Marder, *Angew. Chem. Int. Ed.*, 2008, 47, 242-244.
3. M. Xu, T. Liang, M. Shi and H. Chen, *Chem. Rev.*, 2013, 113, 3766-3798.
4. M. J. D. Bosdet, C. A. Jaska, W. E. Piers, T. S. Sorensen and M. Parvez, *Org. Lett.*, 2007, 9, 1395-1398.
5. C. A. Jaska, D. J. H. Emslie, M. J. D. Bosdet, W. E. Piers, T. S. Sorensen and M. Parvez, *J. Am. Chem. Soc.*, 2006, 128, 10885-10896.
6. C. Tönshoff, M. Müller, T. Kar, F. Latteyer, T. Chassé, K. Eichele and H. F. Bettinger, *ChemPhysChem*, 2012, 13, 1173-1181.
7. P. Kumbhakar, A. K. Kole, C. S. Tiwary, S. Biswas, S. Vinod, J. Taha-Tijerina, U. Chatterjee and P. M. Ajayan, *Adv. Opt. Mater.*, 2015, 3, 828-835.
8. Z. G. Chen, G. Jia, Q. P. Dou, H. T. Ma and T. C. Zhang, *Appl. Phys. B: Lasers Opt.*, 2007, 88, 569-573.
9. N. Marom, J. Bernstein, J. Garel, A. Tkatchenko, E. Joselevich, L. Kronik and O. Hod, *Phys. Rev. Lett.*, 2010, 105, 046801.
10. M. Müller, S. Behnle, C. Maichle-Mössmer and H. F. Bettinger, *Chem. Commun.*, 2014, 50, 7821-7823.
11. M. Krieg, F. Reicherter, P. Haiss, M. Ströbele, K. Eichele, M.-J. Treanor, R. Schaub and H. F. Bettinger, *Angew. Chem. Int. Ed.*, 2015, 54, 8284-8286.

12. S. Biswas, M. Müller, C. Tönshoff, K. Eichele, C. Maichle-Mössmer, A. Ruff, B. Speiser and H. F. Bettinger, *Eur. J. Org. Chem.*, 2012, 2012, 4634-4639.

13. C. Sánchez-Sánchez, S. Brüller, H. Sachdev, K. Müllen, M. Krieg, H. F. Bettinger, A. Nicolaï, V. Meunier, L. Talirz, R. Fasel and P. Ruffieux, *ACS Nano*, 2015, 9, 9228-9235.

14. C. A. Jaska, W. E. Piers, R. McDonald and M. Parvez, *J. Org. Chem.*, 2007, 72, 5234-5243.

15. M. J. D. Bosdet, W. E. Piers, T. S. Sorensen and M. Parvez, *Angew. Chem.*, 2007, 119, 5028-5031.

16. D. J. H. Emslie, W. E. Piers and M. Parvez, *Angew. Chem. Int. Ed.*, 2003, 42, 1252-1255.

17. M. Müller, C. Maichle-Mössmer, P. Sirsch and H. F. Bettinger, *ChemPlusChem*, 2013, 78, 988-994.

18. F. B. Mallory and C. W. Mallory, in *Organic Reactions*, John Wiley & Sons, Inc., 2004.

19. R. B. Woodward and R. Hoffmann, *Angew. Chem. Int. Ed.*, 1969, 8, 781-853.

20. S. A. Brough, A. N. Lamm, S.-Y. Liu and H. F. Bettinger, *Angew. Chem. Int. Ed.*, 2012, 51, 10880-10883.

21. M. A. Neiss and R. F. Porter, *J. Am. Chem. Soc.*, 1972, 94, 1438-1443.

22. R. F. Porter and L. J. Turbini, in *Inorganic Chemistry*, Springer Berlin Heidelberg, 1981, pp. 1-41.

23. D. B. G. Williams and M. Lawton, *J. Org. Chem.*, 2010, 75, 8351-8354.

24. M. Quaranta, M. Murkovic and I. Klimant, 2013, 138, 6243-6245.

25. A. M. Brouwer, *Pure Appl. Chem.*, 2011, 83, 2213-2228.

26. J. A. Snyder and A. E. Bragg, *J. Phys. Chem. A*, 2015, 119, 3972-3985.

27. C. R. Pitts, B. Ling, J. A. Snyder, A. E. Bragg and T. Lectka, *J. Am. Chem. Soc.*, 2016, 138, 6598-6609.

28. M. S. Molloy, J. A. Snyder, J. R. DeFrancisco and A. E. Bragg, *J. Phys. Chem. A*, 2016, 120, 3998-4007.

29. I. Carmichael and G. L. Hug, *J. Phys. Chem. Ref. Data*, 1986, 15, 1-250.

30. I. R. Dunkin, *Matrix-isolation techniques : a practical approach*, Oxford University Press, Oxford ; New York, 1998.

31. A. D. Becke, *J. Chem. Phys.*, 1993, 98, 5648-5652.

32. C. Lee, W. Yang and R. G. Parr, *Phys Rev B Condens Matter*, 1988, 37, 785-789.

33. P. J. Stephens, F. J. Devlin, C. F. Chabalowski and M. J. Frisch, *J. Phys. Chem.*, 1994, 98, 11623-11627.

34. G. W. T. M. J. Frisch, H. B. Schlegel, G. E. Scuseria, M. A. Robb, J. R. Cheeseman, G. Scalmani, V. Barone, B. Mennucci, G. A. Petersson, H. Nakatsuji, M. Caricato, X. Li, H. P. Hratchian, A. F. Izmaylov, J. Bloino, G. Zheng, J. L. Sonnenberg, M. Hada, M. Ehara, K. Toyota, R. Fukuda, J. Hasegawa, M. Ishida, T. Nakajima, Y. Honda, O. Kitao, H. Nakai, T. Vreven, J. A. Montgomery, J. E. Peralta, F. Ogliaro, M. Bearpark, J. J. Heyd, E. Brothers, K. N. Kudin, V. N. Staroverov, R. Kobayashi, J. Normand, K. Raghavachari, A. Rendell, J. C. Burant, S. S. Iyengar, J. Tomasi, M. Cossi, N. Rega, J. M. Millam, M. Klene, J. E. Knox, J. B. Cross, V. Bakken, C. Adamo, J. Jaramillo, R. Gomperts, R. E. Stratmann, O. Yazyev, A. J. Austin, R. Cammi, C. Pomelli, J. W. Ochterski, R. L.

Martin, K. Morokuma, V. G. Zakrzewski, G. A. Voth, P. Salvador, J. J. Dannenberg, S. Dapprich, A. D. Daniels, Ö. Farkas, J. B. Foresman, J. V. Ortiz, J. Cioslowski and D. J. Fox, Gaussian, Inc., Wallingford CT, 2009.

35. P. C. Hariharan and J. A. Pople, *Theor. Chim. Acta*, 1973, 28, 213-222.

36. B. K. Shah, M. A. J. Rodgers and D. C. Neckers, *J. Phys. Chem. A*, 2004, 108, 6087-6089.

37. R. B. Heath, L. C. Busch, X. W. Feng, J. A. Berson, J. C. Scaiano and A. B. Berinstain, *J. Phys. Chem.*, 1993, 97, 13355-13357.

38. A. Bromberg and K. A. Muszkat, *J. Am. Chem. Soc.*, 1969, 91, 2860-2866.

39. K. A. Muszkat and E. Fischer, *J. Chem. Soc. B.*, 1967, 662-678.

40. N. J. Turro, V. Ramamurthy and J. C. Scaiano, *Modern molecular photochemistry of organic molecules*, University Science, Sausalito, Calif., 2004.

41. V. L. Ermolaev and E. B. Sveshnikova, *Opt. Spectrosc.*, 2015, 119, 642-655.

42. N. I. Nijegorodov and W. S. Downey, *J. Phys. Chem.*, 1994, 98, 5639-5643.

43. N. Nijegorodov, V. Zvolinsky and P. V. C. Luhanga, *J. Photochem. Photobiol., A*, 2008, 196, 219-226.

44. S. T. Repinec, R. J. Sension, A. Z. Szarka and R. M. Hochstrasser, *J. Phys. Chem.*, 1991, 95, 10380-10385.

45. K. A. Muszkat, M. Eisenstein, E. Fischer, A. Wagner, Y. Ittah and W. Lüttke, *J. Am. Chem. Soc.*, 1997, 119, 9351-9360.

46. M. C. Smith, J. A. Snyder, B. C. Streifel and A. E. Bragg, *J. Phys. Chem. Lett.*, 2013, 4, 1895-1900.

47. P. Krause, S. Matsika, M. Kotur and T. Weinacht, *J. Chem. Phys.*, 2012, 137, 22A537.

48. R. J. Sension, S. T. Repinec, A. Z. Szarka and R. M. Hochstrasser, *J. Chem. Phys.*, 1993, 98, 6291-6315.

49. N. Minezawa and M. S. Gordon, *J. Phys. Chem. A*, 2011, 115, 7901-7911.

# Chapter 6

# Impacts of Isoelectronic BN-doping on the Photochemistry of Polyaromatic Hydrocarbons: Photocyclization Dynamics of Hexaphenyl Benzene and Hexaphenyl Borazine

Snyder, J. A.; Grüninger, P.; Bettinger, H. F.; Bragg, A. E. *In Preparation*

## 6.0 Abstract

Boron-nitrogen doping of polyaromatic hydrocarbon (PAH) materials can be used to tune their electronic properties while preserving the structural characteristics of pure hydrocarbons. Many multicycle PAHs can be synthesized photochemically; in contrast, very little is known about the photochemistry of their BN-doped counterparts. Here we present results of fs, ns, and μs time-resolved spectroscopic studies on the photoinduced dynamics of hexaphenyl benzene and hexaphenyl borazine in order to examine how BN-doping impacts the prospects for photochemical C-C bond formation via 6π electrocyclization as well as the stability of resulting cyclized structures. Ultrafast measurements reveal different photoinduced behaviors reflecting differences in excited-state decay pathways, with hexaphenyl borazine relaxing from its excited state with a rate that is 2 orders of magnitude faster than that of hexaphenyl benzene (3.0 vs. 428 ps). Tetraphenyl dihydrotriphenylene generated from hexaphenyl benzene is observed to reopen with a ~2 μs lifetime controlled by entropic stabilization of the cyclized structure; in contrast, there is no signature that the borazine-core analogue is formed, and photoinduced dynamics appear to be complete within 100 ps. This significant difference

in photochemical dynamics is reflected in the cyclodehydrogentation yields obtained for the two reactants (25% vs. 0% for hexaphenyl benzene and borazine, respectively). Quantum-chemical computations predict that BN doping gives rise to increased singlet diradical character in cyclized structures and correspondingly lower activation energies for ring opening. Together, these findings indicate that the polarized BN bonds of the borazine core adversely impacts photochemical pathways for bond formation and should also destabilize C-C bonds formed photochemically relative to analogous hydrocarbons.

## 6.1. Introduction

Heteroatom doping of polycyclic aromatic hydrocarbons (PAHs) has gained attention for its potential for tailoring the electronic and optical properties of organic materials for use in organic light emitting diodes (OLEDs) and other optoelectronic devices. Boron-nitrogen doping is of particular interest because it produces structures that are isoelectronic with pure hydrocarbons. Notably, selective BN-substitution can be used to alter the HOMO-LUMO gap, which would modify molecular absorption and emission characteristics or tune nanographene materials between semimetallic and insulating.[1-4] Hence, there is considerable interest in exploring chemical possibilities for synthesizing doped structures.

In this work we examine specifically how BN doping impacts nonadiabatic photochemical bond formation, a key step in photoinduced cyclodehydrogenation reactions that have been utilized commonly for the preparation of PAHs. Nonadiabatic 6π electrocyclizaion is a general consequence of the Woodward-Hoffman rules for orbital symmetry correlations whereby conrotary twisting of pendant rings correlates the π LUMO with a σ bonding HOMO.[5, 6] Relatively little research has explored the photochemistry of BN-doped structures to address their excited-state behavior, in general,[7-9] but most specifically with regards to the dynamics of photochemical bond formation that could be part of the synthetic toolbox for preparing BN-doped structures.

Bettinger and coworkers recently recovered products from the photoinduced cyclodehydrogenation of a borazine-core structure, $B_3N_3$-hexabenzotriphenylene, which implies that a cyclized intermediate structure likely forms before dehydrogenation.[8]

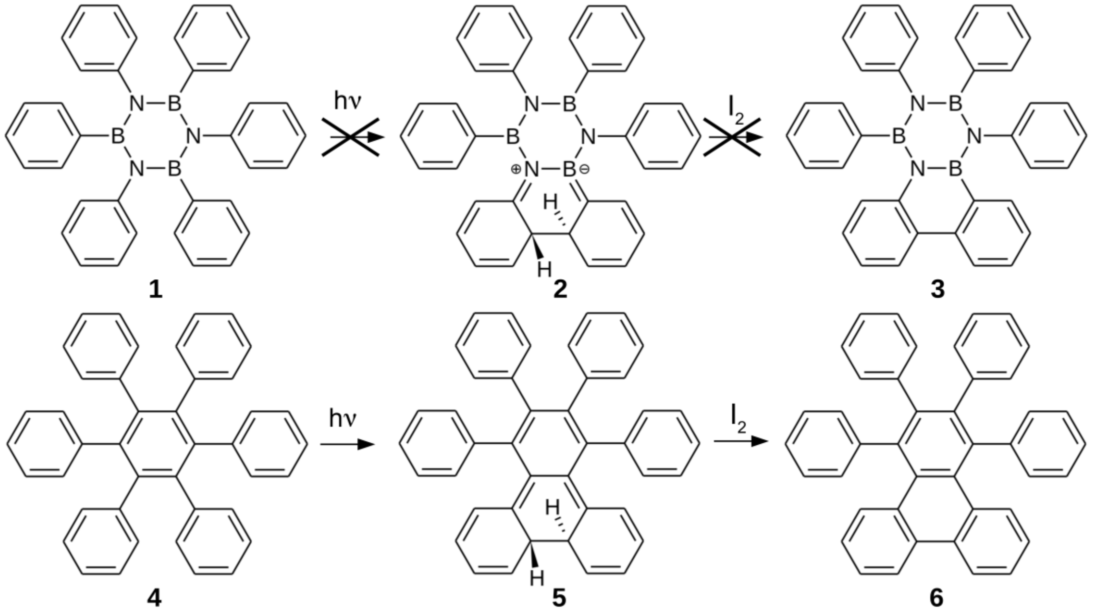

**Scheme 6.1.** Photochemical reaction of hexaphenyl borazine (**1**) and hexaphenyl benzene (**4**). Photoinduced 6π electrocyclization of these reactants is predicted to yield structures **2** and **5** (9,10,11,12-tetraphenyl 4a,4b-dihydrotriphenylene (DHT)), respectively; further oxidation by iodine would generate **3** (1,2-(*o*,*o'*-biphenylylene) 3,4,5,6-tetraphenyl borazine) and **6** (1,2,3,4-tetraphenyl triphenylene).

Subsequently we undertook a comprehensive characterization of the photophysics of this and a related structure in order to assess quantum yields for photoinduced bond formation and competing excited-state deactivation pathways. Those studies revealed that efficient intersystem crossing and fluorescence dominate excited-state relaxation; although no spectroscopic signatures of a cyclized structure was observed for either compound, we were able to estimate the quantum yields for cyclization at ~5-10% or less based on the quantum yields determined for fluorescence and triplet formation. For these compounds, the dominance of the competing relaxation pathways can be interpreted as the consequence of the piecewise-rigid polyaromatic structure of both reactants.

In an effort to reduce the dominance of these competing photophysical relaxation pathways and focus exclusively on the photochemical reactivity of BN-doped structures, here we examine the photoinduced dynamics of a simpler, less rigid reactant structure, hexaphenyl borazine (**1**, Scheme 6.1). Notably, the fluorescence quantum yield ($\Phi_{Fl}$) of **1** has been determined as 1.5 % (compared to 28% for $B_3N_3$-hexabenzotriphenylene), indicating that rapid nonradiative decay pathways, possibly including photocyclization to generate structure **2**, dominate its photophysics.[10] Whereas comparisons with pure hydrocarbon analogues were not possible in our previous study, here we are able to make direct comparisons with the photochemical dynamics of the isoelectronic species hexaphenyl benzene (**4**) in order to assess directly the impact of BN doping on photochemical dynamics.[11] Based on a combination of time-resolved spectroscopic interrogations, photochemical reaction yields, and quantum-chemical computations, we demonstrate that BN substitution results in significant differences in excited-state photophysics and the stability of the photoinduced carbon-carbon bond in their associated photoproducts (**2** and **5**) with implications for the photochemical synthesis of corresponding fused PAH structures (**3** and **6**).

The work presented here is part of a larger effort to understand how structural modifications (both electronic and steric) stifle nonadiabatic photochemical bond formation in larger *ortho*-arenes, beginning from the “core” system *ortho*-terphenyl (OTP) but building to systems with increasing structural complexity.[12-14] In previous work we have demonstrated how structural perturbations to the three-ring cyclizing core (i.e. OTP) can result in drastic changes in orbital symmetry and excited-state potential energy landscape that in turn alter excited-state dynamics and photochemical yields for bond formation. For example, we have shown that 1,2,3-triphenyl benzene (TPB) exhibits qualitatively similar photochemical dynamics as the core structure OTP, but with a relative decrease in cyclization rate and increase in ring-reopening rate; we attribute these differences to steric interactions with the extra phenyl substituent that alter energetic barriers associated with these processes and that possibly require coordinated structural rearrangements. In contrast *ortho*-quaterphenyl (OQTP) exhibits a competing excited-state relaxation pathway to a fluorescent (and non-reactive) excited-state structure stabilized by greater electronic delocalization and that dominates the photophysics of even larger oligo *ortho*-phenylenes.[12, 15]

Much like TPB, hexaphenyl benzene is predicted to yield a single photoproduct (3’,4’,5’,6’-tetraphenyl dihydrotriphenylene, **5**) due to its structural symmetry, and thus presents the possibility to evaluate how structural perturbations impact this fundamental photochemical reaction and the stability of photochemical products. Although we anticipate that steric interactions from pendant rings should reduce the stability of **5** relative to the related, metastable unsubstituted and phenyl-substituted dihydrotriphenylenes generated from excitation of OTP and TPB, it is possible that crowding by the adjacent phenyl substituents in this structure could have an unintended ordering effect: as we demonstrate here, although **5** is only weakly favorable energetically it is highly favorable structure entropically, hinting at possible new considerations for stabilizing switchable photochemical structures.

## 6.2. Experimental

### *6.2.1 Sample Preparation*

Hexaphenylbenzene (**4**) was purchased from Sigma-Aldrich (98%, 149454 Aldrich) and used as received. Hexaphenylborazine (**1**) was synthesized according to literature procedures.[16] Tetrahydrofuran (THF, anhydrous & inhibitor-free, Sigma 401757) was used "as-is" for preparation of solutions of hexaphenylbenzene. Hexaphenylborazine is water-sensitive and therefore THF used to prepare solutions of **1** was dried by storing over dry 3Å Molecular sieves (Sigma 334286) at a 1:5 volume ratio of sieves to THF for at least 24 hours under nitrogen.[17]

Hexaphenyl benzene was dissolved in THF (~5 mM) by sonication. Solutions were saturated with air; solutions saturated with pure nitrogen were prepared as controls to test for quenching of transient states with oxygen. Solutions of **1** were prepared under nitrogen: solid samples were first transferred to a Schlenk flask in a glove bag. The flask was then connected to an air-free manifold in order to provide a constant flow of nitrogen throughout a solvent transfer via cannula. Air-free solutions were sealed and sonicated for 15 minutes.

Two optical cells were utilized in the preparation and optical interrogation of our samples: For measurements requiring air-free conditions (e.g. control solutions for transient quenching experiments on nanoseconds to microsecond timescales) solutions were transferred to a sealed, custom-made Schlenk flask outfitted with a 5 mm pathlength cuvette on a side-arm. Solutions were reduced to an optical density of ~2 at 266 nm and then degassed by 3 freeze-pump-thaw cycles. For measurements of kinetics occurring on timescales ranging from femtoseconds to ~10 nanoseconds, nitrogen-purged solutions were circulated through a custom-made flow cell (250 µm pathlength, 1 mm fused quartz windows AdValue Tech, FQ-S-003, see Figure A4.1) with a peristaltic pump (Newport, Masterflex). Control measurements were performed with both sample cells to ensure consistent results.

### *6.2.2. Femtosecond transient absorption spectroscopy*

The apparatus used for ultrafast transient absorption measurements has been described in detail elsewhere.[12] Ultrafast excitation and probe pulses were derived from the output of an amplified Ti:Sapphire laser system (Coherent Legend Elite, 800 nm, 35 fs FWHM, 1 kHz, 4.0 W). Excitation pulses at 266 nm (< 2 mW) were generated from the fundamental through a frequency doubling+mixing scheme and were focused to a ~1 mm beam diameter at the sample cell. Probe pulses were produced using the 800 nm beam to drive white-light generation in a 2 mm $CaF_2$ plate (United Crystals); the continuum probe was collimated and refocused to a 100 micron beam diameter within the excited region of the sample with a set of parabolic mirrors (Edmund Optics). Probe light transmitted through the sample was dispersed onto a photodiode array (Hammamatsu) for detection using a home-built prism-based spectrometer. Both the pump and probe beams were chopped at one-quarter of the laser repetition rate and in appropriate phases in order to actively remove background signals (i.e. fluorescence and stray pump or room light) prior to calculation of transient absorbance. National Instruments LabVIEW was used for all instrument control, data acquisition, and data processing.

### *6.2.3 Nanosecond transient absorption spectroscopy*

The apparatus used for nanosecond time-resolved absorption measurements has been described in detail elsewhere.[12] This set-up utilizes the same excitation and detection scheme described above, with the exception that the excited sample is probed with the output from a 405 nm laser diode (Thorlabs L405P20) that is pulsed at 500 Hz (Highland Technologies T165). The transmitted probe beam was focused across multiple pixels on a photodiode array using a convex cylindrical lens; probe light intensity was averaged across all pixels after background subtraction, and transient absorption was calculated for consecutive pairs of probe pulses (pump on vs. pump off). The pump-probe time delay was controlled electronically via the signal delay generator from the amplified laser (Coherent SDG Elite).

### *6.2.4 μs-resolved broadband transient absorption spectroscopy*

The signal delay generator from the amplified laser was used to provide an electronically controlled time delay between the fs photoexcitation pulse and an electronic pulse with variable output pulse width and voltage generated with a signal delay generator (Berkeley Nucleonics BNC 555) and that was amplified with transistors (Central Semiconductor 2N2222A). The amplified voltage pulse was used to drive emission from a white-light LED (Thorlabs LEDWE-15, 410-700nm) for use as a broadband probe. The nominal time-resolution of these measurements was 300 nanoseconds, limited by the lifetime of the LED's phosphor emission. The white-light

LED was collimated using a 75 mm convex lens and focused using a parabolic mirror to a variable diameter, typically 1-2 mm, using an iris before the lens to control the image size. The pump beam was matched in size to that of the probe diameter and the two beams transmitted through the sample at an angle of ~10 degrees. The probe beam was then recollimated and filtered to remove pump scatter and detected using a CCD camera (Princeton Instruments, Pixis-100BR). Mechanical chopping of the pump (250 Hz) and electronically pulsing of the probe (500 Hz) light were synchronized so that 4 phases were collected consisting of all combinations of pump and probe illumination at the sample to enable active removal of background and fluorescence signals.

In addition to measurements of room temperature kinetics on microsecond timescales, the temperature dependence of the photoproduct kinetics was investigated down to 193 K. The samples were cooled with a cryostat (Unisoku USP-203), stirred continuously, and purged continuously with dry $N_2$.

### *6.2.5 Photochemical cyclodehydrogenation reactions of 1 and 4*

A 0.5 mM solution of hexaphenyl benzene in cyclohexane (spectrophotometric grade, Acros, 16774) was prepared with 1:1 molar equivalent of $I_2$ (Sigma 207772). The resultant solution was degassed with Ar in a quartz test tube and irradiated for 24 hours with the 254-nm light from a UV reactor lamp (Rayonet) to drive cyclodehydrogentation of the reactant. Iodine was removed by extraction with aqueous sodium thiosulfate. Identical retention times for the reactant and product hindered their separation by chromatography, such that reaction mixtures were analyzed with UV/VIS, NMR, and Mass Spectrometry. Quantitative NMR[18] was performed in order to determine the relative concentrations of product and reactant and therefore calculate a photochemical reaction yield.

### *6.2.6 Quantum-chemical computations*

Density functional theory (DFT) or time-dependent DFT (TDDFT) calculations were conducted with Gaussian 09.[19] Computations were done in order to compare results of spin restricted (R), unrestricted (U) and broken-symmetry (BS) approaches. All reported computations were performed using the range-corrected CAM-B3LYP[20] functional with a 6-31G* or 6-311+G* basis set; calculated energies are corrected for zero-point energy (ZPE) unless otherwise noted. TDDFT calculations were carried out to determine energies and strengths of vertical transitions of cyclized structures; computationally predicted absorption spectra were generated by broadening with a 0.2 eV FWHM Gaussian. Transition states for C-C bond breaking (i.e. ring reopening) in cyclized photoproducts were first approximated with potential-energy scans along the C-C bond coordinate and then located formally by a transition state search using broken-symmetry formalism. Reported transitions states were confirmed to have only one imaginary vibrational frequency, unless otherwise noted.

State-averaged complete active space (SA-CASSCF)[21] computations were performed with GAMESS by averaging over 2 states, including 8 active ($\pi$, $\pi^*$) orbitals and electrons, and using a 6-31G basis set.[22, 23] Natural orbital occupation numbers (NOON) were obtained following orbital visualization with Macmolplt.[24]

## 6.3. Results

### *6.3.1 Photophysical characterization of 1 and 4 with time-resolved spectroscopies*

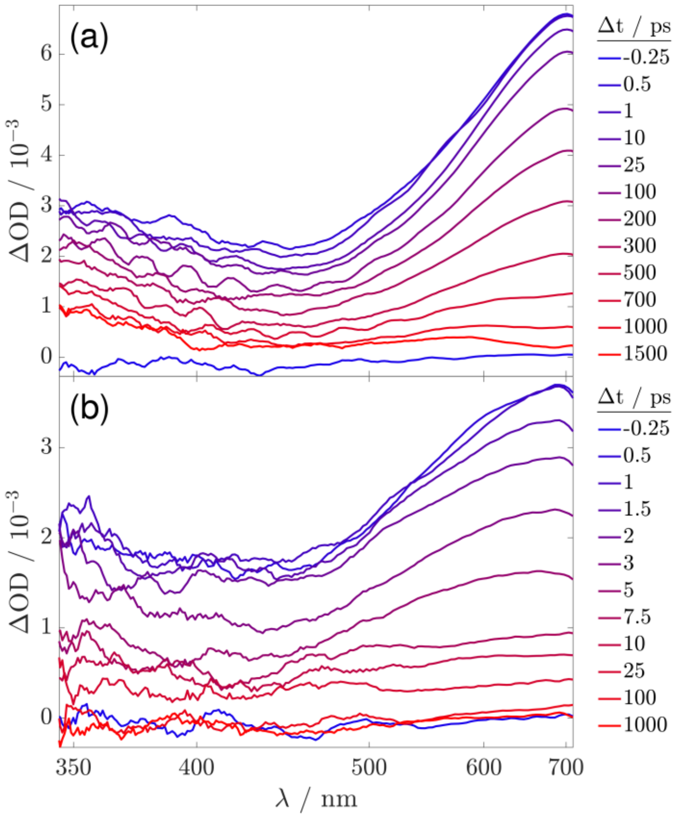

**Figure 6.1.** Femtosecond transient absorption spectra of (a) hexaphenyl benzene (**4**), and (b) hexaphenyl borazine (**1**) in THF under 266 nm excitation.

Femtosecond transient absorption spectra of hexaphenyl benzene (**4**) and hexaphenyl borazine (**1**) in THF obtained by photoexcitation at 266 nm are presented in Figure 6.1. Transient spectra of **4** plotted in Figure 6.1(a) exhibit near-UV and visible/near-IR transitions that both decay over the course of several 100 picoseconds, giving rise to two weaker but distinct features by 1500 ps. Figure 6.2 presents a single-exponential fit of the time-dependent spectral intensity measured at 650 nm that recovers a 428-ps lifetime for the corresponding transient state of **4**.

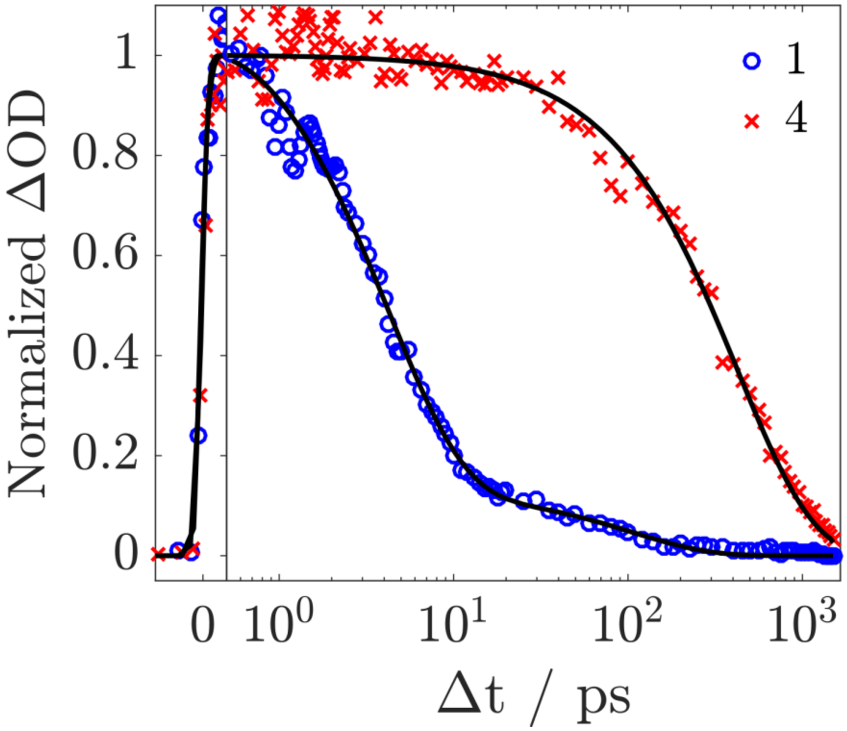

**Figure 6.2.** Normalized fs-TA traces of **1** and **4** at 600 and 650 nm, respectively, following photo-excitation at 266 nm. The single exponential lifetime of **4** (428 ps) is an order of magnitude longer than the slowest timescale from a triexponential fit of the transient signal intensity from photoexcited **1** ($\tau_{rise} = 0.63$, $\tau_{decay} = 3.0$, 75 ps).

The time-dependence of the weaker, long-lived absorption features observed with **4** was investigated further into the nanosecond and microsecond time regimes. Notably, the transient absorption exhibits a similar feature in the visible at both 10 and 1500 ns time delays, as highlighted in Figure 6.3. The lifetime of this transient in aerated solution was determined to be 1950 ns according to the time dependent absorption at 639 nm (inset of Figure 6.3). Ultrafast, nanosecond, and microsecond measurements therefore indicate that the photoproduct visible by 1500 ps does not convert or react to another spectroscopically observable species on a microsecond timescale. Furthermore the nanosecond decay at 639 nm is unaffected by the presence of oxygen, as demonstrated through comparison with control experiments performed in deaerated THF (see Figure A4.2). The spectrum of this meta-stable species is highly similar to the

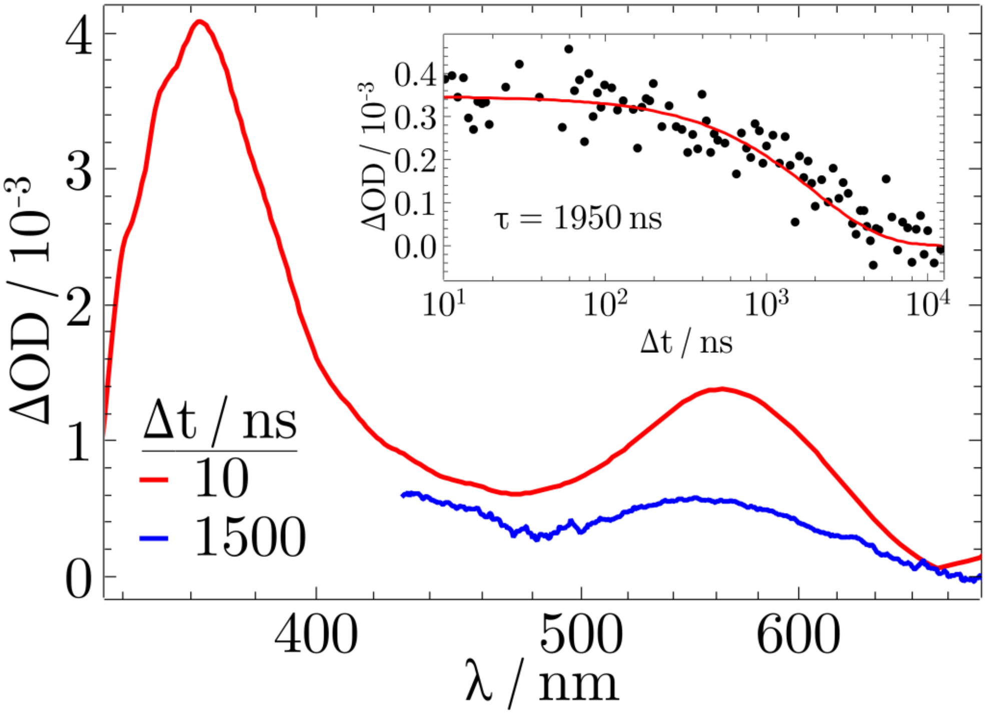

**Figure 6.3.** Ns- and μs-resolved TA spectra obtained following 266-nm excitation of **4** in aerated THF at 298 K. Similarity in the spectra collected at 10 and 1500 ns indicates that the corresponding transient persists from the nanosecond to microsecond regimes. (Inset) Single wavelength trace collected by probing transient absorption at 639 nm (black circles) fit with an exponential decay (red line, τ = 1950 ns).

dihydrotriphenylenes (DHTs) that have been characterized spectroscopically following the photocyclization of OTP, TPB and OQTP,[12] with absorption features peaking at 580 and 370 nm. Therefore we ascribe these features to the cyclized structure **5**.

Transient spectra of photoexcited **1** are shown in Figure 6.1(b) and exhibit features that are qualitatively similar to those from **4**. Upon close comparison, the transient absorption from photoexcited **1** is only slightly broader and bluer by a few nanometers at early time delays following excitation (<10 ps). Overall the spectral dynamics are slightly more complex than what is observed for **4**. Figure 6.2 presents a fit to the transient intensity at 600 nm that can only be fit with a triexponential function ($\tau_{rise} = 0.63$, $\tau_{decay} = 3.0$, 75 ps). The slowest relaxation timescale only accounts for 13% of the total observed signal decay, during which the transient spectral shape is relatively flat and featureless. Most noticeable is the absence of absorption beyond 100 ps, indicating that any photoprepared transient states of **1** are very short-lived or spectroscopically dark.

These TAS results are consistent with fluorescence lifetimes recently measured for both systems. The excited-state lifetime for **4** was reported as < 0.3 ns by time-correlated single photon counting (TCSPC), which is in agreement with lifetimes from our TAS results. The same authors reported the fluorescence lifetime for **1** as < 2.8 ns, much longer than the timescales extracted from our ultrafast TAS measurements but most likely limited by the instrument response of their measurements.[10]*

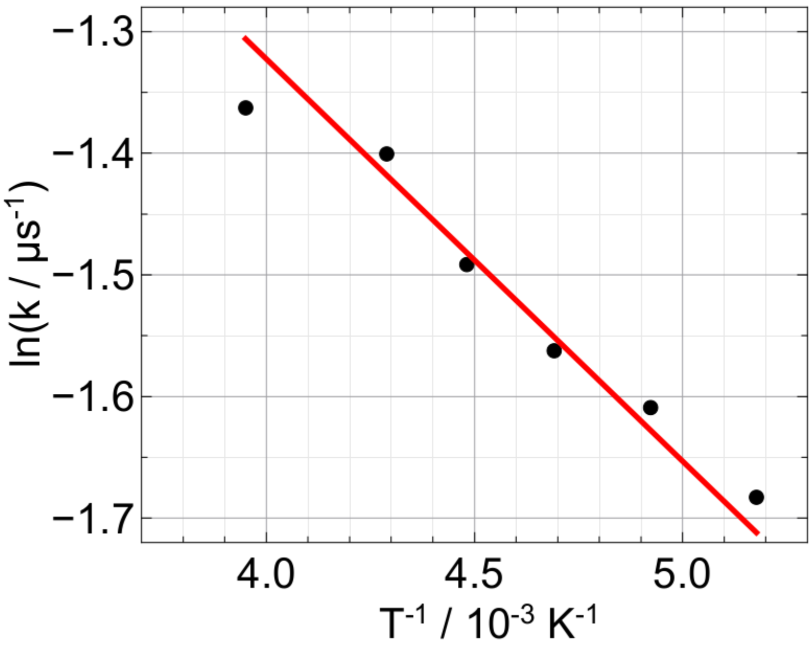

**Figure 6.4**. Arrhenius fit ($R^2$=0.97) to the temperature-dependent ring-opening rate for **5** determined by μs-TA following 266-nm excitation of **4**. See Table 6.1 for fit details and associated thermodynamic parameters.

### *6.3.2. Temperature-dependent kinetics: Thermodynamic parameters for the ring opening of 5*

The temperature-dependent kinetics of the transient photoproduct generated by excitation of **4** was explored between room temperature and 193 K using μs-TA spectroscopy. No change in the transient spectral shape was observed as temperature was decreased (Figure A4.3) but a slight increase in lifetime was observed. Figure 6.4 plots an Arrhenius fit to the temperature-dependent ring-opening rate determined from the decay in transient absorption measured at 580 nm. In addition the thermodynamic parameters $\Delta H^{\ddagger}$, $\Delta S^{\ddagger}$ and $\Delta G^{\ddagger}$ for ring opening at T = 298.15 K were determined from the Arrhenius prefactor ($A$) and activation energy ($E_a$) via the Eyring Equation for unimolecular reactions (Eqn 6.1);[12] all determined parameters are listed in Table 6.1.

$$k(T) = \frac{k_B T}{h} \exp\left(\frac{\Delta S^{\ddagger}}{R}\right) \exp\left(\frac{-E_a + RT}{RT}\right) \tag{6.1}$$

Due to the small activation energy, $k(T)$ is roughly linear with temperature as predicted for the case of barrierless ring opening ($E_a = 0$, Figure A4.4).

**Table 6.1.** Kinetic and thermodynamic parameters for the ring opening of **5** obtained from Arrhenius and Eyring analysis of temperature-dependent μs-TA data (see Figure 6.4).

| $A$ / μs$^{-1}$ | $E_a$ / eV | $\Delta H^{\ddagger}$/ kJ/mol | $\Delta S^{\ddagger}$ / kJ/mol K | $\Delta G^{\ddagger}$ (298 K)/ kJ/mol |
|---|---|---|---|---|
| 1.3±1.1 | 0.024± 0.002 | -2.67 | -0.50 | 145.15 |

Temperature-dependent measurements between 298 and 193 K were also attempted for **1** following 266-nm excitation, but no significant dilation in the slowest relaxation timescale measured by ultrafast TAS could be observed.

### *6.3.3. Photoinduced cyclodehydogenation of 4 and 1*

A solution of **4** and iodine was prepared following the procedure given in Section 2.5 and exposed to UV light (254 nm) to drive cyclodehydrogenation to make **6**. The NMR spectrum of the reaction mixture was compared to that of the pure reactant; nuclear relaxation lifetimes were determined in order to calculate an accurate molar ratio of **4** and **6** (Figures A4.5-A4.7). Identification of NMR signals arising from the product **6** was aided by quantum-chemical calculations (R-CAM-B3LYP/6-31+G*, see Table A4.1) and comparison to NMR spectra of unsubstituted triphenylene; triphenylene exhibits a large downfield chemical shift due to the increase in planarity (relative to the corresponding reactant *ortho*-terphenyl) that enhances $^1$H deshielding. The molar ratio of **4** to **6** was determined to be ~3:1, indicating a 25 % yield of **6** following the assumption that additional reactions were negligible (as verified by EI mass spectrometry, Figure A4.8). The change in UV/VIS observed before and after the reaction is shown in Figure A4.9.

Photooxidation of **1** showed no reaction under the reaction conditions studied.

### *6.3.4 Quantum chemistry and computational spectroscopy of photoproducts 2 and 5*

Density functional theory was used to investigate the electronic structure and spectroscopy of tetraphenyl dihydrotriphenylene, **5**, and its borazine analogue **2** (Scheme 6.1). We also examined the electronic properties of unsubstituted dihydrotriphenylene (DHT, **7**) and its isoelectronic BN-doped analogue **8** shown in Scheme 6.2. These smaller compounds (20-32 for **7** and **8** vs. 72 atoms for **2** and **5**) are more tractable for in-depth computational exploration and provide useful comparisons for assessing the impact of BN doping and phenyl substitution on the central ring of **2** and **5**.

A major goal of our calculations was to quantify the activation energy for thermally activated ring reopening of these metastable structures in order to understand the disparity in lifetimes observed in our time-resolved measurements (both between the two systems studied here and in comparison to systems we have studied previously). Attempts to locate transition states using R-DFT methods failed and rather a broken-symmetry (BS-UHF) formalism was required due to significant singlet diradical character (SDRC) of the cyclized structures. Diradical character has been noted previously for a similar pericyclic reaction product.[25] These findings imply that a pure singlet state is not the true ground-state electronic configuration for these cyclized structures. Spin contamination of the BS-UKS singlet is signified by non-zero values of $<S^2>_{\text{BS-UKS}}$, which provides a qualitative diagnostic of impure singlet ground states;[26] $<S^2>_{\text{BS-UKS}}$ values for all compounds are presented in Table 6.2. Importantly, two stable conformations were identified for **5** (**5a** and **5b**) at the BS-UKS level that differ largely according to configuration of the phenyl substituents relative to the cyclized (DHT) core; in contrast, only one conformer (analogous to **5b**) was found for **2**. The properties of these conformers are discussed in more detail below. Representative HOMO and LUMO orbitals for **1** and **4** at the R-CAM-B3LYP level are presented in Figure A4.10; frontier orbitals of **2b** and **5b** determined at the BS-U-CAM-B3LYP level are presented in Figures A4.11 and A4.12.

Two reliable quantitative metrics of SDRC are the energy differences between the optimized BS-UKS and RKS singlets ($\Delta E\ S_0$), and the UKS singlet-triplet gap ($\Delta E(T_1\text{-}S_0)$).[27] $\Delta E\ S_0$ (Table 6.2) is consistently positive for all molecules examined here, illustrating that the BS-UHF solution stabilizes the ground state in all cases; note that **2** and **8** exhibit greater stabilization than **5** and **7**, implying greater SDRC with BN doping. In contrast, a small singlet-triplet gap $\Delta E(T_1\text{-}S_0)$ implies greater spin contamination through state mixing. Calculated $\Delta E(T_1\text{-}S_0)$ values illustrate that the $T_1$ state is quite close in energy to the $S_0$ state for all systems (both vertically, $T_1\text{-}S_0^{\text{Min}}$, and adiabatically, $T_1^{\text{Min}}\text{-}S_0^{\text{Min}}$), but smallest for **2** and **8**. In fact, for the BN-doped structures $\Delta E(T_1\text{-}S_0)$ is lower than available thermal energy at room temperature ($k_BT$ at 298 K = 0.026 eV). This relative increase in diradical character with BN-doping was also verified at the MCSCF level. Impure closed-shell character is encoded in the natural orbital occupation number (NOON), which can be used to define the biradical index ($y_{\mathrm{NOON}}$); the latter ranges from 0 for an unoccupied LUMO to 1 for a singly occupied LUMO.[28] For **7** and **8**, which are computationally accessible with the SACAS method (SA-2-CAS(8,8)-6-31G), the biradical index increases from 0.744 to 0.940, respectively.

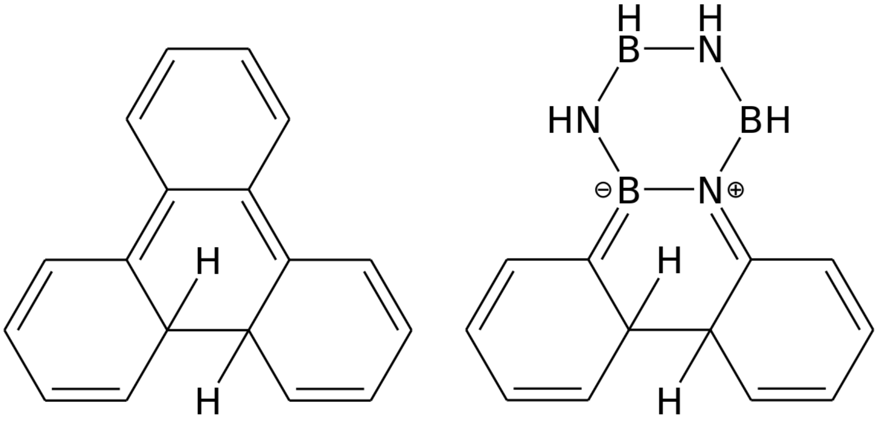

**7** **8**

**Scheme 6.2**. Dihydrotriphenylene (**7**) and its BN-doped analogue (**8**).

**Table 6.2.** Characterization of singlet diradical character (SDRC) of cyclized structures at the CAM-B3LYP/6-311+G* level. Structures of conformers **a** and **b** are shown in Figure 6.6; all other molecules are defined in Scheme 6.2.

| Molecule | $\langle S^2\rangle_{BS\text{-}UHF}$ | ΔE $S_0$ /eV[b] | ΔE ($T_1$-$S_0^{Min}$) /eV | ΔE ($T_1^{Min}$-$S_0^{Min}$) /eV | $E_a$ /eV | $\Delta E_{RC}$ /eV[d] |
|---|---|---|---|---|---|---|
| **7** | 1.330 | 0.246 | 0.141 | 0.097 | 0.132 | 2.430 |
| **8** | 0.948 | 0.849 | 0.010 | 0.015 | 0.021 | 2.599 |
| **5a**[a] | 1.246 | 0.4962 | 0.0556 | 0.0451 | 0.008[c] | 2.742 |
| **5b**[a] | 0.688 | 0.0498 | 0.5234 | 0.0969 | - | 2.876 |
| **2b**[a] | 1.057 | 0.6322 | 0.0116 | 0.0046 | - | 2.998 |

[a] CAM-B3LYP/6-311+G*//CAM-B3LYP/6-31G*

[b] $\Delta E\ S_0 = E(S_0^{RHF}) - E(S_0^{BS\text{-}UHF})$

[c] Value given before ZPE correction, $E_a$=0 eV after ZPE correction.

[d] $\Delta E_{RC} = E(S_0\ \text{Closed}_{\ UHF}) - E(S_0\ \text{Open}_{\ RHF})$.

True transition states to ring opening were located for **7**, **8**, and **5a**; activation energies for ring opening ($E_a$) are listed in Table 6.2, as are calculated energy differences between the cyclized and ring open structures of all systems ($\Delta E_{RC}$). Finally, TD-U-CAM-B3LYP was used to predict the electronic spectra of **2b**, **5a**, and **5b**. The simulated absorption spectra for **5b** is quite similar to that of other DHT analogs and shows reasonable agreement with the spectrum measured experimentally (Figures 6.2 and 6.5). In contrast, the experimental spectrum measured at delays >10 ps following excitation of **1** do not match the predicted spectrum of **2b** (particularly below 400 nm), suggesting that this cyclized structure is not generated

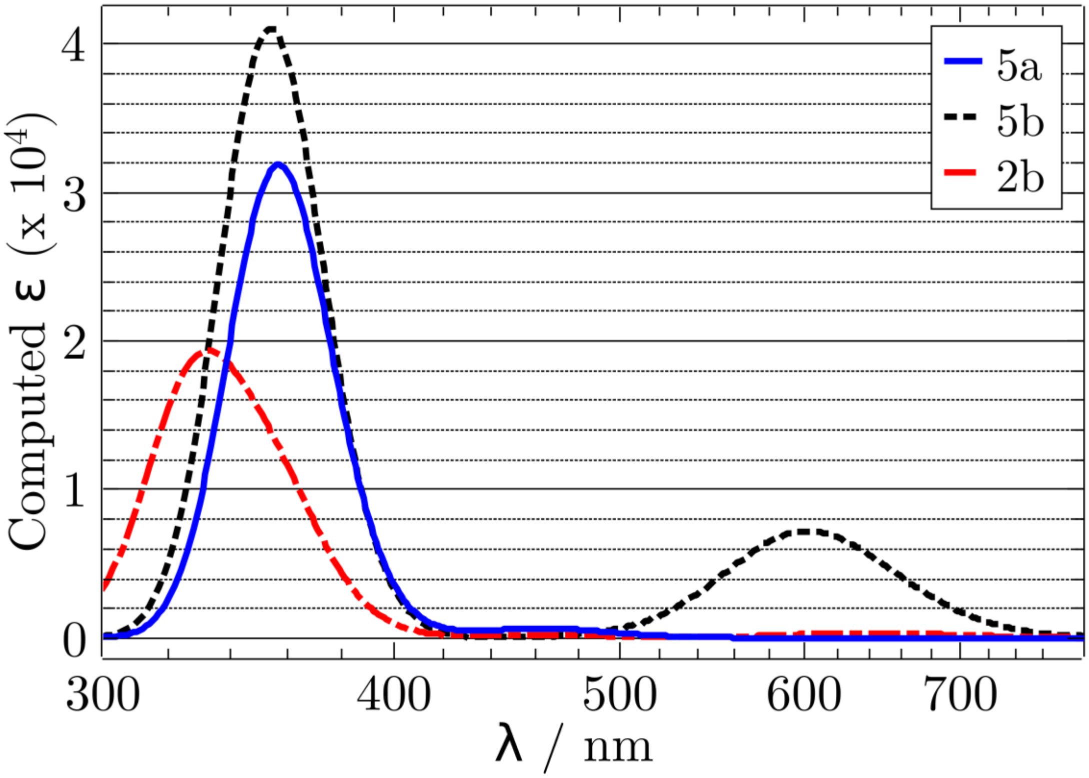

**Figure 6.5.** Comparison of simulated UV-Vis Spectra (0.2 eV FWHM) of $S_0$ **2b**, **5a** and **5b** predicted from computations at the TD-U-CAM-B3LYP/6-311+G* level.

## 6.4. Discussion

### *6.4.1. Photophysics of 1 and 4 and the photochemistry of C-C bond formation*

The absorption and fluorescence spectroscopy of **4** and **1** were reported recently and provide some insights on the photophysics of these isoelectronic species.[10] The lowest energy band in the steady-state absorption spectrum of **1** exhibits a vibronic progression (260-280 nm) resembling the absorption spectrum of benzene. In contrast the lowest absorption band for **4** centered at ~240 nm is much broader and nearly featureless. This difference indicates that **1** may be described in its ground state as having weak coupling between peripheral phenyl and central borazine rings that results in more isolated electronic features compared to that of **4**; this inference is supported by comparison of the HOMOs of these compounds (Figure A4.10). Nonetheless, the fluorescence spectra of **1** and **4** are quite similar, with peak emission wavelengths that are separated only by 4 nm; visible transient absorption features measured for **1** and **4** in this work (Figure 6.1) at time delays ≤ 3ps after excitation are likewise similar. Together, these data suggest that the two compounds have similar electronic character in their excited and emissive states, which is supported by a comparison of the LUMOs of **1** and **4** (Figure A4.10) that shows delocalization across the central ring in both structures.

As noted in the Introduction, the fluorescence quantum yields ($\Phi_{Fl}$) for **4** and **1** have been determined as 0.5 and 1.5 %, respectively, consistent with our observations that relatively rapid nonradiative processes dominate their photophysics.[10] The differences in $\Phi_{Fl}$ with BN doping of hexaphenyl benzene are consistent with changes in

$\Phi_{Fl}$ with BN doping of pyrene, although the magnitude of the increase in quantum yield with doping is smaller for the systems studied here.[2] Despite similar fluorescence quantum yields, however, Figures 6.1 and 6.2 reveal significant differences in the excited-state kinetics of photoexcited **1** and **4**, with BN doping giving rise to a reduction in the excited-state lifetime by 1-2 orders of magnitude. This reduction in excited-state lifetime could be ascribed to differences in the properties of the excited state (e.g. localized vs. delocalized excitation) or shapes of the excited-state potential energy surfaces (i.e. specifically, differences in the size of the activation barrier or relative energies of conical intersections for cyclization from the excited state).

In our previous work with OQTP and TPB, we found that 6π photocyclization was very sensitive to the extent of delocalization in larger *ortho*-arenes and requires an excited state localized around a DHT core (e.g. TPB); in contrast, significant delocalization over four or more rings could stabilize an excited state against bond formation, as is observed for OQTP and larger oligo *ortho*-arenes.[12, 15] Because transient absorption and fluorescence as well as quantum-chemical calculations do not suggest a significant difference in electronic delocalization in the excited states of **1** and **4**, BN doping must perturb the $S_1$ potential energy landscape by some other means. The fact that no clear spectroscopic signature in Figure 6.1(b) can be ascribed to the appearance of **2b**, photoexcited **1** very likely relaxes via a conical intersection not related to bond formation. For example, alternative, faster nonadiabatic relaxation pathways could arise from deformation of the borazine core or phenyl substituents.[28] An important point is that nonadiabatic excited-state decay via a conical intersection associated with cyclization is not a guarantee and has been shown to be dependent on the chromophore.[29, 30]

### *6.4.2 Structure and stability of cyclized intermediate 5*

In previous work we investigated the photochemistry of various *ortho*-arenes, including OTP, TPB, and OQTP. That work revealed formation of metastable cyclized photoproducts dihydrotriphenylene (DHT), 9-phenyl DHT, and 1-phenyl DHT, respectively, that exhibit distinct absorption features peaking in the visible (~580 nm) and near-UV (~340 nm) and that persist for <50 nanoseconds.[12, 13] The transient absorption spectrum of the metastable transient observed following photoexcitation of **4** is highly similar, and assignment of the transient features observed in Figure 6.2 to those of a substituted DHT photoproduct is supported by a TDDFT calculated spectrum (Figure 6.5). The formation of a cyclized product following excitation of **4** is supported by photochemical oxidation experiments, as **5** is an assumed intermediate for the photochemical generation of **6**. The fact that the transient spectral signatures that we attribute to **5** are not significantly quenched by the presence of oxygen on the nanosecond to microsecond timescales further supports assignment to a metastable chemical structure in its singlet electronic ground state: Singlet diradicals are quenched by $O_2$ much more slowly than triplets, with quenching rates of $10^7$ versus $10^9$ $M^{-1}$ $s^{-1}$. For the concentration of oxygen expected for air-saturated solutions, quenching of a singlet diradical would account for a 10% reduction in the lifetime of **5**.[31] The fact that no quenching effect is observed for **5** suggests low SDRC and therefore a weak interaction with $O_2$ concentration at best.

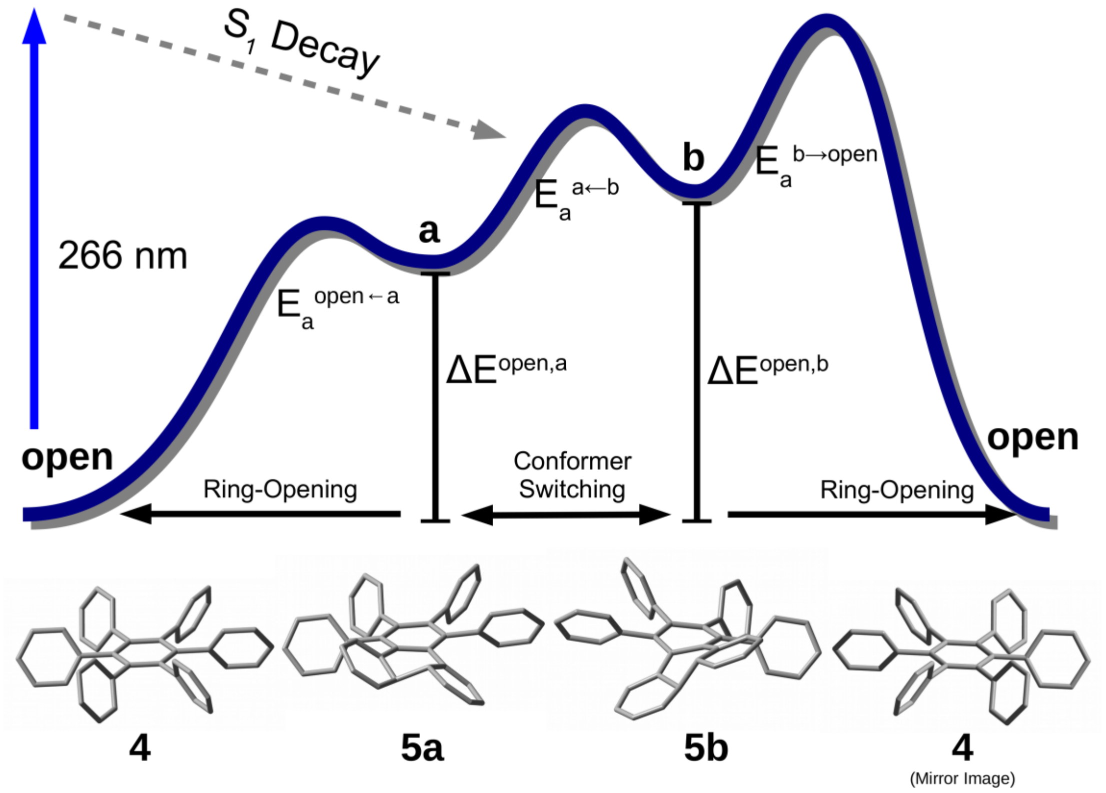
$S_1$ Decay
266 nm
open
$E_a^{open \leftarrow a}$
a
$E_a^{a \leftarrow b}$
b
$E_a^{b \rightarrow open}$
$\Delta E^{open,a}$
$\Delta E^{open,b}$
open
Ring-Opening
Conformer Switching
Ring-Opening
4
5a
5b
4
(Mirror Image)

**Figure 6.6.** Conformers of **5** and associated potential energy landscape; hydrogens have been omitted for clarity. Following photo-excitation and excited-state decay the formation of two conformers is possible with **5a** being weakly bound relative to **5b**. Note that for conversion of **5b** to **4** the fused rings would need to rotate counter-clockwise, which results in a larger $E_a$ than for the clockwise rotation from **5b** to **5a**.

As noted above, we have identified two stable conformers of **5** computationally; the structures of these conformers are highlighted in the bottom of Figure 6.6. **5b** differs from **5a** with respect to relative dihedrals and torsions of the four phenyl substituents on the DHT core. **5a** and **5b** are analogous to the conformers of substituted dihydrophenanthrenes (DHP) noted by Muszkat *et. al*.; those conformers were labeled **L** and **S** according to the relative wavelength of their lowest energy/wavelength(???) absorption transitions ("long" or "short").[32, 33] For 2,4,5,7-tetramethyl-DHP, it was shown that the **L** conformer is formed directly in the relaxation that follows photoexcitation and that the **S** conformer is only formed subsequently by thermal activation with $E_a$'s ranging from 0.43 to 0.73eV. We therefore suspected that a similar relationship between photoproduct conformations **5a** and **5b** could be relevant for the photochemistry of **4**. Figure 6.5 demonstrates that the UV/Vis spectra of conformers **5a** and **5b** simulated from computations show substantial differences, much like the **L** and **S** conformers of modified DHPs.

When compared to results of our previous studies, a significant finding here is that the lifetime of **5** is 1.9 μs, >40 times longer than that of unsubstituted DHT and >400 times longer than that of the phenyl-DHT generated from excitation of TPB. The relatively long lifetime of **5** might suggest increased bond order compared to other substituted DHTs due to stabilization of its singlet diradical character. Indeed, our calculations show less stabilization with inclusion of unrestricted spins (i.e. smaller $\Delta E$ $S_0$) and a greater vertical singlet-triplet gap ($\Delta E$ ($T_1$-$S_0^{Min}$)) for **5b** compared to **7** (whereas their adiabatic gaps are comparable), suggesting less SDRC for the former; in contrast, these metrics for conformer **5a** predict greater SDRC relative to **7**. Our temperature-dependent measurements reveal considerably smaller activation energy for ring opening of **5** relative to **7**, which could be consistent with photochemical generation of the conformer with greater SDRC, **5a**, and would suggest that other factors impact its overall stability.

In order to assess the relative stability of conformers **5a** and **5b** we have explored the potential energy landscape between these conformers in addition to the landscape from **5b** to **4** and **5a** to **4** (Figure A4.13). Although we could identify a true transition state between **5a** and **4** (i.e. exhibiting only one imaginary frequency along the C-C bond stretch), we could only identify pseudo transition states between **5a**/**5b** and **5b**/**4** (i.e. with two imaginary frequencies, a distortion of the DHT moiety and C-C bond stretch); hence, the relative energies of the latter can only provide an upper limit to the activation energies for converting between those structures. The calculated activation energies are ordered as $E_a^{5a \rightarrow 4} < E_a^{5b \rightarrow 4} < E_a^{5b \rightarrow 4}$ (Table 6.3), suggesting that **5b** is the more stable conformer with respect to breaking the nascent photochemical C-C bond, despite the fact that **5a** has a lower absolute energy than **5b**. This extra stability is likely due to an energetic penalty associated with the steric "locking" of the DHT core in **5b** by the peripheral phenyl rings.

**Table 6.3.** Energetic barriers along the potential energy landscape between ring-open structures **1** and **4** and cyclized structures **2** and **5** (confomers **a** and **b**) (U-CAM-B3LYP/6-31G*).

| | $E_a^{a\rightarrow open}$/eV | $E_a^{b\rightarrow a}$ /eV[1] | $E_a^{b\rightarrow open}$/eV[1] | $\Delta E^{open,b}$/eV | $\Delta E^{a,b}$/eV |
|---|---|---|---|---|---|
| **4/5** | 0.008 | 0.186 | 0.648 | 2.876 | 0.133[2] |
| **1/2** | - | 0.141[3] | 0.289 | 2.998 | 0.164[3] |

[1] $E_a^{b\rightarrow a}$ and $E_a^{b\rightarrow open}$ are upper limits given that vibrational analysis resulted in 2 imaginary vibrational frequencies. Details pertaining to the constrained potential energy scans are provided in the SI.

[2] U-CAM-B3LYP/6-311+G*

[3] Conformer **2a** does not correspond to a true stationary point with the 6-31G* basis. However, under the constrained conditions a ΔE can be provided for comparison.

Based on our experimental data the ring opening of **5** was determined to be nearly barrierless energetically (see Figures 6.4 and A4.4), with the enthalpy of bond breaking slightly negative; in contrast, DHT, 1-phenyl DHT and 9-phenyl were all determined previously to have positive bond enthalpies of activation.[12] Hence the relative stabilization of **5** compared to other DHT structures must be entirely entropic in nature (i.e. $\Delta G^{\ddagger}=-T\,\Delta S^{\ddagger}$). $\Delta S^{\ddagger}$ for **5** is the largest observed amongst the DHT analogues we have studied yet and also correlates with increasing levels of phenyl substitution from DHT (-0.362 kJ/mol K), 9-phenyl DHT (-0.375 kJ/mol K) and 1-phenyl DHT (-0.398 kJ/mol K), to **5** (-0.50 kJ/mol K).[12] In broad terms, entropic stabilization of **5** against ring opening can be interpreted as a need to search configurational phase space to reach the near-barrierless transition state. This search could be ascribed in part to coordinated reorganization of the phenyl substituents that crowd the central DHT core.

Although the calculated activation energy for **5a→4** is predicted to be nearly barrierless, the much better agreement between the experimental spectrum and the calculated spectrum of **5b** suggests to us that this conformer is formed preferentially and that the true transition states for **5b→4** or **5b→5a** are much lower in energy than the pseudo transition states we have located computationally. We observe no spectral changes on the nanosecond to microsecond timescale that would be consistent with the interconversion **5b→5a** even at low temperatures. This would imply that the true barrier for bond fission **5b→4** is lower than the true barrier for interconversion **5b→5a**. Alternatively, this could mean that **5a** has both weaker net stabilization than **5b** such that capturing the short-lived population of the former is not possible due to the long, entropically dilated lifetime of the latter. Certainly the calculated activation energy for ring reopening of **5a** is virtually negligible, and this second scenario would be plausible if the rate of decay for **5a** was similar to that of phenyl- and methyl-substituted DHTs, which have lifetimes <100 ns.

### *6.4.3 Electronic structure and properties of cyclized intermediate 2*

Although we see no evidence for the formation of the BN-doped photoproduct **2**, computations allow us to consider the relative stability of this species compared to its pure hydrocarbon analogue. The relative stability of cyclized structures is frequently attributed to the aromaticity of the pendant rings of the reactant structure. An increase in aromaticity of these rings is associated with an increased ΔE between $S_0$ open and cyclized structures and decreased activation energies.[34] This principle has been central to the design of thermally stable photoswitchable materials that tend to incorporate pendant thiophene, furan, or pyrole rings to increase ring-opening barriers.[35-38]

Based on these considerations the computational prediction of a less stable photo-intermediate **2** (and also of **8** compared to its pure hydrocarbon analogue **7**, see Tables 6.2 and 6.3) suggests that the aromaticity of borazine might be greater than that of benzene. However, a comparison of computed nucleus-independent chemical shifts (NICS) has been used to predict that borazine is less aromatic than benzene with a more localized electronic structure, such that increased electronic localization is more likely to be relevant for the properties of **2**.[39] Indeed, unlike **5**, the HOMO of **2** is localized in the region of the central (borazine) ring closest to the nascent σ bond. Although this is consistent with a lower aromaticity of borazine, the high singlet diradical character found for **2** is also consistent with a weaker σ bond and rather suggests that the two rings are isolated by charge-separated character of the bridging BN unit, thereby inhibiting delocalization of electrons across the DHT-like backbone.

## ***6.5. Conclusion***

From a combination of experimental and computational investigations we have found that isoelectronic hexaphenyl benzene (**4**) and hexaphenyl borazine (**1**) exhibit drastically different molecular photophysics and photochemistry: The excited state of hexaphenyl benzene is much longer-lived than that of hexaphenyl borazine (~428 vs. 3 ps, respectively). Whereas a clear spectroscopic signature attributable to a cyclized product **5** appears following the relaxation of photoexcited **4**, no clear evidence for cyclization of **1** is observed. Similarly a modest (25%) photochemical yield of tetraphenyl triphenylene (**6**) is obtained by cyclodehydrogenation of **4**, whereas no analogous product is recovered for **1**. These observations suggest that **1** relaxes nonadiabatically from the excited state following a pathway that does not include cyclization. Although we cannot rule out that the broad, weak short-lived (<100 ps) transient observed following the excitation of **1** is not associated with a cyclized product **2**, we note that such a short lifetime would also be consistent with no recovery of **3** via cyclodehydrogenation and a lower predicted stability of such an intermediate based on our quantum-chemical calculations.

Quantum-chemical computations provide considerable insight on the electronic and structural features that underlie the observed and predicted stabilities of photochemical products from these reactants. Electronically, borazine greatly reduces conjugation across the DHT-like core and coupling between phenyl rings, which manifests itself in increased diradical character and a lower predicted $E_a$ for ring opening of **2** relative to **5** (as well as **8** relative to **7**). Qualitatively this can be explained by the electron localization of borazine by the ionic bonding character of the BN bond that interrupts conjugation between the π bonded cycles in **2**. Interestingly, we find that the cyclized structure **5** to be strongly stabilized entropically when compared to related cyclized structures. We attribute this to the configuration of phenyl substituents on the central ring of the cyclized core: the initial formation of what appears to be the preferred photoproduct conformer (**5b**) is expected to come at an energetic penalty in the excited state when compared to related *ortho*-arene systems; however, steric interactions and the need for coordinated structural fluctuations ultimately extend the lifetime of **5b**. It is unclear whether this stabilization is unique to **5b**, or would also apply to conformer **5a** and conformers of **2**. A "hot" photoproduct with the activation energies determined and predicted here could be expected to reopen rapidly (10's of ps) without entropic stabilization. This could explain in part why spectroscopic evidence for other conformers of **5** is not observed and would also be consistent with a short-lived photoproduct **2** following excitation of **1** that plausibly could be associated with 75-ps component observed in our transient measurements.

This photophysical and photochemical study of borazine substitution demonstrates that BN doping that can be used to tune HOMO-LUMO gaps for material application (e.g. OLEDs) has a dramatic impact on the photochemistry of precursor materials. Specifically, in the case of nonadiabatic photocyclization, which is a key step in the photochemical generation of polyaromatic structures, BN doping introduces a resistance to photochemical bond formation via fast excited-state decay and decrease in predicted stability of cyclized photoproducts. Our results provide a unique view of the impact of isoelectronic substitution that might be expected to give rise to similar chemical behaviors and properties: In essence, isoelectronic does not imply isodynamic.

## *6.6. Acknowledgements*

Spectroscopic investigations described in this work were supported by the National Science Foundation (NSF), CHE-1455009 (A.B.). J.S. gratefully acknowledges support from the Langmuir-Cresap fellowship (JHU). We thank the Fairbrother Lab (JHU) for use of their photochemical reactor.

## 6.7. References

1. Bosdet, M. J. D.; Piers, W. E.; Sorensen, T. S.; Parvez, M., 10a-Aza-10b-borapyrenes: Heterocyclic Analogues of Pyrene with Internalized BN Moieties. *Angewandte Chemie* **2007,** *119* (26), 5028-5031.

2. Bosdet, M. J. D.; Jaska, C. A.; Piers, W. E.; Sorensen, T. S.; Parvez, M., Blue Fluorescent 4a-Aza-4b-boraphenanthrenes. *Organic Letters* **2007,** *9* (7), 1395-1398.

3. Kim, G.; Lim, H.; Ma, K. Y.; Jang, A. R.; Ryu, G. H.; Jung, M.; Shin, H.-J.; Lee, Z.; Shin, H. S., Catalytic Conversion of Hexagonal Boron Nitride to Graphene for In-Plane Heterostructures. *Nano Letters* **2015,** *15* (7), 4769-4775.

4. Xu, M.; Liang, T.; Shi, M.; Chen, H., Graphene-Like Two-Dimensional Materials. *Chemical Reviews* **2013,** *113* (5), 3766-3798.

5. Woodward, R. B.; Hoffmann, R., The Conservation of Orbital Symmetry. *Angewandte Chemie International Edition in English* **1969,** *8* (11), 781-853.

6. Hoffmann, R.; Woodward, R. B., Conservation of Orbital Symmetry. *Accounts Chem Res* **1968,** *1* (1), 17-&.

7. Brough, S. A.; Lamm, A. N.; Liu, S.-Y.; Bettinger, H. F., Photoisomerization of 1,2-Dihydro-1,2-Azaborine: A Matrix Isolation Study. *Angewandte Chemie International Edition* **2012,** *51* (43), 10880-10883.

8. Müller, M.; Behnle, S.; Maichle-Mössmer, C.; Bettinger, H. F., Boron–nitrogen substituted perylene obtained through photocyclisation. *Chemical Communications* **2014,** *50* (58), 7821-7823.

9. Su, M.-D., Mechanistic Investigations on the Photoisomerization Reactions of 1,2-Dihydro-1,2-Azaborine. *Chemistry – A European Journal* **2013,** *19* (29), 9663-9667.

10. Kervyn, S.; Fenwick, O.; Di Stasio, F.; Shin, Y. S.; Wouters, J.; Accorsi, G.; Osella, S.; Beljonne, D.; Cacialli, F.; Bonifazi, D., Polymorphism, Fluorescence, and Optoelectronic Properties of a Borazine Derivative. *Chemistry – A European Journal* **2013,** *19* (24), 7771-7779.

11. Liu, Z.; Marder, T. B., B-N versus C-C: How Similar Are They? *Angewandte Chemie International Edition* **2008,** *47* (2), 242-244.

12. Snyder, J. A.; Bragg, A. E., Structural Control of Nonadiabatic Bond Formation: The Photochemical Formation and Stability of Substituted 4a,4b-Dihydrotriphenylenes. *The Journal of Physical Chemistry A* **2015,** *119* (17), 3972-3985.

13. Molloy, M. S.; Snyder, J. A.; Bragg, A. E., Structural and Solvent Control of Nonadiabatic Photochemical Bond Formation: Photocyclization of o-Terphenyl in Solution. *The Journal of Physical Chemistry A* **2014,** *118* (22), 3913-3925.

14. Smith, M. C.; Snyder, J. A.; Streifel, B. C.; Bragg, A. E., Ultrafast Excited-State Dynamics of ortho-Terphenyl and 1,2-Diphenylcyclohexene: The Role of "Ethylenic Twisting" in the Nonadiabatic Photocyclization of Stilbene Analogs. *The Journal of Physical Chemistry Letters* **2013,** *4* (11), 1895-1900.

15. Hartley, C. S., Excited-State Behavior of ortho-Phenylenes. *The Journal of Organic Chemistry* **2011,** *76* (21), 9188-9191.

16. Groszos, S. J.; Stafiej, S. F., Organoboron Compounds .1. A New Synthesis of B-Trialkyl and Triaryl-N-Triphenylborazoles. *J Am Chem Soc* **1958,** *80* (6), 1357-1360.

17. Williams, D. B. G.; Lawton, M., Drying of Organic Solvents: Quantitative Evaluation of the Efficiency of Several Desiccants. *The Journal of Organic Chemistry* **2010,** *75* (24), 8351-8354.

18. Bharti, S. K.; Roy, R., Quantitative 1H NMR spectroscopy. *TrAC Trends in Analytical Chemistry* **2012,** *35*, 5-26.

19. Gaussian 09, R. D., Frisch, M. J.; Trucks, G. W.; Schlegel, H. B.; Scuseria, G. E.; Robb, M. A.; Cheeseman, J. R.; Scalmani, G.; Barone, V.; Petersson, G. A.; Nakatsuji, H.; Li, X.; Caricato, M.; Marenich, A. V.; Bloino, J.; Janesko, B. G.; Gomperts, R.; Mennucci, B.; Hratchian, H. P.; Ortiz, J. V.; Izmaylov, A. F.; Sonnenberg, J. L.; Williams-Young, D.; Ding, F.; Lipparini, F.; Egidi, F.; Goings, J.; Peng, B.; Petrone, A.; Henderson, T.; Ranasinghe, D.; Zakrzewski, V. G.; Gao, J.; Rega, N.; Zheng, G.; Liang, W.; Hada, M.; Ehara, M.; Toyota, K.; Fukuda, R.; Hasegawa, J.; Ishida, M.; Nakajima, T.; Honda, Y.; Kitao, O.; Nakai, H.; Vreven, T.; Throssell, K.; Montgomery, J. A., Jr.; Peralta, J. E.; Ogliaro, F.; Bearpark, M. J.; Heyd, J. J.; Brothers, E. N.; Kudin, K. N.; Staroverov, V. N.; Keith, T. A.; Kobayashi, R.; Normand, J.; Raghavachari, K.; Rendell, A. P.; Burant, J. C.; Iyengar, S. S.; Tomasi, J.; Cossi, M.; Millam, J. M.; Klene, M.; Adamo, C.; Cammi, R.; Ochterski, J. W.; Martin, R. L.; Morokuma, K.; Farkas, O.; Foresman, J. B.; Fox, D. J. Gaussian, Inc: Wallingford CT, 2013.

20. Yanai, T.; Tew, D. P.; Handy, N. C., A new hybrid exchange–correlation functional using the Coulomb-attenuating method (CAM-B3LYP). *Chem Phys Lett* **2004,** *393* (1–3), 51-57.

21. Docken, K. K.; Hinze, J., LiH Potential Curves and Wavefunctions for X $^1\Sigma^+$, A $^1\Sigma^+$, B $^1\Pi$, $^3\Sigma^+$, and $^3\Pi$. *The Journal of Chemical Physics* **1972,** *57* (11), 4928-4936.

22. Gordon, M. S.; Schmidt, M. W., Chapter 41 - Advances in electronic structure theory: GAMESS a decade later A2 - Dykstra, Clifford E. In *Theory and Applications of Computational Chemistry*, Frenking, G.; Kim, K. S.; Scuseria, G. E., Eds. Elsevier: Amsterdam, 2005; pp 1167-1189.

23. Schmidt, M. W.; Baldridge, K. K.; Boatz, J. A.; Elbert, S. T.; Gordon, M. S.; Jensen, J. H.; Koseki, S.; Matsunaga, N.; Nguyen, K. A.; Su, S.; Windus, T. L.; Dupuis, M.; Montgomery, J. A., General atomic and molecular electronic structure system. *Journal of Computational Chemistry* **1993,** *14* (11), 1347-1363.

24. Bode, B. M.; Gordon, M. S., Macmolplt: a graphical user interface for GAMESS. *Journal of Molecular Graphics and Modelling* **1998,** *16* (3), 133-138.

25. Williams, R. V.; Edwards, W. D.; Mitchell, R. H.; Robinson, S. G., A DFT Study of the Thermal, Orbital Symmetry Forbidden, Cyclophanediene to Dihydropyrene Electrocyclic Reaction. Predictions to Improve the Dimethyldihydropyrene Photoswitches. *J Am Chem Soc* **2005,** *127* (46), 16207-16214.

26. Bendikov, M.; Duong, H. M.; Starkey, K.; Houk, K. N.; Carter, E. A.; Wudl, F., Oligoacenes: Theoretical Prediction of Open-Shell Singlet Diradical Ground States. *J Am Chem Soc* **2004,** *126* (24), 7416-7417.

27. Abe, M., Diradicals. *Chemical Reviews* **2013,** *113* (9), 7011-7088.

28. Doehnert, D.; Koutecky, J., Occupation numbers of natural orbitals as a criterion for biradical character. Different kinds of biradicals. *J Am Chem Soc* **1980,** *102* (6), 1789-1796.

29. Ward, C. L.; Elles, C. G., Cycloreversion Dynamics of a Photochromic Molecular

Switch via One-Photon and Sequential Two-Photon Excitation. *The Journal of Physical Chemistry A* **2014**, *118* (43), 10011–10019.

30. Harabuchi, Y.; Yamamoto, R.; Maeda, S.; Takeuchi, S.; Tahara, T.; Taketsugu, T., Ab Initio Molecular Dynamics Study of the Photoreaction of 1,1′-Dimethylstilbene upon $S_0 \rightarrow S_1$ Excitation. *The Journal of Physical Chemistry A* **2016,** *120* (44), 8804-8812.

31. Heath, R. B.; Busch, L. C.; Feng, X. W.; Berson, J. A.; Scaiano, J. C.; Berinstain, A. B., Absolute rates of heterocyclic singlet biradical reactions determined by nanosecond time-resolved absorption spectroscopy. Dimerizations and cycloadditions to alkenes and to dioxygen. *The Journal of Physical Chemistry* **1993,** *97* (50), 13355-13357.

32. Muszkat, K. A.; Eisenstein, M.; Fischer, E.; Wagner, A.; Ittah, Y.; Lüttke, W., The Two Conformations of Hindered Photochromic 4a,4b-Dihydrophenanthrenes. *J Am Chem Soc* **1997,** *119* (40), 9351-9360.

33. Ittah, Y.; Jakob, A.; Muszkat, K. A.; Castel, N.; Fischer, E., Photocyclization of cis-di(2-naphthyl)-ethylene and its fluorine derivatives: formation of two coloured interconvertible modifications of dibenzo-4a,4b- dihydrophenanthrene derivatives. *Journal of Photochemistry and Photobiology A: Chemistry* **1991,** *56* (2–3), 239-247.

34. Irie, M., Diarylethenes for Memories and Switches. *Chemical Reviews* **2000,** *100* (5), 1685-1716.

35. Fukaminato, T.; Hirose, T.; Doi, T.; Hazama, M.; Matsuda, K.; Irie, M., Molecular Design Strategy toward Diarylethenes That Photoswitch with Visible Light. *J Am Chem Soc* **2014,** *136* (49), 17145-17154.

36. Irie, M.; Fukaminato, T.; Matsuda, K.; Kobatake, S., Photochromism of Diarylethene Molecules and Crystals: Memories, Switches, and Actuators. *Chemical Reviews* **2014,** *114* (24), 12174-12277.

37. Hu, F.; Cao, M.; Ma, X.; Liu, S. H.; Yin, J., Visible-Light-Dependent Photocyclization: Design, Synthesis, and Properties of a Cyanine-Based Dithienylethene. *The Journal of Organic Chemistry* **2015,** *80* (15), 7830-7835.

38. Fredrich, S.; Göstl, R.; Herder, M.; Grubert, L.; Hecht, S., Switching Diarylethenes Reliably in Both Directions with Visible Light. *Angewandte Chemie International Edition* **2016,** *55* (3), 1208-1212.

39. Chen, Z.; Wannere, C. S.; Corminboeuf, C.; Puchta, R.; Schleyer, P. v. R., Nucleus-Independent Chemical Shifts (NICS) as an Aromaticity Criterion. *Chemical Reviews* **2005,** *105* (10), 3842-3888.

# Chapter 7

# Sub-Picosecond Nonadiabatic Bond Formation in *ortho*-arenes Revealed with Pump-repump-probe Spectroscopy

Snyder, J. A.; Bragg, A. E. *In Preparation.*

## 7.1 Introduction

The influence of structure on the chemical dynamics of excited states of photoswitchable molecules (such as photocyclizable structures) is an important aspect to the design of efficient and robust materials with predictable photoresponses. Structure-dynamics relationships are likewise critical for supporting photo-induced bond formation via cyclodehydrogentation as a useful synthetic tool for generating complex polycyclic aromatic hydrocarbon (PAH) networks, such as graphene nanoribbons.[1] Photochemical synthetic methods often use milder reaction conditions and have the potential to utilize sustainable solar energy that can reduce waste and promote "green" chemistry.[2-4] A better understanding of excited-state properties, reaction mechanisms, and how they are impacted by reactant structure is critical for optimizing the performance of photoswitchable materials and the efficacy of photochemical synthetic reactions.

A large effort has focused on the study of the excited-state properties and dynamics of cyclizable thiophene-based photoswitches given the promising stabilities of both their ring-open and cyclized isomers.[5, 6] The general consensus from time-resolved photophysical studies is that the excited-state deactivation of these photoswitches is highly sensitive to the molecular conformation: molecules with "parallel" terminal rings undergo rapid (~100 fs) cyclization, whereas molecules with "antiparallel" thiophene groups deactivate via slower pathways, including intersystem crossing to the triplet manifold. The latter introduces an inherent efficiency loss for photoresponsive bond formation that is eliminated in ordered environments, such as crystals or molecular assemblies. Conformational dependence to excited-state relaxation pathways may likewise explain complex deactivation of excited states in E/Z thienyl-ethene photoswitches.[7, 8]

Even for an ensemble of molecules with relatively uniform conformation competing relaxation pathways can be responsible for excited-state deactivation with very different photochemical results. For example, *cis*-stilbene, arguably the original photoswitch prototype first observed by Lewis *et. al.* in 1940,[9] is typically appreciated within the context of cis/trans isomerization.[10-14] However, photocyclization of *cis*-stilbene to 4a,4b-dihydrophenanthrene (DHP) accounts for a non-negligible 10% of the quantum yield for non-radiative relaxation of *cis*-stilbene (compared to 35% for the formation of the isomerization product *trans*-stilbene).[15, 16] Recent photophysical investigations with *cis*-stilbene and its analogs have suggested that cyclization and isomerization do not occur as parallel kinetic processes, but rather that the wavepacket launched onto the excited-state potential energy surface as a result of photon absorption bifurcates shortly after leaving the Franck-Condon region with structural evolution that results in these different products.[17-19]

Our examination of photocylization in various *ortho*-arenes, such as *ortho*-terphenyl (OTP), its alkylated analogs, 1,2,3-triphenylbenzene, *ortho*-quaterphenyl and hexaphenylbenzene (HPB), has shown that cyclization is a favorable excited-state deactivation pathway in all of these systems and with rare exceptions is relatively insensitive to structural modifications of the core OTP chromophore.[20-23] To date, our understanding of excited-state deactivation mechanisms in these systems is based on global spectral analysis of broadband transient absorption spectra, which can be used to extract the timescales for excited-state relaxation and photoproduct (e.g. 4a,4b-dihydrotriphenylene, DHT) formation as well as the spectra associated with principle photochemical species. For example, global analysis of transient spectral dynamics measured following the 266-nm excitation of OTP with both a one-step and two-step sequential kinetic model extract reasonable excited-state and photoproduct spectra, as determined by the quality of residuals between the experimental data and global fits. (The two-step model invokes initial relaxation of the OTP excited state, $S_1^* \rightarrow S_1$.) However, the determination of both relaxation timescales and species associated spectra is subject to the assumed kinetic model. Notably, the spectra of the $S_1$ excited state of OTP and ground-state DHT photoproduct overlap considerably across the visible and near-UV, which has made unambiguous assignment of the kinetics of photocyclization in these systems inherently difficult by pump-probe spectroscopy alone.

Motivated by the recent successes with the application of three-pulse “pump-repump-probe” (PRP) and “pump-dump-probe” spectroscopies to unravel complex dynamics in photoactivated molecular materials, we have applied variations of PRP to disentangle and clarify the nature of competing kinetic pathways in the excited-state relaxation deactivation of *ortho*-arenes.[24-28] This work focuses on deactivation of excited OTP and HPB, which exhibit fairly different excited-state behavior as inferred from pump-probe spectroscopy, with $S_1$ relaxation timescales dominated by processes that occur on ~3 and 400 ps timescales, respectively. Application of PRP spectroscopy on these systems offers insight into the common photochemical behavior of *ortho*-arenes despite variations in structure and furthermore suggests that the variations in excited-state relaxation behavior observed by pump-probe spectroscopy is more likely to be connected with how structural differences impact nonradiative pathways other than cyclization.

## 7.2 Experimental

### 7.2.1 Sample Preparation

5 mM solutions of *ortho*-terphenyl (Sigma) and hexaphenylbenzene (Sigma) in tetrahydrofuran (SPS) or ethylene glycol (Sigma) were prepared by sonication; gentle heating was applied to dissolve HPB (~40 °C). Solutions were transferred to a 0.5 mm pathlength fused silica flow cell (Spectrocell), circulated with a peristaltic pump (Cole-Palmer) and were sparged with $N_2$ for 15 minutes.

### 7.2.2 fs Pump-Repump-Probe Spectroscopy

The laser system and experimental setup has been described previously.[29] The output of a Ti:Sapphire Amplifier (Coherent Legend Elite, 1kHz, 4 mJ, 35 fs) was split into three fractions to generate three independent laser pulses: 266 nm pump/excitation pulses were generated as the third harmonic of the fundamental (specifically via a SHG + SFG mixing cascade); ultraviolet (340 nm) and visible (580 nm) repump pulses were generated using an optical parametric amplifier (Light Conversion) or by second harmonic generation of the fundamental (400 nm); and supercontinuum probe pulses were generated by focusing the fundamental or its 2nd harmonic into crystalline plates (United Crystals) to drive white-light generation. The visible supercontinuum (400-800 nm) was generated by focusing the fundamental into Sapphire (2 mm), whereas the ultraviolet supercontinuum (280-400 nm) was generated with the 2nd harmonic focused into $CaF_2$ (2 mm). The polarization of the 266-nm pump was selected using a zero-order waveplate (Thorlabs) and was determined to have a ~70 fs FWHM duration based on autocorrelation via two photon absorption (2PA) in a 200 μm BBO crystal (United

Crystals) (see Figure A5.9). Visible repump pulses (>400 nm) were determined to have duration of 40-60 fs FWHM based on autocorrelation via 2PA in a GaN LED or by SHG in the aforementioned BBO crystal (see Figure A5.8). The duration of the visible & UV supercontinuum were determined to be 200-250 fs FWHM by cross-correlation in the aforementioned BBO crystal or a BK7 coverslip (Fischer). Importantly, as key PRP results described below examine depletions of probe absorption induce by the repump at time delays much greater than the supercontinuum pulsewidth, the instrument response function is associated with the cross-correlation between the pump and repump pulses.

The pump and repump were delayed independently with two independent translation stages (Newport, ILS250). Both beams were focused towards the sample with lenses. The polarization of all these beams was set immediately before the sample. The probe was focused at the sample using a parabolic mirror (Edmund), with its polarization set with the broadband waveplate immediately before the sample; transmitted probe light was collimated with a lens after the sample and filtered with a U-340 filter for the UV and a 400 nm long pass filter for the visible. All beams were chopped using two optical choppers (Thorlabs). One chopper was equipped with a dual-phase blade allowing for the pump and repump beams to be chopped in a phase-locked sequence using one optical chopper. A second chopper was alternately blocked and unblocked the probe beam at a rate of 250 Hz. Chopping all three beams results in 8-phase data collection that enables simultaneous collection of pump-probe, repump-probe, and pump-repump-probe signals with correction for background, fluorescence and laser scatter (Equation 2.9). Probe light was dispersed with a grating spectrograph (Princeton Acton) and detected with a CCD

(Princeton Pixis 100). Data collection and computation of spectra was performed with an acquisition program written with Labview 2016.

### *7.2.3 Definition of States, Lifetimes and PRP Schemes*

The steady-state absorption spectrum of OTP and transient excited state and photoproduct spectra previously measured by pump-probe spectroscopy are shown in Figure 7.1. The lowest energy absorption features of the $S_0$ ground state of OTP spans 250-300 nm and is readily pumped with 266-nm laser pulses. The $S_1$ OTP absorption spectrum has two characteristic bands centered at 375 and 600 nm that decay with a ~3 ps lifetime; their decay reveals the underlying absorption spectrum of $S_0$ DHT. The DHT absorption spectrum has two characteristic bands centered at 340 and 580 nm that decay with a 45 ns lifetime that corresponds with thermally activated ring-reopening to regenerate the reactant, OTP. Based on these differences in the excited state and photoproduct spectra and the observable lifetime of the OTP excited state, appropriate PRP schemes can be designed to more closely interrogate the mechanism of DHT formation.

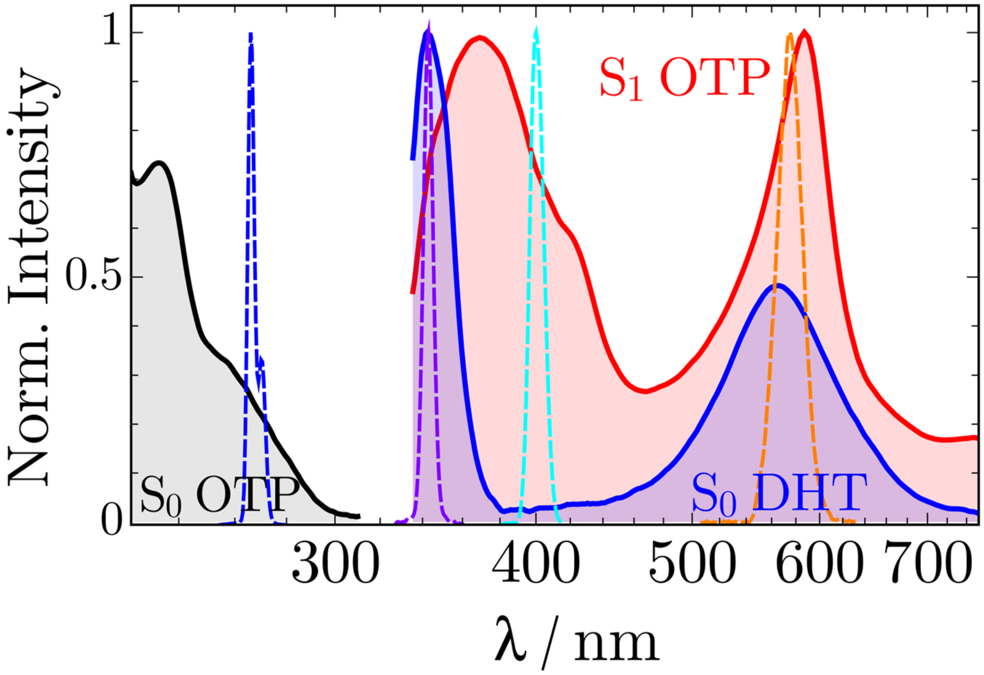

**Figure 7.1.** $S_0$ OTP (steady state), $S_1$ OTP (1 ps), and $S_0$ DHT (1 ns) absorption features as well as spectra of the pump and repump wavelengths used in the present study.

The general PRP experiment includes three time delays between pump-repump, pump-probe and repump-probe ($\Delta t_{1,2}$, $\Delta t_{1,3}$ and $\Delta t_{2,3}$, respectively) as denoted in Figure 7.2a. In practice only two time delays must be defined as the third is constrained by the other two. One variation of PRP spectroscopy is to monitor the effect of a repump pulse on the spectrum of a long-lived species (in this case the DHT photoproduct) long after the initial pump excitation; a critical condition for this experiment is that $\Delta t_{1,3}$ is much larger than the timescale for formation of this species (Figure 7.2b). If the effect of the repump pulse is to increase or deplete the entire spectrum of the photoproduct, this approach can be considered PRP "action" spectroscopy.[30-32] This method is implemented by fixing $\Delta t_{1,3}$

at a delay much longer than that the excited state decay ($\Delta t_{1,3}$=1 ns) and photoproduct thermalization and scanning $\Delta t_{1,2}$ (or alternatively $\Delta t_{2,3}$) from 0-100 ps. For small molecular systems the polarization of the probe need not be defined so long as the rotational diffusion is complete before a time delay of $\Delta t_{1,3}$ is reached; under these conditions a relative angle of pump and repump of 54.7 degrees (magic angle) will ensure that only changes in photoproduct population yield are observed. A second approach is to monitor the effect of the repump on the transient spectral dynamics shortly after excitation by monitoring the "hole" or "bleach" induced by the repump (Figure 7.2c). This experiment involves fixing $\Delta t_{2,3}$ and varying $\Delta t_{1,2}$ (or $\Delta t_{1,3}$). As this measurements may involve both short $\Delta t_{1,2}$ and $\Delta t_{2,3}$ it is not capable of eliminating the influence of polarization anisotropy on bleaching efficiency. (A related experiment involves fixing $\Delta t_{1,2}$ and scanning $\Delta t_{1,3}$. This approach allows one to monitor the impact of the repump pulse on the overall population of pump-induced excited state and photoproduct.) This is used to verify which and how excited-state signals respond to the repump pulse.

A key to each of these experiments is to choose repump wavelengths that can selectively depopulate one state or the other where possible. For example, repumping at 400 nm is strongly selective for excitation of $S_1$ OTP, and therefore enables evaluation of what features from the transient spectrum in other regions (e.g. the visible) are associated with this state.

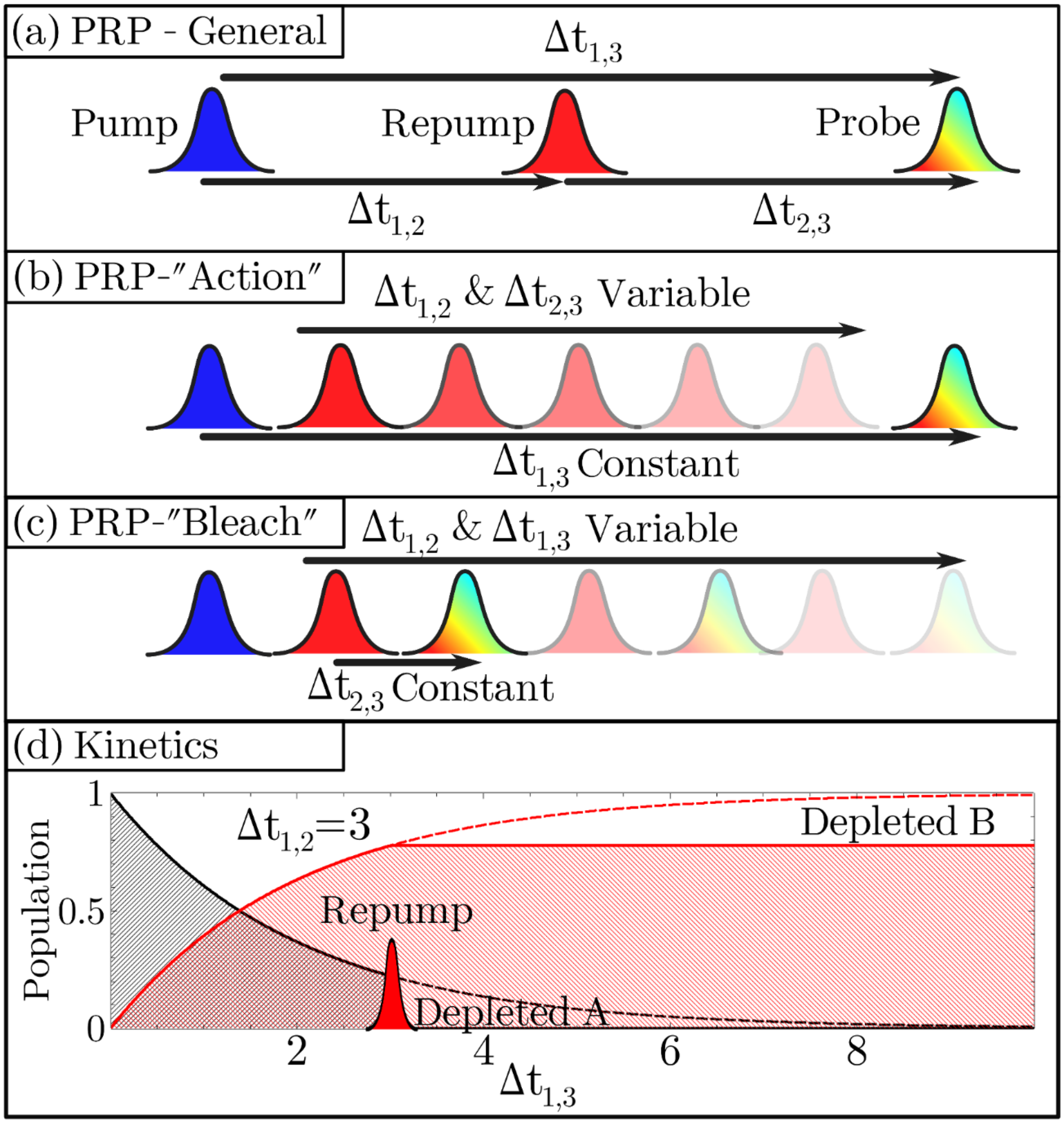
(a) PRP - General
$\Delta t_{1,3}$
Pump
Repump
Probe
$\Delta t_{1,2}$
$\Delta t_{2,3}$
(b) PRP-"Action"
$\Delta t_{1,2}$ & $\Delta t_{2,3}$ Variable
$\Delta t_{1,3}$ Constant
(c) PRP-"Bleach"
$\Delta t_{1,2}$ & $\Delta t_{1,3}$ Variable
$\Delta t_{2,3}$ Constant
(d) Kinetics
Population
1
0.5
0
$\Delta t_{1,2}=3$
Depleted B
Repump
Depleted A
2
4
6
8
$\Delta t_{1,3}$

**Figure 7.2.** Definition of (a) the general PRP Scheme and relevant time delays, as well as more specific definitions of (b) PRP "Action" and (c) PRP "Bleach" experiments. (d) The kinetic influence on repumping and depleting state A for sequential kinetics ($\tau$ = 2) at $\Delta t_{1,2}$=3 results in a corresponding depletion of B. If $\Delta t_{1,2}$ is varied to perform the PRP-Action experiment the relative depletion of B can be used to isolate the kinetics of formation for B.

## 7.3 Results and Discussion

### *7.3.1 PRP "Action" and "Bleach" Spectroscopy of DHT and OTP*

The PRP action of DHT was performed through re-excitation of each of the UV and visible bands of DHT with a 580 and 340 nm repump, respectively (Figures 7.1, 7.3 and 7.4). The influence of the repump was monitored according to changes in intensity of the other product transition (e.g. repump visible, probe UV) in order to avoid collection of intense pump and repump pulse scattering. In addition, the complementary PRP action experiment was performed with a 400 nm repump pulse that is resonant predominantly with the ESA of OTP (see Figure 7.1). Both experiments were performed with $\Delta t_{1,3}$=1 ns in order to eliminate effects from evolution in the polarization anisotropy of molecular transition dipoles between the application of the repump and probe pulses. A half-wave plate was used to fix the relative angle between pump and repump to magic angle to ensure that application of the repump pulse reflects changes in transient populations and not transition dipole polarization. The time-dependent signal shown for PRP action experiments is the Relative PRP Depletion (RPD) of the photoproduct, which has been band integrated, inverted and normalized to compare against the hypothetical kinetic model for photoproduct formation via a sequential kinetic relaxation model.

Figure 7.3 shows the PRP action kinetics of OTP with a 580 nm repump pulse and the RPD band integrated from 320-360 nm. The analogous action experiment with a 340 nm repump pulse and the RPD band integrated from 500-670 nm is shown in Figure 7.4. Note that the rise in RPD in both cases is nearly instantaneous with a very weak time dependence, much in contrast with the kinetics of photoproduct formation associated with previously applied global fitting models.

As the excited reactant and ground-state photoproduct both absorb strongly at these two repump wavelengths, this data could suggest that the photoproduct population is depleted as a result of the reexcitation that disrupts deactivation of the $S_1$ state of OTP via cyclization. Alternatively, since it is well known that cyclized structures like DHT readily undergo photoinduced bond fission, these results might rather reflect that reexcitation only depletes the photoproduct population itself. This latter interpretation would imply that the photoproduct is formed instantaneously upon photoexcitation and

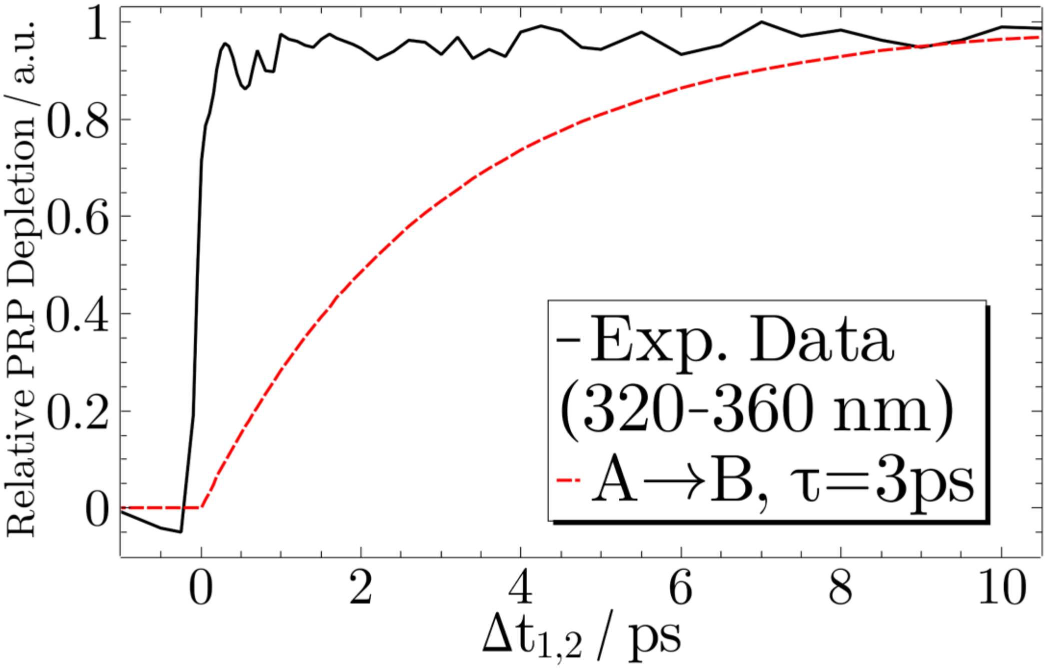

**Figure 7.3.** PRP Action Spectroscopy of DHT following 266 nm photoexcitation of OTP and re-excited with 580 nm (black solid line). Here $\Delta t_{1,3}$ is set at 1 ns, the pump-repump polarization was set to magic angle, and the action was probed in the UV (320-360 nm) to avoid collection of scattered repump. The rise in signal expected for a hypothetical sequential mechanism ($S_1$ OTP → $S_0$ DHT) with $\tau = 3$ ps is given for comparison (red dashed line).

that the excited-state population that persists for the few picoseconds thereafter relaxes by some other nonradiative pathway.

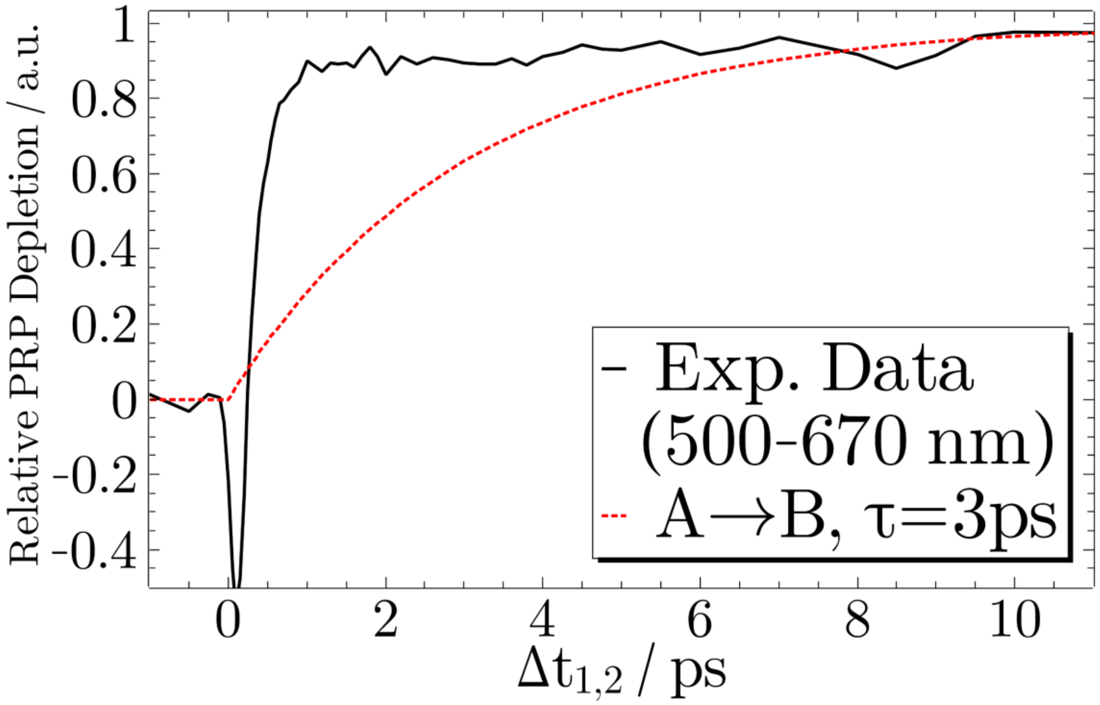

**Figure 7.4.** PRP Action of DHT with a 340 nm repump pulse. In addition $\Delta t_{1,3}$=1 ns and the probe range was in the visible to avoid scattering effects.

One way to differentiate between these two possibilities is to repump at a wavelength that is strongly selective for only the OTP excited state (i.e. 400 nm, Figure 7.1). In pump-probe measurements the relative intensity of the peak OTP $S_1$ absorption intensity at 400 nm is roughly 25-30 times stronger than the absorption of DHT product absorption apparent after the excited state has decayed. The 400 nm PRP action trace is plotted in blue in Figure 7.5 and shows the same temporal response observed with the 340 and 580 nm repump (Figures 7.3 and 7.4), i.e. an instantaneous rise followed by a plateau in signal. Notably, the intensity of this depletion is significantly weaker than what is observed at these other two wavelengths, as reflected in the significant reduction in signal to noise at this repump wavelength. Because the latest repump delays correspond with exciting pure photoproduct, which has very weak absorption at 400 nm, this response strongly suggests that the reexcitation of the $S_1$ state has negligible impact on the photoproduct bleach.

To complement the PRP action experiment a PRP bleach experiment was performed to confirm that the 400 nm repump does in fact bleach the $S_1$ OTP signal. The scaled bleach signal plotted in red in Figure 7.5 is the absolute value of the ratio of the PRP bleach signal to the PP signal i.e. $\Delta\Delta OD_{Fl.\ Corr.} / \Delta OD_{Fl.\ Corr.}$ (see Equations 2.6 and 2.9). This scaled signal is useful for determining the percentage of $S_1$ signal bleached, which in turn can be used to infer the maximum reduction in DHT signal if the photoreaction does indeed follow sequential kinetics. Therefore the corresponding 400 nm action spectra should show a 25 % depletion in DHT signal at $\Delta t_{1,2}$=500 fs that decays with a ~3 ps lifetime. The observed 400 nm action spectra shows neither effect but only a very weak depletion signal that remains constant across the range of $\Delta t_{1,2}$. The conclusion of these PRP experiments is that the observed $S_1$ decay is completely uncoupled to the formation of DHT and that the reaction seems to proceed “instantaneously” (i.e. timescales < PRP instrument response) possibly by wavepacket bifurcation immediately following projection onto the Franck-Condon region of the $S_1$ PES.[33]

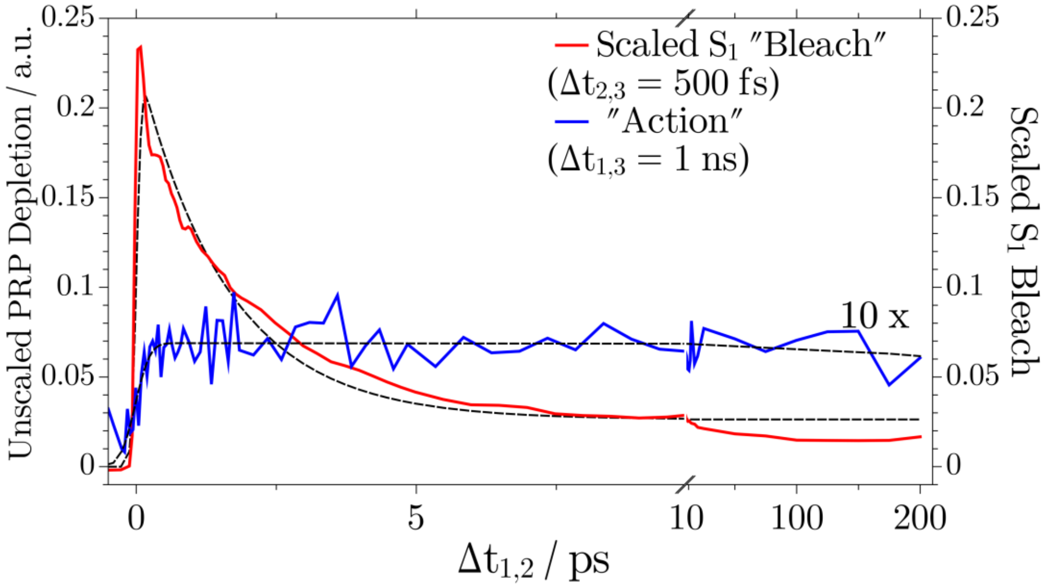

**Figure 7.5.** PRP action (blue line) and bleach (red line) traces for OTP in THF with a 400 nm repump (all parallel polarizations). Note that the PRP depletion for the Action experiment is unscaled while the scaled bleach signal represents the absolute amount of ESA transient absorption signal bleached (-ΔΔOD/ΔOD). This comparison shows that while the $S_1$ signal is strongly bleached there is no corresponding modulation in DHT depletion (i.e. Action trace) on the timescale of the bleach. Hence it is concluded that the spectral signatures associated with the $S_1$ OTP and $S_0$ DHT populations are not connected kinetically.

### *7.3.2 Anisotropy of the OTP to DHT photoreaction*

Polarized pump-probe fs-TAS measurements were performed with 266-nm excitation of OTP to track the decay of polarization anisotropy, r(t), in the photoinduced signal that arises from a combination of OTP ESA and DHT GSA. Figure 7.6 plots the anisotropy obtained at the peak of the OTP ESA band, between 595 to 605 nm (solid black line); a scaled trace of the excited state population decay is plotted for comparison. Assignment of the r(t) to a single species is obscured by the overlapping spectral components. An exponential fit results in a r(t) decay lifeimte of 11 ± 0.5 ps, but this timescale reflects a combination of both the excited-state decay as well as contributions from the scrambling of transition dipole moments due to rotational diffusion or structural dynamics. Nonetheless, the data shows an initial anisotropy of 0.23 indicating a 32 degree change in the transition dipole occurring on a sub-100 fs timescale.[34] These values are quite similar to those determined for the *cis*-stilbene to DHP reaction.[35]

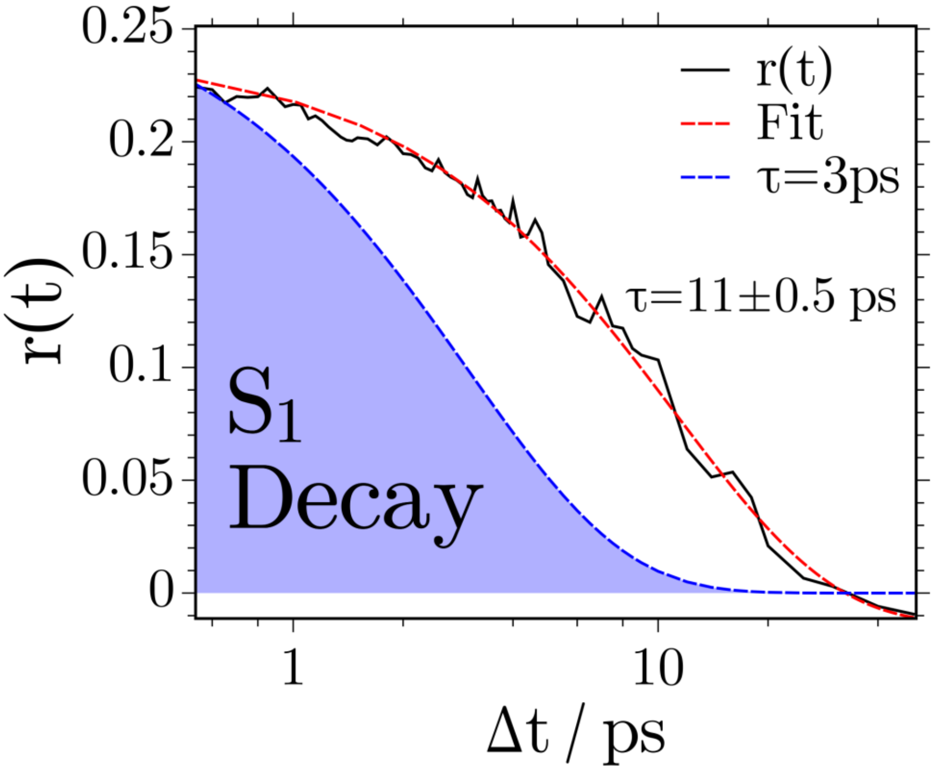

**Figure 7.6**. Traditional 2-pulse polarization anisotropy of OTP following 266 nm excitation and band integration from 595-605 nm.

The complementary experiment for deconvolving the rotational anisotropy of $S_1$ OTP and $S_0$ DHT is by a polarized action PRP experiment. The polarized action experiment is similar to the 2-pulse polarized experiment except that the repump bleaches the evolving rotational population and the probe monitors the corresponding decrease in population after all polarization memory has been lost (i.e. $\Delta t >> \tau_{rotation}$). Therefore a similar parallel (∥) and perpendicular (⊥) pump-repump polarization response for the polarized action experiment is expected compared to that of the traditional 2-pulse measurement.[36-38] Figure 7.7 compares the polarization dependence of parallel, perpendicular and "magic" relative pump-repump angle showing a weak or negligible polarization dependence. The apparent contradiction of the 2-pulse polarized and 3-pulse polarized action results indicate that the 2-pulse experiment may include significant contamination from the DHT product as predicted. This is not surprising considering the OTP ESA feature is approximately 6 times that of the DHT absorption over the integrated range of 595-605 nm. The 3-pulse polarized action results further indicates that the reaction coordinate from OTP to DHT results in an apparent "scrambling" of the polarization memory that has been proposed for the *cis*-stilbene to DHP reaction.[35] The alternative interpretation that the initial transition dipole moment of $S_0$ OTP changes drastically following formation of DHT is contrary to the calculated change in angle of the transition dipole moment (6°) determined using time-dependent density functional theory[39, 40] (TD-B3LYP/6-31+G*). A 6° change in transition dipole moment, similar to the prediction for the CS/DHP reaction[35], would result in an unnoticeable change in the initial anisotropy from 0.4 to 0.39.[34]

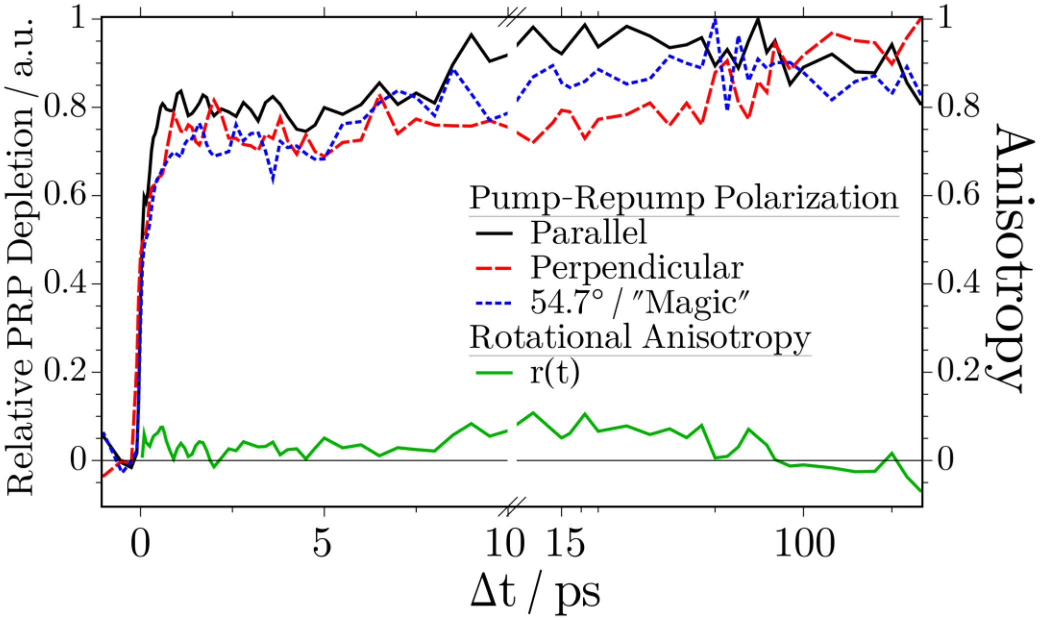

**Figure 7.7.** 3-pulse polarized Action PRP of photoexcited OTP with a 266 nm pump, 580 nm repump, $\Delta t_{13}$=1 ns, and the RPD signal of DHT integrated from 310-360 nm. The RPD of DHT shows anomalous anisotropy behavior with a relatively constant r(t) of < 0.1.

### *7.3.3 PRP Action Spectroscopy of Hexaphenylbenzene*

To further demonstrate that ultrafast photocyclization is a common chemical process of *ortho*-arenes we chose to interrogate the photophysics of hexaphenylbenzene (HPB). This system is highly modified structurally compared with OTP and has much longer excited state $S_1$ lifetime as measured by pump-probe spectroscopy. However, both systems have similar ESA and photoproduct absorption features, suggesting that photophysical differences are due to perturbations of the structural modifications. The isotropic PRP action trace is plotted in Figure 7.8 with $\Delta t_{1,3}$=1.2 ns and a 360 nm repump that is matched to the $\lambda_{max}$ of the HPB photoproduct, tetraphenyl-DHT (TphDHT). While some short time behavior is observed at time delays < 2 ps the kinetics remain fairly constant on the timescale for the $S_1$ decay; a hypothetical induction to the photoproduct based on a sequential relation model is shown for comparison (red dashed line). The flat, constant signal observed on a logarithmic scale from 10-500 ps makes it clear that the kinetic formation of TphDHT is not coupled to the slow $S_1$ decay since a constant depletion is obtained across this time regime. This mechanism is consistent with results

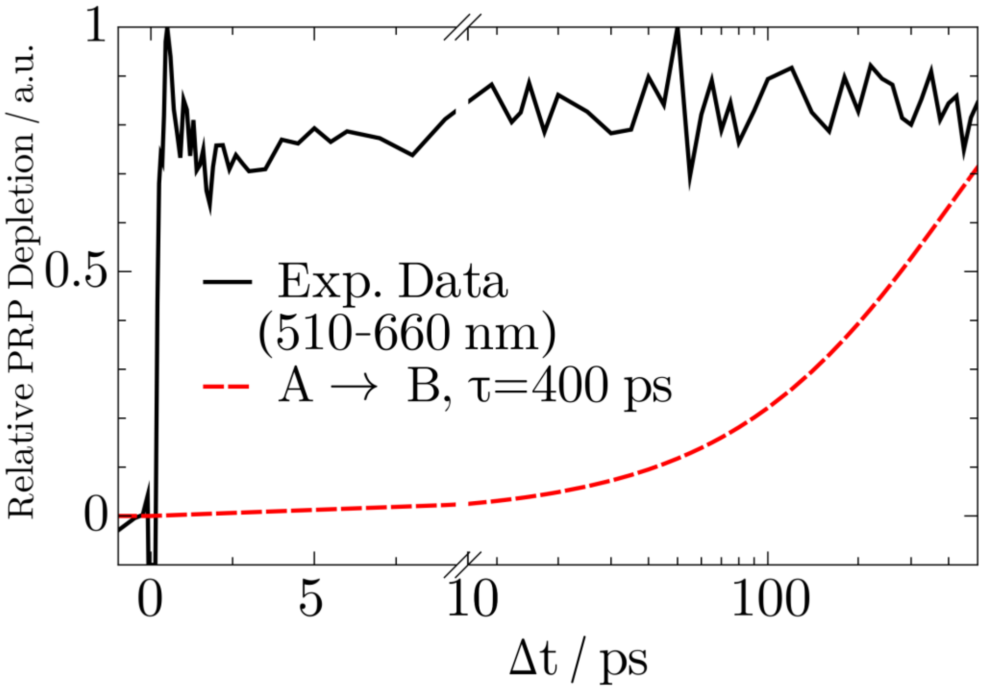

**Figure 7.8** Isotropic PRP action of HPB in THF pumped with 266 nm, repumped with 360 nm and probed in the visible with the RPD integrated from 510-660 nm. In addition $\Delta t_{1,2}$=1.2 ns and the pump-repump polarization was set to magic angle.

on OTP that seem to suggest that most of the photoproduct is formed on a faster or instantaneous timescale relative to that of the longer $S_1$decay.

## 7.4 Conclusions

Pump-Repump-Probe spectroscopy indicates an apparent disconnect between the observed ESA of OTP with a lifetime of ~3 picoseconds and the formation of DHT which based on PRP action results is formed instantaneously in < 100 femtoseconds. This indicates that wavepacket branching must occur immediately following photoexcitation that results in 2 distinct nonadiabatic deactivation pathways. An identical result was obtained for hexaphenylbenzene with a much longer excited-state lifetime of ~400 ps further indicating the kinetic separation between the cyclization product (TphDHT) and the observed ESA. Additionally, anisotropy analysis using PRP indicates a randomization of transition dipole moments following photocyclization that is not observable using traditional 2 pulse polarization anisotropy experiments.

## 7.5 References

1. Marom, N.; Bernstein, J.; Garel, J.; Tkatchenko, A.; Joselevich, E.; Kronik, L.; Hod, O., Stacking and Registry Effects in Layered Materials: The Case of Hexagonal Boron Nitride. *Phys Rev Lett* **2010,** *105* (4).

2. Oelgemöller, M.; Jung, C.; Mattay, J., Green photochemistry: Production of fine chemicals with sunlight. *Pure and Applied Chemistry* **2007,** *79* (11).

3. Albini, A.; Fagnoni, M., Green chemistry and photochemistry were born at the same time. *Green Chemistry* **2004,** *6* (1), 1.

4. Schiel, C.; Oelgemöller, M.; Ortner, J. r.; Mattay, J., Green photochemistry: the solar-chemical 'Photo–Friedel–Crafts acylation' of quinones. *Green Chemistry* **2001,** *3* (5), 224-228.

5. Irie, M.; Fukaminato, T.; Matsuda, K.; Kobatake, S., Photochromism of Diarylethene Molecules and Crystals: Memories, Switches, and Actuators. *Chemical Reviews* **2014,** *114* (24), 12174-12277.

6. Irie, M., Diarylethenes for Memories and Switches. *Chemical Reviews* **2000,** *100* (5), 1685-1716.

7. Guo, X.; Zhou, J.; Siegler, M. A.; Bragg, A. E.; Katz, H. E., Visible-Light-Triggered Molecular Photoswitch Based on Reversible E/Z Isomerization of a 1,2-Dicyanoethene Derivative. *Angewandte Chemie International Edition* **2015,** *54* (16), 4782-4786.

8. Zhou, J.; Guo, X.; Katz, H. E.; Bragg, A. E., Molecular Switching via Multiplicity-ExclusiveE/ZPhotoisomerization Pathways. *J Am Chem Soc* **2015**, *137* (33), 10841–10850.

9. Lewis, G. N.; Magel, T. T.; Lipkin, D., The Absorption and Re-emission of Light by cis- and trans-Stilbenes and the Efficiency of their Photochemical Isomerization. *J Am Chem Soc* **1940,** *62* (11), 2973-2980.

10. Quick, M.; Dobryakov, A. L.; Ioffe, I. N.; Granovsky, A. A.; Kovalenko, S. A.; Ernsting, N. P., Perpendicular State of an Electronically Excited Stilbene: Observation by Femtosecond-Stimulated Raman Spectroscopy. *The Journal of Physical Chemistry Letters* **2016**, 4047-4052.

11. Takeuchi, S.; Ruhman, S.; Tsuneda, T.; Chiba, M.; Taketsugu, T.; Tahara, T., Spectroscopic Tracking of Structural Evolution in Ultrafast Stilbene Photoisomerization. *Science* **2008,** *322* (5904), 1073-1077.

12. Ishii, K.; Takeuchi, S.; Tahara, T., A 40-fs time-resolved absorption study on cis-stilbene in solution: observation of wavepacket motion on the reactive excited state. *Chem Phys Lett* **2004,** *398* (4–6), 400-406.

13. Quenneville, J.; Martínez, T. J., Ab Initio Study of Cis−Trans Photoisomerization in Stilbene and Ethylene. *The Journal of Physical Chemistry A* **2003,** *107* (6), 829-837.

14. Sension, R. J.; Repinec, S. T.; Szarka, A. Z.; Hochstrasser, R. M., Femtosecond Laser Studies of the Cis-Stilbene Photoisomerization Reactions. *J Chem Phys* **1993,** *98* (8), 6291-6315.

15. Muszkat, K. A.; Fischer, E., Structure Spectra Photochemistry and Thermal Reactions of 4a,4b-Dihydrophenanthrenes. *J Chem Soc B* **1967,** (7), 662-&.

16. Wismonski-Knittel, T.; Fischer, G.; Fischer, E., Temperature dependence of photoisomerization. Part VIII. Excited-state behaviour of 1-naphthyl-2-phenyl- and 1,2-dinaphthyl-ethylenes and their photocyclisation products, and properties of the latter. *Journal of the Chemical Society, Perkin Transactions 2* **1974,** (15), 1930.

17. Harabuchi, Y.; Keipert, K.; Zahariev, F.; Taketsugu, T.; Gordon, M. S., Dynamics Simulations with Spin-Flip Time-Dependent Density Functional Theory: Photoisomerization and Photocyclization Mechanisms of cis-Stilbene in $\pi\pi^*$ States. *The Journal of Physical Chemistry A* **2014**.

18. Harabuchi, Y.; Yamamoto, R.; Maeda, S.; Takeuchi, S.; Tahara, T.; Taketsugu, T., Ab Initio Molecular Dynamics Study of the Photoreaction of 1,1′-Dimethylstilbene upon $S_0 \rightarrow S_1$ Excitation. *The Journal of Physical Chemistry A* **2016,** *120* (44), 8804-8812.

19. Prlj, A.; Došlić, N.; Corminboeuf, C., How does tetraphenylethylene relax from its excited states? *Phys. Chem. Chem. Phys.* **2016,** *18* (17), 11606-11609.

20. Molloy, M. S.; Snyder, J. A.; DeFrancisco, J. R.; Bragg, A. E., Structural Control of Nonadiabatic Photochemical Bond Formation: Photocyclization in Structurally Modified ortho-Terphenyls. *The Journal of Physical Chemistry A* **2016,** *120* (23), 3998-4007.

21. Snyder, J. A.; Bragg, A. E., Structural Control of Nonadiabatic Bond Formation: The Photochemical Formation and Stability of Substituted 4a,4b-Dihydrotriphenylenes. *The Journal of Physical Chemistry A* **2015,** *119* (17), 3972-3985.

22. Molloy, M. S.; Snyder, J. A.; Bragg, A. E., Structural and Solvent Control of Nonadiabatic Photochemical Bond Formation: Photocyclization of o-Terphenyl in Solution. *The Journal of Physical Chemistry A* **2014,** *118* (22), 3913-3925.

23. Smith, M. C.; Snyder, J. A.; Streifel, B. C.; Bragg, A. E., Ultrafast Excited-State Dynamics of ortho-Terphenyl and 1,2-Diphenylcyclohexene: The Role of "Ethylenic Twisting" in the Nonadiabatic Photocyclization of Stilbene Analogs. *The Journal of Physical Chemistry Letters* **2013,** *4* (11), 1895-1900.

24. Ward, C. L.; Elles, C. G., Cycloreversion Dynamics of a Photochromic Molecular Switch via One-Photon and Sequential Two-Photon Excitation. *The Journal of Physical Chemistry A* **2014,** *118*, 10011-10019.

25. Fitzpatrick, A. E.; Lincoln, C. N.; van Wilderen, L. J. G. W.; van Thor, J. J., Pump–Dump–Probe and Pump–Repump–Probe Ultrafast Spectroscopy Resolves Cross Section of an Early Ground State Intermediate and Stimulated Emission in the Photoreactions of the Pr Ground State of the Cyanobacterial Phytochrome Cph1. *The Journal of Physical Chemistry B* **2012,** *116* (3), 1077-1088.

26. Fischer, M. K.; Gliserin, A.; Laubereau, A.; Iglev, H., Ultrafast electron transfer processes studied by pump-repump-probe spectroscopy. *Journal of Biophotonics* **2011,** *4* (3), 178-183.

27. Busby, E.; Carroll, E. C.; Chinn, E. M.; Chang, L.; Moulé, A. J.; Larsen, D. S., Excited-State Self-Trapping and Ground-State Relaxation Dynamics in Poly(3-hexylthiophene) Resolved with Broadband Pump–Dump–Probe Spectroscopy. *The Journal of Physical Chemistry Letters* **2011,** *2* (21), 2764-2769.

28. Papagiannakis, E.; Vengris, M.; Larsen, D. S.; van Stokkum, I. H. M.; Hiller, R. G.; van Grondelle, R., Use of Ultrafast Dispersed Pump−Dump−Probe and Pump−Repump−Probe Spectroscopies to Explore the Light-Induced Dynamics of Peridinin in Solution. *The Journal of Physical Chemistry B* **2006,** *110* (1), 512-521.

29. Yu, W.; Magnanelli, T. J.; Zhou, J.; Bragg, A. E., Structural Heterogeneity in the Localized Excited States of Poly(3-hexylthiophene). *The Journal of Physical Chemistry B* **2016,** *120* (22), 5093-5102.

30. Yatsyna, V.; Bakker, D. J.; Salén, P.; Feifel, R.; Rijs, A. M.; Zhaunerchyk, V., Infrared Action Spectroscopy of Low-Temperature Neutral Gas-Phase Molecules of Arbitrary Structure. *Phys Rev Lett* **2016,** *117* (11), 118101.

31. Nei, Y. w.; Crampton, K. T.; Berden, G.; Oomens, J.; Rodgers, M. T., Infrared Multiple Photon Dissociation Action Spectroscopy of Deprotonated RNA Mononucleotides: Gas-Phase Conformations and Energetics. *The Journal of Physical Chemistry A* **2013,** *117* (41), 10634-10649.

32. Adamson, B. D.; Coughlan, N. J. A.; da Silva, G.; Bieske, E. J., Photoisomerization Action Spectroscopy of the Carbocyanine Dye DTC+in the Gas Phase. *The Journal of Physical Chemistry A* **2013,** *117* (50), 13319-13325.

33. Krause, P.; Matsika, S.; Kotur, M.; Weinacht, T., The influence of excited state topology on wavepacket delocalization in the relaxation of photoexcited polyatomic molecules. *J Chem Phys* **2012,** *137* (22), 22A537.

34. Nickel, B., On the elimination of the polarization bias of the luminescence or transient absorption of photoexcited isotropic solutions. *Journal of Luminescence* **1989,** *44* (1-2), 1-18.

35. Repinec, S. T.; Sension, R. J.; Szarka, A. Z.; Hochstrasser, R. M., Femtosecond laser studies of the cis-stilbene photoisomerization reactions: the cis-stilbene to dihydrophenanthrene reaction. *The Journal of Physical Chemistry* **1991,** *95* (25), 10380-10385.

36. Johnson, J. M.; Chen, R.; Chen, X.; Moskun, A. C.; Zhang, X.; Hogen-Esch, T. E.; Bradforth, S. E., Investigation of Macrocyclic Polymers as Artificial Light Harvesters: Subpicosecond Energy Transfer in Poly(9,9-dimethyl-2-vinylfluorene). *The Journal of Physical Chemistry B* **2008,** *112* (51), 16367-16381.

37. Lessing, H. E.; Von Jena, A., Separation of rotational diffusion and level kinetics in transient absorption spectroscopy. *Chem Phys Lett* **1976,** *42* (2), 213-217.

38. Gaab, K. M.; Bardeen, C. J., Nonstationary Rotational Diffusion in Room Temperature Liquids Measured by Femtosecond Three-Pulse Transient Anisotropy. *Phys Rev Lett* **2004,** *93* (5), 056001.

39. Casida, M. E.; Huix-Rotllant, M., Progress in Time-Dependent Density-Functional Theory. *Annual Review of Physical Chemistry* **2012,** *63* (1), 287-323.

40. Hirata, S.; Head-Gordon, M.; Szczepanski, J.; Vala, M., Time-Dependent Density Functional Study of the Electronic Excited States of Polycyclic Aromatic Hydrocarbon Radical Ions. *The Journal of Physical Chemistry A* **2003,** *107* (24), 4940-4951.

# Appendix 1

## Supporting Information for Chapter 3:

## Ultrafast Excited-State Dynamics of ortho-Terphenyl and 1,2-Diphenylcyclohexene: The Role of "Ethylenic Twisting" in the Non-Adiabatic Photocyclization of Stilbene Analogs

### A1.1. Sample Preparation:

***A1.1.1. Synthesis of 1,2-diphenyl-cyclohexene (DPCH).*** 1,2-dibromocyclohexene was prepared according to literature procedures .[1] Tributylphenylstannane and toluene were purchased from Sigma Aldrich. Tributylphenylstannane was used as received, and toluene was dried over 4Å molecular sieves and sparged with dry $N_2$ for 30 min prior to use. $(PPh_3)_2PdCl_2$ was purchased from Strem Chemical and used as received.

1,2-dibromocyclohexene (100.0 mg, 0.42 mmol), tributylphenylstannane (0.300 mL, 0.92 mmol), and $(PPh_3)_2PdCl_2$ (14.6 mg, 0.021 mmol) were added to a 25 mL flame dried, air free Schlenk flask charged with a stir bar. The flask was then evacuated and refilled with dry $N_2$ three times, after which 7 mL of dry, degassed toluene was added by syringe. The flask was covered in foil to exclude ambient light and the mixture was heated to 105 °C for 16 h, after which the reaction mixture was allowed to cool to ambient temperature, and poured into a rapidly stirring mixture of 20 mL 1M aq. KF and 20 mL ether. The mixture was stirred for 15 minutes in the dark, at which point the solid was filtered off, and the organic layer separated and dried over $MgSO_4$. The solvent was evaporated and the crude oil was purified by column chromatography ($SiO_2$, hexanes as eluent). Pure product was isolated as a light yellow waxy solid (24.9 mg, 25% yield). Characterization data ($^1H$ and $^{13}C$ NMR) matched with literature data.[2]

***A1.1.2. Solution preparation, handling, and characterization***. *ortho*-terphenyl (OTP) was purchased from Sigma-Aldrich and used "as-is." Tetrahydrofuran (THF, unstabilized, Sigma Aldrich) was deaerated through multiple freeze-pump-thaw cycles prior to solution preparation. OTP solutions were made with concentrations of both 5 and 20 mM; time-resolved measurements exhibit no concentration dependence in this range. In order to prevent any possible accumulation of long-lived photoproducts during spectroscopic measurements all samples were circulated through a 0.5mm path-length quartz flowcell (Spectrocell) using a peristaltic pump (Masterflex). The sample flow circuit is constructed entirely of materials that are chemically compatible with THF (e.g. PTFE tubing and compression fittings, a quartz flowcell, a glass reservoir) and has a circulation volume of less than 20 mL.

DPCH solutions in freshly distilled THF were prepared with a concentration of 5-10 mM. The DPCH cyclization photoproduct (9,10-cyclohexano-4a,4b-dihydrophenanthrene) readily oxides in presence of oxygen to form a phenanthrene derivative (9,10-cyclohexano-phenanthrene), as validated through mass spectrometry of DPCH samples both before and after UV irradiation (in contrast, dihydrotriphenylene generated from the photocyclization of OTP does not oxidize readily in presence of air, but only when stronger oxidizing agents, such as $I_2$, are added.[3] Furthermore, the oxidized photoproduct has a substantially stronger absorption cross-section in the UV than DPCH Consequently solutions of DPCH had to be studied immediately after preparation even in solutions made with freshly distilled solvent. A fiber-optically coupled minispectrometer (StellarNet) was used to measure the sample absorbance between 250 and 400 nm roughly 1" downstream from the laser interaction region in the flow cell in order to monitor production and potential accumulation of oxidized photoproduct during the course of time-resolved measurements. Together these measures facilitated collection of time-resolved signals prior to spectroscopically significant accumulation of oxidized photoproduct. As noted in the main text, transient spectroscopic features measured with DPCH closely match those measured from the isochromophoric molecule *cis*-stilbene. This spectroscopic similarity with *cis*-stilbene and the absence of a UV photo-induced transient absorption above 600 nm from highly oxidized solutions of DPCH validates our assignment of the observed spectral dynamics to population decay of $S_1$ DPCH.

## A1.2. Ultrafast Transient Absorption measurements:

***A1.2.1. Experimental set-up and data collection.*** All experiments utilize our lab's regeneratively amplified Ti:Sapphire laser (Coherent Legend Elite, 4.5 mJ/pulse, 1 kHz repetition rate, 35-fs pulse duration, 800-nm peak wavelength). Roughly 1 mJ of this output is used to generate ~20 μJ UV photoexcitation pulses by frequency conversion: ~500 μJ are used to generate the second harmonic at 400 nm in a 200-micron-thick Type I BBO crystal (United Crystals); 266-nm photoexcitation pulses are generated by mixing the second harmonic with ~500 μJ of 800-nm fundamental in a type-II BBO crystal (150 microns, United Crystal). Weak broadband probing pulses are obtained through white-light generation in specific crystalline plates (4). For the visible transient absorption measurements, less than 10 μJ at 800 nm was focused into a sapphire plate to produce a stable white-light continuum at 470-720 nm. The visible continuum was generated using 800 nm pulses polarized at 45 degrees; a thin broadband wire-grid polarizer (Thorlabs) was then used to select the polarization of the visible probe light immediately before the sample. In this way the probe beam polarization could be controlled simply by adjusting the orientation of the wire-grid polarizer.

UV photoexcitation pulses were collimated to a 4-mm beam diameter before the flowcell. The broadband probe pulse was focused at the sample and overlapped at a small angle with respect to the photoexcitation pulse in the sample. The excitation pulse was blocked after the sample with a beam dump, and residual pump scatter along the probe propagation direction was blocked with a 280-nm long-pass filter. Visible and UV continua were also passed through appropriate bandpass filters to shape spectra for detection and to remove residual 800 or 400-nm light that was used to drive continuum generation. In our set-up the probe continuum is dispersed using a 0.3-m spectrograph (Acton-2360, Princeton Instruments) outfitted with a low-resolution grating (800nm blaze, 150 lines/mm). Probe spectra are detected using a CCD camera (Pixis-100BR, Princeton Instruments), which collects the continuum probe on each laser shot at 1 kHz. The photoexcitation beam is synchronously chopped at 500 Hz, such that transient absorption spectra can be calculated using consecutive pairs of probe spectra. The relative pump-probe pulse delay is controlled by retroreflecting the pump pulse off of 266-nm high reflectors mounted to a motorized translation stage (Newport), which was adjusted to change the relative optical pathlength of the pump and probe pulses.

Transient spectra shown here were collected by averaging at each time delay, with 30,000-50,000 on/off ratios for visible TAS. Positioning of the translation stage, collection of probe spectra, synchronization with the chopper phase, and calculation and averaging of transient spectra were all coordinated through a home-built LabVIEW data acquisition program. Pump-probe measurements of neat solvents were made such that transient spectra could be chirp corrected according to the time-dependence of the non-linear, two-pulse solvent response.

***A1.2.2. Data Analysis.*** TAS spectra were chirp-corrected using routines written in MATLAB. A routine was used to determine the wavelength-dependence in time zero from the two-pulse solvent response measurements. This program identifies the onset wavelength of the solvent peak measured at each time delay. From this information a low-order polynomial was determined that characterized the variation in time zero with probe wavelength. This polynomial was then used to correct chirped TAS intensity data from the OTP and DPCH sample scans and to rectify experimental timescales via a series of thresholding and interpolating steps. Data analysis procedures first were performed on the data sets collected using each polarization independently, and "magic-angle" spectra then were calculated using chirp-corrected parallel and perpendicular spectra. Spectral intensities at very long time delays (times longer than the time-dependent changes in rotational anisotropy) were scaled to compensate for any differences in the intensities due to changes in the experimental conditions between the two polarizations.

Cuts through transient spectra plotted in Figure 3.1(c) of the main text were fitted with single or biexponential decay functions convoluted with the instrument response using a fitting algorithm written in MATLAB. The experimental time resolution (~150-200 fs) was limited primarily by group-velocity mismatch within the sample. OTP TA at 605 nm was fitted with a single exponential plus a constant offset to account for DHT absorption at this wavelength following cyclization. DPCH data were better fit with a biexponential function, although more than 50% of the excited-state decay occurs on sub-ps timescales. Fitting parameters for transients are provided in Table A1.1.

**Table A1.1.** Parameters for fits to transients plotted in the main text.

| | $A_1$ | $\tau_1$ | $A_2$ | $\tau_2$ |
|---|---|---|---|---|
| OTP | 0.00324 | 2.91 ps | 0.000522 | ($\infty$) |
| DPCH | 0.000194 | 0.44 ps | 0.000114 | 2.53 ps |

## A1.3. Electronic structure calculations.

***A1.3.1. Electronic structure calculations at the $S_0$ minimum, $S_1$ minimum and lowest-energy $S_1/S_0$ conical intersection***. All calculations were performed using GAMESS (5). Geometries on the $S_0$ and $S_1$ surfaces were determined at the State-Averaged Complete Active Space (SA-CASSCF) level[6], abbreviated as SA-x-CAS(y/z) (x averaged states, y active electrons and z active orbitals) with a STO-3G or 6-31G basis set, equal weighting of states, and no symmetry restrictions. All visualization of results were performed using MacMolPlt[7]. The minimal energy Conical Intersection (CI) searches utilized the method of Bearpark *et.al.*[8]; this local searching procedure was important for determining CI geometries that are closest in proximity to the $S_1$ minima.[9,10]

The procedure for optimizations was to first determine the $S_0$ minimum geometry, and then use the optimized geometry and orbitals as the initial values for the $S_1$ minimum optimization. The $S_0$/$S_1$ conical intersection (CI) search was similarly initiated with the optimized $S_1$ minimum structure and orbitals. When using larger active spaces, the $S_0$ minimum was not determined due to computation expense (which we designate with an "X" in Table A1.2 below) and the optimization process began with the optimized $S_1$ geometries and orbitals determined using a smaller active space.

Calculations with different active spaces were performed in order to investigate how the size of the active space affects the relative size of the $S_1$-minimum-to-CI energy for OTP and DPCH. For the SA-2-CAS calculations the active space was selected to be minimalistic due to the computational expense of working with these methods and relatively large molecules. The most appropriate active spaces would correspond to: 18 π, π* orbitals for OTP, 14 π, π* orbitals for DPCH, 16 π, π* and 2 σ, σ* orbitals for DHT, and 12 π, π* and 2 σ, σ* orbitals for CDHP. The active spaces used in our calculations utilized an equal split of π and π* orbitals (up to 4 π and 4 π* orbitals with the (8/8) active space). While the energetics and geometries change slightly between each active space the same relative differences between OTP and DPCH are still observed, which suggest that the smaller active spaces are satisfactory in describing the relative characteristics of the $S_1$ surfaces of these molecules.

Numeric results obtained from our calculations with OTP and DPCH using various active-spaces and basis sets are summarized in Table A1.2. The first several rows report characteristic structural properties (the dihedrals θ and φ as defined in the main text) for the optimized $S_0$ and $S_1$ and the lowest-energy CI geometries. The final four rows report energy gaps between the $S_0$ and $S_1$ surfaces at each of their optimized geometries (e.g., "$S_0 \rightarrow S_1$ @ $S_0$ Min" gives the $S_0$-$S_1$ gap at the optimized geometry of the $S_0$ minimum), as well as the energy differences between geometries along the $S_1$ surface.

The use of the State-Averaged Complete Active Space (SA-CASSCF) method in comparison to less demanding methods, such as Time-Dependent Density Functional Theory (TDDFT), can be explained by the nature of the points along the photocyclization coordinate. The deficiencies of TDDFT are well known and can result in skewed results near CI's, due to its inability to describe double excitations.[11,12] Recent results from Hartley illustrate this problem by the inability of a PBE0/TDDFT optimization to locate a $S_1$ minimum for *ortho*-Terphenyl, but rather converging towards cyclization.[13] While SA-CASSCF is well equipped for the problem of interest it is noted for the increased accuracy of excitation energies multireference perturbation theory is required to recover dynamical correlation.[14]

It is not our intent to provide a complete computational study of the potential energy surfaces or of the cyclization process, but rather a survey of important landmarks along the potential energy landscape. Energies and geometries (as characterized by the two dihedral angles discussed in the main text) are provided in Table A1.2 for various active spaces and basis set choices. Comparisons with experimentally determined values are given where appropriate.

***A1.3.2. Calculation of the lowest-energy absorption in DHT and DHP***. TDDFT is well-suited for calculating accurate excitation energies and simulating UV-VIS spectra of various systems.[15-17] In order to identify the long-lived band in the TA spectrum of

OTP as a ground-state absorption of the DHT intermediate, we used TDDFT[18] with the B3LYP functional[19,20] and a 6-31+G*[21,22] basis set to calculate the lowest-energy vertical transitions for DHT and DHP. First both DHP and DHT were optimized in the ground state using DFT, and it was confirmed by vibrational analysis that these optimized structures correspond with stationary points (no imaginary frequencies). Using these optimized geometries a single-point energy calculation was performed to obtain the $S_0 \rightarrow S_1$ excitation energy for each molecule. The difference of these two excitation energies was then subtracted from the experimental transition energy for DHP ( $\lambda_{max}$= 450 nm)[23] in order to determine the transition energy relative to the position of the experimental band. Using this method the computed position of the lowest-energy DHT absorption band is predicted to appear at 556 nm, in reasonable agreement with the measured TA spectra. Calculated vertical excitation energies, oscillator strengths, and structural parameters for DHT and DHP are provided in Table A1.3.

**Table A1.2.** Comparison of dihedral angles and Energy Gaps from SA-2-CAS(x/y)

| | Active Space | 2/2 | 2/2 | 6/6 | 6/6 | 8/8 | 8/8 | 2/2 | 2/2 | Exp (OTP) |
|---|---|---|---|---|---|---|---|---|---|---|
| Basis | | 6-31G | 6-31G | 6-31G | 6-31G | 6-31G | 6-31G | STO-3G | STO-3G | X |
| | | OTP | DPCH | OTP | DPCH | OTP | DPCH | OTP | DPCH | X |
| $S_0$ Min | Twist (φ) /Degree | 2.64 | 8.36 | X | X | X | X | 3.12 | 6.55 | 5.18(24),7.13(25) |
| | Torsion (θ) / Degree | 55.43, 61.98 | 56.30, 58.54 | X | X | X | X | 59.01, 51.03 | 53.39, 53.60 | (62.1, 42.1)(24), (62.1, 42.5)(25) |
| $S_1$ Min | Twist (φ) /Degree | 12.22 | 21.84 | 12.23 | 21.41 | 17.21 | 20.7 | 8.76 | 14.87 | X |
| | Torsion (θ) / Degree | 13.20, 14.13 | 11.48, 6.21 | 13.64, 14.68 | 11.89, 8 | 12.01, 12.78 | 12.33, 8.02 | 12.31, 19.23 | 14.92, 12.27 | X |
| $S_0/S_1$ CI | Twist (φ) /Degree | 24.97 | 24.16 | 25.01 | 30.7 | 24.57 | 35.31 | 35.76 | 16.34 | X |
| | Torsion (θ) / Degree | 1.3, 9.77 | 2.82, 11.44 | 18.71, 19.03 | 12.86, 9.90 | 19.07, 19.48 | 12.33, 8.02 | 7.68, 4.48 | 7.00, 29.47 | X |
| $S_0 \rightarrow S_1$ @ $S_0$ Min | Energy / eV | 6.90 | 6.65 | X | X | X | X | 8.39 | 8.28 | 4.3 (absorption onset in THF) |
| $S_1 \rightarrow S_0$ @ $S_1$ Min | Energy / eV | 0.50 | 0.12 | 1.02 | 0.46 | 1.27 | 1.12 | 1.25 | 0.75 | X |
| $S_1$ FC → $S_1$ Min | Energy / eV | 1.75 | 2.06 | X | X | X | X | 3.20 | 3.41 | X |
| $S_1$ Min → $S_0/S_1$ CI | Energy / eV | 0.147 | 0.019 | 0.995 | 0.235 | 0.94 | 0.82 | 0.71 | 0.47 | X |

**Table A1.3.** Computed Properties of the Ring-closed Intermediates DHT and DHP (Ground State Optimized Structural parameters from DFT B3LYP/6-31+G* and Vertical excitation energies from TDDFT B3LYP/6-31+G*).

| Geometry | Twist (φ) /Degree | Torsion (α) / Degree | $\Delta E$: $S_0 \rightarrow S_1$ / eV | Oscillator Strength |
|---|---|---|---|---|
| DHT | 7.61 | 5.21, 5.18 | 1.849 | 0.168 |
| DHP | 8.82 | 5.33, 5.39 | 2.376 | 0.167 |

## A1.4. Assessment of relative cyclization quantum yields from integrated band intensities.

The transient spectral intensities measured from the ring-open and ring-closed states of OTP and DPCH, $I(\nu)$, are proportional to the molar absorptivity for each of these states, $\epsilon(\upsilon)$, to within a constant determined by the number of transient species probed. Thus, quantitative determination of cyclization quantum yields is possible *if* the molar absorptivities are known. As these values are not known, the relative quantum yield for cyclization of two systems can be deduced as follows:

The oscillator strength of each transition is proportional to the corresponding frequency-integrated band intensity

$$f \propto \int_0^\infty \epsilon(\nu)d\nu = \int_0^\infty \frac{\epsilon(\lambda)d\lambda}{\lambda^2}$$

We define the quantity, $j$, given by

$$j = \int_0^\infty I(\nu)d\nu = \int_0^\infty \frac{I(\lambda)d\lambda}{\lambda^2}$$

By virtue of the proportionality between absorptivity and the measured spectral intensity,

$$j \propto f.$$

For this analysis we assume that the oscillator strength for the lowest-energy transitions of $S_0$ DHT and CDHP are roughly the same (our TDDFT calculations suggest that this is a reasonable assumption; see last column of Table A1.3). We also assume that the oscillator strength for the lowest-energy transition of the $S_1$ state is roughly the same for OTP and DPCH because these systems are nearly isochromophoric. To assess the validity of this assumption, we have performed a set of single-point SA-4-CAS(2/3)-sto3g calculations (2 active electrons and 3 active orbitals with equally weighted states) at the geometries of their $S_0$ and $S_1$ minima (geometries previously determined through optimization at the SA-2-CAS(2/2)-sto3g level); from these calculations we can obtain oscillator strengths for transitions between any of the 4 lowest-lying singlet states. The inherent difficulty associated with assigning experimentally measured TA bands to a specific geometry complicates the comparison of calculated excited state oscillator strengths, as multiple points along the photocyclization coordinate may need to be considered. However, these calculations do show modest agreement at each geometry for the $S_1 \rightarrow S_3$ transition, with the remaining $S_1 \rightarrow S_2$ transition having negligible oscillator strengths (<0.005): At the $S_0$ minima the oscillator strengths are 0.92 and 0.80 and for the $S_1$ minima they are 0.56 and 0.64 for OTP and DPCH, respectively. Thus, these computational estimates support our assumption of comparable oscillator strengths in order to determine the relative cyclization yield.

We estimate the full $I(\lambda)$ for the lowest-energy $S_1$ transition of DPCH by fitting the band centered near 650 nm to a Gaussian peak shape. We use this fitted peak shape to evaluate the integrated band intensity; in contrast, we have numerically integrated over the lowest-energy absorption band from $S_1$ OTP centered at 605 nm. The values of $j$ thus obtained will be used for relative normalization of transient spectral features measured from each system. This approach is superior to normalizing data to a common peak molar absorptivity for both $S_1$ transitions as their spectral line-shapes differ considerably.

We have similarly evaluated band-integrated intensities for the long-lived absorption bands assigned to ring-closed products CDHP and DHT. Assuming that 100% of the pumped molecules are in the $S_1$ states at time $t = 0$, the integrated intensity $j$ determined from the transient spectrum of the ring-closed state will be proportionate to the product of the transition oscillator strength AND the fractional yield for cyclization:

$$j_{DHT} \propto \Phi_{cycl} f_{DHT}$$

If absolute oscillator strengths could be determined independently for the excited-state and ring-closed transitions, the cyclization yield could be quantified as

$$\Phi_{cycl} = \frac{j_{DHT}}{f_{DHT}} \cdot \frac{f_{OTP}}{j_{OTP}}$$

since the ratio $j/f$ is proportional to the population of each state. Alternatively, under the assumption that the absolute transition oscillator strengths are the same for the two $S_1$ transitions and also the same for the two ground-state transitions for the ring-closed configurations,

$$\frac{\Phi_{DHT}}{\Phi_{CDHP}} = \frac{\left(\frac{j_{DHT}}{f_{RC}} \cdot \frac{f_{S1}}{j_{OTP}}\right)}{\left(\frac{j_{CDHP}}{f_{RC}} \cdot \frac{f_{S1}}{j_{DPCH}}\right)} = \left(\frac{j_{DHT}}{j_{OTP}}\right) / \left(\frac{j_{CDHP}}{j_{DPCH}}\right)$$

Thus, using only the assumption that the corresponding electronic states in these related molecules have similar oscillator strengths, we can assess whether the quantum yield for cyclization differs between DHT and DPCH.

Band integrals associated with OTP photochemical states were determined using magic angle data plotted in Figure 3.1(b) of the main text. We determined the value of $j_{OTP}$ by numerically integrating the OTP excited-state absorption band between 500 and 700 nm; spectral intensity at lower wavelengths was left out as a higher excited-state transition appears below 500 nm. $j_{DHT}$ was evaluated by numerical integration of the entire visible transient band collected at later delays (20 ps). Band integrals associated with DPCH photochemical states were determined using broadband magic angle data collected using visible white-light generated with calcium fluoride, which covers the range between 420 and 700 nm. $j_{DPCH}$ was determined by first fitting the lowest-energy transition to a Gaussian line shape and then using this shape to determine the band integral. The experimental spectrum collected at later delays was integrated numerically to determine $j_{CDHP}$. An additional intensity correction was required to account for the resolution-limited excited-state decay measured with DPCH (fastest decay component is 440 fs, with effective resolution limited at 150 fs); in contrast, the OTP excited-state limit exceeds the effective spectral resolution by a factor of 20 and does not require an intensity correction.

Based on this band intensity analysis we find that the relative quantum yield for cyclization is

$$\frac{\Phi_{DHT}}{\Phi_{CDHP}} = \left(\frac{j_{DHT}}{j_{OTP}}\right) / \left(\frac{j_{CDHP}}{j_{DPCH}}\right) = \frac{0.21}{0.22} = 0.95$$

That is, the relative yield for cyclization from both $S_1$ OTP and DPCH is roughly the same. This back-of-the-envelope estimate of relative quantum yields suggests that difference in excited-state decay rate for OTP and DPCH is not associated with the presence of an additional competing non-adiabatic pathway, which would be expected to alter the cyclization quantum yield between systems. As argued in the main text, this similarity in the cyclization yield rather indicates that excited-state decay occurs through a single state-crossing region through which the excited-state wave packet branches between cyclization and ground-state recovery.

## A1.5. References:

(1) Voight, K.; Zezschwitz, P. V.; Rosauer, K.; Lansky, A.; Adams, A.; Reiser, O.; de Meijere, A. The Twofold Heck Reaction on 1,2-Dihalocycloalkenes and Subsequent 6π-Electrocyclization of the Resulting (E, Z, E)-1,3,5-Hexatrienes: A New Formal {2+2+2}-Assembly of Six-Membered Rings. *Eur. J. Org. Chem.* **1998**, *8*, 1521-1534.

(2) Xia, Y.; Liu, Z.; Xiao, Q.; Qu, P.; Ge, R.; Zhang, Y.; Wang, J. Rhodium(II)-Catalyzed Cyclization of Bis(N-tosylhydrazone)s: An Efficient Approach towards Polycyclic Aromatic Compounds. *Angew. Chem. Int. Ed.* **2012**, *51*, 5714-5717.

(3) Sato, T.; Shimada, S.; Hata, K. A New Route to Polycondensed Aromatics: Photolytic Formation of Tripheneylene and Dibenzo[fg,op]naphthacene Ring Systems. *Bull. Chem. Soc. Jpn.* **1971**, *44*, 2484-2490.

(4) Nagura, C.; Suda, A.; Kawano, H.; Obara, M.; Midorikawa, K. Generation and Characterization of Ultrafast White-Light Continuum in Condensed Media. *Appl. Opt.*

**2002**, *41*, 3735-3742.

(5) Schmidt, M. W.; Baldridge, K. K.; Boatz, J. A.; Elbert, S. T.; Gordon, M. S.; Jensen, J. H.; Koeski, S.; Matsunaga, N.; Nguyen, K. A.; Su, S. J. *et al.* General Atomic and Molecular Electronic Structure System. *J. Comput. Chem.* **1993**, *14*, 1347-1363.

(6) Docken, K. K.; Hinze, J. LiH Potential Curves and Wavefunctions for $X^1\Sigma^+$, $A^1\Sigma^+$, $B^1\Pi$, $^3\Sigma^+$, and $^3\Pi$. *J. Chem. Phys.* **1972**, *57*, 4928-4936.

(7) Bode, B.; Gordon, M. S. MacMolPlt: A Graphical User Interface for GAMESS. *J. Mol. Graphics Modell.* **1998**, *16*, 133-138.

(8) Bearpark, M. J.; Robb, M. A.; Schlegel, H. B. A Direct Method for the Location of the Lowest Energy Point on a Potential Surface Crossing. *Chem. Phys. Lett.* **1994**, *223*, 269-274.

(9) Bearpark, M. J.; Bernardi, F.; Clifford, S.; Olivucci, M.; Robb, M. A.; Vreven, T. Cooperating Rings in *cis*-Stilbene Lead to an $S_0/S_1$ Conical Intersection. *J. Phys. Chem. A* **1997**, *101*, 3841-3847.

(10) Boggio-Pasqua, M.; Ravaglia, M.; Bearpark, M. J.; Garavelli, M.; Robb, M. A. Can Diarylethene Photochromism be Explained by a Reaction Path Alone? A CASSCF Study with Model MMVB Dynamics. *J. Phys. Chem. A* **2003**, *107*, 11139-11152.

(11) Elliott, P.; Goldson, S.; Canahui, C.; Maitra, N. T. Perspectives on Double-excitations in TDDFT. *Chem. Phys.* **2011**, *391*, 110-119.

(12) Levine, B. G.; Ko, C.; Quenneville, J.; Martínez, T. J. Conical Intersections and Double Excitations in Time-dependent Density Functional Theory. *Mol. Phys.* **2006**, *104*, 1039-1051.

(13) Hartley, C. S. Excited-State Behavior of *ortho*-Phenylenes. *J. Org. Chem.* **2011**,

*76*, 9188-9191.

(14) Jensen, F. *Introduction to Computational Chemistry*; 2nd ed.; Wiley: Chichester, U.K., 2007.

(15) Casida, M. E.; Huix-Rotlant, M. Progress in Time-Dependent Density-Functional Theory. *Annu. Rev. Phys. Chem.* **2012**, *63*, 287-323.

(16) Furche, F. On the Density Matrix Based Approach to Time-Dependent Density Functional Response Theory. *J. Chem. Phys.* **2001**, *114*, 5982-5992.

(17) Parac, M.; Grimme, S. A TDDFT Study of the Lowest Excitation Energies of Polycyclic Aromatic Hydrocarbons. *Chem. Phys.* **2003**, *292*, 11-21.

(18) Runge, E.; Gross, E. K. U. Density-Functional Theory for Time-Dependent Systems. *Phys. Rev. Lett.* **1984**, *52*, 997-1000.

(19) Becke, A. D. Density-Functional Thermochemistry. III. The Role of Exact Exchange. *J. Chem. Phys.* **1993**, *98*, 5648-5652.

(20) Stephens, P. J.; Devlin, J. F.; Chabolowski, C. F.; Frisch, M. J. *Ab Initio* Calculation of Vibrational Absorption and Circular Dichroism Spectra Using Density Functional Force Fields. *J. Phys. Chem.* **1994**, *98*, 11623-11627.

(21) Frisch, M. J.; Pople, J. A.; Binkley, J. S. Self-Consistent Molecular Orbital Methods 25. Supplementary Functions for Gaussian Basis Set. *J. Chem. Phys.* **1984**, *80*, 3265-3269.

(22) Hehre, W. J.; Ditchfeld, R.; Pople, J. A. Self-Consistent Molecular Orbital Methods. XII. Further Extensions of Gaussian-Type Basis Sets for Use in Molecular Orbital Studies of Organic Molecules. *J. Chem. Phys.* **1972**, *56*, 2257-2261.

(23) Muszkat, K. A.; Fischer, E. Structure, Spectra, Photochemistry, and Thermal

Reactions of the 4a,4b-Dihydrophenanthrenes. *J. Chem. Soc. B* **1967**, *1967*, 662-678.

(24) Brown, G. M.; Levy, H. A. o-Terphenyl by Neutron Diffraction. *Acta Cryst. B* **1979**, *35*, 785-788.

(25) Aikawa, S.; Maruyama, Y.; Ohashi, Y.; Sasada, Y. 1,2-Diphenylbenzene (*o*-Terphenyl). *Acta Cryst. B* **1978**, *34*, 2901-2904.

# Appendix 2

# Supporting Information for Chapter 4:

# Structural Control of Nonadiabatic Bond Formation: The Photochemical Formation and Stability of Substituted 4a,4b-dihydrotriphenylenes.

## A2.1. Experimental Methods

### *A2.1.1 Synthesis of ortho-quaterphenyl (OQTP)*

Synthesis was adapted from the literature[1] as follows: 1.08 g of 2-Iodobiphenyl (Alfa Aesar) was mixed with 1.28 g of copper powder (Fisher Scientific) and heated at 260 °C for 20 minutes . After sample had cooled to room temperature sample was purified on an alumina column with a hexane to dichloromethane gradient. *Ortho*-quaterphenyl: 0.146 g (25% yield) of colorless crystals; mp 118 °C; 1H NMR (300 MHz, CDCl3) ; 13C NMR(300 MHz, CDCl3). Mass. Spec. M+ 306.2.

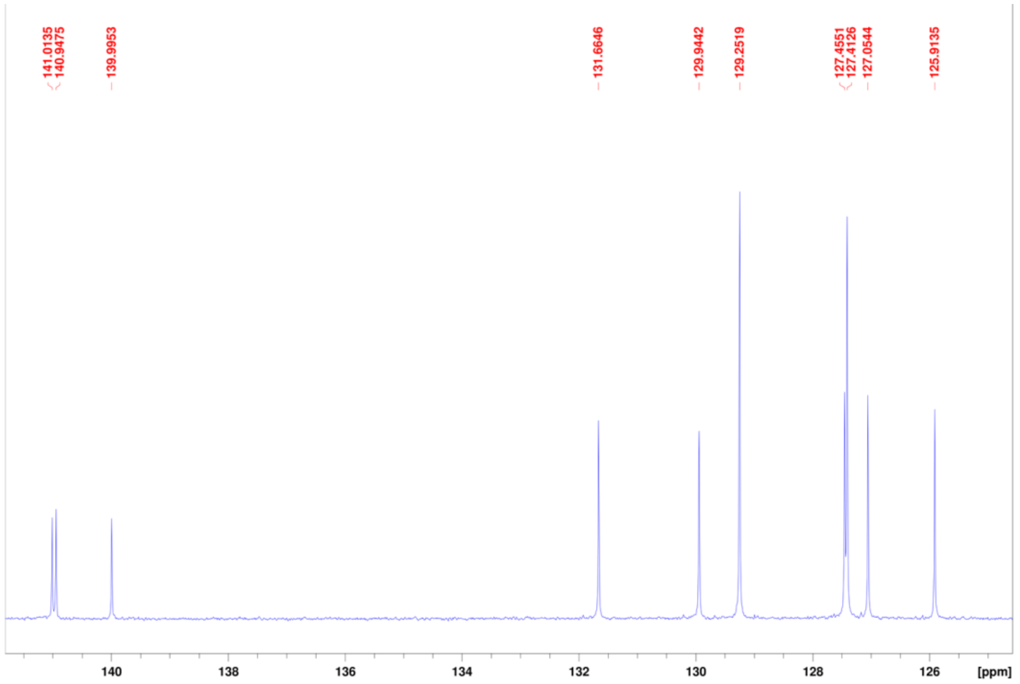

**Figure A2.1.** $^{13}$C NMR Spectrum of OQTP

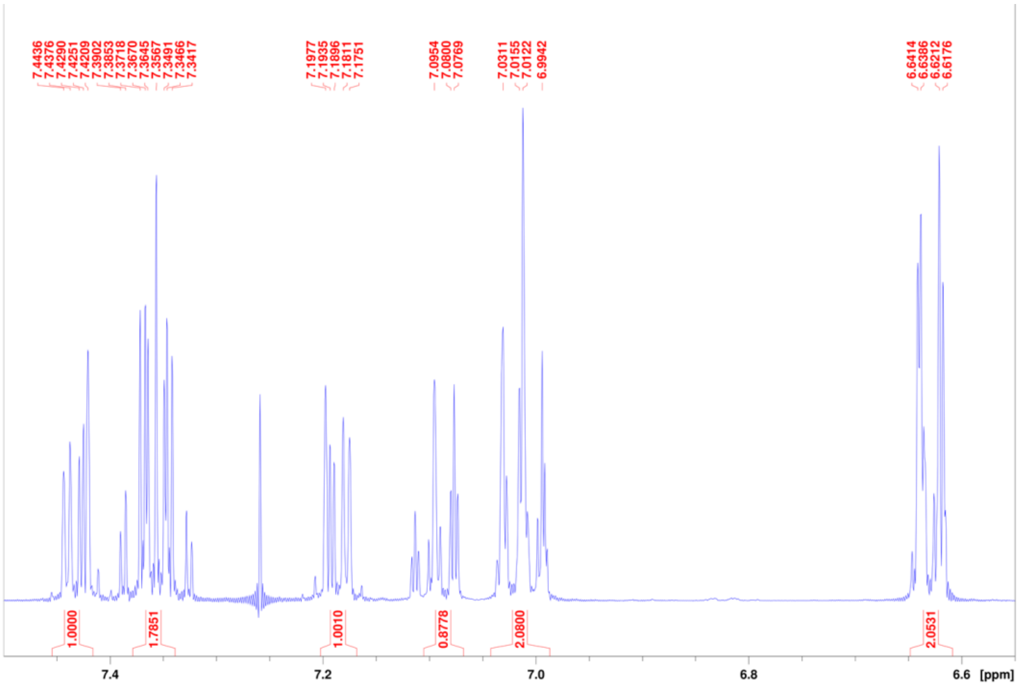

**Figure A2.2.** $^{1}$H NMR Spectrum of OQTP

### *A2.1.2 Fluorescence/Excitation Spectra of OQTP and TPB*

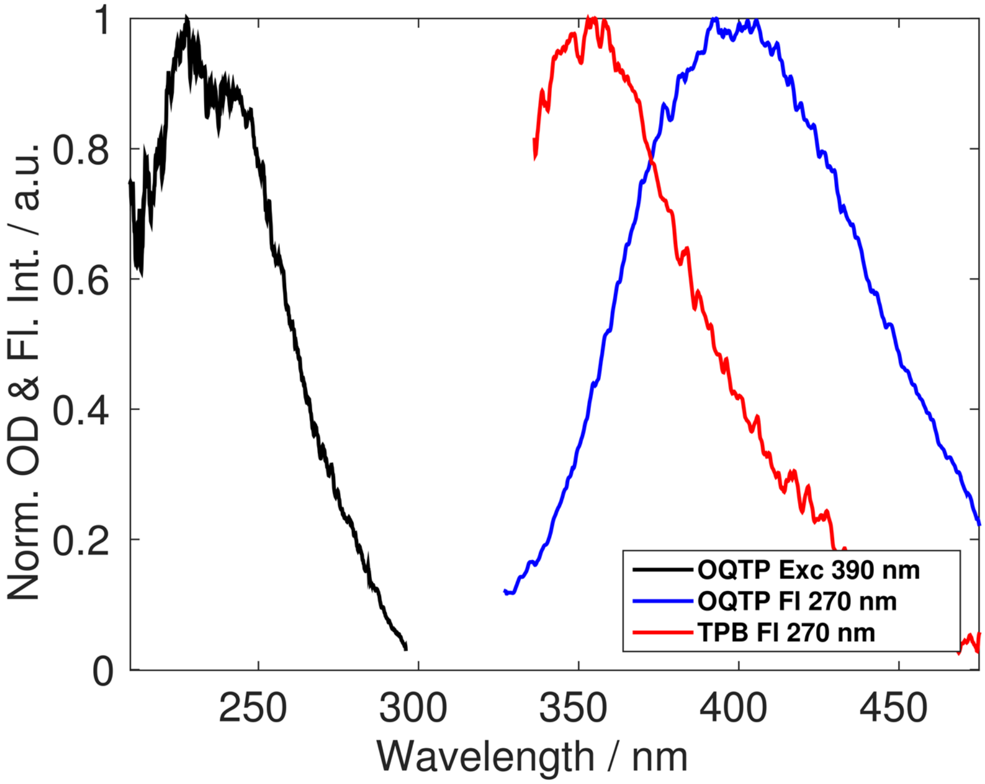

**Figure A2.3**. Fluorescence and excitation spectra of OQTP and TPB in cyclohexane. Collected with a Perkin Elmer LS-5b. The fluorescence spectrum of TPB under the same conditions (identical excitation/emission slit widths, wavelength ranges, and optical density) as OQTP was not observable, therefore the slits were fully opened to obtain signal. This qualitatively predicts the fluorescence quantum yield of TPB to be much less than OQTP ($\Phi_{Fl}$=0.01).[2]

### *A2.1.3 Nanosecond Transient Absorption Spectroscopy: Time Resolution*

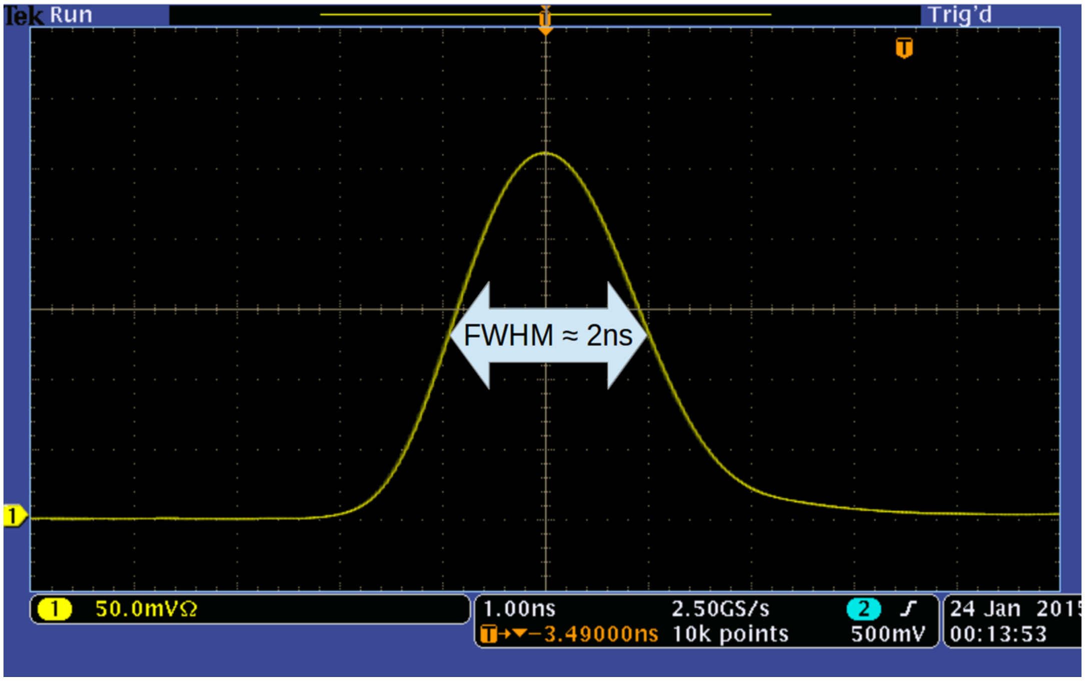

**Figure A2.4.** Temporal Profile of 639 nm laser diode (Opnext) under experimentally optimized pulsing conditions. Collected with a photodiode (Thorlabs, DET10A, 1 ns risetime) and Tektronix DPO 3052 oscilloscope (500 MHz Bandwidth / 700 ps rise time, 2.5 GHz sampling rate).

### *A2.1.4 Femtosecond Transient Absorption Spectroscopy: Details of Home-Built Instrumentation*

Ultrabroadband femtosecond transient absorption was performed with prism dispersion based on the design of Megerle *et. al*.[3] Supercontinuum generation using a 2mm $CaF_2$ plate (United Crystals) and <1 μJ 800 nm beam focused with a 20 cm FL Convex Lens (UV-FS CVI) producing a probe pulse spanning 300-1100 nm. Following collimation with a 75 mm UV-Enhanced Aluminum Concave Mirror (Thorlabs), to minimize aberrations, a 20 cm FL concave parabolic mirror (Edmund Optics) focused into the sample cell and was then recollimated with a 5 cm FL concave parabolic mirror (Edmund Optics). For supercontinuum conditioning various filters were used for different probe ranges. For UV/VIS measurements (300-700 nm) a specialty 800 nm High-Reflector (CVI) with high transmittance from 300-750 nm was used for filtering the fundamental. The UV/VIS probe was dispersed with a UV-Fused Silica Prism (CVI) and imaged onto the detector using a 25 cm FL UV-enhanced Concave Mirror (Newport). For VIS/NIR measurements (500-1000 nm) the fundamental was suppressed using IR-140 dye (Sigma-Aldrich) in chloroform with an absorption maximum of ~815 nm and the concentration of the dye solution was empirical adjusted (1-2 OD at 815 nm) to tailor the intensity of the probe beam. Additionally the center of the beam was removed with a ~3mm diameter circular beam stop at a ~2.5 cm collimated beam size to remove the most intense portion of the fundamental beam. The VIS/NIR probe was dispersed with a NSF-11 prism (Edmund Optics) and imaged onto the detector using a 15 cm FL UV-enhanced concave mirror (Edmund Optics). For further probe intensity shaping in both ranges a continuously variable reflective neutral density filter (Thorlabs) was utilized directly before the detector to attenuate wavelengths on and near the fundamental while allowing the weaker intensity of the red and blue edges to pass with high transmission.

Calibration of both UV/VIS and VIS/NIR detectors is performed using a BG-36 filter (Schott) with the various absorption maxima, minima and 50 %T features serving as calibration points. The position of these absorption features are mapped from pixel number to wavelength according to a function that includes the index of refraction of each prism material.[3] This function is fit using an Levenberg–Marquardt algorithm in NI LabView.

Two 256 pixel NMOS photodiode arrays (Hammatsu S3901-256Q) were utilized for detection of UV/VIS and VIS/NIR regions of the supercontinuum probe. Each array collects and exports data at the laser repetition rate allowing for shot-to-shot correlation with synchronization and control from a National Instruments data-acquisition device (PCI-6122) and NI LabView. Typically 2000-3000 consecutive pump on/off cycles were averaged for transient absorption measurements.

## A2.2. Data Analysis

### *A2.2.1 Global Analysis: Details of Algorithm*

For this analysis, the matrix of time and wavelength-dependent data (**A**) was first decomposed by SVD: $\mathbf{A} = \mathbf{USV}^T$, where **U** contains the spectral eigenvectors in column space, **S** contains the weights for each vector in **U** and **V**, and **V** contains the temporal eigenvectors in row space. The number of significant, unique contributing spectral components was assessed from the diagonal elements of **S**. The time-dependence of each relevant species for any given kinetic model was calculated with initial-guess kinetic parameters and assigned to a specific column of a matrix **F**; **F** does not include another column or function that accounts for coherent artifacts within the pump-probe temporal overlap. The kinetics defined in **F** are convoluted with the instrument response to reproduce the onset of transient absorption and the resolution of the measurement. Best-fit kinetic parameters were then determined using a nonlinear least squares surface fitting routine: In short, model parameters that determine the values of **F** were adjusted until the product $\mathbf{A^*}=\mathbf{D^*}\ \mathbf{F}^T$ best fit the matrix **A**, where $\mathbf{D^*}=\mathbf{A}\ \mathbf{F}^{T+}$ and is commonly known as the

Species-Associated-Spectra or SAS. Specifically this form of global analysis is a Direct-MLS (Matrix Least-Squares) technique in which SVD assists by determining the number of spectral components in **S** and therefore aids in choosing appropriate kinetic models.[4] Goodness of fit was assessed from the size of residuals between **A** and **A***. The global analysis algorithm was homebuilt in MATLAB 2014b.

### *A2.2.2 Species-Associated Spectra (SAS) / D-Matrix Spectra*

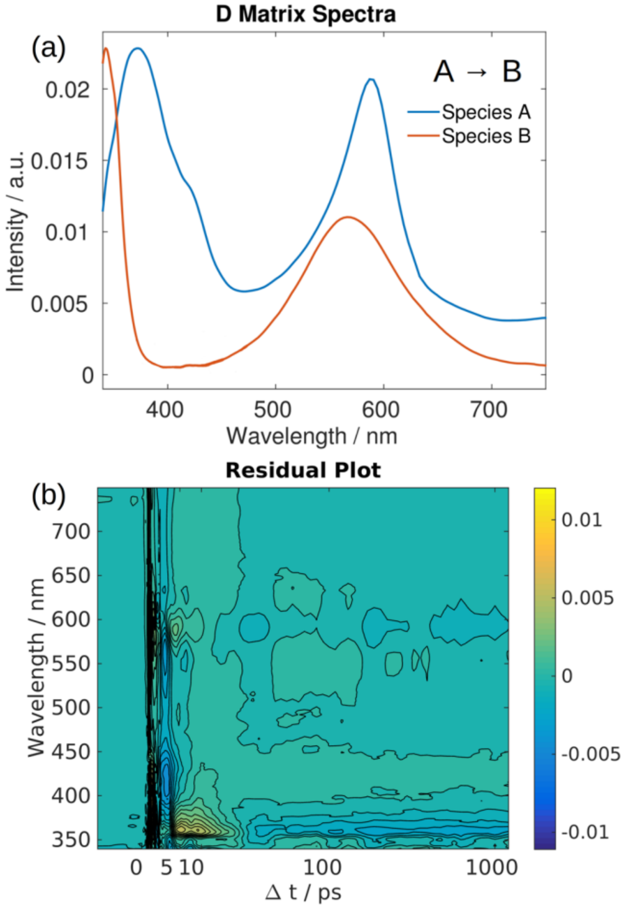

**Figure A2.5.** Global analysis of OTP using a 2 state sequential model (A → B). (a) The D Matrix / SAS for the 2-state model reproduce the observed spectra at early time delays (~1 ps, species A) and late delays (> 100 ps, species B) , which is supported by the major spectral contributions along the diagonal of **S** (0.735, 0.19, 0.021, 0.012,...). The slow 38 ns decay of DHT allows for a satisfactory fit with this model over the experimental timescale. (b) Residual plot of global fit on a quasi-logarithmic time axis. Note the positive to negative trend in residuals at ~355 nm where vibrational relaxation is observed for DHT.

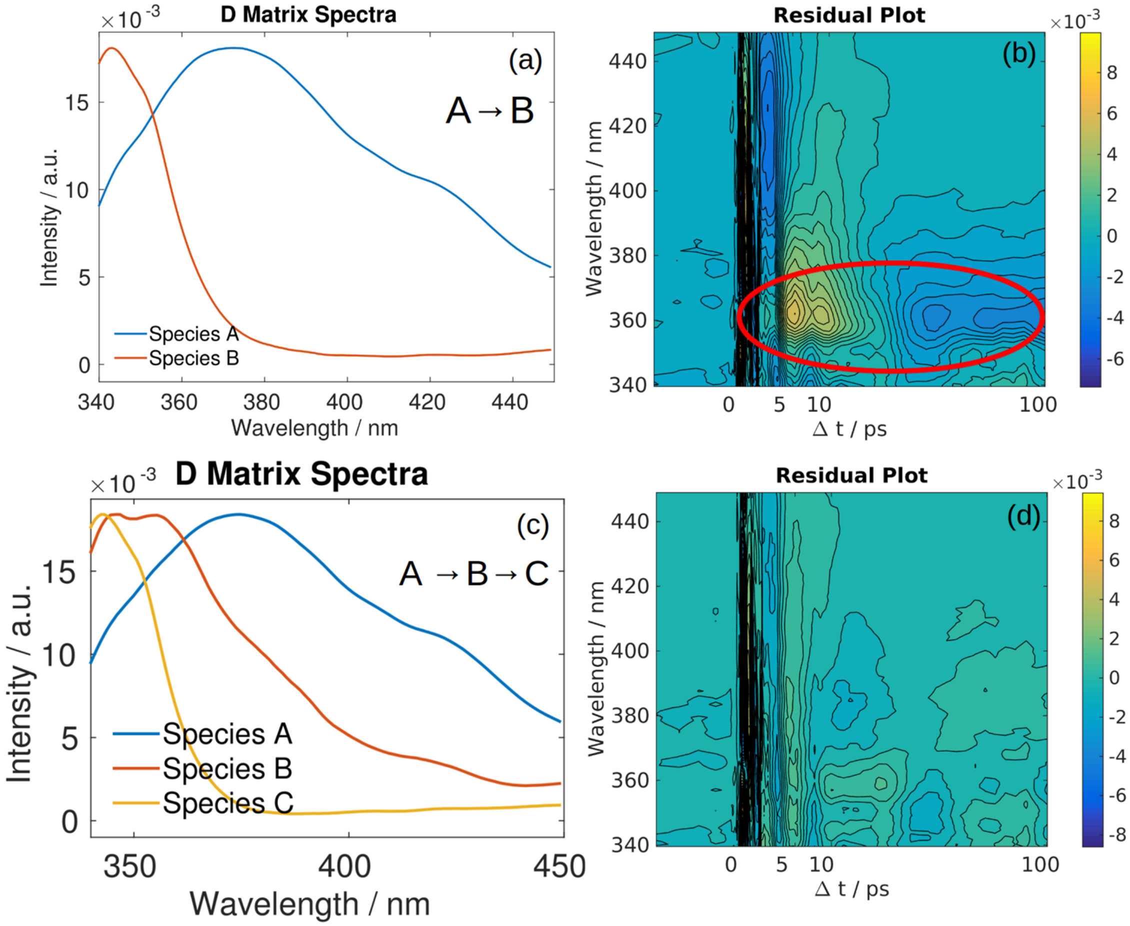

**Figure A2.6.** SVD Analysis focused on vibrational relaxation of OTP. Reducing both the wavelength range and longest time delay to 100 ps focuses the 3-state global fit on the peak narrowing due to vibration relaxation. (a) and (b) show the SAS and residuals for a 2-state model that poorly fits the region from 350-380 nm, where vibrational relaxation is observed. (c) and (d) show the SAS spectra and residuals for a 3-state model that greatly improves the fit. Species B closely resembles the spectrum of vibrationally hot DHT, while species C resembles the spectrum of vibrationally cool DHT at time delays > 100 ps. The resultant timescales are $\tau_1$=1.92 ps and $\tau_2$ =6.92 ps.

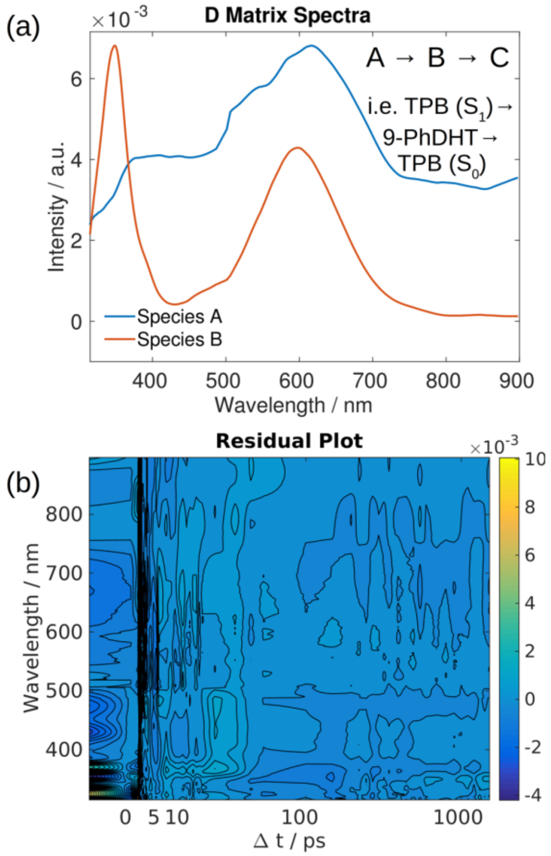

**Figure A2.7.** Global Analysis of TPB using a sequential 3-state model. The model utilizes only two experimentally observable states A and B, while the second rate that forms C is required to fit the disappearance of 9-PhDHT with a nanosecond timescale. The resultant timescales are $\tau_1$=8.1 ps and $\tau_2$ =4392 ps, which are similar to the timescales determined by exponential fits at single wavelengths from fs and ns transient spectroscopies. The diagonal elements of **S** are 0.737, 0.136, 0.028, 0.021, 0.013,... . (a) The SAS of the global fit closely matches the initial (Species A) and final (Species B) time delays of the fs-TA spectra. (b) Residual plot of global fit to data.

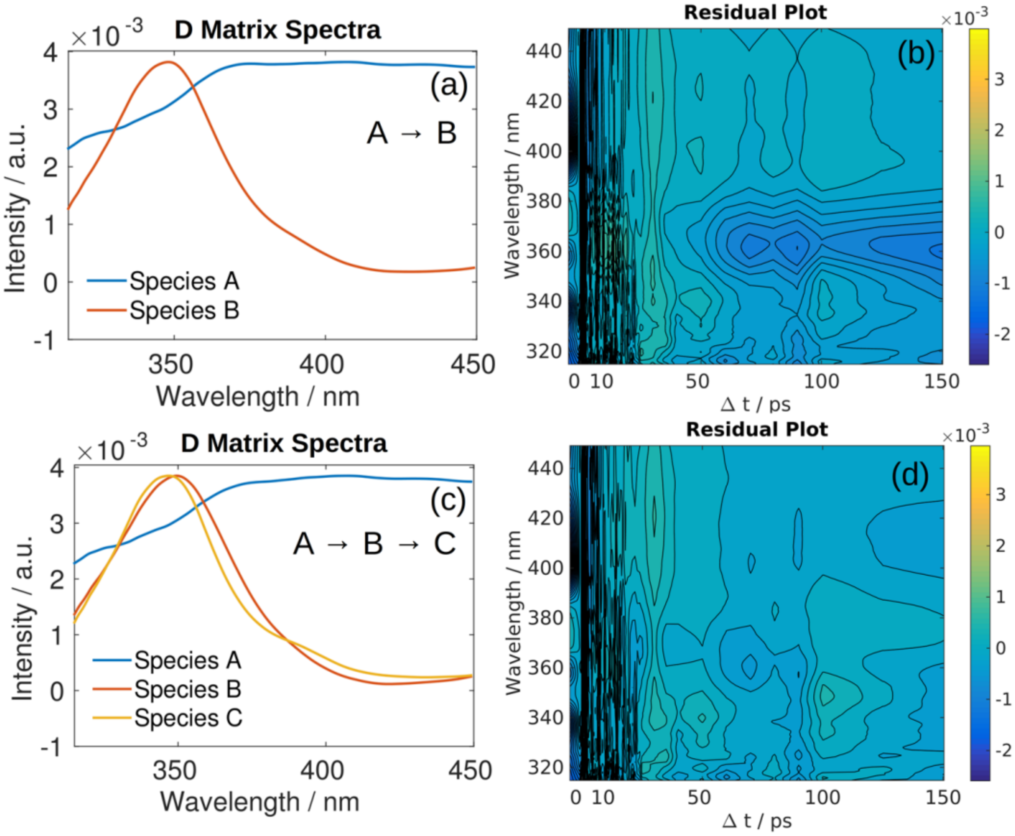

**Figure A2.8.** SVD Analysis focused on vibrational relaxation of TPB. Reducing both the wavelength range and longest time delay to 150 ps focuses the 3-state global fit on the peak narrowing due to vibration relaxation. (a) and (b) show the SAS and residuals for a 2-state model that poorly fits the region from 350-380 nm, suggesting the presence of vibrational relaxation similar to that of OTP. (c) and (d) show the SAS spectra and residuals for a 3-state model that greatly improves the fit. Species B closely resembles the spectrum of species C suggesting that vibrational relaxation is more subtle than that of OTP. The shorter initial lifetime was constrained to 8 ps, resulting in a vibrational cooling timescale ($\tau_2$) of 32.6 ps.

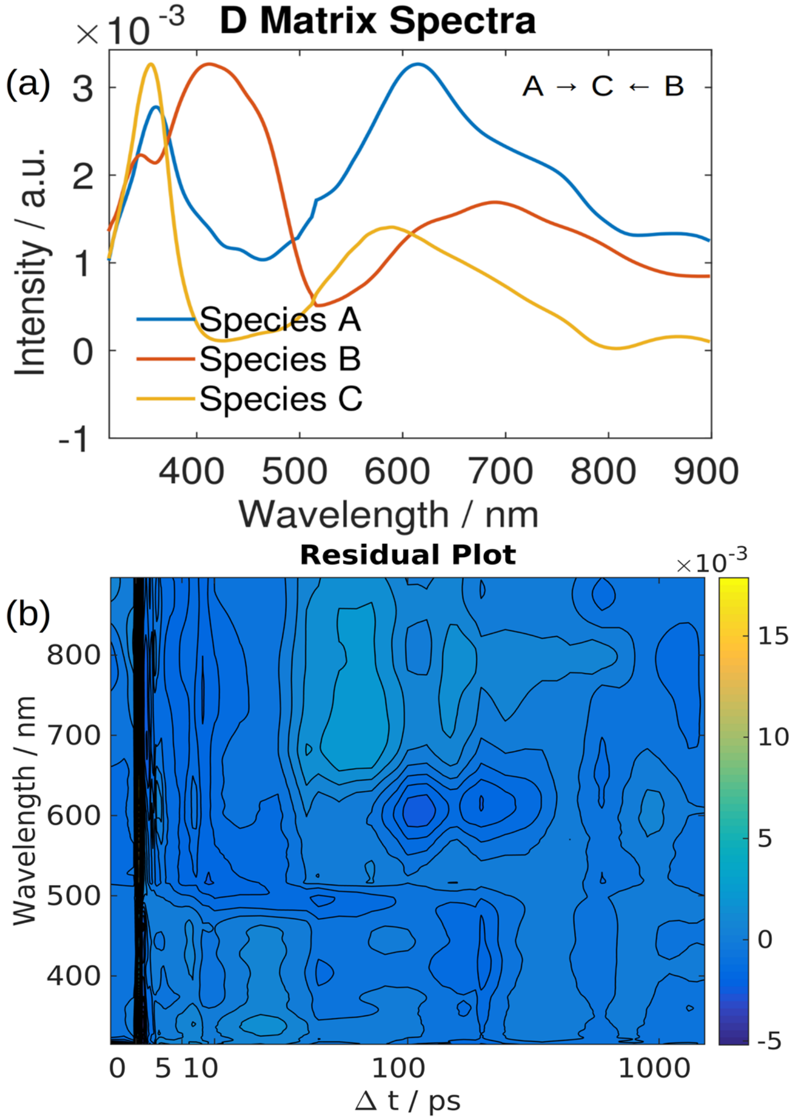

**Figure A2.9.** Global Analysis of OQTP fs-TA spectra. The SVD analysis of the data predicts that 3 components make up 95% of the observed signal. The diagonal of **S** was 0.82, 0.09, 0.05, 0.02, 0.01, … . (a) The resultant SAS from the fit of the shown 3-state kinetic model (inset). (b) Residual plot from fit to experimental data with the largest error in the region between 0-0.5 ps that contains coherent artifacts due to pump-probe overlap.

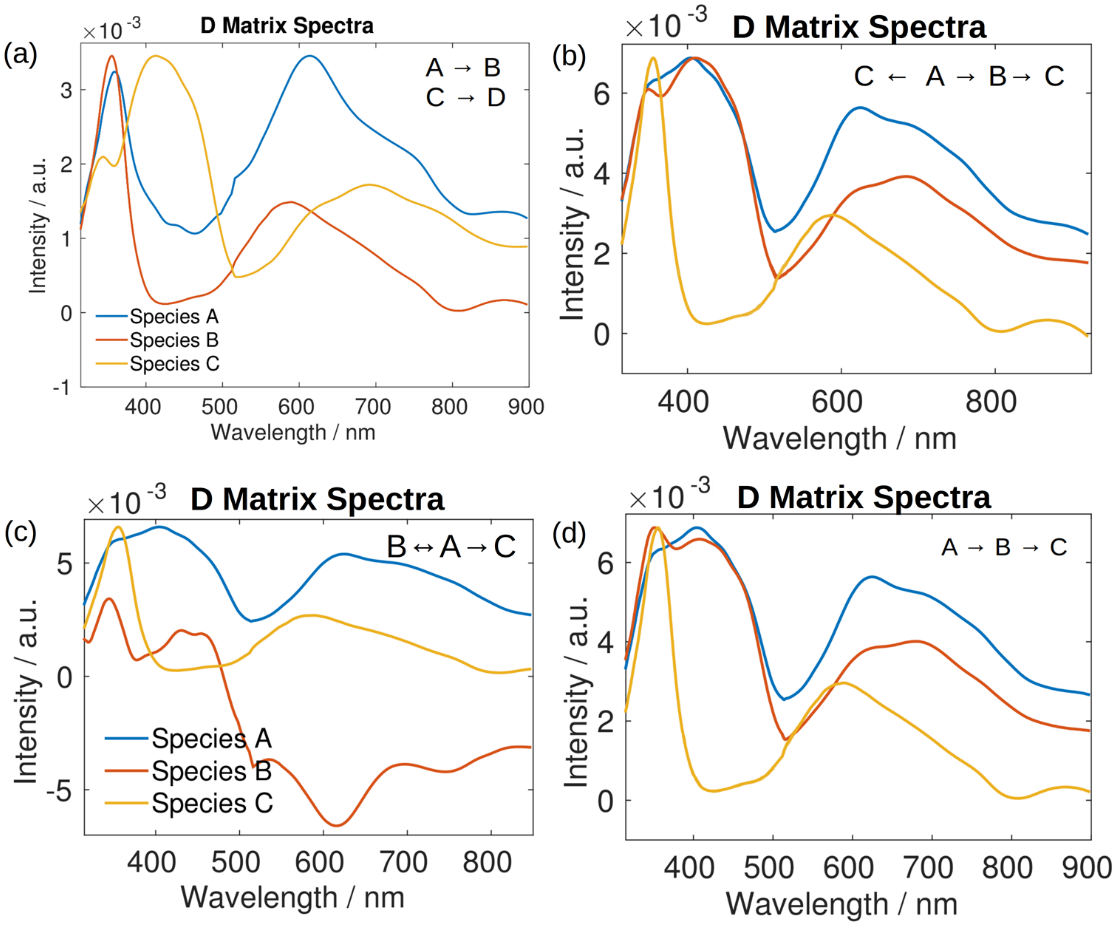

**Figure A2.10.** SAS of OQTP from various kinetic models. (a) Parallel kinetics with one unobserved product, D. (b) Sequential 3-state kinetics also with direct reaction between the first (A) and last (C) species. (c) 3-state kinetics with an equilibrium between the reactant (A) and an intermediate (C). (d) Sequential 3-state kinetic model.

## A2.3. Computational Results

All Calculations performed in GAMESS[5] without Symmetry (NOSYM=1) and are with the default convergence criteria.

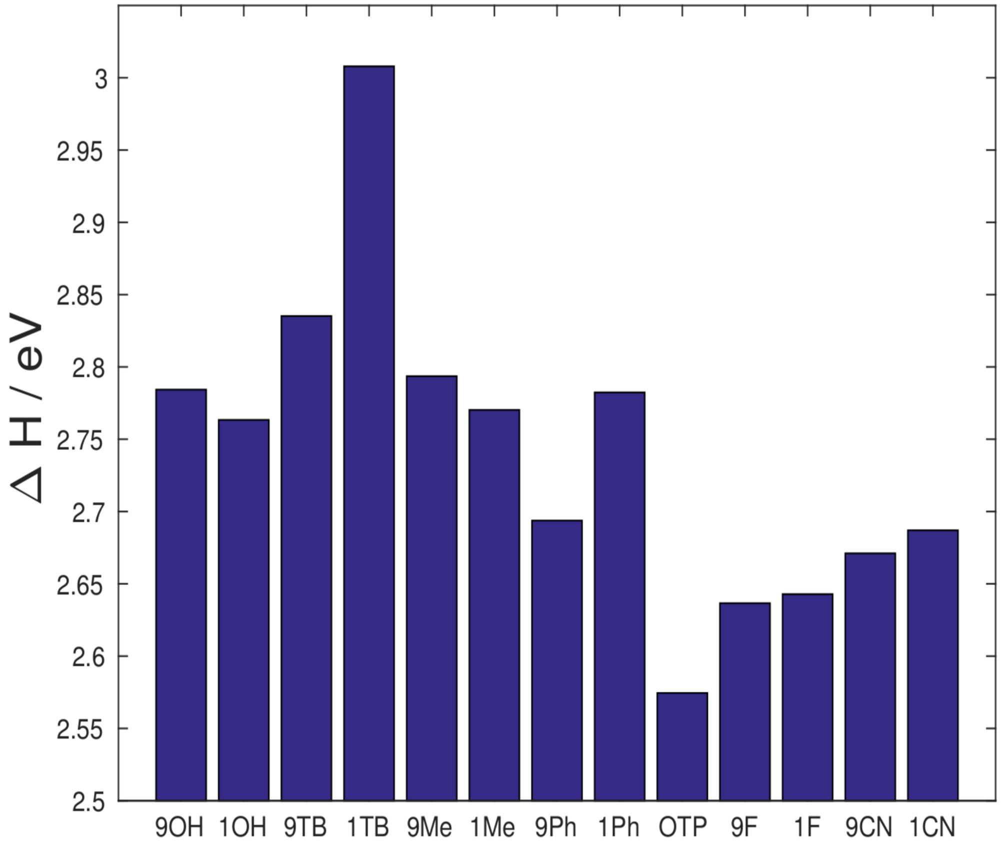

**Figure A2.11.** The difference in energy between open and closed isomers (ΔH) of various substituted OTPs produced from B3LYP/6-31+G* computations. Note that that all closed forms are **L** conformers, except for the 9-F and 9-OH substituted DHTs. All substituted OTPs have consistently higher energy differences than that of unsubstituted OTP.

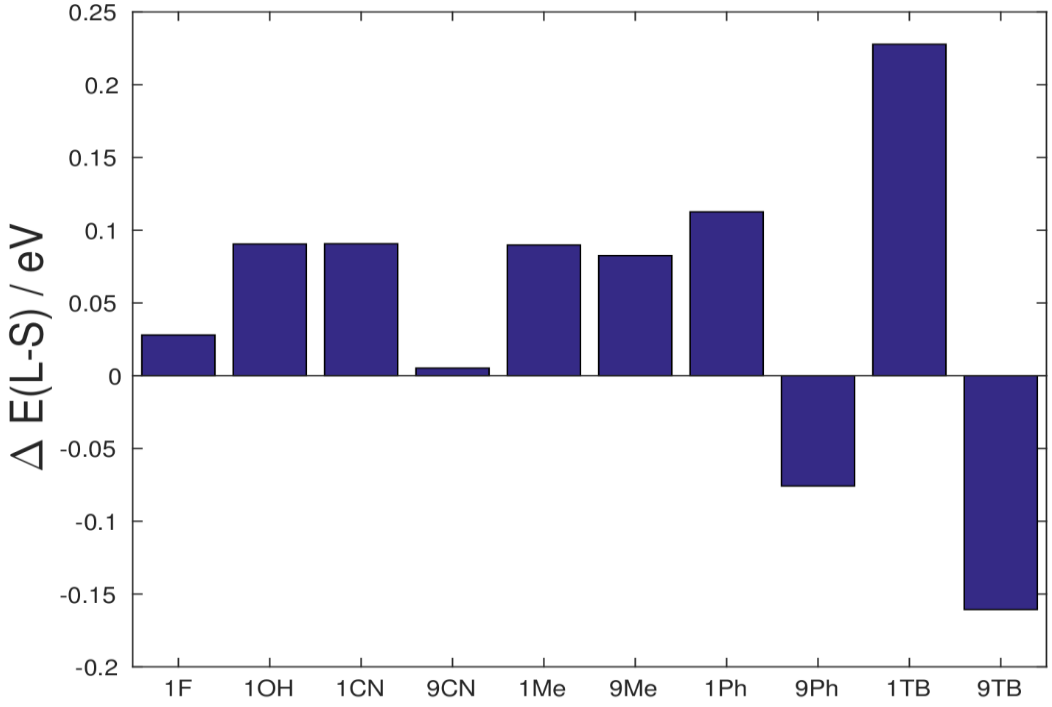

**Figure A2.12.** Energy differences between **L** and **S** conformers of various substituted DHTs. The 9-OH and 9-F substitutions are absent due to the presence of only **S** conformers. Large substituents (Ph, TB) with increased steric influence raise ΔE but with opposite sign for 1 and 9 substitutions.

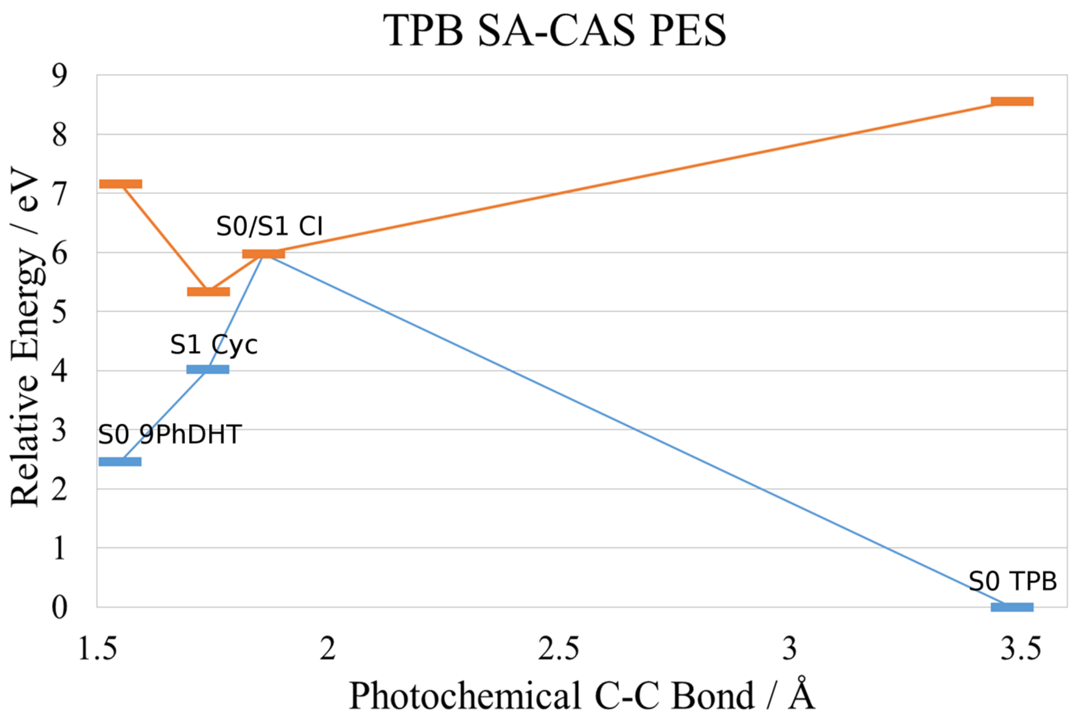

**Figure A2.13.** Potential energy surface of TPB constructed from SA-CAS(2,2)-sto3g computations. TPB and OQTP show similarities along the reaction coordinate from 1.5 to 2 Å but are different at larger distances. Most noticeable is that TPB does not have a quinoidal minimum and the FC region above the $S_0$ TPB minima is ~2.5 eV above the $S_0/S_1$ CI.

## A2.4 Discussion of Quantum Chemistry Methods: Multi-Excitation Character and Dynamic Correlation

The discrepancies between $S_1$ minima located from the SACAS and TDDFT methods warrants a brief explanation in terms of their general applicability towards our systems.[6-9] While the multireference SACAS method allows for description of multiple excitations, conventional LR-TDDFT describes only single excitations but is much more economical and less computationally demanding allowing for larger systems and basis sets. TDDFT also includes dynamic correlation while its recovery for the SACAS method is dependent on active space and multireference perturbation theory (CASPT2, QDPT2) is required for its more complete recovery.[10] Inspection of the OQTP **B** $S_1$ quasi-quinoidal minima using the SACAS method shows approximately 18% single excitation character, 54% double-excitation character and 19% triple-excitation character. Therefore TDDFT is ill-equipped to describe this $S_1$ minima as well as conical intersections that are known to possess double-excitation character but the small active space and basis of the SACAS method makes TDDFT results complementary.[11] Together they provide a more rounded description of the excited-state showing the qualitative differences in the optimized structures resultant of different but complementary methods.

## A2.5 References

(1) Bachmann, W. E.; Clarke, H. T. The Mechanism of the Wurtz-Fittig Reaction. *J. Am. Chem. Soc.* **1927**, *49*, 2089–2098.

(2) Mathew, S. M.; Hartley, C. S. Parent O-Phenylene Oligomers: Synthesis, Conformational Behavior, and Characterization. *Macromolecules* **2011**, *44*, 8425–8432.

(3) Megerle, U.; Pugliesi, I.; Schriever, C.; Sailer, C. F.; Riedle, E. Sub-50 Fs Broadband Absorption Spectroscopy with Tunable Excitation: Putting the Analysis of Ultrafast Molecular Dynamics on Solid Ground. *Appl. Phys. B.* **2009**, *96*, 215–231.

(4) Hendler, R. W.; Shrager, R. I. Deconvolutions Based on Singular Value Decomposition and the Pseudoinverse: A Guide for Beginners. *J. Biochem. Biophys. Methods* **1994**, *28*, 1–33.

(5) Schmidt, M. W.; Baldridge, K. K.; Boatz, J. A.; Elbert, S. T.; Gordon, M. S.; Jensen, J. H.; Koseki, S.; Matsunaga, N.; Nguyen, K. A.; Su, S.; Windus, T. L; Dupuis, M.; Montgomery, J. A. General Atomic and Molecular Electronic Structure System. *J. Comput. Chem.* **1993**, *14*, 1347–1363.

(6) Dreuw, A.; Head-Gordon, M. Single-Reference Ab Initio Methods for the Calculation of Excited States of Large Molecules. *Chem. Rev.* **2005**, *105*, 4009–4037.

(7) Casida, M. E.; Huix-Rotllant, M. Progress in Time-Dependent Density-Functional Theory. *Annu. Rev. Phys. Chem.* **2012**, *63*, 287–323.

(8) Docken, K. K.; Hinze, J. LiH Potential Curves and Wavefunctions for $X^1\Sigma^+$, $A^1\Sigma^+$,

$B^1\Pi$, $^3\Sigma^+$, and $^3\Pi$. *J. Chem. Phys.* **1972**, *57*, 4928–4936.

(9) Schmidt, M. W.; Gordon, M. S. The Construction and Interpretation of Mcscf Wavefunctions. *Annu. Rev. Phys. Chem.* **1998**, *49*, 233–266.

(10) Borden, W. T.; Davidson, E. R. The Importance of Including Dynamic Electron Correlation in Ab Initio Calculations. *Acc. Chem. Res.* **1996**, *29*, 67–75.

(11) Levine, B. G.; Ko, C.; Quenneville, J.; Martinez, T. J. Conical Intersections and Double Excitations in Time-Dependent Density Functional Theory. *Mol. Phys.* **2006**, *104*, 1039–1051.

# Appendix 3

## Supporting Information for Chapter 5:

## Excited-state Deactivation Pathways and the Photocyclization of BN-doped Polyaromatics

### A3.1. Sample Preparation

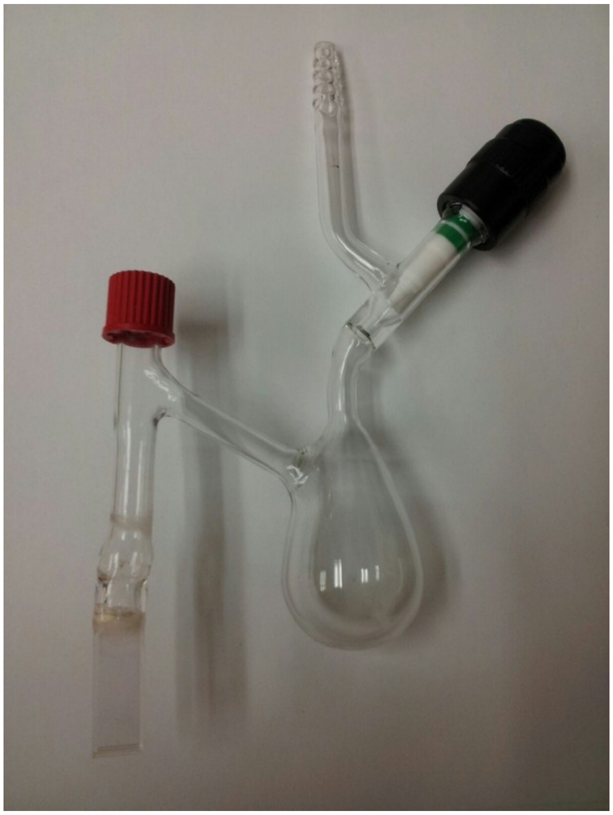

**Figure A3.1.** Schlenk cuvette (5 mm pathlength) used for air and water-free solution preparation. The barbed inlet (top) connects to a schlenk line (vacuum or $N_2$); the red cap utilizes a PTFE coated septum to allow for addition or removal of solutions. Solutions are deaerated by Freeze-Pump-Thaw in the pear-shaped flask and are then transferred into the cuvette by tilting the flask.

## A3.2. Fluorescence Quantum Yield Determination

Integrated fluorescence was determined for samples with various absorbances between OD 0.01 and 0.2 at 270 nm. The fluorescence quantum yield was determined using Equation A3.1.[1]

$$\Phi_{\mathrm{fl}} = \frac{\frac{\Delta \mathrm{I}}{\Delta \mathrm{Abs}}}{\frac{\Delta \mathrm{I}_{\mathrm{Ref}}}{\Delta \mathrm{Abs}_{\mathrm{Ref}}}} \frac{\mathrm{n}}{\mathrm{n}_{\mathrm{Ref}}} \Phi_{\mathrm{fl\ Ref}} \qquad \text{(Eqn. A3.1)}$$

Here $\frac{\Delta \mathrm{I}}{\Delta \mathrm{Abs}}$ is the slope obtained by plotting integrated emission as a function of sample absorbance (whereas $\frac{\Delta \mathrm{I}_{\mathrm{Ref}}}{\Delta \mathrm{Abs}_{\mathrm{Ref}}}$ is the same for the reference standard) and was determined by a linear least-squares regression (Figure A3.2). n is the refractive index of the solvent environment for the sample, $\mathrm{n}_{\mathrm{Ref}}$ is the refractive index of the solvent in the standard solution. Reproducibility of the determined quantum yields and soundness of method were verified by using two reference standards.

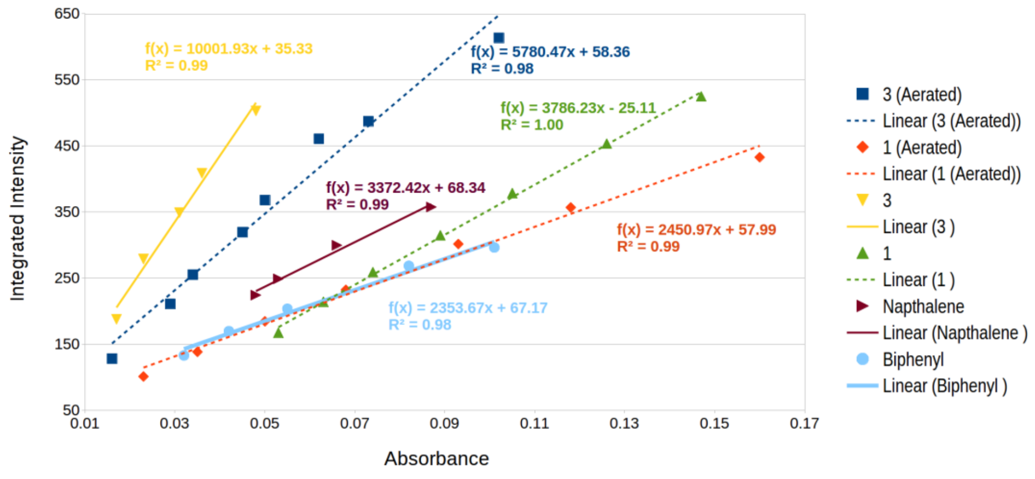

**Figure A3.2.** Integrated emission intensities vs. sample absorbance used to determine fluorescence quantum yields ($\Phi_{fl}$) of **1** and **3** in cyclohexane with naphthalene and biphenyl as standards.[1,2, 3]

### A3.3. Transient Absorption Spectroscopy

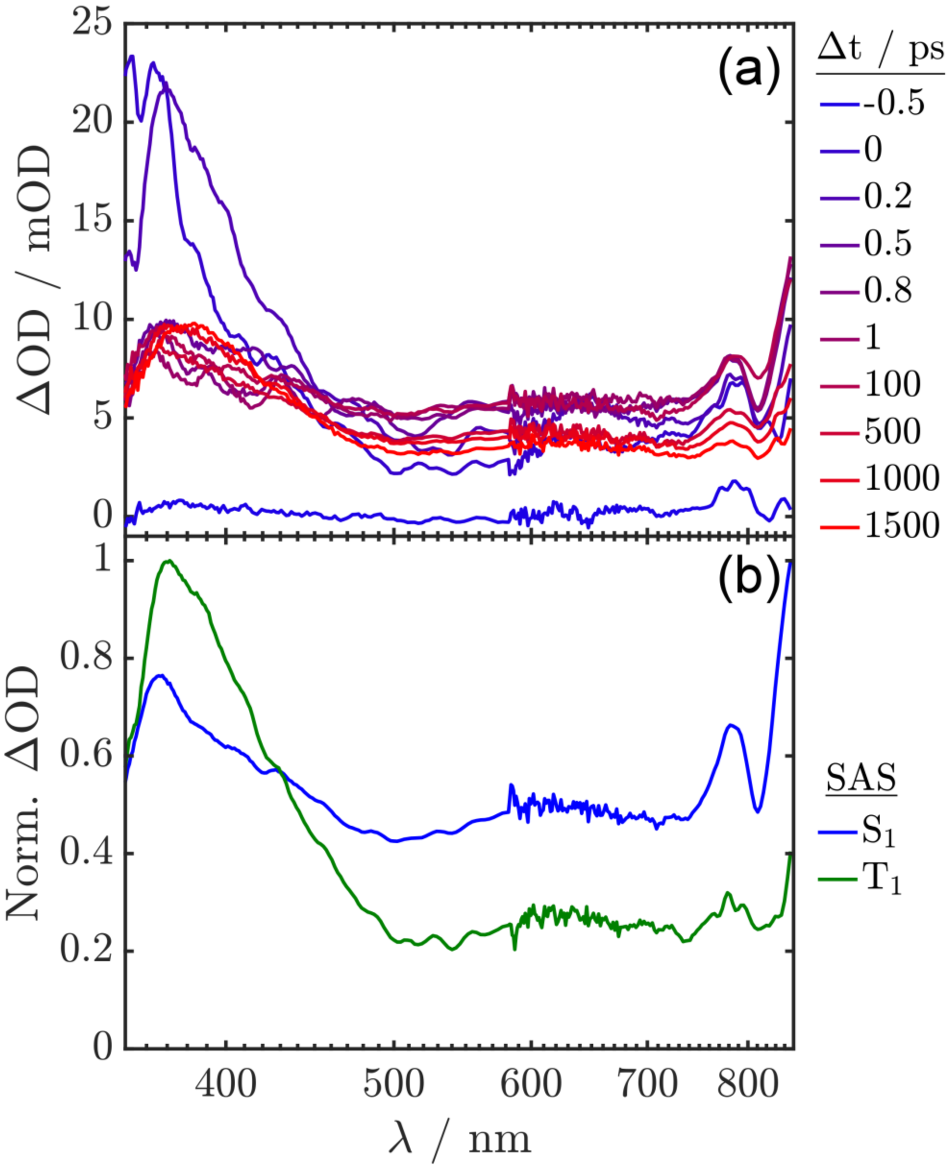

**Figure A3.3.** (a) fs-TA spectra obtained with **1** in THF upon 330 nm excitation. (b) Species associated spectra obtained from global analysis using a kinetic interconversion model ($S_1 \rightarrow T_1$, τ = 933 ps).

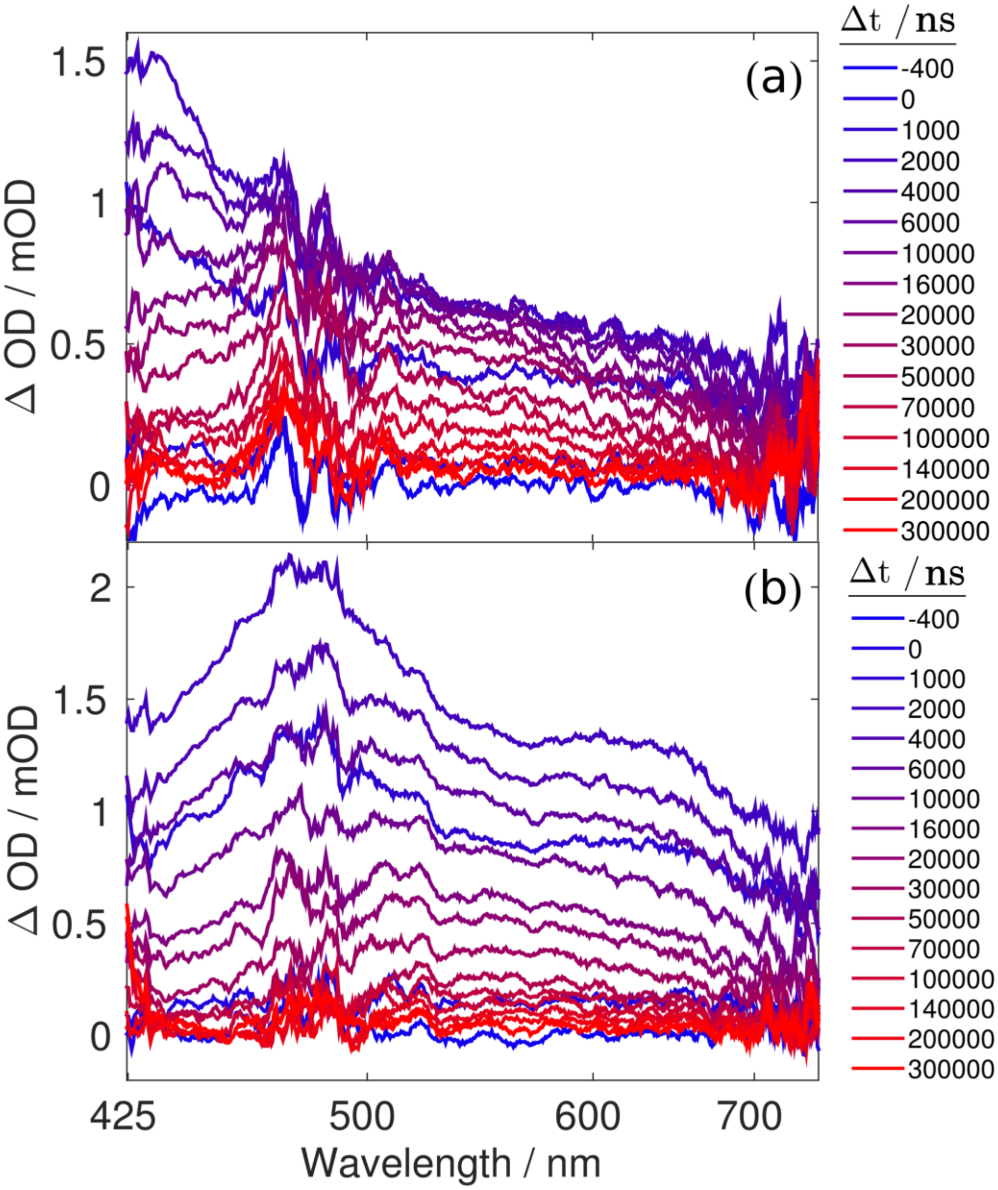

**Figure A3.4**. μs-TA spectra of (a) **1** and (b) **3** in deaerated THF with 330 nm photoexcitation.

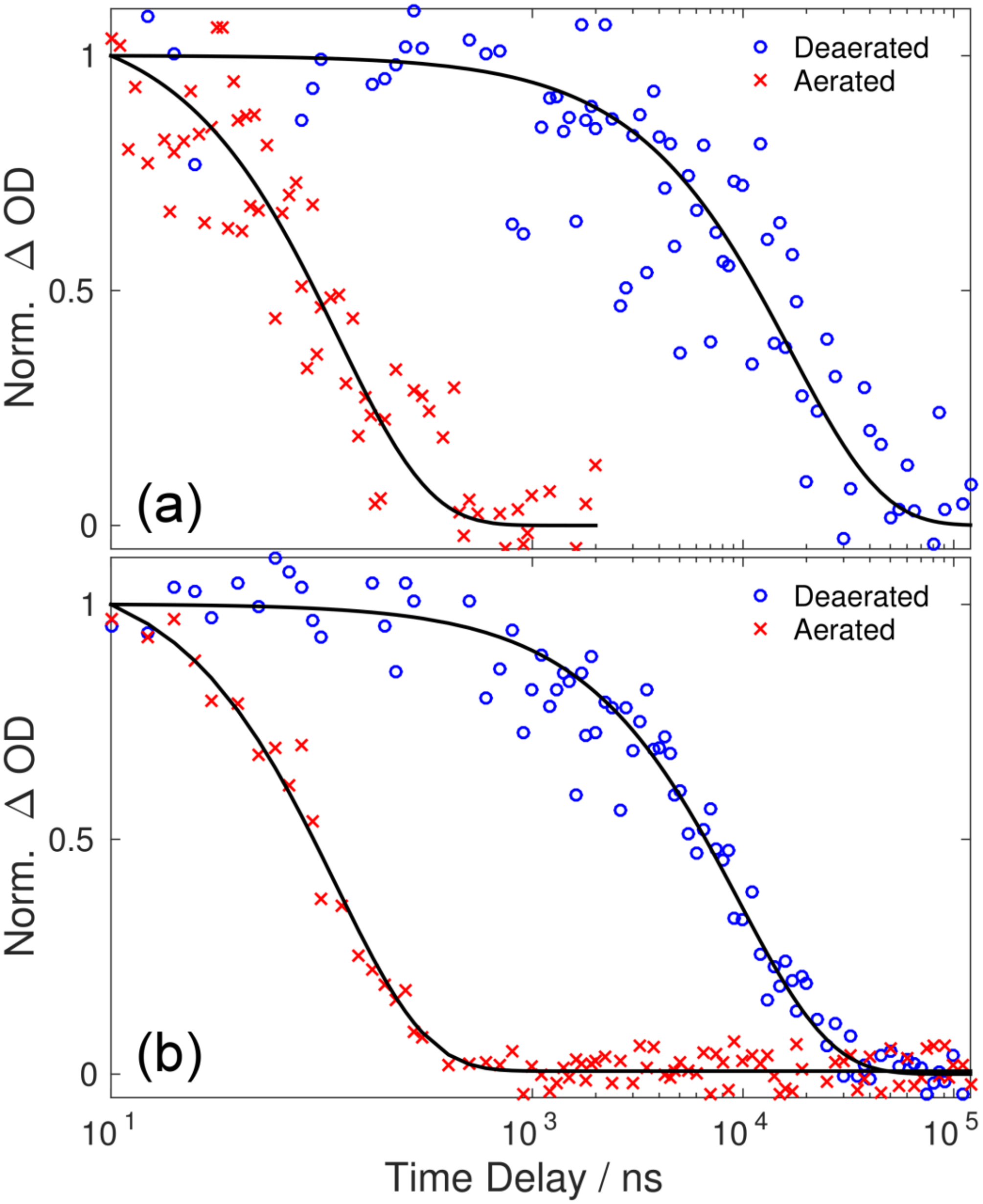

**Figure A3.5**. ns-TA traces for (a) **1** and (b) **3** in deaerated THF with 320 and 330 nm photoexcitation, respectively. The probe wavelength was 405 nm for **1** and 450 nm for **3**.

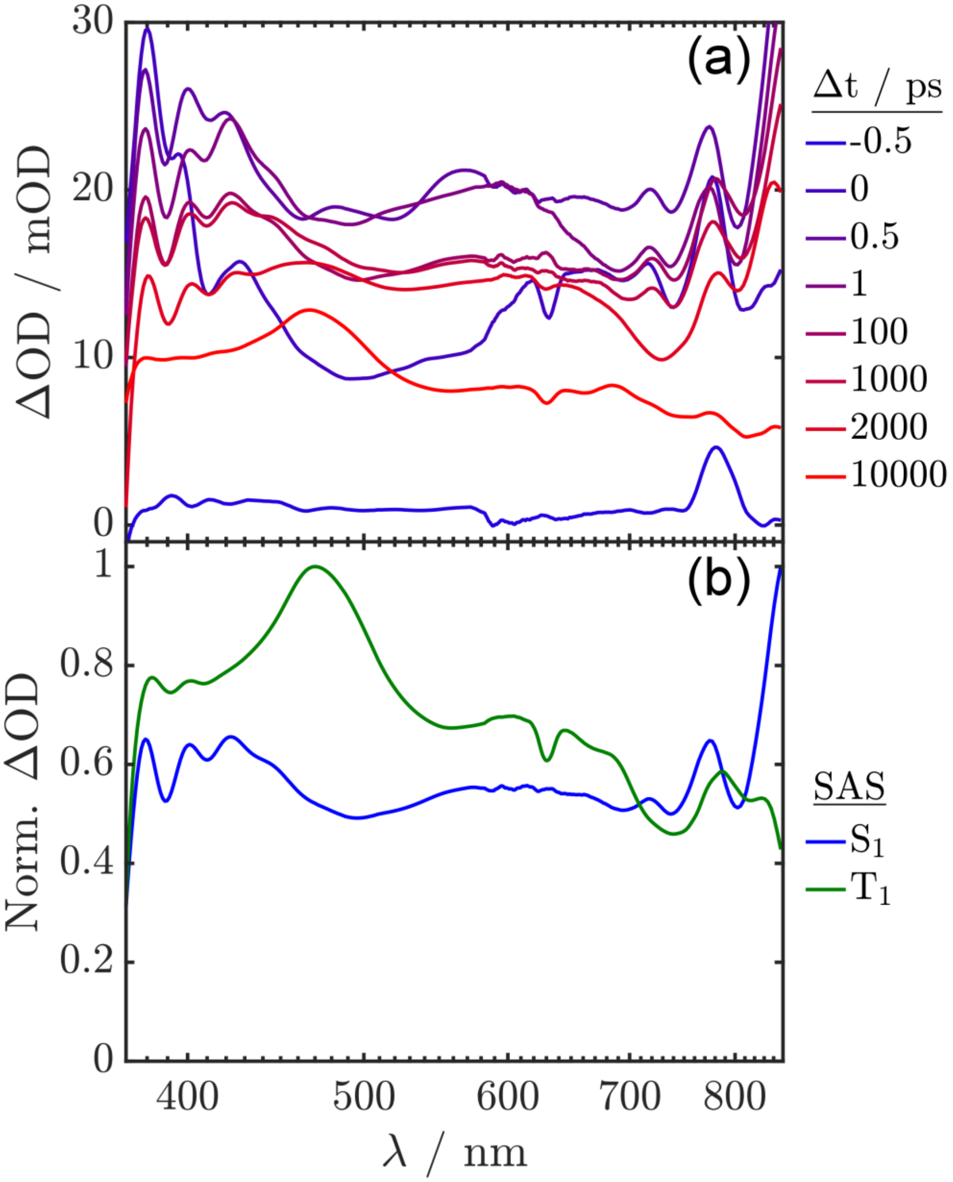

**Figure A3.6.** (a) fs-TA spectra obtained with **3** in THF upon 330 nm excitation. (b) Species associated spectra obtained from global analysis using a kinetic interconversion model ($S_1 \rightarrow T_1$, $\tau$ = 2.49 ns).

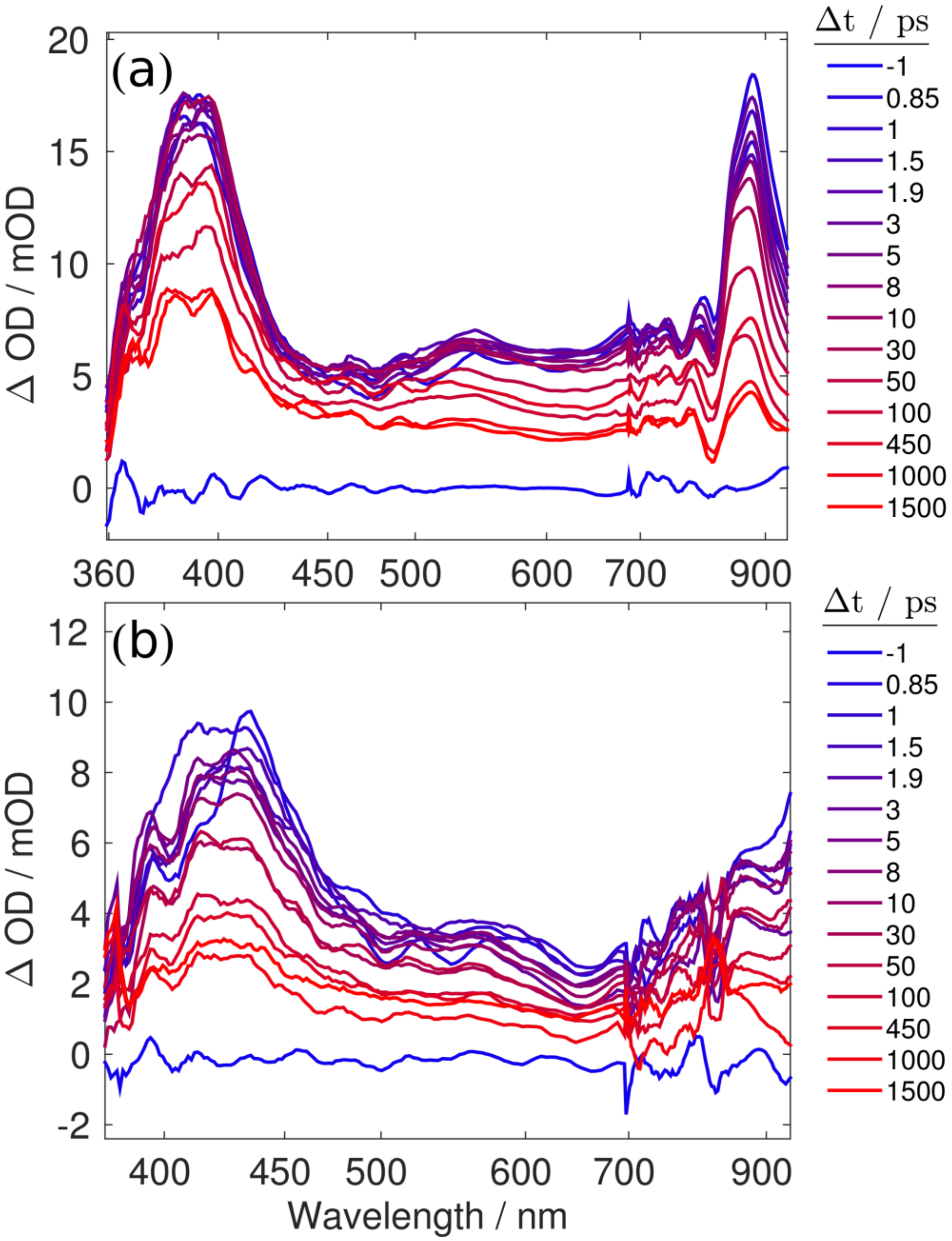

**Figure A3.7.** fs-TAS of **1** (a) and **3** (b) in a 95:5 THF:$H_2O$ solution by volume following 330 nm photoexcitation. Solutions were prepared by adding water followed by heating (50 °C) and sonication for 30 minutes. Note that the spectral shapes are distinct from those collected with dry solutions and presented in Figures A3.2 and A3.3.

## A3.4. Triplet Quantum-Yield Determination

All the kinetic corrections for triplet quantum-yield determination described herein are based on procedures and equations taken from Carmichael and Hug.[4] Since the probability of energy transfer from donor to acceptor is not always 100%, or alternatively that triplet donors relax via competing deactivation pathways, corrections must be introduced for the probability of energy transfer $P_{tr}$. This requires the determination of $k_D$ and $k_{et}$ which are calculated by measuring the decay rate for the donor in the absence ($\tau_D^{Exp}$, Eqn. A3.5) and presence of acceptor ($\tau_{D+A}^{Exp}$, Eqn. A3.6).

$$^3D \overset{k_D}{\rightarrow} {}^1D \qquad \text{(Eqn. A3.2)}$$

$$^3D + {}^1A \overset{k_{et}}{\rightarrow} {}^1D + {}^3A \qquad \text{(Eqn. A3.3)}$$

$$^3A \overset{k_A}{\rightarrow} {}^1A \qquad \text{(Eqn. A3.4)}$$

$$\tau_D^{Exp} = \frac{1}{k_D} \qquad \text{(Eqn. A3.5)}$$

$$\tau_{D+A}^{Exp} = \frac{1}{k_{et}[{}^1A]+k_D} \qquad \text{(Eqn. A3.6)}$$

$$P_{tr} = \frac{k_{et}[{}^1A]}{k_{et}[{}^1A]+k_D}\,[{}^1A] \qquad \text{(Eqn. A3.7)}$$

An additional correction is applied if $k_A$ is not small compared to $k_{et}[{}^1A]+k_D$ that is a modification to the maximum ΔOD of the acceptor ($\Delta OD_A$). The correction is given by calculating the time at which the acceptor absorption peaks, $t_{max}$ (Eqn. A3.8), and scaling $\Delta OD_A$ as shown in Eqn A3.9.

$$t_{max} = ln(\frac{k_A}{k_{et}[{}^1A]+k_D})(k_A - k_{et}[{}^1A] - k_D)^{-1} \qquad \text{(Eqn. A3.8)}$$

$$\Delta OD_A \cdot P_{TD} = \Delta OD_A(t_{max})\, e^{k_A t_{max}} \qquad \text{(Eqn. A3.9)}$$

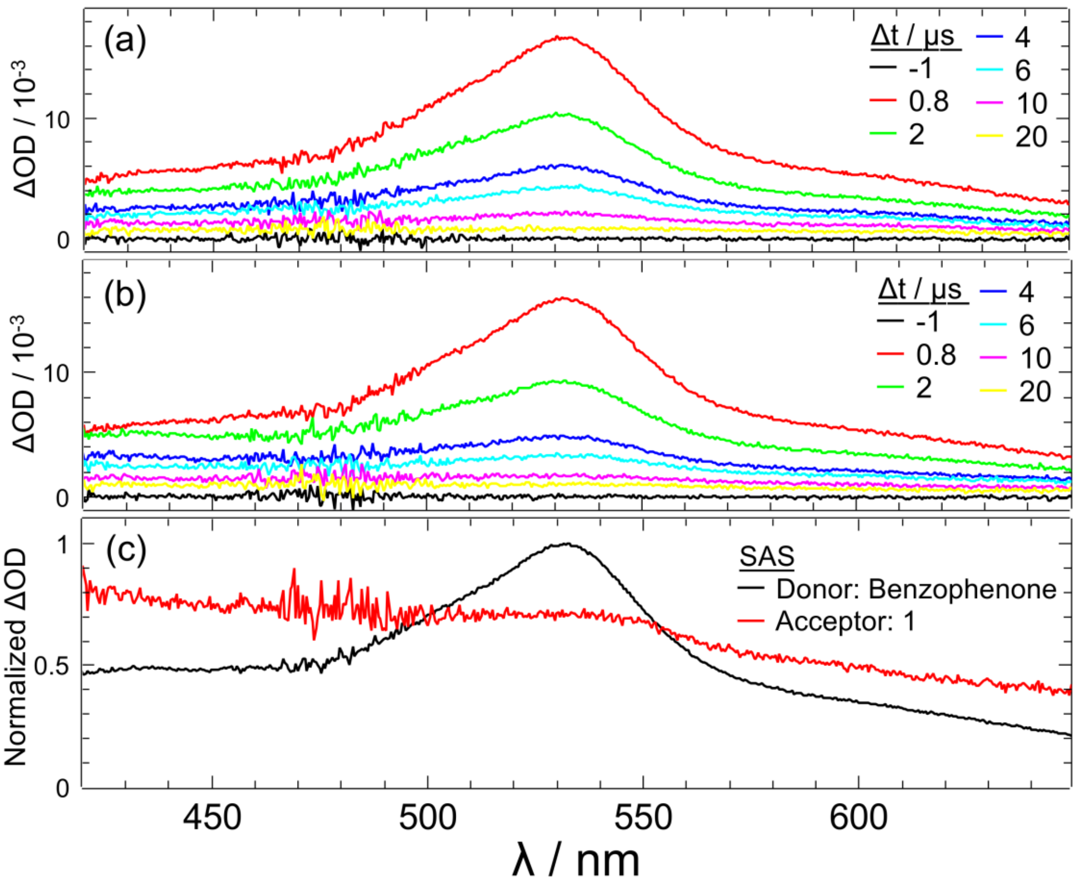

**Figure A3.8.** μs-TA spectra obtained with benzophenone (a) and benzophenone/**1** (b) photosensitization in benzene upon 360 nm excitation. (c) Species associated spectra (SAS) obtained from global analysis of benzophenone/**1** using a kinetic interconversion model used to determine the extinction coefficient for the triplet of **1** (Donor → Acceptor, $\tau_{D+A}^{Exp}$ =2.35 μs). The lifetime of benzophenone in benzene ($\tau_D^{Exp}$) was determined by an exponential fit at 532 nm to be 3.01 μs.

## A3.5. Computational Results

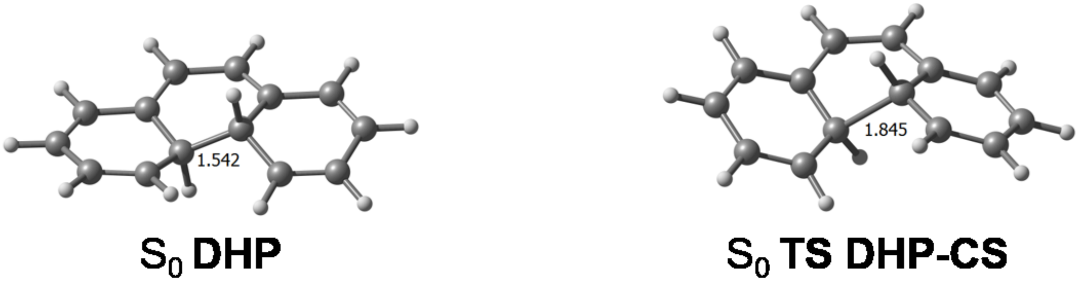

$S_0$ DHP

$S_0$ TS DHP-CS

**Figure A3.9.** Structures of dihydrophenanthrene (DHP) and the transition state for ring opening on the $S_0$ (UB3LYP/6-31G*). The inter-ring C-C bond length is given in Å.

## A3.6. References

1. A. M. Brouwer, *Pure and Applied Chemistry*, **2011**, *83*, 2213-2228.
2. R. R. Hautala, N. E. Schore and N. J. Turro, *J Am Chem Soc*, **1973**, *95*, 5508-5514.
3. I. B. Berlman, *J Chem Phys*, **1970**, 52, 5616-5621.
4. I. Carmichael and G. L. Hug, *Journal of Physical and Chemical Reference Data*, **1986**, *15*, 1-250.

# Appendix 4

# Supporting Information for Chapter 6: Impacts of Isoelectronic BN-doping on the Photochemistry of Polyaromatic Hydrocarbons: Photocyclization Dynamics of Hexaphenyl Benzene and Hexaphenyl Borazine

## A4.1 Experimental Methods

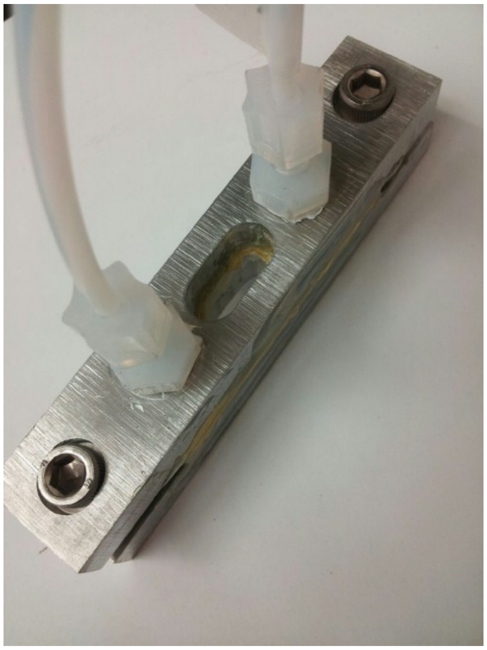

**Figure A4.1.** Custom-built 250 μm pathlength flow cell. The flow cell frame is constructed from 2 pieces of aluminum bar stock with milled holes for windows, compression hardware and PFA tubing adapters (Cole-Palmer). The windows are 1-mm fused quartz microscope slides (AdValue Tech, FQ-S-003). The window facing the inlet and outlet adapters are drilled with 0.5 cm holes for the passage of solvent into the cell. The optical path length is adjustable by use of PTFE seals of various thicknesses. [For a 250 μm path length, the PTFE seal is made from McMaster-Carr 8569k18 PTFE film).

Additional PTFE film was placed on the outside of the windows that seal the cell and provide a slight cushion between the glass and aluminum frame. Because PTFE provides excellent chemical resistivity but poor sealing properties the exterior of the flow cell was sealed with removable epoxy that has excellent chemical compatibility with many organic solvents (cyclohexane, hexane, ethanol, THF, $CH_2Cl_2$, etc.). The total cost of materials is ~ $150 providing an economical, low cost alternative for a short-path length flow cell.

## A4.2 Experimental Results

### *A4.2.1 Time-Resolved Spectroscopy*

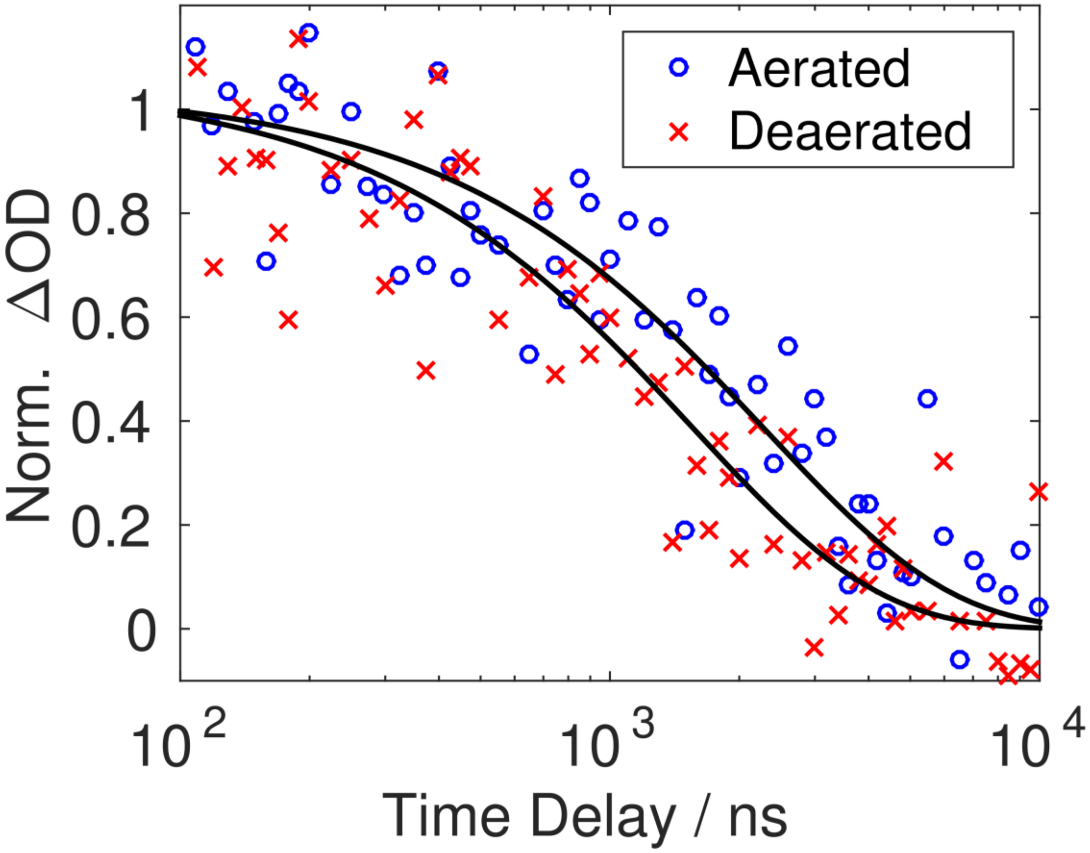

**Figure A4.2.** Comparison of nanosecond time-resolved transient absorption of **4** in THF, under aerated (blue circles) and deaerated (red Xs) conditions, following photoexcititation at 266 nm and probed at 405 nm. The lifetimes under aerated and deaerated conditions are 2300 ± 300 ns and 1600 ± 300 ns, respectively.

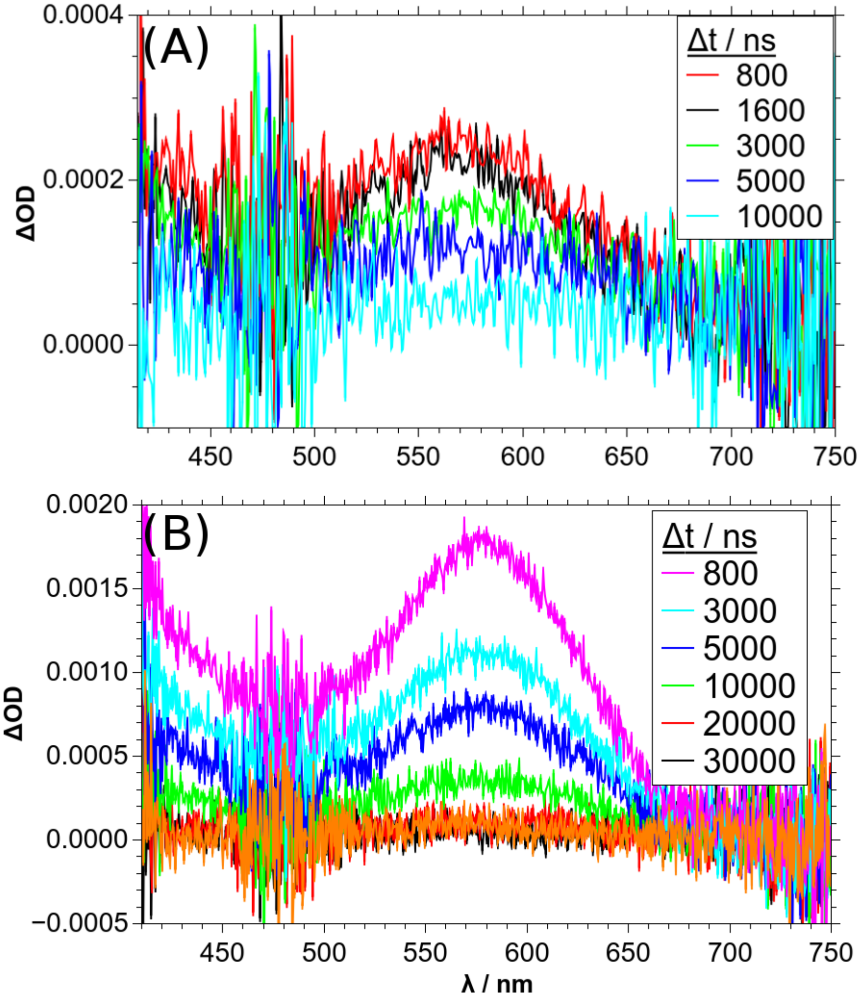

**Figure A4.3.** Representative temperature dependent μs-TA data for 266 nm photoexcitation of **4** in THF as probed with a white-light LED at (A) 273 K and (B)193 K.

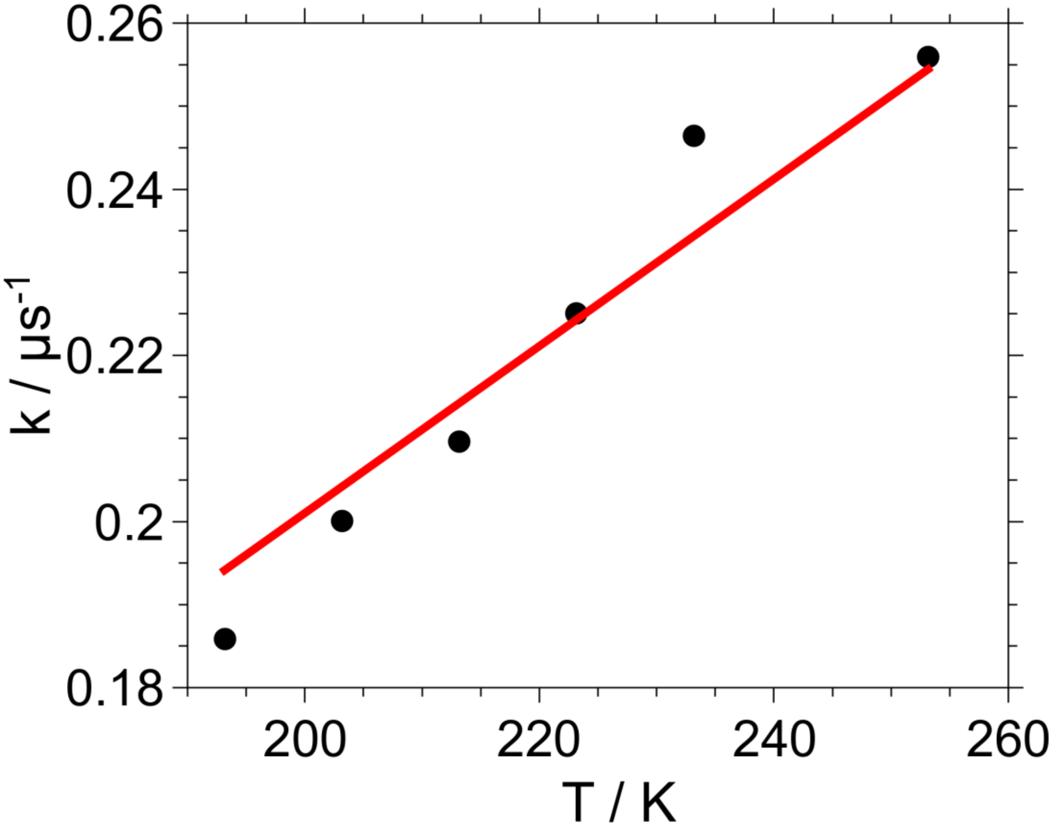

**Figure A4.4**. Modified Eyring analysis for an activationless reaction (i.e. with $E_a$=0 in Equation 6.1 of the main text) showing reasonable agreement to a linear fit with temperature ($R^2$=0.93).

### *A4.2.2 Characterization of Photochemical Products*

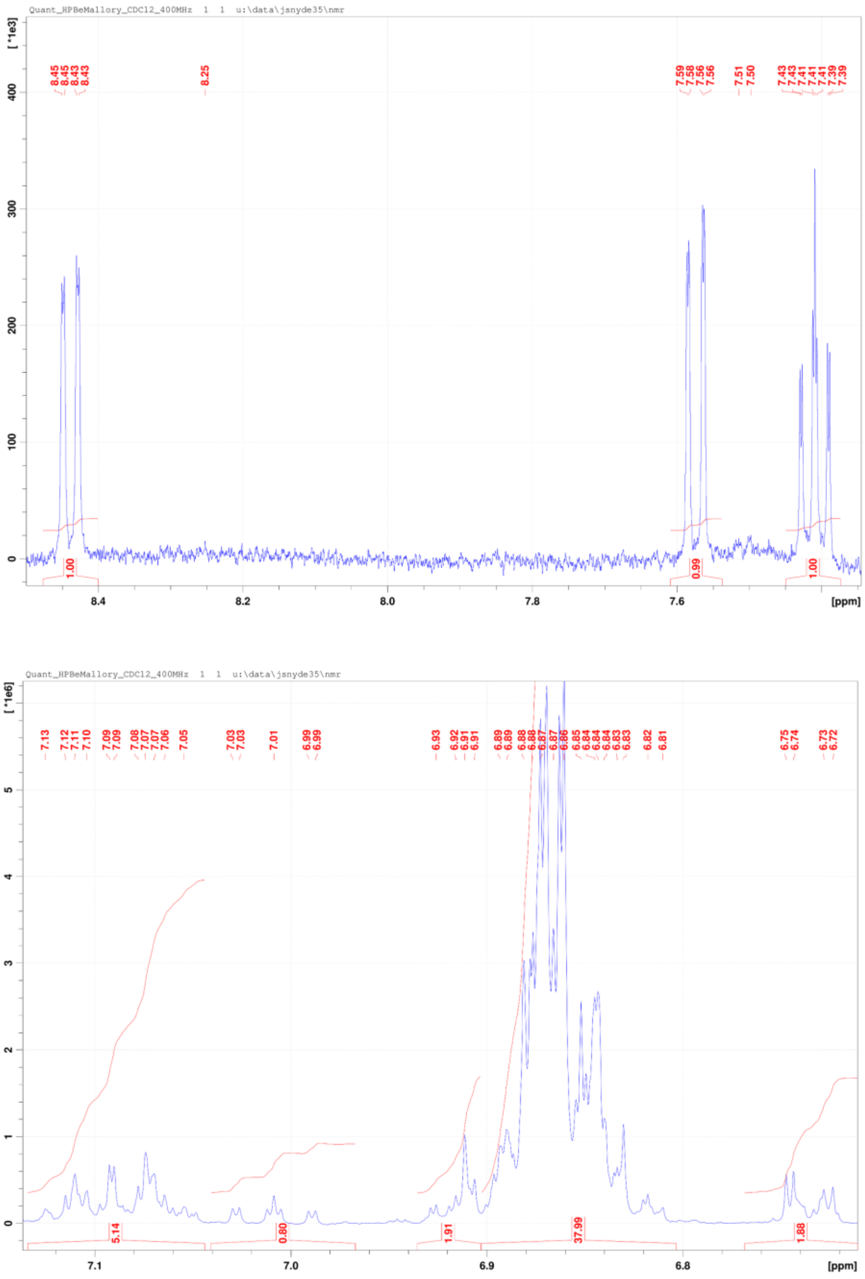

**Figure A4.5.** Quantitative $^{1}$H NMR (400 MHz, $CD_2Cl_2$) of **4** collected with a relaxation time of 5 $T_1$, where $T_1$ was determined to be 2.242 s.

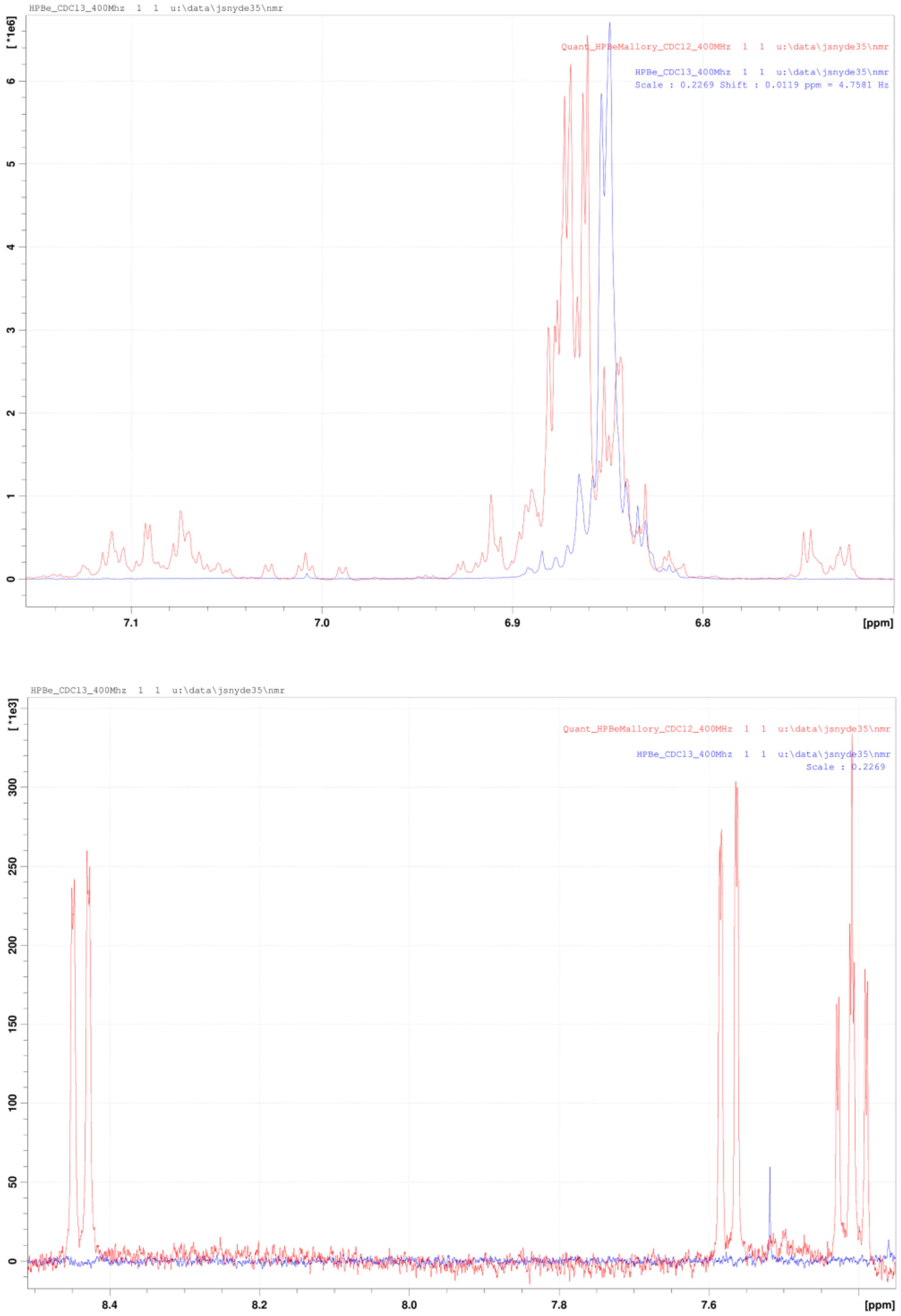

**Figure A4.6.** Comparison of $^1$H NMR (400MHz) of **4** before (blue) and after (red) irradiation in a Rayonet reactor.

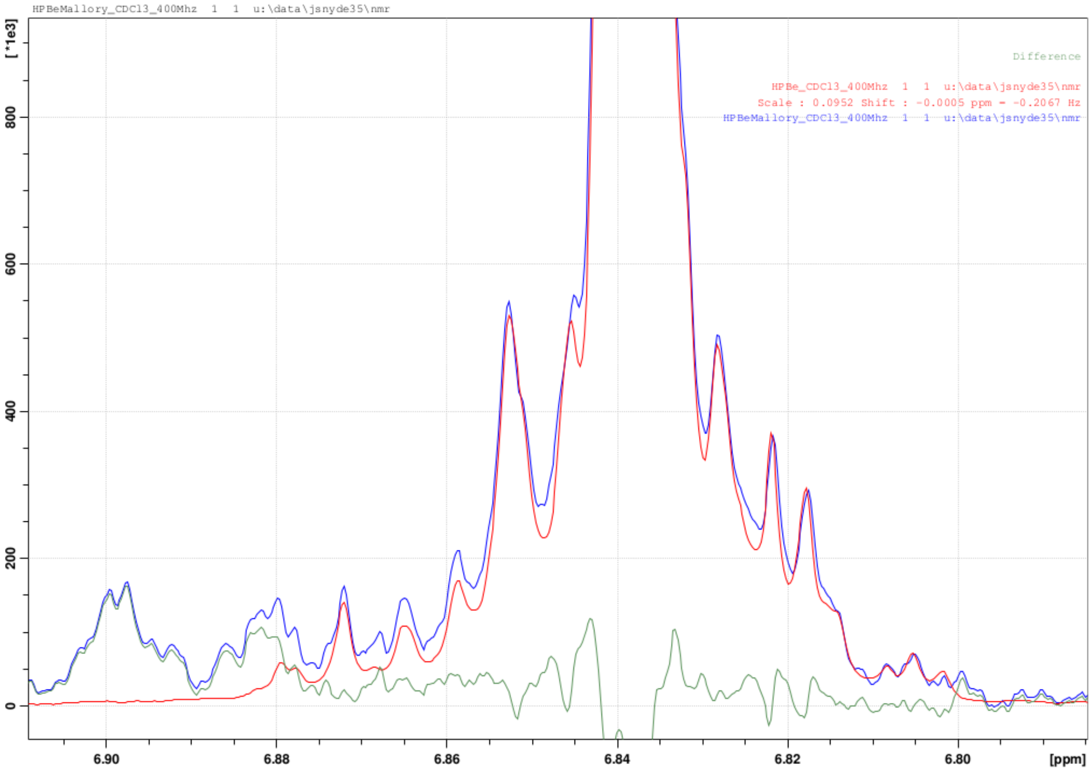

**Figure A4.7.** Spectral overlap of $^1$H NMR of **4** and **6**. The pure spectrum of **4** (red) was subtracted from the reaction mixture (blue) that shows the pure spectrum of **6** (green). Signal subtraction results in an adequate baseline and minimal spectral overlap such that accurate signal integration can be achieved with quantitative NMR.

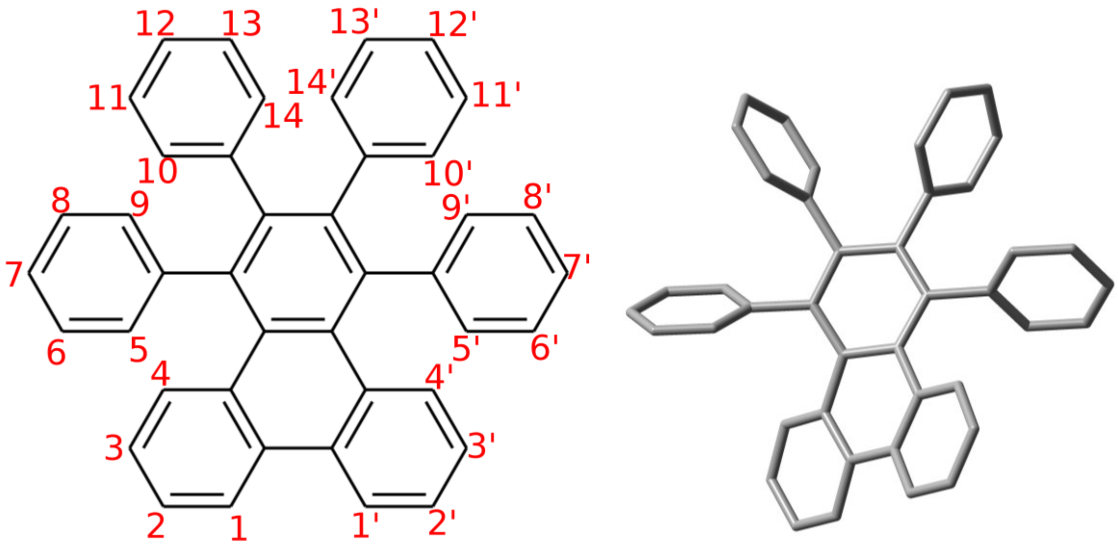

**Table A4.1.** Calculated NMR shifts of **6** (R-CAM-B3LYP/6-31+G*) referenced to TMS (B3LYP/6-311+G(2d,p) GIAO) and further shifted by +0.25 ppm. The 3D illustration shown above at the right illustrates the propeller-like symmetry that results in similar shifts for n and n’ atoms.

| Atom Number | Shift (ppm) |
|---|---|
| 1, 1’ | 8.395 |
| 2, 2’ | 7.498 |
| 3, 3’ | 7.153, 7.104 |
| 4, 4’ | 7.668, 7.573 |
| 5, 5’ | 7.042, 7.134 |
| 6, 6’ | 7.246, 7.178 |
| 7, 7’ | 7.212, 7.274 |
| 8, 8’ | 7.282, 7.123 |
| 9, 9’ | 7.341, 7.439 |
| 10, 10’ | 6.786, 6.631 |
| 11, 11’ | 7.067, 7.156 |
| 12, 12 ‘ | 7.145, 7.129 |
| 13, 13’ | 7.042, 7.134 |
| 14, 14’ | 7.216, 7.050 |

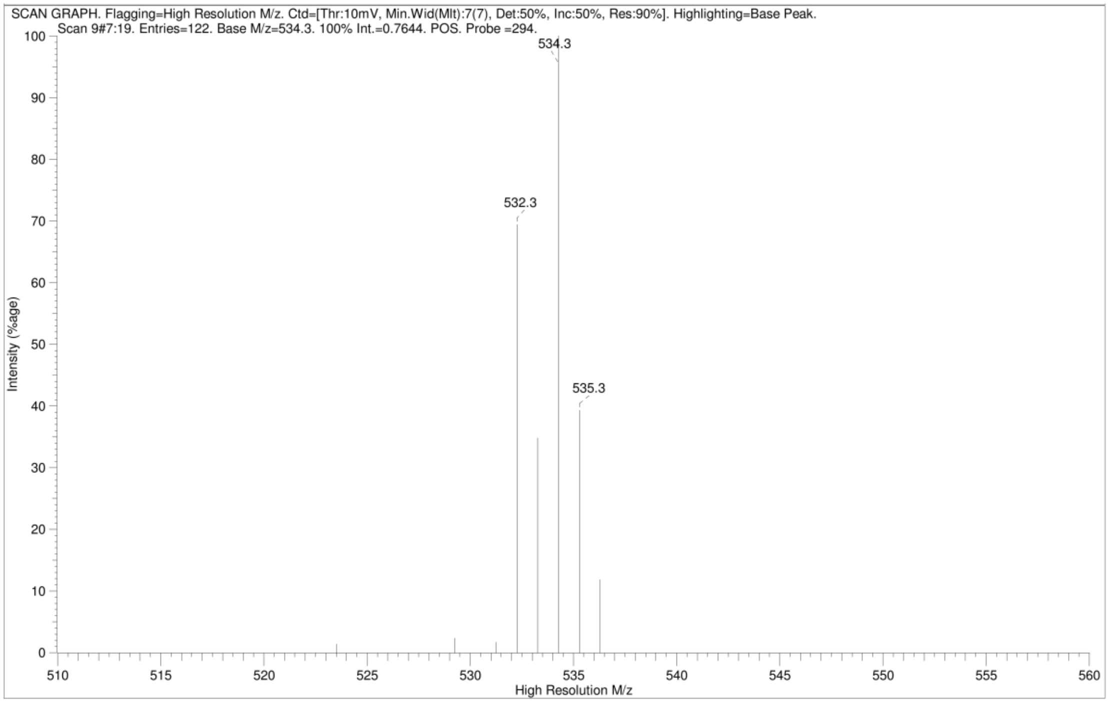

**Figure A4.8.** Mass spectrum of a sample solution of **4** following UV irradiation for 24 hours in the presence of $I_2$.

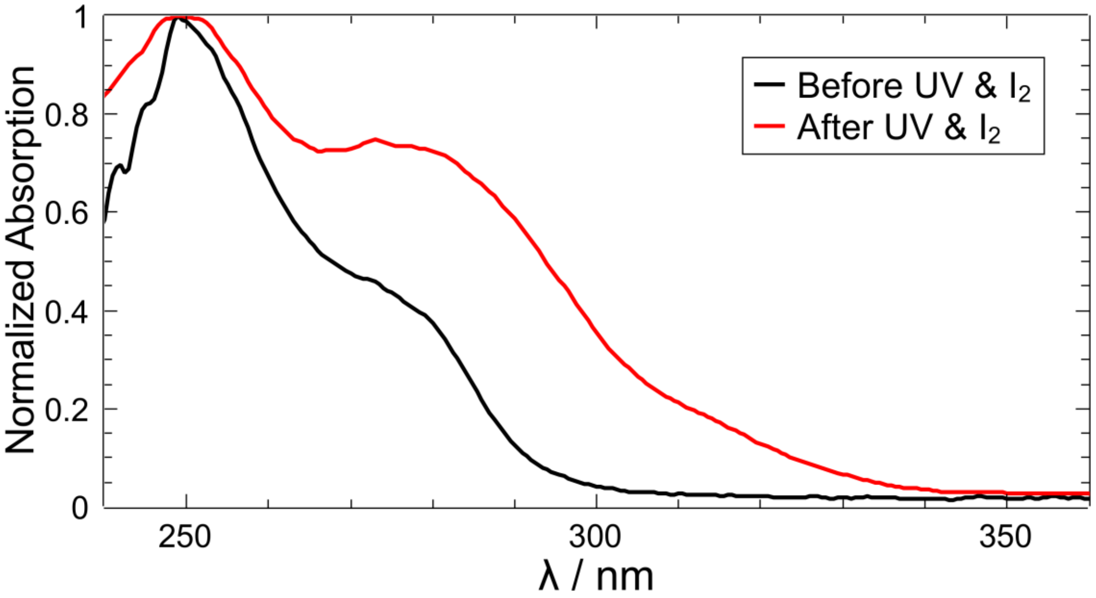

**Figure A4.9.** UV-Vis spectra of a solution of **4** in cyclohexane before and after Mallory reaction, i.e. UV irradiation and oxidation with $I_2$, corresponding to pure **4** and a mixture of **4** and **6**, respectively.

## A4.3 Computational Results

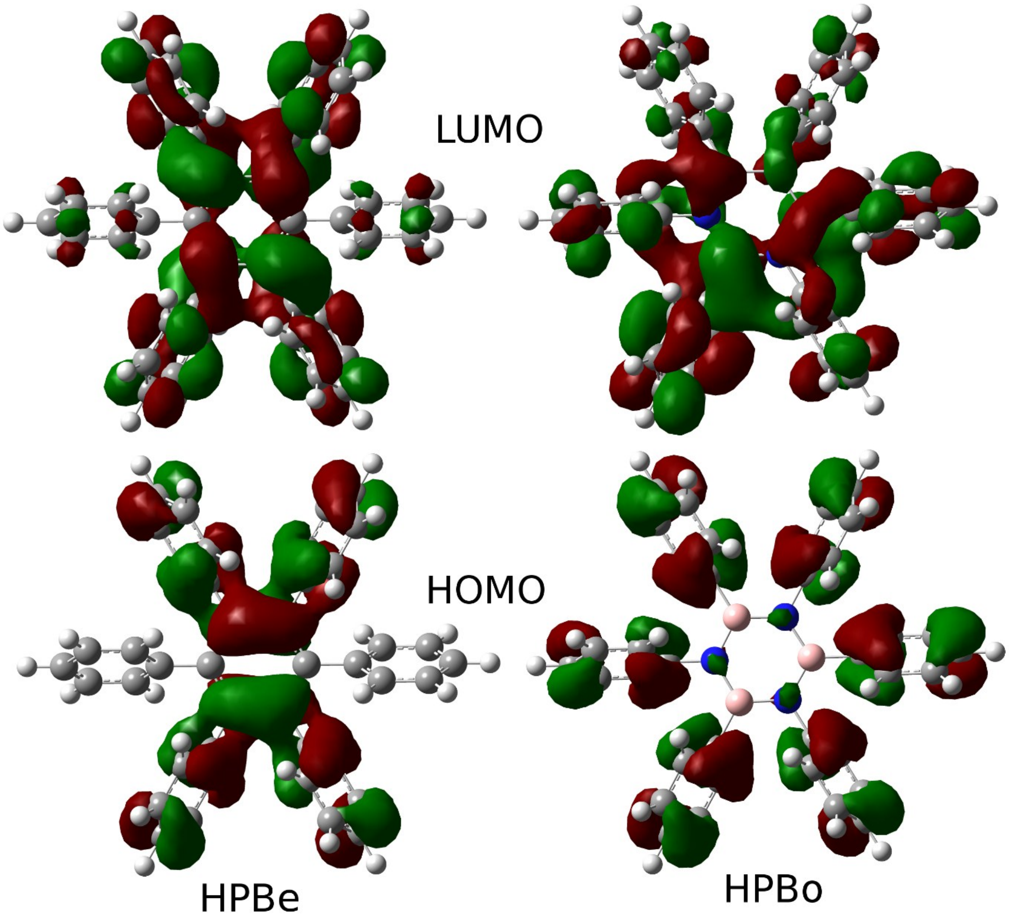

LUMO
HOMO
HPBe
HPBo

**Figure A4.10.** HOMO and LUMO of **1** and **4** from R-CAM-B3LYP//6311+G*.

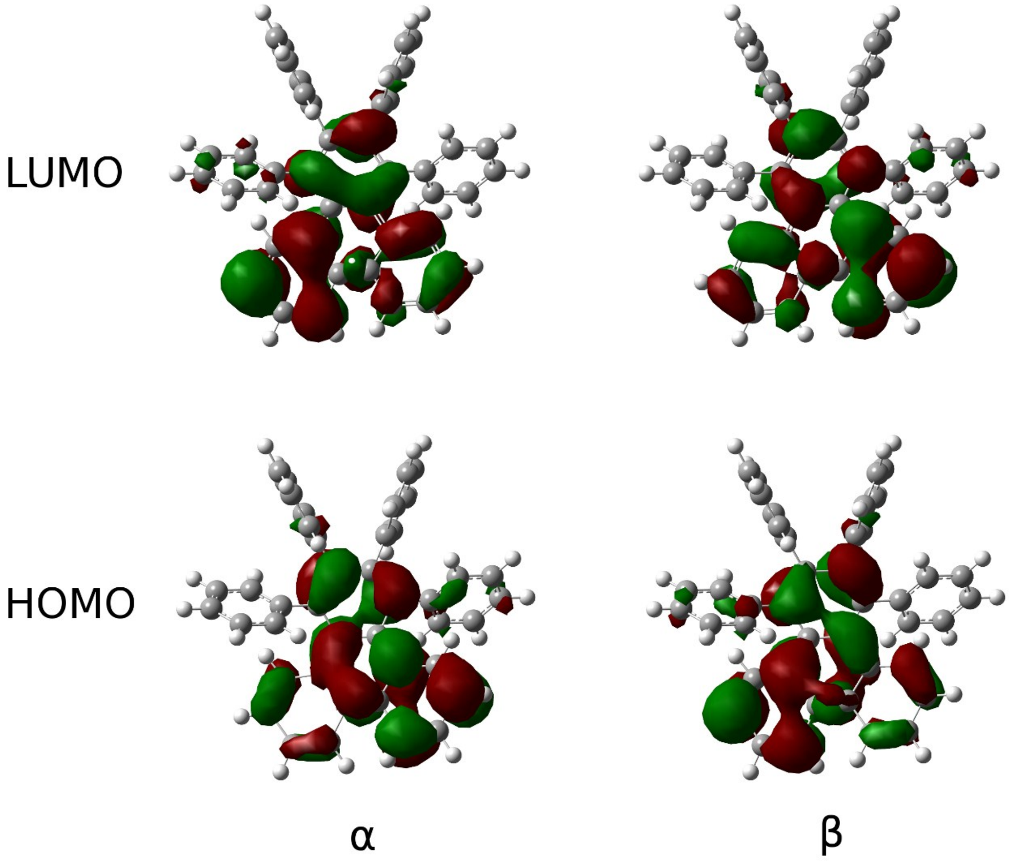
LUMO
HOMO
α
β

**Figure A4.11.** BS-U-CAM-B3LYP Kohn-Sham orbitals of **5b**.

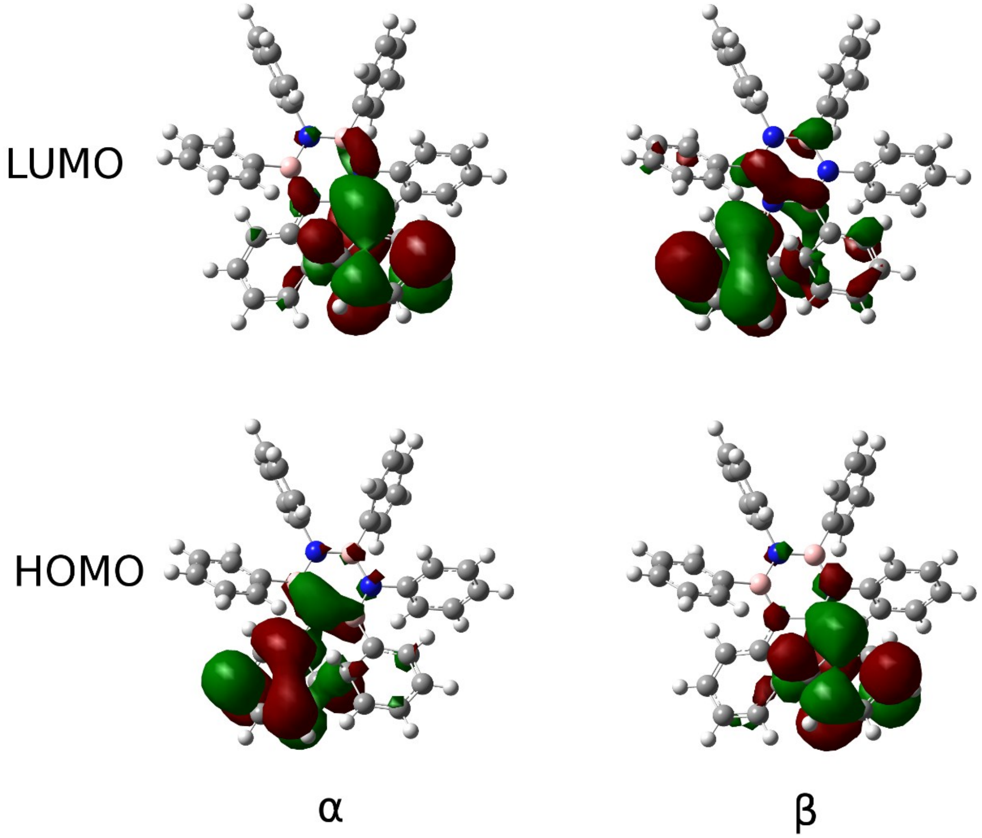
LUMO
HOMO
α
β

**Figure A4.12.** BS-U-CAM-B3LYP Kohn-Sham orbitals of **2b**.

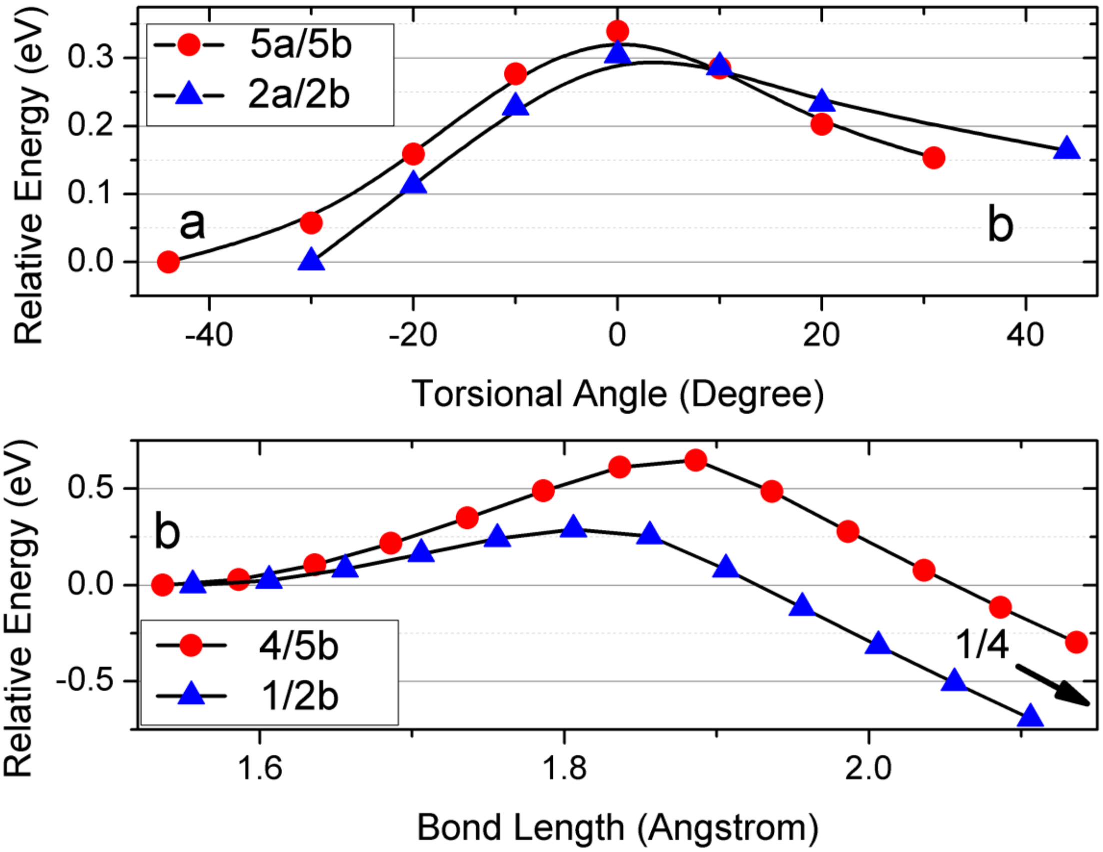

**Figure A4.13.** Scans of potential energy surfaces between **1/4** and conformers **2a/5a** and **2b/5b** at the U-CAM-B3LYP//6-31G* level For the PES scan between conformers **2a/5a** and **2b/5b** (top) the torsional angle of the DHT subgroup was scanned, while for the scan between **1/4** and **2b/5b** the photochemically formed CC bond was varied while freezing the rotational angle of the remaining 4 phenyl rings to prevent conformer switching mid-scan.

# Appendix 5

# Autocorrelator Operation Guide for Pulse Characterization

## A5.1 Function of Autocorrelator and Components

An autocorrelator is used for the determination of the time duration of a sub-nanosecond laser pulse. Since the time response of the fastest (and most expensive) photodiodes and oscilloscopes are on the order of > 20 ps, a femtosecond or few picosecond duration laser pulse is much too fast to be resolved in time with such equipment. Therefore we use the self-gated nonlinear response of the laser pulse itself, or autocorrelation, to determine the time duration of the pulse.

The general layout and design for an autocorrelator is shown in Figure A5.1. Generally an autocorrelator consists of three parts: an interferometer, the optical mixing and detection of the autocorrelation signal, and the electronics that drive any optomechanical components and perform data acquisition. Since we self-gate the laser pulse, an interferometer serves to produce a replica of the input pulse that has been shifted in time. The optical mixing step is where the pulse self-interaction occurs and is described in the following section (A5.2). A description of the electronic components is provided in section A5.3.

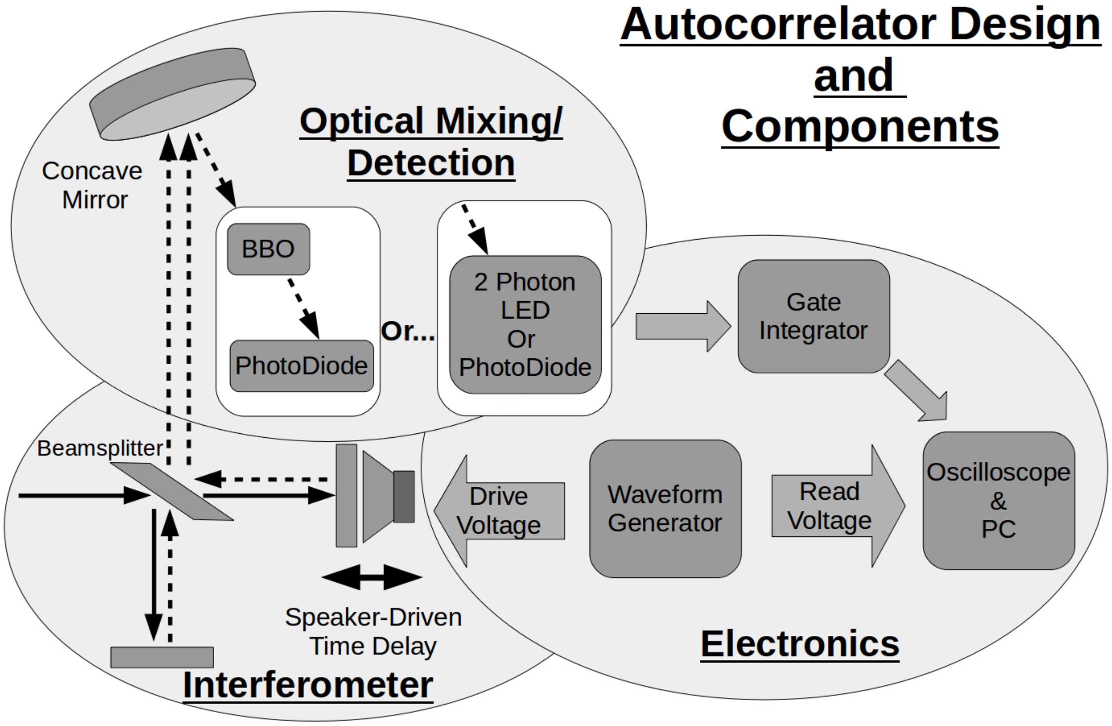
Autocorrelator Design and Components
Optical Mixing/ Detection
Concave Mirror
BBO
PhotoDiode
Or...
2 Photon LED Or PhotoDiode
Gate Integrator
Oscilloscope & PC
Beamsplitter
Drive Voltage
Waveform Generator
Read Voltage
Speaker-Driven Time Delay
Interferometer
Electronics

**Figure A5.1.** Experimental setup of a autocorrelator. The interferometer provides a replica of the initial pulse that is optically mixed in BBO or by 2 photon absorption in a LED. The electronics simultaneously scan the time delay, collect the integrated signals and output the intensity autocorrelation on a calibrated time scale.

## A5.2 Optical Setup

A Michelson interferometer serves two purposes: to generate a replica of the input pulse and control the time delay between the input and replica pulse. For the purpose of autocorrelation one arm of the interferometer has its end mirror mounted on a speaker and a translation stage to provide coarse optical delay. To align the interferometer, ensure that the beamsplitter is tilted to 45 degrees relative to the input so that the beam is split into a perpendicular and collinear leg. Each path is retroreflected and should be spatially overlapped roughly with the input beam at the beamsplitter. Finally the recombined beams from the interferometer should be spatially overlapped far field (2-3 feet from the beam splitter) by adjustment of one end mirror while the speaker-mounted mirror is fixed. Note that the speaker displacement as a function of voltage must be calibrated by interferometric measurement of a CW HeNe laser.[1,2]

The overlapped beams are then focused with a concave mirror and for visible wavelengths two options are available for intensity autocorrelation: a two-photon detector (LED, laserdiode or photodiode) or SHG in BBO.[1,3,4] From an operational standpoint the two-photon detector is the simplest since it only requires the two-photon detector to be placed at the focal plane of the overlapped beams. Any device that emits or detects light can be used as a two-photon detector provided that the incident light is above the band gap of the material (for a list of commercial devices see reference).[5] For example, GaN laser diodes and LEDs emit ~400 nm light, are useful for autocorrelation from ~425-800 nm and are readily available for under $10.[6,7] Alternatively, SHG in BBO can be used for intensity autocorrelation, which requires the BBO crystal to be placed at the focal plane and the subsequent output wavelength to be filtered by a dichroic or bandpass filter.[1] Comparison of results between the two approaches in our lab with pulse widths >=35 fs shows that they provide nearly equivalent results (Figure A5.8).

## A5.3 Electronics Setup

The autocorrelation requires multiple electronics to simultaneously scan time delay and collect signals for characterization including: an oscilloscope, speaker driver/waveform generator, and gate integrator for the photodiode signal.

Waveform Generator: Generates a saw-tooth (preferably 80% rise/20% fall time) wave at a 1-2 Hz frequency for real-time feedback for pulse compression adjustment. This voltage is output to an oscilloscope and speaker.

Gate Integrator: Integrates the autocorrelation signal for ns-μs's to reduce noise from dark background. The signal is first sent to a preamplifier and then to the gate integrator module. A trigger is also necessary as an input for synchronization to the laser repetition rate. The gated region and signal must be inspected simultaneously on an oscilloscope and overlapped using the delay and width knobs. Make sure the integration mode is set to "last sample" that will output the result on the next shot.

## A5.4 Modification for Deep-UV/266 nm Autocorrelation

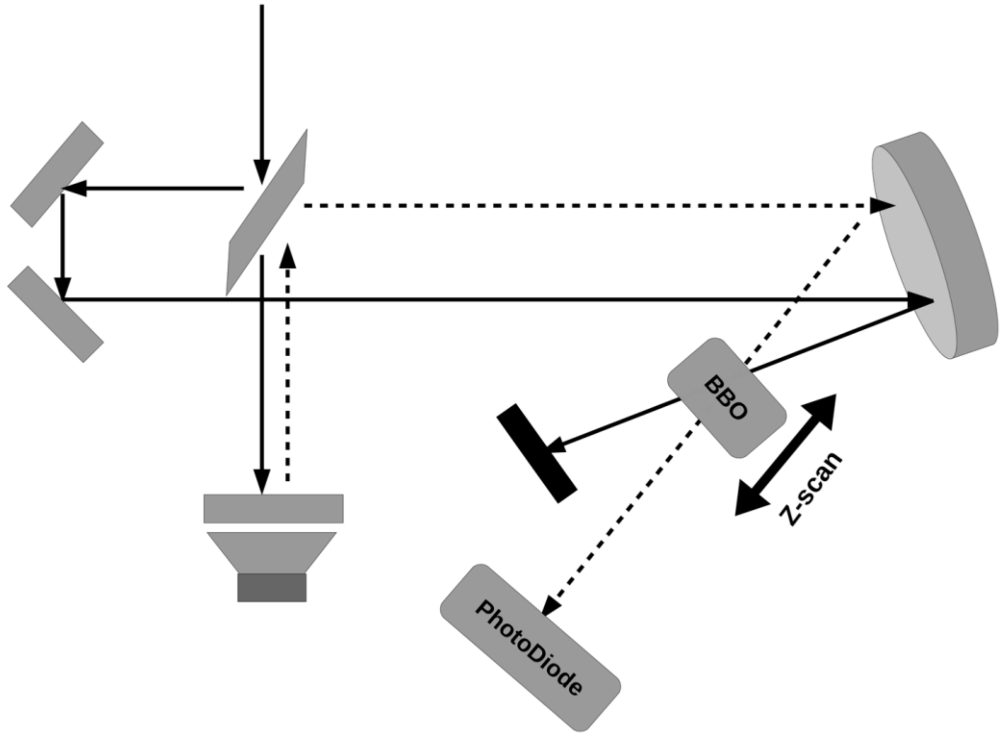

**Figure A5.2.** Modifications to autocorrelator for 266 nm measurement based on 2PA in BBO. A pump-probe geometry is used for the decrease in probe transmission on a photodiode. Note that to obtain optimal signal the BBO crystal should be translated ("Z-scanned") to find the true focal point.

Autocorrelation of 266 nm pulses can be performed by two-photon absorption in BBO.[8,9] However this is performed in a pump-probe geometry that requires a few modifications to the autocorrelator. The one interferometer end mirror is replaced with a retroreflector and that beam is used as the pump. Both beams are focused using the concave mirror and the focal point is found by translating the BBO crystal on a pinion stage ("Z-scan") until the pump beam is visibly attenuated. The initial setup and locating the pump-probe overlap is greatly simplified by using a 1cm cuvette of chloroform which has a substantial 2PA coefficient.[9] The location of optimal overlap is difficult to locate however because thermal lensing effects (beam profile distortions) will occur when the beams are nearly overlapped. Once signal is located with chloroform the process can be repeated again with BBO but with the use of much lower pump power (<1 mW will provide sufficient signal) to prevent damage to the crystal. Note that other simpler autocorrelation methods for deep UV autocorrelation are possible with the most attractive and economical being two-photon induced fluorescence of $BaF_2$.[10–12]

## A5.5 Experimental Results

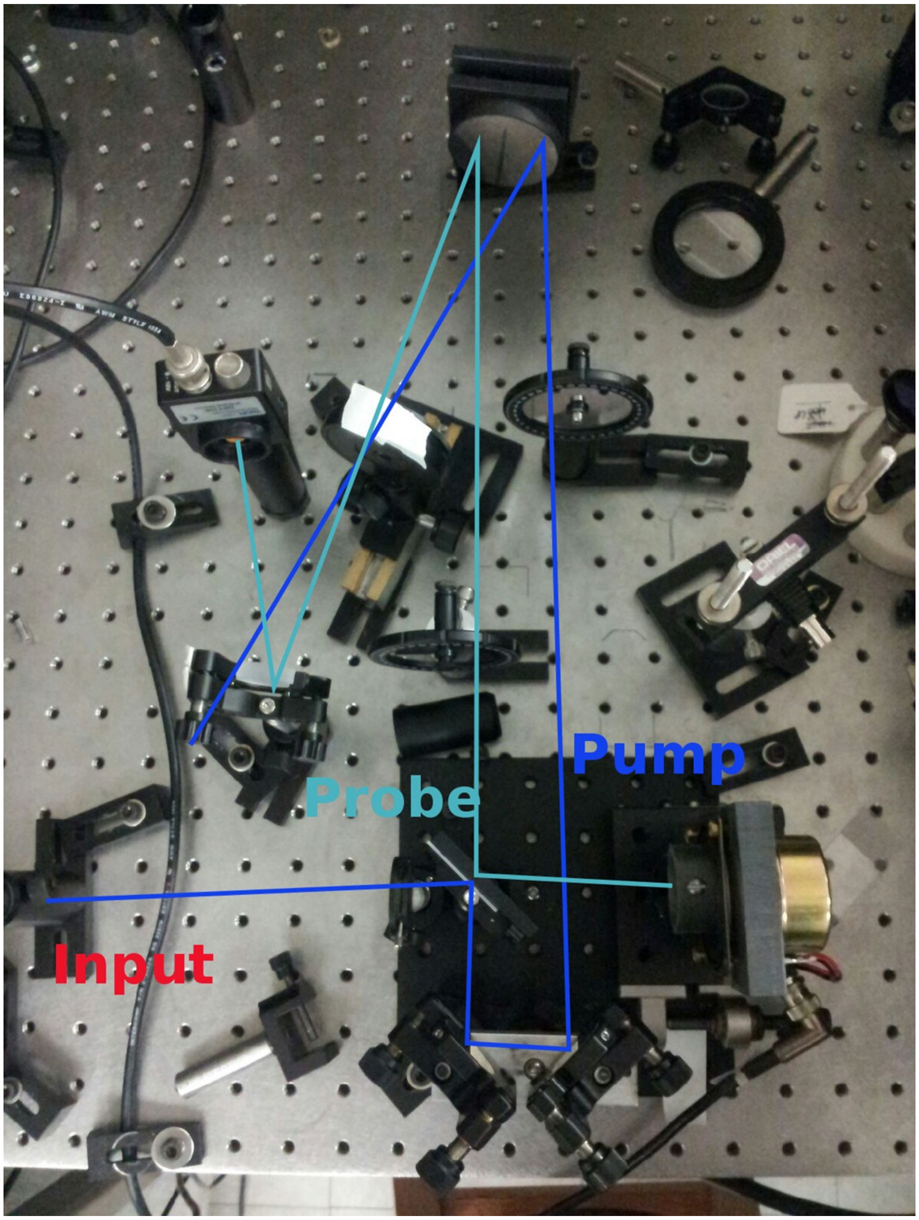
Pump
Probe
Input

**Figure A5.3.** Experimental Setup of two-photon absorption (TPA) autocorrelator for the determination of 266 nm pulse widths.

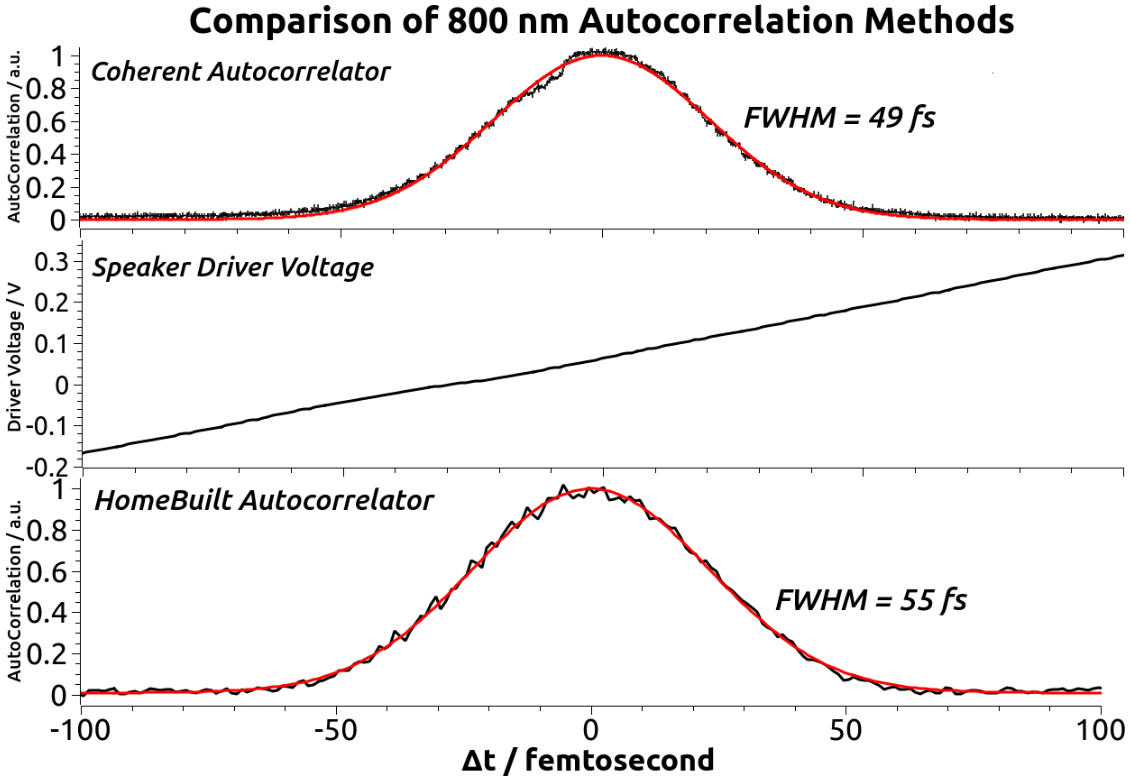

**Figure A5.4.** Comparison of commercial autocorrelator (top) and homebuilt autocorrelator (bottom) collected using SHG in BBO. The voltage waveform used to drive the speaker for scanning time delay (middle).

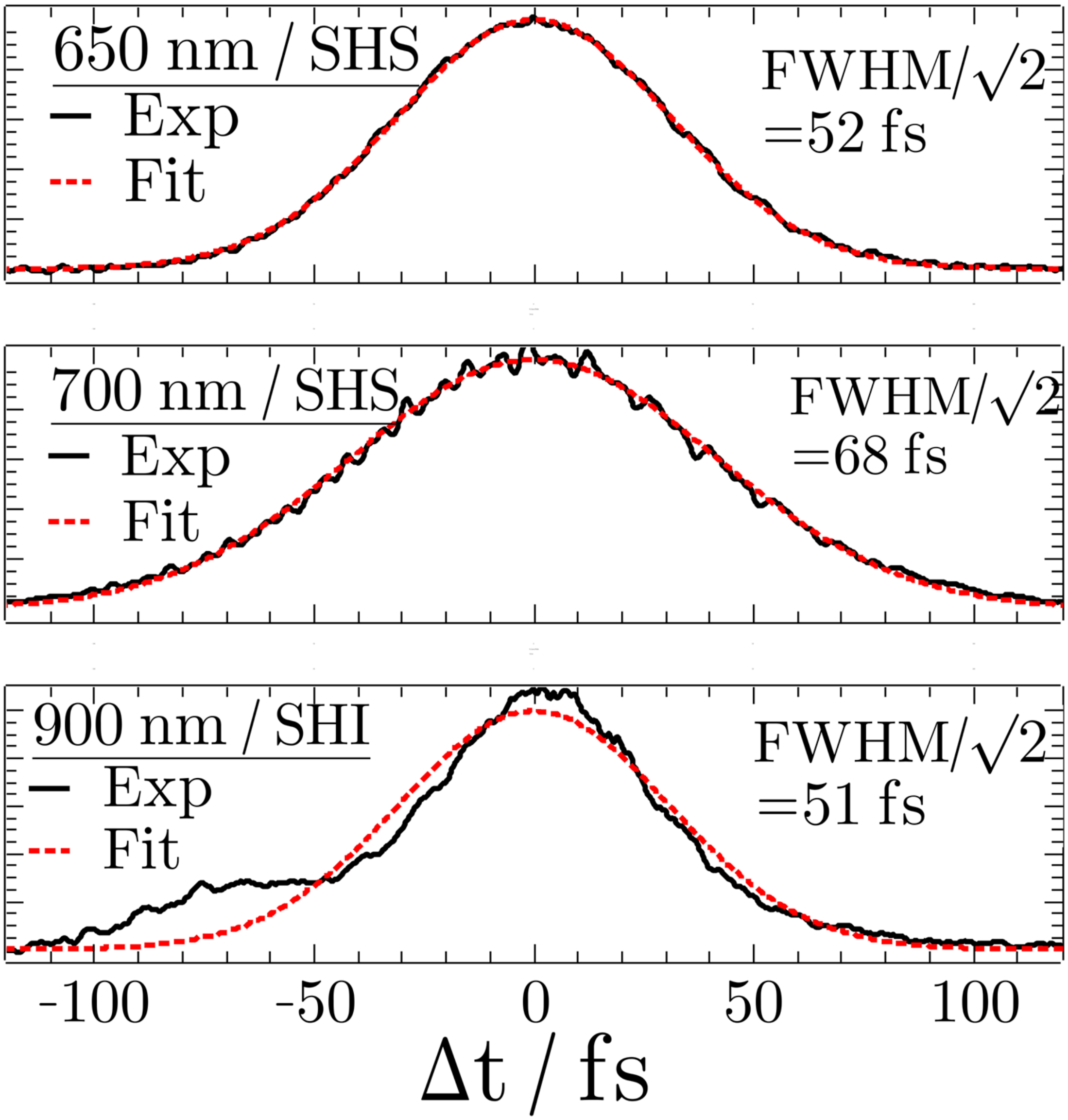

**Figure A5.5.** Autocorrelation of various OPA wavelengths using SHG in BBO.

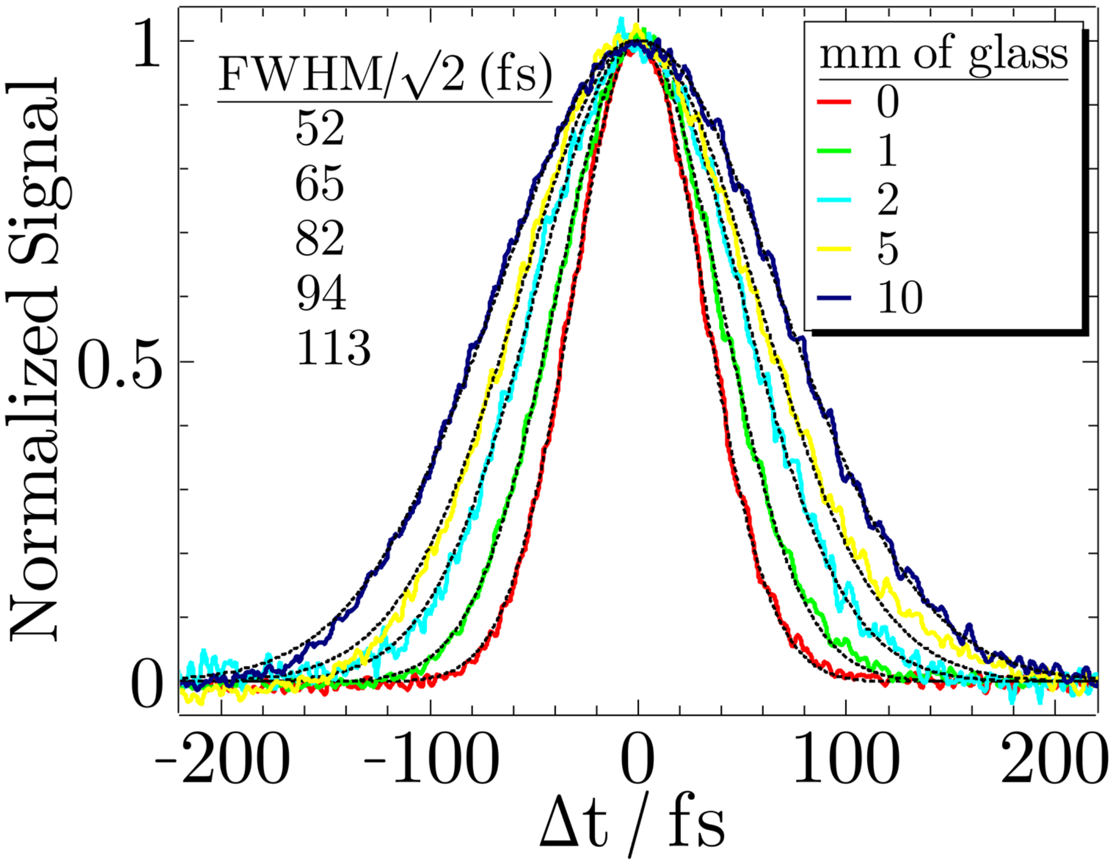

**Figure A5.6.** Observation of pulse broadening due to BK7 glass following autocorrelation of 650 nm using SHG in BBO.

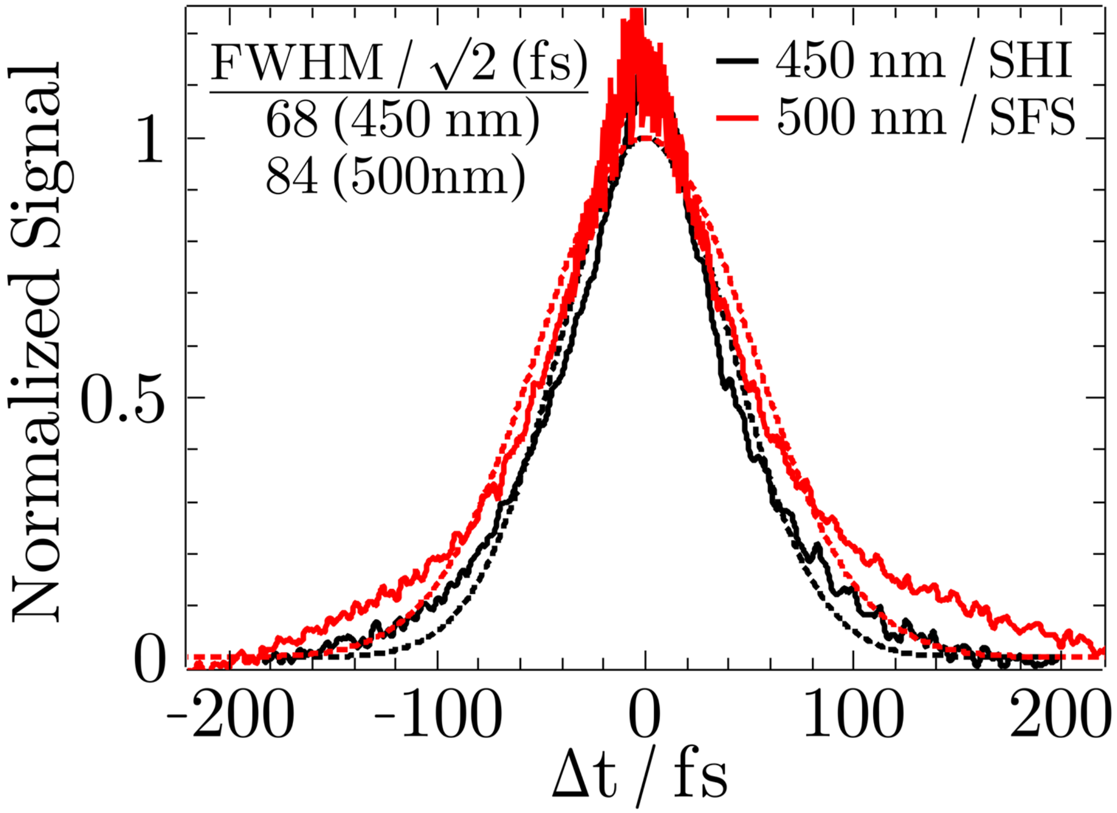

**Figure A5.7.** Autocorrelation of 450 & 500 nm using two-photon signal from a GaN (405 nm) laser diode.

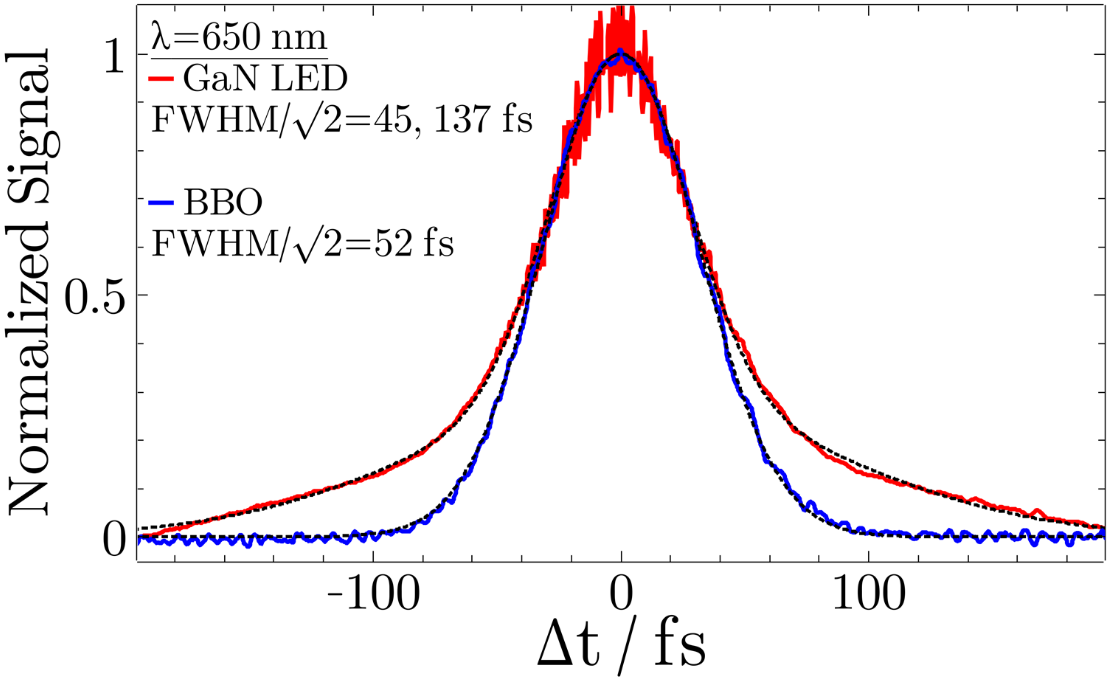

**Figure A5.8.** Comparison of autocorrelation methods for 650 nm by SHG in BBO or by two-photon signal in GaN. Note that the GaN LED has a broad Gaussian background that requires a bi-Gaussian Fit in order to extract the true, sharper autocorrelation feature that is within 15% of the autocorrelation results in BBO.

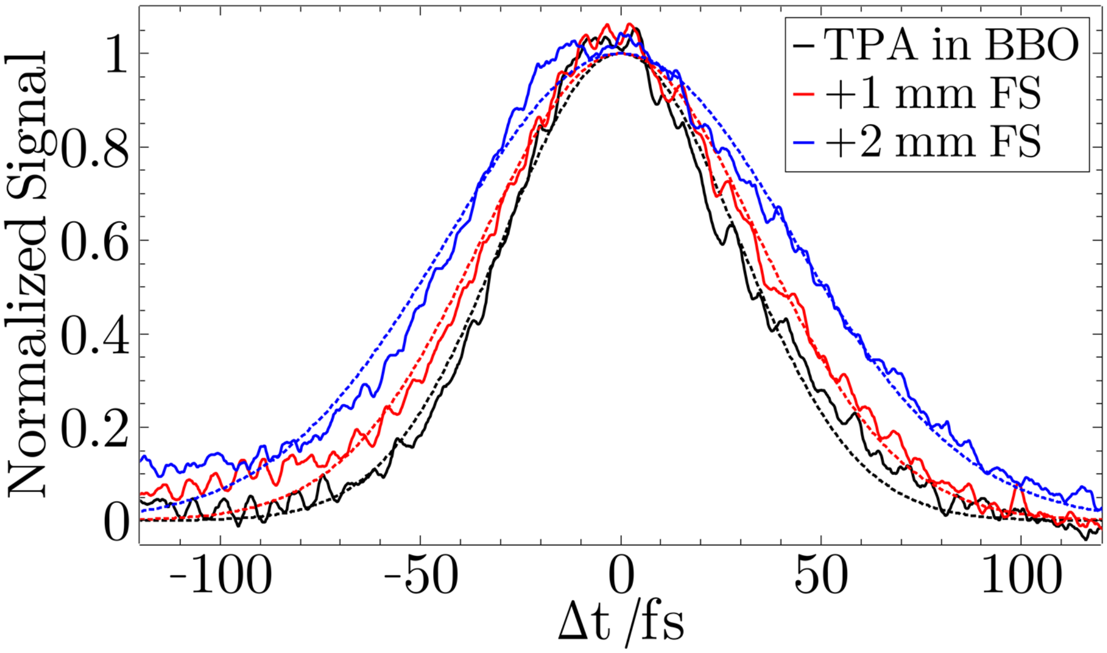

**Figure A5.9.** TPA autocorrelation of 266 nm in 200 µm BBO in addition to the pulse broadening induced by the addition of fused silica to the beam path. The FWHM/√2= 49, 57 and 71 fs as the pathlength of fused silica increases from 0 to 2 mm.

## A5.6 References

(1) Kozma, I. Z.; Baum, P.; Schmidhammer, U.; Lochbrunner, S.; Riedle, E. Compact Autocorrelator for the Online Measurement of Tunable 10 Femtosecond Pulses. *Rev. Sci. Instrum.* **2004**, *75* (7), 2323–2327.

(2) Cannone, F.; Chirico, G.; Baldini, G.; Diaspro, A. Measurement of the Laser Pulse Width on the Microscope Objective Plane by Modulated Autocorrelation Method. *J. Microsc.* **2003**, *210* (2), 149–157.

(3) Feurer, T.; Glass, A.; Sauerbrey, R. Two-Photon Photoconductivity in SiC Photodiodes and Its Application to Autocorrelation Measurements of Femtosecond Optical Pulses. *Appl. Phys. B Lasers Opt.* **1997**, *65* (2), 295–297.

(4) Sharma, A. K.; Naik, P. A.; Gupta, P. D. Real-Time Autocorrelator with Enhanced Temporal Scan Range for Measurements of Ultrashort Laser Pulses. *Opt. Laser Technol.* **2007**, *39* (3), 465–469.

(5) Dudley, J. M.; Reid, D. T.; Sibbett, W.; Barry, L. P.; Thomsen, B.; Harvey, J. D. Commercial Semiconductor Devices for Two Photon Absorption Autocorrelation of Ultrashort Light Pulses. *Appl. Opt.* **1998**, *37* (34), 8142.

(6) Loza-Alvarez, P.; Sibbett, W.; Reid, D. T. Autocorrelation of Femtosecond Pulses from 415–630 Nm Using GaN Laser Diode. *Electron. Lett.* **2000**, *36* (7), 631.

(7) Streltsov, A. M.; Moll, K. D.; Gaeta, A. L.; Kung, P.; Walker, D.; Razeghi, M. Pulse Autocorrelation Measurements Based on Two- and Three-Photon Conductivity in a GaN Photodiode. *Appl. Phys. Lett.* **1999**, *75* (24), 3778–3780.

(8) Homann, C.; Krebs, N.; Riedle, E. Convenient Pulse Length Measurement of Sub-20-Fs Pulses down to the Deep UV via Two-Photon Absorption in Bulk Material. *Appl. Phys. B* **2011**, *104* (4), 783.

(9) Dragonmir, A.; McInerney, J. G.; Nikogosyan, D. N. Femtosecond Measurements of Two-Photon Absorption Coefficients at λ = 264 Nm in Glasses, Crystals, and Liquids. *Appl. Opt.* **2002**, *41* (21), 4365.

(10) Osvay, K.; Ross, I. N.; Hooker, C. J.; Lister, J. M. D. Laser-Excited Nonlinear Properties of BaF2 and Its Application in a Single-Shot Spatially Insensitive Autocorrelator. *Appl. Phys. B Lasers Opt.* **1994**, *59* (3), 361–365.

(11) Le Blanc, S. P.; Szabo, G.; Sauerbrey, R. Femtosecond Single-Shot Phase-Sensitive Autocorrelator for the Ultraviolet. *Opt. Lett.* **1991**, *16* (19), 1508.

(12) Kleimeier, N. F.; Haarlammert, T.; Witte, H.; Schühle, U.; Hochedez, J.-F.; BenMoussa, A.; Zacharias, H. Autocorrelation and Phase Retrieval in the UV Using Two-Photon Absorption in Diamond Pin Photodiodes. *Opt. Express* **2010**, *18* (7), 6945.

# Appendix 6

# Details Regarding Prism-Based Femtosecond Transient Absorption Experiment: PDA Operation, Optical Setup and Instructions for Daily Use

## A6.1 PDA operation and synchronization

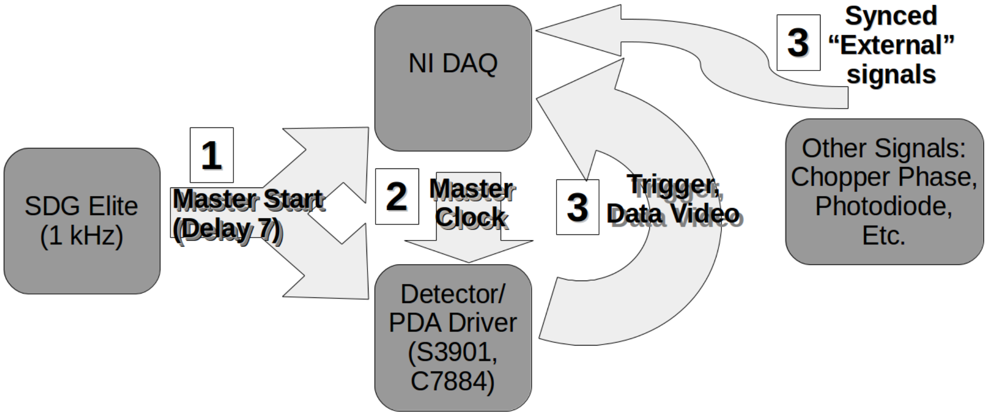
NI DAQ
3
Synced
“External”
signals
Other Signals:
Chopper Phase,
Photodiode,
Etc.
SDG Elite
(1 kHz)
1
Master Start
(Delay 7)
2
Master
Clock
3
Trigger,
Data Video
Detector/
PDA Driver
(S3901,
C7884)

**Figure A6.1.** Flowchart for operation of photodiode arrays (PDA). (1) The laser timing box (SDG Elite) initiates data acquisition by triggering a DAQ that (2) outputs a clock to the PDA driver for reading pixels. (3) Finally the PDA driver outputs a trigger to read the pixel data that can also be used to synchronize other external signals, such as choppers and photodiodes.

### *A6.1.1 Start-up*

- Turn on power supply (check the following parameters: 12-12.5 V, and series)

- NEVER input start and clock signals before the PDA power supply has been turned on! The labview program has checks in place to prevent this from happening.

- connect start to Delay 7 and master clock to clk

## A6.2 Synchronizing the START and Clock signals

### *A6.2.1 Background and Timing Diagram*

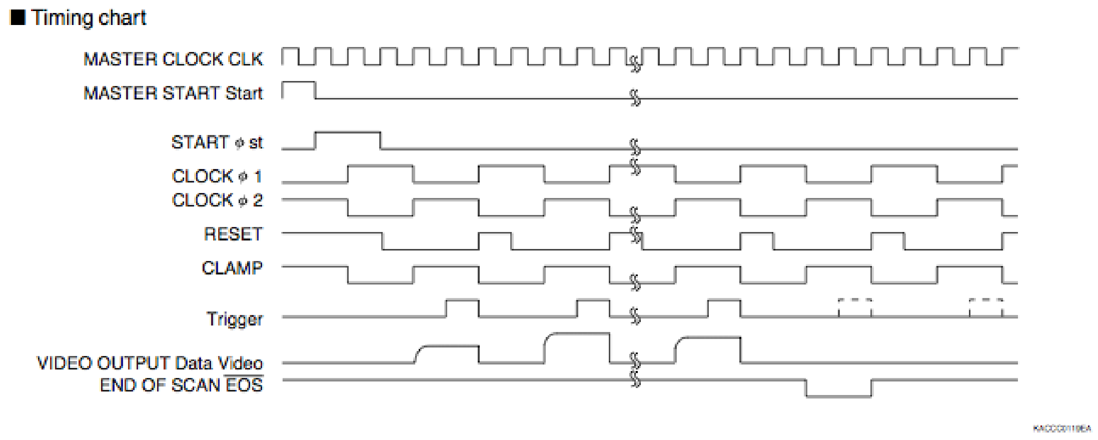
■ Timing chart
MASTER CLOCK CLK
MASTER START Start
START φ st
CLOCK φ 1
CLOCK φ 2
RESET
CLAMP
Trigger
VIDEO OUTPUT Data Video
END OF SCAN EOS

**Figure A6.2.** Timing diagram for S3901 NMOS array using C7884 driver. The master clock (CLK) and master start (Start) are the necessary inputs for driving pixel readout. The C7884 driver uses CLK and Start to generate the rest of the signals with Trigger providing the synchronization for data collection of the Video output (Data Video) using a DAQ.

It is VERY important that the start and clock signals are synchronized. Briefly, Delay 7 (PFI 0) is used to initiate the clock pulse train that reads off each pixel and this pulse train is assigned to Master Clock (PFI 12). The PDA requires a single start pulse which is split from Delay 7.

### *A6.2.2 How to perform Synchronization*

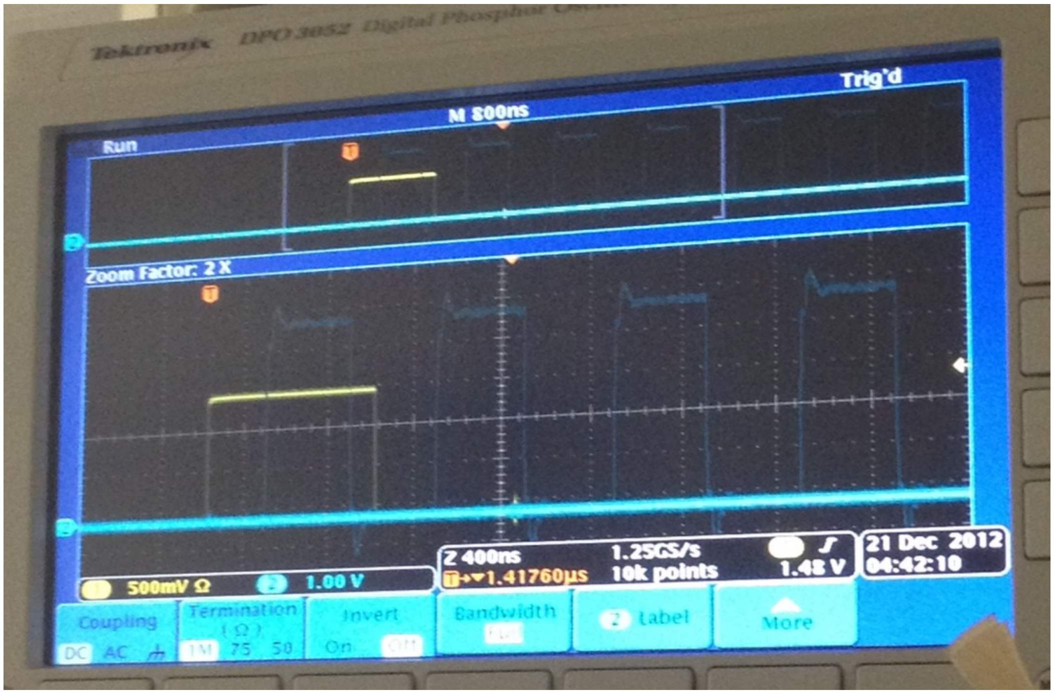
Tektronix DPO 3052 Digital Phosphor Oscilloscope
Trig'd
M 800ns
Run
Zoom Factor: 2 X
500mV Ω
1.00 V
Z 400ns
1.41760µs
1.25GS/s
10k points
1.48 V
21 Dec 2012
04:42:10
Coupling
DC AC
Termination (Ω)
1M 75 50
Invert
On Off
Bandwidth
Full
Label
More

**Figure A6.3.** Picture of Synchronization waveforms with the master start in yellow and master clock in blue. Note that the start pulse encompasses the first master clock pulse.

- Insert master clock and Delay 7 into an oscilloscope. Use Delay 8 as your trigger on the oscilloscope as well.

- Open "PDA_Driver_v1.vi". Use frequency 1.1 e+6. This utilizes an appropriate integration time without extending beyond the 1 ms time between pulses (1kHz rep rate).

- Adjust the pulse width (0.8-1 us) and delay time of Delay 8 using the SDG elite until the trigger covers the 1st clock pulse. Make sure the delay is set so that the trigger fall signal is between the 1st and 2nd clock pulse and is outside of the clock jitter.

## A6.3 Overview of Experimental fs-TAS Setup and Dual Spectrographs

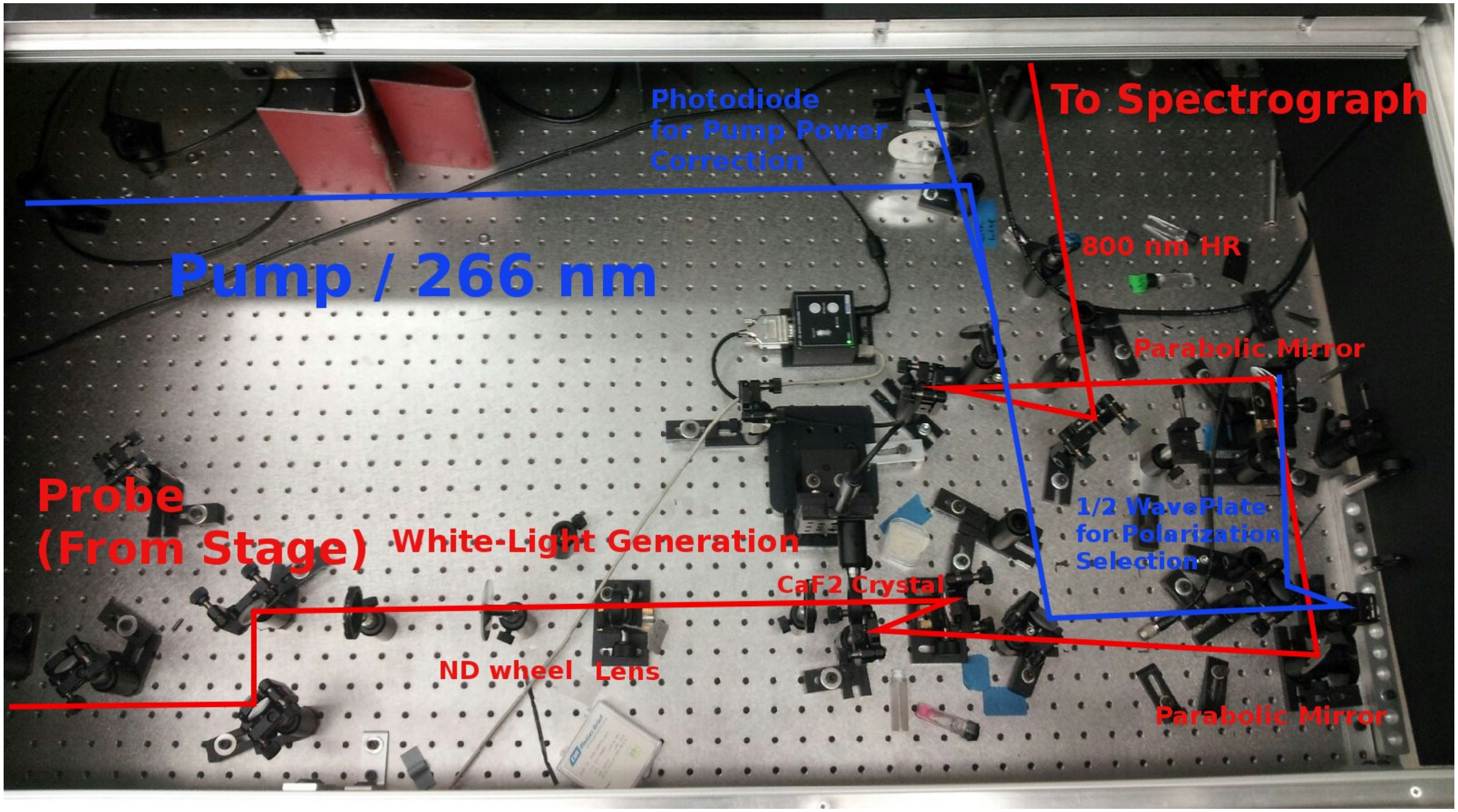
Photodiode for Pump Power Correction
To Spectrograph
Pump / 266 nm
800 nm HR
Parabolic Mirror
Probe (From Stage)
White-Light Generation
1/2 WavePlate for Polarization Selection
CaF2 Crystal
ND wheel
Lens
Parabolic Mirror

**Figure A6.4.** Layout of Broadband fs-TAS Experiment with annotated Pump (blue line/text) and Probe (red line/text) lines.

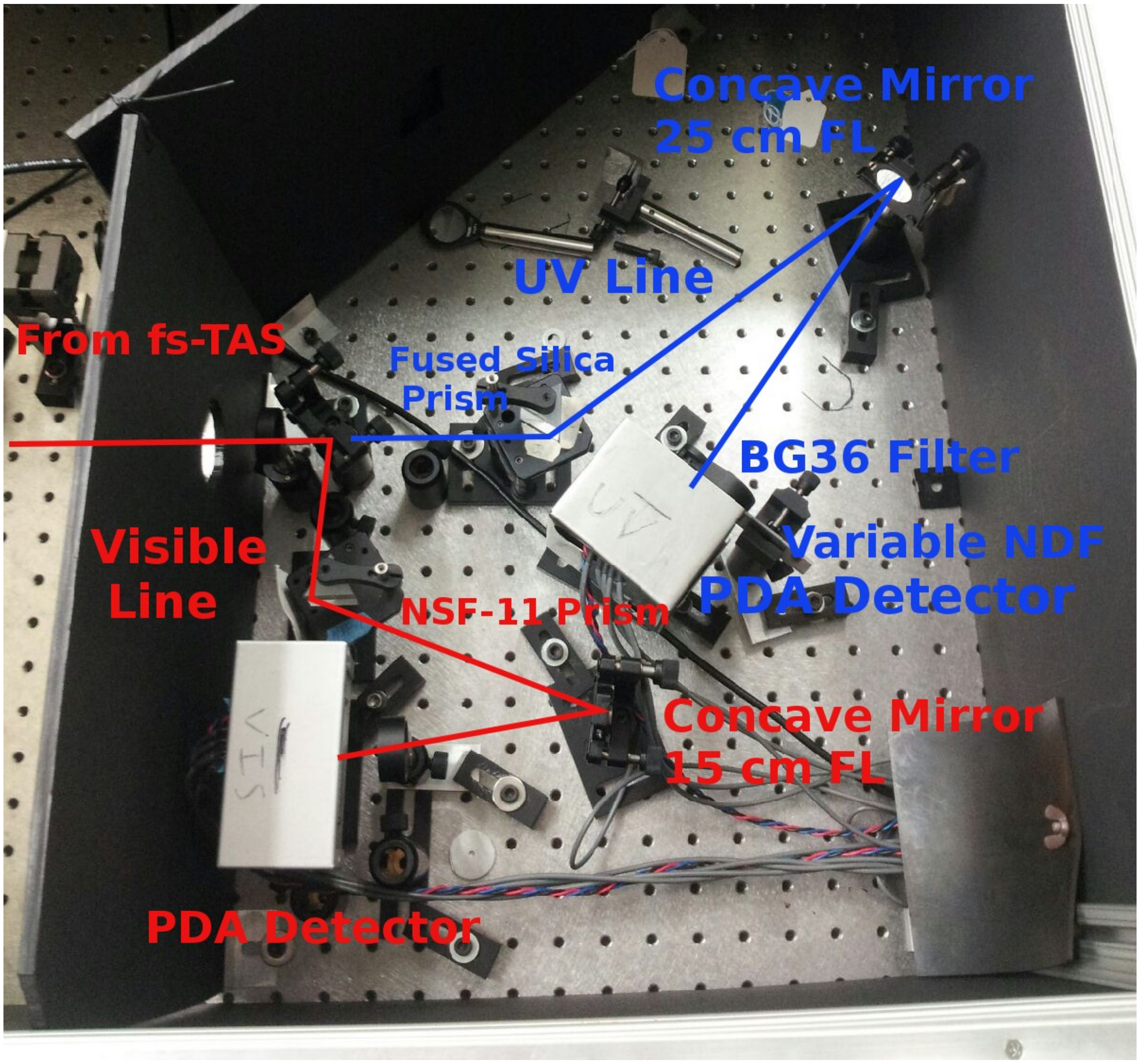
Concave Mirror
25 cm FL
UV Line
From fs-TAS
Fused Silica
Prism
BG36 Filter
Visible
Line
Variable NDF
PDA Detector
NSF-11 Prism
Concave Mirror
15 cm FL
UV
VIS
PDA Detector

**Figure A6.5.** Dual Spectrographs for wavelength dispersion of UV (blue line/text) and Visible (red line/text) wavelengths allowing for simultaneous ultra-broadband (300-1000 nm) collection of fs-TAS spectra.

## A6.4 Calibration and Setup Procedure for Prism-Based fs-TAS Instrument

### 1. Pre-Experimental Setup: Alignment & Calibration

### 1A. Optical Set-up

1. Align Stage by using permanent iris pair running parallel to WLG.

2. Adjust Focusing & collimation of probe beam.

3. Center diverging WL onto concave mirror.

4. Adjust pinion stage of concave mirror to collimate beam (roughly)

5. Use mirror after 2nd parabolic mirror to direct WL beam far distant to check collimation..

6. Place beamblock/card as far away from 2nd parabolic mirror as possible. This will be used for optimizing the collimation of the probe.

7. Adjust pinion stage of second parabolic mirror, until the beam spot is as small/collimated as possible. **Adjust pinion stage but don't adjust the position on table! (See Note below)**

8. Adjust the position of the concave mirror, until the beam spot is as small/collimated as possible.

9. Adjust horizontal and vertical tilt of mirror between concave mirror and 1st parabolic mirror to make beam as circular as possible. You will notice the beam will streak, or look like a comet when you are too far up or down or side to side.

10. Repeat steps 5-7 until beam is circular and well collimated.

11. Remove mirror after 2nd parabolic mirror.

Note: It is important to **never move the position of both parabolic mirrors.** They are aligned good enough that fine adjustment is controlled by the mirror before them. It is incredibly difficult to adjust the parabolic mirrors finely by hand so the easiest solution is to keep them in place. Don't move them, only adjust the knob for the pinion stage.

12. Align WL beam through Irises into prism spectrograph by "dog-legging".

### 1B. Collect Calibration File(s)

1. Collect Reference and Background file with an average of >1000, making sure to close spectrograph lid.

2. Use flip mounts to collect transmission of LP filters or absorption of bg-36 filter. Close lid, click absorption or transmission, and save spectra.

### 1C. Pixel to Wavelength Mapping

1. Import filter file(s) and enter the wavelength at each pixel for a peak, valley or half rise.

2. Re-run program and check that the fit to experimental points is good.

### 2. TA Experiment Setup & Data Collection

### 2A. TA Tweak Mode

1. Turn on Chopper, make sure its set at 500 Hz.

2. Turn on TA Tweak mode, set averaging ~100.

3. Move to a Delay/Position after time zero. If time zero is not known it can be found within ~.5 ns using a photodiode and oscilloscope.

4. After preparing pump beam: Align beam through chopper (checking phase), through lense, and into sample on top of probe spot. The lens position should be adjusted so that the pump spot is ~5 times larger than the probe spot. When the pump and probe spot become nearly equal in size overlaps become difficult to find, the pump can excite a fraction of the probe spot (spatial chirp), and as the stage moves the overlap can change. So always keep your pump spots big compared to the probe.

5. Finely adjust overlap while monitoring TA tweak mode until the maximum signal is acheived. Flip chopper if signal is inverted.

6. Find time zero by finding the stage position directly before the first sign of TA signal is seen. Take note of the stage position.

### 2A. TA Data Collection Mode

1. Enter Time-Zero, set chopper flip, name your file, set averages, and enter time delay text file.

2. Start Program. TA data collection will begin.

# Appendix 7

# Nanosecond to Microsecond Transient Absorption

## A7.1 Experimental Details for Nanosecond to Microsecond Transient Absorption

The ns/μs TA experiment utilizes an auxiliary light source, a LED or laser diode, that can be electronically triggered relative to the amplifier output allowing for time delays to be achieved up to the laser repetition rate. The experimental setup requires the synchronization of the pump and probe as illustrated in Figure A7.1 The lasing timing electronics (SDG Elite) provide a 1 kHz signal to a chopper that is reduced to 250 Hz for optical chopping of the pump pulse and another 500 Hz signal that triggers the pulsing of the LED or laser diode at the same rate. The 4 resultant optical phases are shown in the inset of Figure A7.1 that allow for fluorescence correction of the transient absorption signal.

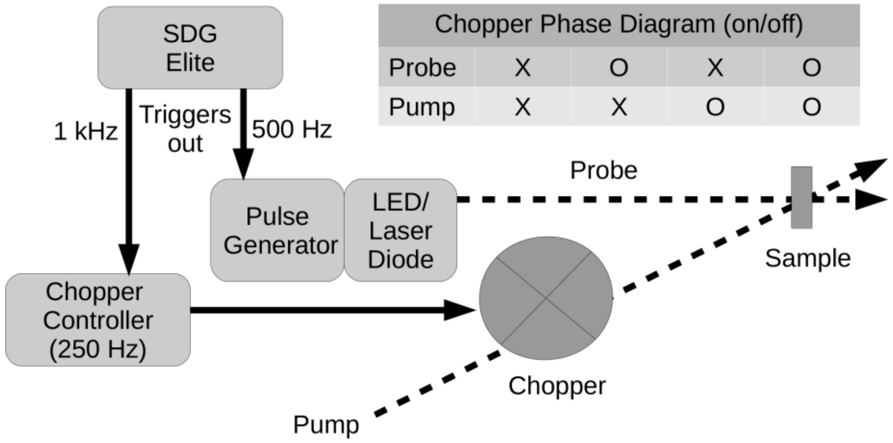
SDG Elite
1 kHz
Triggers out
500 Hz
Pulse Generator
LED/ Laser Diode
Probe
Sample
Chopper Controller (250 Hz)
Chopper
Pump

| Chopper Phase Diagram (on/off) | | | | |
|---|---|---|---|---|
| Probe | X | O | X | O |
| Pump | X | X | O | O |

**Figure A7.1.** Schematic for experimental ns/μs TA setup

## A7.2 Description of Pulse Generation Electronics

Two pulse generators are available in the lab that vary in their output voltage/current and time resolution. The first is a commercial ps to ns laser diode driver (Highland Technology T165) that provides ~1 ns time-resolution but with low current/voltage limited to 400 mA/~1V. The reader is directed to the manufacturer's website for a list of specifications and an operation manual for this piece of equipment. The second pulse generator is a home-built circuit with >1 A and ~18 V pulse output that offers higher light intensity, broadband spectral coverage when coupled with a white-light LED, and a time resolution of ~300 ns. The circuit is comprised of 2 parts: a pulse width modulator (PWM) and the amplification stage. The PWM delays a replica of the input pulse using a Schmitt trigger and RC circuit that is followed by an AND TTL logic gate. The timing diagram for the PWM circuit is shown in Figure A7.2. The PWM circuit

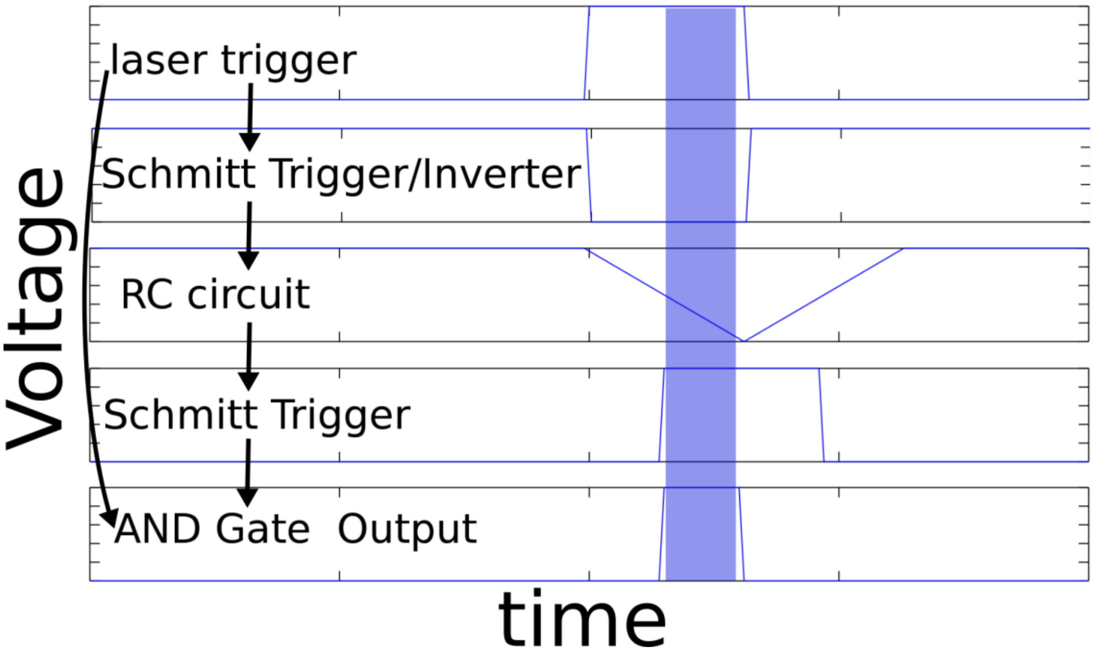

**Figure A7.2** Timing diagram for PWM circuit.

allows for pulse widths less than that achievable using the SDG Elite with a minimum pulse width of 500 ns. The output of the PWM circuit is then amplified using a MOSFET driver and MOSFET to generate a 18V and few Amp pulse from the weak initial TTL pulse. The circuit is shown in Figure A7.3 and the corresponding part numbers for the IC's are provided in Table A7.1.

**Table A7.1.** Description and part numbers for IC components shown in Figure A7.3

| Label | Description | Part number |
|---|---|---|
| A | 5V Linear Voltage Regulator | MC78M05BTG |
| B | Schmitt Trigger Inverter | SN74HC14N |
| C | TTL AND Logic Gate | SN74HC08N |
| D | MOSFET Driver | MIC4452YN |
| E | N-channel Enhancement Mode MOSFET | DMG4N65CTI |

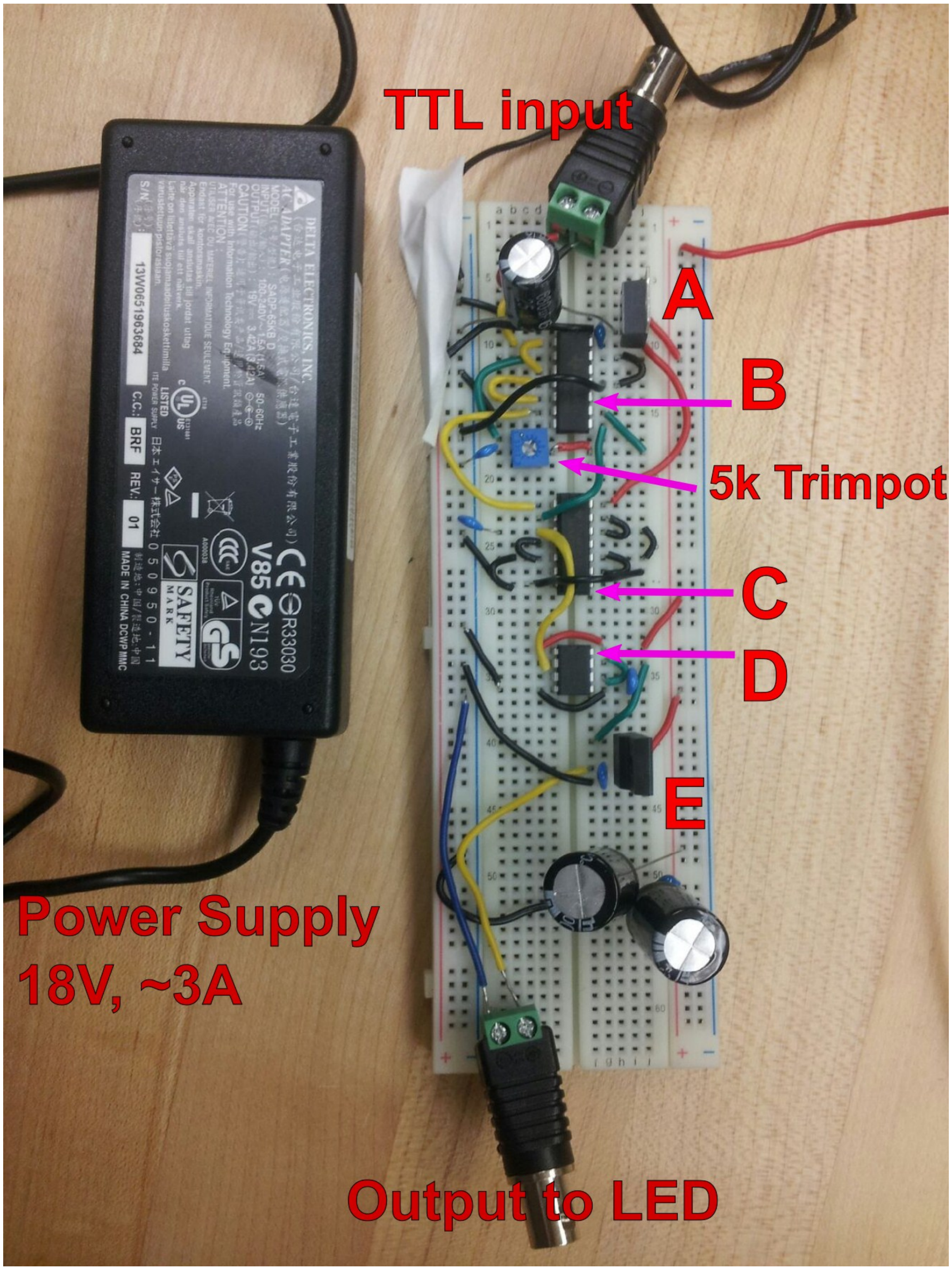
TTL input
A
B
5k Trimpot
C
D
E
Power Supply
18V, ~3A
Output to LED

**Figure A7.3.** Homebuilt LED pulsing circuit with IC description and part numbers provided in Table A7.1. Small blue capacitors are 1 nF while large black capacitors are 1 F.

# Appendix 8

## Global Analysis Algorithm

### 7.1 MATLAB Code for Global Analysis of Transient Absorption Spectra

```
function MultiSVDconv_wEr_v3(file,lambda,Range1,Range2,stop,model,fitTyp1)
%% Singular Value Decomposition
% The Kinetic Model must be adjusted to fit the Data!
% lambda: use this wavelength for determining the instrument response.
% stop: last time delay to fit.
%       rank *(!Set automatically now!): sets the number of spectral components.
%           Choose a value by viewing the columns of the U and S matrix and
%           noting how many columns have data/a trend compared to random
%           noise.
% Range1 & Range2 : Lower and Upper Bounds on Wavelengths to Fit
% fitTyp1: Choose SVD (fit to V*-V) = 0
%       or SVD-Based MLS (fit A*-A) = 1
%           See Hendler & Shrager. J. Biochem. Biophys. Meth. 1994, 28, 1-33.
% Model: Choose kinetic model-
% * All models contain one extra species/function that is not part of the kinetic
%       fit. It includes the IRF and is used to account for coherent
%       artifacts that should clean up the fit within the pump-probe
%       temporal overlap.

%              !!!Rank 2!!!
%           Kinetic Interconversion Models
%           9. A -> B
%           10. A -> B, A -> C
%           11. A -> B (biexp decay of A, B=1-A)
%           12. B <-> A -> C, B is undetected!
%           13. A -> B -> C (C is undetected!)
%           14. A -> B -> C -> D (A , D is unobserved)
%           15. A -> B -> C, A -> D , (A and B are detected!)

%              !!!Rank 3!!!
%           17. A -> B -> C
%           18. A -> B, C -> D (D is undetected!)
%           20. A -> B -> C, Bo is not equal to Zero!
%           21. A -> B (biexp decay of A, B=1-A), C -> D (D is undetected!)
%           22. A -> B -> C, A -> D , (A, B, and D are detected!)
%           23. B <-> A -> C
%           24. C <- A -> B -> C
%           25. A -> C <- B
%           26. A -> C <- B (Ao =X Bo)
%           27. A -> B -> C -> D , (D is undetected!)

%% Import Data
full = importdata(file);
[r c] = size(full);

t=full(1,2:c);
WL=full(2:r,1);
[LastWL x]=size(WL);
data = full(2:r,2:c);

%% Trim Data to Range1 to Range2
MinWL = WLIndex(Range1,WL);
MaxWL = WLIndex(Range2,WL);
data=data(MinWL:MaxWL,:);
[r3 c3] = size(data);
WL=WL(MinWL:MaxWL);

%% Trim Time Array set-up %%%%%%%%%%%

% Stop Data At
StopT=tIndex(stop,t);
t=t(1:StopT);

%remove Long Time points from data matrix
data=data(:,1:StopT);

%%%%%%%%%%%%%%%%%%%%%%%%%%%%%%%

%% ---   Specify Wavelengths to Display Trace    ---%%%
WLtrace1 = lambda;
trace1row = WLIndex(WLtrace1,WL);

%% Define Data Trace
trace1  = data(trace1row, :);

%% Set Data Fitting Values
options = optimset('TolFun',1.e-12,'MaxFunEvals',200,'MaxIter',200,'TolX',1e-12);

%% Determine stepsize for interpolation
[Blah, maxt0]=max(trace1);

if trace1(maxt0)>10
inc=2;
else
inc=0.05;
```

```
end
inc
%% Determine t0 (redefine t1) and Sigma!!!

shortt0=tIndex(-0.5,t)
ts=t(shortt0-1:maxt0+2)
trace1s=trace1(shortt0-1:maxt0+2)

%% Determine conditions for us or fs TAS
if trace1(maxt0)>10
%Initial Conditions;
x0=[400 5e-4 0.01];
%lower bounds
xl=[50 0 -700];
%upper bounds
xu=[500 10 700];
else
 %Initial Conditions;
x0=[0.1 5e-4 0.01];
%lower bounds
xl=[0.05 0 -5];
%upper bounds
xu=[0.2 10 5];
end

[x resnorm residual exitflag output]=
lsqcurvefit(@fitFunct0ANDsigma,x0,ts,trace1s,xl,xu,options);
'Sigma      Amplitude      t0 adjust'
x
figure('name','Instrument Response');
plot(ts,fitFunct0ANDsigma(x,ts),ts,trace1s);

t0adj=x(3);
t=t+t0adj;

sigma1=x(1);
FWHMinfs=(sqrt(-2.*(sigma1.^2).*log(0.5)).*2).*1000
stop=stop+t0adj;

%% Select Rank
if model<=16
   rank=3;
else
   rank=4;
end
```

```
%%%%%%% Global Time Setup %%%%%%%%%%%%%%

% SVD %%%%%%%%%%%%%%
Data2=data;
transData=data;
[U,S,V]=svd(transData);

A=transData;
[Ur, Uc]=size(U);
[Vr, Vc]=size(V);

hold off;

%% Analysis of S
U=U(1:Ur,1:rank);

normalizeS=sum(sum(S));
Norm_S=S(1:8,1:8)./normalizeS

figure('name','S matrix Diagonal');
plot(1:1:8,diag(S(1:8,1:8)./normalizeS));

S=S(1:rank,1:rank);
V=V(1:Vr,1:rank);

%% Model Specific Surface Fitting
options = optimset('TolFun',1.e-15,'MaxFunEvals',500,'TolX',1e-15,'MaxIter',750);

%% Rank 2
%% Kinetic Models

% Kinetic: A -> B
if model==9
x0b = [10];
low = [1];
high = [5000];

if fitTyp==0
[x resnorm residual exitflag output]=
lsqcurvefit(@Vstar_K_AtoB,x0b,t,V,low,high,options);
else
[x resnorm residual exitflag output]=
lsqcurvefit(@Vstar_K_AtoB,x0b,t,A,low,high,options);
end
VstarFinal=Vstar_K_AtoB(x,t);
y=x;
```

```
% Uncomment next line to determine error in lifetime
%ErrAtoB(y,V,t,residual)
VstarFinal=Vstar_K_AtoB(x,t);
end

% Kinetic: A -> B, A -> C
if model==10
x0b = [1000 1000];
low = [1 1];
high = [10000 10000];

if fitTyp==0
[x resnorm residual exitflag output]=
lsqcurvefit(@Vstar_K_AtoB_AtoC,x0b,t,V,low,high,options);;
else
[x resnorm residual exitflag output]=
lsqcurvefit(@Vstar_K_AtoB_AtoC,x0b,t,A,low,high,options);;
end

VstarFinal=Vstar_K_AtoB_AtoC(x,t);
end

%% output Results and Residual for V

x
ResidualSquaredOfV=sum(transpose(sum(residual.*residual)))

%%%%%%%%%%%%%%%%%%%%%%%%%

%% Build Surface Fit
FFinal=F;
%H=transpose(pinv(HstarT));

H=transpose(V)*transpose(pinv(F));

Dstar=U*S*H;
Astar=Dstar*transpose(F);

%% Residual Plot
figure('name','Residual Plot','Position',[1 1 800 500])

EndT=length(t);
DataResidual=Astar-data;

%%%%%%%%% error analysis %%%%%%%%%%%
```

```
 preSSE=DataResidual.*DataResidual;
 SSE=sum(transpose(sum(preSSE)))

 FitMean=mean(mean(data));
 preSST=Astar-FitMean;
 SST=sum(transpose(sum(preSST.*preSST)));

 Rsquared=1-(SSE./SST)

 %% Plot and Normalize D Matrix or Species Associated Spectra (SAS)
figure('name','D Matrix','Position',[1 1 800 500])
D1=Dstar(:,1);
D2=Dstar(:,2);
maxD1 =max(abs(D1));
maxD2 =max(abs(D2));
scaleD2=maxD1./maxD2

 if rank==2
plot1=plot(WL,D1,WL,scaleD2.*D2,'LineWidth',2);
 end

  if rank==3
D3=Dstar(:,3);
maxD3 =max(abs(D3));
scaleD3=maxD1./maxD3

plot1=plot(WL,D1,WL,scaleD2.*D2,WL,scaleD3.*D3,'LineWidth',2);
  end

    if rank==4
D3=Dstar(:,3);
maxD3 =max(abs(D3));
scaleD3=maxD1./maxD3
D4=Dstar(:,4);
maxD4 =max(abs(D4));
scaleD4=maxD1./maxD4

plot1=plot(WL,D1,WL,scaleD2.*D2,WL,scaleD3.*D3,WL,scaleD4.*D4,'LineWidth',2);
    end

%% Save SVD Fit to Data %%%%%
FullSpec=[ [0 ; WL] [t-t0adj ; Astar]];
dir= pwd;
lines=[dir,'/SVDFitOut_', file];
dlmwrite(lines, FullSpec,'delimiter','\t');
```

```
FullSpec2=[ [0 ; WL] [t-t0adj ; data]];
dir= pwd;
lines=[dir,'/DataFitOut_', file];
dlmwrite(lines, FullSpec2,'delimiter','\t');

%%%%%%%%%%%%% Auxillary Functions %%%%%%%%%%%%%%%%%

%% Rank 2 %%%%%%%%%%%%%%%%
%% Kinetic Models
function Vstar1 = Vstar_K_AtoB(A,t)
%% A -> B
tau1=A(1);
Ao=1;

% Species A
Exp1=heaviside(mt).*Ao.*exp(-mt./tau1);
% Species B
Exp2=heaviside(mt).*Ao.*(1-exp(-mt./tau1));
% Convolute and Interpolate
GE1=conv(Gaus,Exp1);
GE2=conv(Gaus,Exp2);
GE1=interp1(mt,GE1(1,t0IndexConv-FirstTOZero:t0IndexConv-1+ZeroTOLast),t);
GE2=interp1(mt,GE2(1,t0IndexConv-FirstTOZero:t0IndexConv-1+ZeroTOLast),t);
% Coherent Artifact
CA=interp1(mt,Gaus,t);

F=transpose([GE1 ; GE2 ; CA]);

if fitTyp1==0
HstarT=pinv(F)*V;
Vstar1=F*HstarT;
else
H=transpose(V)*transpose(pinv(F));
Dstar=U*S*H;
Astar=Dstar*transpose(F);
Vstar1=Astar;
end
end

%% %%%%%%%%%%%%%%Rank 3 %%%%%%%%%%%%%%%%%
function Vstar1 = Vstar_K_AtoBtoC(A,t)
% #17
%% A -> B -> C
Ao=1;
tau1=A(1);
tau2=A(2);
```

```
k1=1./tau1;
k2=1./tau2;
% Species A
Exp1=heaviside(mt).*(Ao.*exp(-mt.*k1));
% Species B
Exp2=heaviside(mt).*((Ao.*k1./(k2-k1)).*(exp(-mt.*k1)-exp(-mt.*k2)));
% Species C
Exp3=heaviside(mt).*(Ao.*(1 + (1./(k1-k2)).*(k2.*exp(-mt.*k1)-k1.*exp(-mt.*k2))));
% Coherent Artifact
CA=interp1(mt,Gaus,t);

GE1=conv(Gaus,Exp1);
GE2=conv(Gaus,Exp2);
GE3=conv(Gaus,Exp3);
Exp1i=interp1(mt,GE1(1,t0IndexConv-FirstTOZero:t0IndexConv-1+ZeroTOLast),t);
Exp2i=interp1(mt,GE2(1,t0IndexConv-FirstTOZero:t0IndexConv-1+ZeroTOLast),t);
Exp3i=interp1(mt,GE3(1,t0IndexConv-FirstTOZero:t0IndexConv-1+ZeroTOLast),t);

F=transpose([Exp1i ; Exp2i ; Exp3i ; CA]);
if fitTyp1==0
HstarT=pinv(F)*V;
Vstar1=F*HstarT;
else
H=transpose(V)*transpose(pinv(F));
Dstar=U*S*H;
Astar=Dstar*transpose(F);
Vstar1=Astar;
end
end

% Find t0 and sigma
function fitFunc=fitFunct0ANDsigma(a,t3)
sigma1=a(1);
A1=a(2);
t0=a(3);

if inc<0.99
t4=t3(1):inc:(t3(end)+0.2);
else
t4=t3(1):inc:(t3(end)+5);
end
modTime=t3+t0;
t4=t4+t0;
LasttIndex=length(t4);
t0Index=tIndex(0,t4);
```

```
FirstTOZero=t0Index;
ZeroTOLast=LasttIndex-t0Index;

Q1=A1.*exp(-(t4.^2)./(2.*(sigma1.^2)));
Q2=heaviside(t4);
ExpConv=conv(Q1,Q2,'full');
Gconv=conv(Q1,Q1);

[maxI Ind]=max(Gconv);
t0IndexConv=Ind;
ExpConv=ExpConv(1,t0IndexConv-FirstTOZero:t0IndexConv-1+ZeroTOLast);

fitFunc=interp1(t4,ExpConv,modTime,'pchip','extrap');
end

function IndexF = FIndex(FindF,FArray)

   for o=1:length(FArray)
      if FArray(o) == FindF
         IndexF=o;
         break
      end
      if FArray(o) > FindF
         IndexF=o-1;
         break
      end
      if o==length(FArray)
      %If no element exists give the last one!
      'FDIst not found!'
       IndexF=o;
       break
      end
   end
end

function Index = WLIndex(FindWL,WLArray)

   for o=1:length(WLArray)
      if WLArray(o) == FindWL
         Index=o;
         break
      end
      if WLArray(o) > FindWL
         Index=o-1;
         break
      end
```

```
    end

end
function IndexT = tIndex(FindT,tArray)
    for o=1:length(tArray)
            if tArray(o) == FindT
                IndexT=o;
                 break
            end
            if tArray(o) > FindT
                IndexT=o-1;
                 break
            end
    end
end
end
```

## Appendix 9

## Curriculum Vitae

# Joshua A. Snyder

**Business Address:**
Department of Chemistry
The Johns Hopkins University
138 Remsen Hall
3400 N. Charles Street
Baltimore, MD 21218
(410) 516-4851
jsnyde35@jhu.edu

**Home Address:**
5812 Western Run Drive
Apt D.
Baltimore, MD 21209
(443) 255-3320

Education

**The Johns Hopkins University** Baltimore, MD
Graduate Student. Department of Chemistry. Research: Structure-dependence of nonadiabatic photochemistry in ortho-arenes and their cyclized intermediates. (2011-Present).

**Shippensburg University** Shippensburg, PA
Bachelor of Science, Chemistry, Magna Cum Laude, May 2011. Research: Correlation functions using complex and real time propagators

**Duquesne University** Pittsburgh, PA
National Science Foundation Research Experience for Undergraduates (NSF-REU),Summer 2010. Research: Computational Study of Carboxyphosphate in N5-CAIR Synthetase.

**Enzo Life Sciences Inc.** Plymouth Meeting, PA
Organic Laboratory Technician, Summer 2009. Research: Synthesis of SKI-1.

Awards

Langmir-Cresap Award/Fellowship (Fall 2014-Spring 2015)

NSF-REU Travel Award for Spring ACS Meeting of 2011, Anaheim, California

Dr. Louise Lienemann Scholarship, Shippensburg University (2010-2011)

New Economy Technology Scholarship, Pennsylvania Higher Education Assistance Agency (2009-2011)

Undergraduate Award for Achievement in Organic Chemistry
Sponsored by the American Chemical Society and the Joint
Polymer Education Committee (2009)

Research Experience

**The Johns Hopkins University** Baltimore, MD
Advisor:Arthur Bragg

Investigating structure-dependence of nonadiabatic photochemistry (electrocyclization) of ortho-arenes and the associated stabilities of photoproducts. Time-Resolved spectroscopies allow for experimental interrogation of the reaction progress and dynamics on the femtosecond and nanosecond time-scales. Techniques used include transient absorption spectroscopy (ultrafast to microsecond), femtosecond stimulated Raman spectroscopy, TCSPC and fluorescence spectroscopy. Experience with air-free and water-free sample preparation techniques (Glove-bag and Schlenk line) and various quantitative photo-physical/chemical analyses (Quantum yield of fluorescence and triplet formation, Fluorescence quenching/Stern-Volmer Analysis). Development and design projects include femtosecond and nanosecond transient absorption instrumentation, utilizing NMOS detection arrays, prism-based spectrograph design and calibration, implementation and design of LED based nanosecond pulsed light sources, as well as computer clustering for quantum chemistry calculations (GAMESS, Gaussian). Proficient in the use of modern computational chemistry methods (CASSCF, SF-TDDFT, Broken Symmetry DFT) and data acquisiton/analysis software (LabVIEW, MATLAB, Origin). (2011-Present).

**Shippensburg University** Shippensburg, PA
Advisor: Jeb Kegerreis

Development of fortran programs for evaluation of correlation functions useful for determining rate constants, raman cross-sections and diffusion coefficients. A focus on reducing computational time was approached using cyclic invariance within a trace and Monte-Carlo Integration. Gained invaluable experience with Fortran Programming, and Computational Methods. (2010-2011)

**Duquesne University** Pittsburgh, PA
Advisor: Jeffrey Evanseck

My project was to explore the life cycle of carboxyphosphate (CP) within $N^5$-CAIR Synthetase, a viable antibacterial drug target, using computational chemistry methods. Using the Gaussian computational package I developed a reaction coordinate for the formation and deactivation of the transient CP molecule. (Summer 2010)

Teaching Experience

**The Johns Hopkins University** Baltimore, MD

Physical Chemistry Lab I. Teaching Assistant.
Instructor for the Joule Thompson Experiment. Graded prelabs, lab reports, and answered questions from students. Responsible for stocking laboratory gases. (Fall 2011)

Introductory Chemistry II. Teaching Assistant.
Responsible for grading and proctoring exams, as well as one-on-one help sessions weekly with students. (Spring 2012)

Physical Chemistry Lab I. Teaching Assistant.
Instructor for the Joule-Thompson experiment. Graded Prelabs, Lab Reports, and answered questions from students. Assistant for the Speed of Sound experiment. (Fall 2012)

Physical Chemistry Lab III (Engineering Section). Teaching Assistant.
Instructor for the Joule-Thompson and Speed of Sound experiments. Graded prelabs, lab reports, and answered questions from students. (Fall 2012)

Experimental Methods in Physical Chemistry. Teaching Assistant & Lecturer.
Provided lectures for LabVIEW, Matlab, SolidWorks & Simion. Prepared and graded assignments for each topic. (Spring 2013)

Physical Chemistry Lab I. Teaching Assistant.
Instructor for the Joule-Thompson, Bomb Calorimetry and Effusion of Gases experiments. Graded Prelabs, Lab Reports, and answered questions from students. (Fall 2015)

Presentations

Student Oral and Poster Presentation for 2010 Summer Undergraduate Research Symposium at Duquesne University on "Computational Study of Carboxyphosphate in N5-CAIR Synthetase".

Poster Presentation at Spring ACS Meeting of 2011, Anaheim, California on "Life cycle of carboxyphosphate in N5-CAIR synthetase".

Oral and Poster Presentation on "Correlation functions using complex and real time propagators" at Shippensburg University Student Research Conference (Spring 2011).

Seminar on the Chemical Literature at Johns Hopkins University. "Coherent Control: Altering Molecular Destiny" (Spring 2014)

Recruitment Seminar at Shippensburg University.
"A Graduate Student's Guide to Graduate School and Photochemical Bond Formation" (Fall 2014)

Poster Presentation at Atomic and Molecular Interactions (AMI) Gordon Research Conference (GRC) "Structural control of nonadiabatic bond formation: The photochemical formation and stability of substituted 4a,4b- dihydrotriphenylenes" (Summer 2014)

Publications

"Ultrafast Excited-State Dynamics of *ortho*-Terphenyl and 1,2-Diphenylcyclohexene: The Role of "Ethylenic Twisting" in the Nonadiabatic Photocyclization of Stilbene Analogs." Smith, M. C.*; Snyder, J.*; Streifel, B.; Bragg, A. *The Journal of Physical Chemistry Letters.* **2013**, *4,* 1895.

"Structural and Solvent Control of Nonadiabatic Photochemical Bond Formation: Photocyclization of ortho-Terphenyl in Solution" Molloy, M.; Snyder, J.; Bragg, A. *The Journal of Physical Chemistry A.* **2014**, *118*, 3913.

"Structural Control of Nonadiabatic Bond Formation: The Photochemical Formation and Stability of Substituted 4a,4b-Dihydrotriphenylenes" Snyder, J.; Bragg, A. *The Journal of Physical Chemistry A.* **2015**, *119*, 3972.

"Aminofluorination of Cyclopropanes: A Multifold Approach through a Common, Catalytically Generated Intermediate" Pitts, C.; Ling, B.; Snyder, J.; Bragg, A.; Lectka, T. *Journal of the American Chemical Society.* **2016**, *138*, 6598.

"Structural Control of Nonadiabatic Photochemical Bond Formation: Photocyclization in Structurally Modified *ortho*-Terphenyls" Molloy, M.; Snyder, J.; DeFrancisco, J.; Bragg, A. *The Journal of Physical Chemistry A.* **2016**, *120*, 3998.

"Excited-state Deactivation Pathways and the Photocyclization of BN-doped Polyaromatics" Snyder, J.; Grüninger, P.; Bettinger, H.;

Bragg, A. **Under Review**.

"Impacts of Isoelectronic BN-doping on the Photochemistry of Polyaromatic Hydrocarbons: Photocyclization Dynamics of Hexaphenyl Benzene and Hexaphenyl Borazine." Snyder, J.; Grüninger, P.; Bettinger, H; Bragg, A. **In preparation**.

"Sub-Picosecond Nonadiabatic Bond Formation in *ortho*-arenes Revealed with Pump-repump-probe Spectroscopy." Snyder, J.; Bragg, A. **In preparation**.

* The authors contributed equally to this work.

References

Professor Arthur Bragg
Department of Chemistry
The Johns Hopkins University
138 Remsen Hall
3400 N. Charles Street
Baltimore, MD 21218
artbragg@jhu.edu

Professor Paul Dagdigian
Department of Chemistry
The Johns Hopkins University
138 Remsen Hall
3400 N. Charles Street
Baltimore, MD 21218
pjdagdigian@jhu.edu

Professor Thomas Lectka
Department of Chemistry
The Johns Hopkins University
New Chemistry Building 315
3400 N. Charles Street
Baltimore, MD 21218
lectka@jhu.edu

Professor Jeb Kegerreis
Department of Chemistry
Shippensburg University
Franklin Science Center
Shippensburg, PA 17257
jskegerreis@ship.edu

Professor Jeffrey Evanseck
Department of Chemistry & Biochemistry
Duquesne University
Mellon Hall
600 Forbes Avenue
Pittsburgh, PA 15282
evanseck@duq.edu